THÈSE

En vue de l'obtention du

DOCTORAT DE L'UNIVERSITÉ DE TOULOUSE

Délivré par :

Institut Supérieur de l'Aéronautique et de l'Espace

Présentée et soutenue par :
Audrey BIGAND
le vendredi 16 octobre 2020

Titre :
Évaluation de l'endommagement dans les structures composites en aéronautique généré par la contrainte foudre

Damage assessment on aircraft composite structure due to lightning constraints

---

École doctorale et discipline ou spécialité :
ED AA : Génie mécanique, mécanique des matériaux - Ingénierie des plasmas

Unité de recherche :
Institut Clément Ader

Directeur(s) de Thèse :

Mme Christine ESPINOSA (directrice de thèse)
M. Jean-Marc BAUCHIRE (co-directeur de thèse)

Jury :
M. Philippe TEULET Professeur Université Toulouse III (Paul Sabatier) - Président
M. Michel ARRIGONI Professeur ENSTA Bretagne - Rapporteur
M. Jean-Marc BAUCHIRE Professeur Université d'Orléans - Co-directeur de thèse
M. Pedro M. P. R. DE CASTRO CAMANHO Professeur Universidade do Porto
Mme Christine ESPINOSA Professeure ISAE-SUPAERO - Directrice de thèse
M. Franck FLOURENS Expert Exécutif Airbus
M. Philippe LALANDE Expert ONERA Palaiseau
M. Adrian MURPHY Professeur Queen's University Belfast - Rapporteur

Acknowledgements

Contents

Glossary

_____

Alu	_Aluminium_
CFRP	_Carbon Fibre Reinforced Polymer_
CS	_Certification Specifications_
Cu	_Copper_
DC	_Direct Current_
DCB	_Double cantilever beam_
DDM	_Diffuse Damage Model_
DGA-TA	_Direction Générale de l'Armement - Techniques Aéronautiques_
DIC	_Digital Image Correlation_
DMA	_Dynamic Mechanical Analysis_
ECF	_Expanded Copper Foil_
EDIFISS	_Effets DIrects de la Foudre Induits sur les Structures et Systèmes_
EEW	_Electrical Explosion of Wire_
ENF	_End Notch Flexure_
EOS	_Equation Of State_
EUROCAE	_EURopean Organisation for Civil Aviation Equipment_
fps	_Frame per second_
GFRP	_Glass Fibre Reinforced Polymer_
GREMI	_Groupe de Recherches sur l'Energétique des Milieux Ionisés_
gsm	_gram per square meter_
ICA	_Institut Clément Ader_
JWL	_Jones-Wilkins-Lee_
kA	_kiloAmpere_
LSP	_Lightning Strike Protection_
LWD	_Long Way of the Diamond_
MHD	_Magneto-Hydro-Dynamic_
N/A	_Not Applicable_
NDT	_Non Destructive Test_
ONERA	_Office National d'Etudes et de Recherches Aérospatiales_
PTFE	_PolyTetraFluoroEthylene_
SAE	_Society of Automotive Engineers_
SCF	_Solid Copper Foil_
SWD	_Short Way of the Diamond_
TTL	_Through-The-Lens_
VDLOAD	_Abaqus® Explicit user-Defined LOAD subroutine_
VUMAT	_Abaqus® Explicit User-defined MATerial subroutine_
W	_Tungsten_
WF	_WaveForm_
WFD	_WaveForm D_

Chapter 1

General Introduction

In the last 40 years, the use of composites has significantly increased in the aircraft industry, as carbon fibre reinforced composites present a higher strength and stiffness to mass ratio compared to metallic structures. These advantages have led aircraft manufacturers to progressively introduce composite technology in their products. Within the Airbus fleet, composites accounted for about 10% in the first model and rose to 50% with the brand-new A350 XWB. The big step has been to use composites for the fuselage and wing primary structures compared to previous programs.
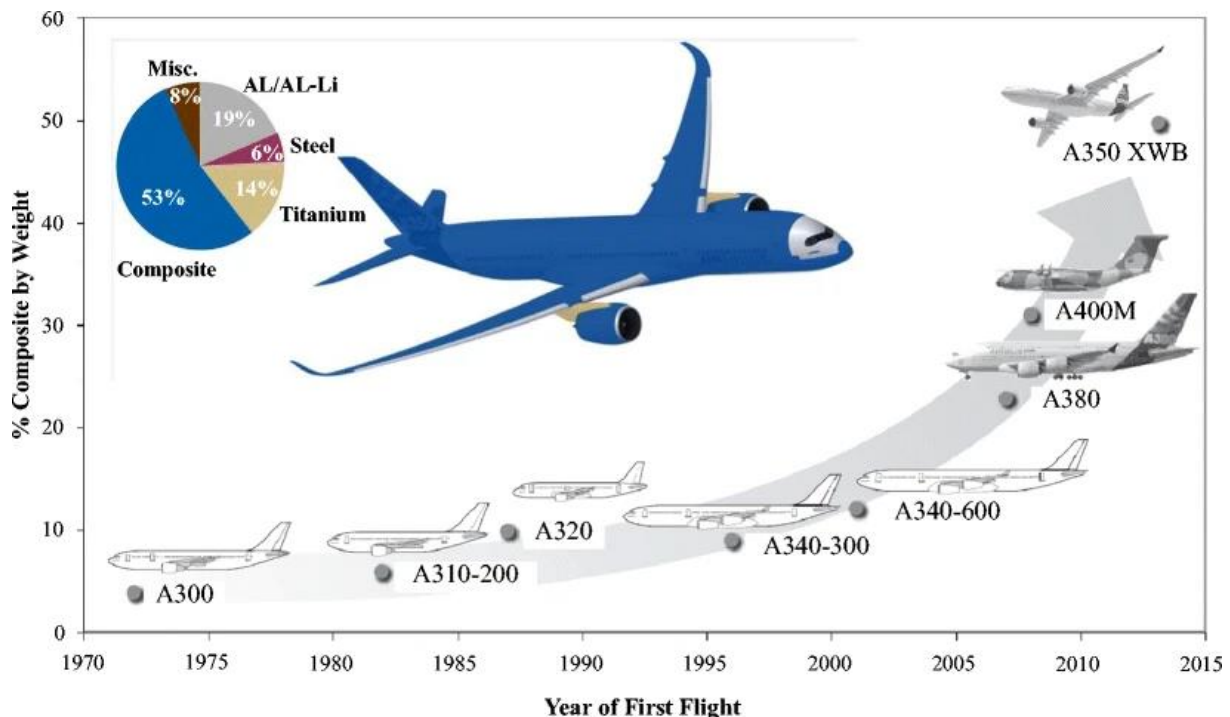
Figure 1-1: Composite use evolution in Airbus fleet [1]

The introduction of composites has strongly impacted the lightning certification strategy for this program. Metallic structures can easily sustain a lightning strike due to their high electrical conductivity that will dissipate the current without any major damage, which is limited to a small melting point in the worst case. Despite their excellent mechanical properties, composites are poor conductors, making them more susceptible to serious damage due to a lightning strike such as severe delamination, burning and possibly puncture [2]. In order to protect the composite structures, a lightning strike protection layer is applied on the external surface. This protection is usually a thin mesh made of metal (copper, bronze...) which has the function of a sacrificial ply that will dissipate the current and vaporize. Unfortunately, the presence of paint decreases the protective effect of the metallic

layer. As the damage is not completely avoided and can even be serious in thin structures, lightning tests are performed in laboratories in order to assess this damage and demonstrate a continuous safe flight and landing after a severe lightning strike. However, a lightning test campaign is very expensive and time-consuming. In the context of the development of an aircraft program, lightning validation can enter in the critical path for design validation as a modification of the structure or lightning strike protection may be necessary. It is thus important to have the right means to support design validation in line with the program milestones. During the A350 development, many lightning tests were performed prior to certification in order to validate the design of all the aircraft composite components, tests that cost hundreds of thousands of euros and took several months. For future programs, it is necessary to develop a better understanding of the lightning damage mechanism in painted structures and to build a modelling capability to support smoother development.

In this context, a research project funded by DGAC with industrial partners from the aircraft industries and academics was launched in 2015. The project named EDIFISS (Effets DIrects de la Foudre Induits sur les Structures et Systèmes) aimed to study the different consequences of a lightning strike. While not included in the EDIFISS project, this PhD contributes to it and has the objective of understanding the key parameters that influence the damage due to lightning in painted composites. Lightning is, indeed, an extremely rapid and multi-physics phenomenon which interacts with the structure, making the study and understanding very complex. Most of the existing scientific approaches consider two separate events: the lightning arc, on the one hand, is taken as a fixed and independent source of current; the bare composite, on the other hand, is considered as a collector which will be damaged due to electro-thermal induced effects, sometimes combined with mechanical ones. This PhD is a first attempt to analyse the complex interaction phenomena arising in the protection layers and the detrimental effect of the paint. Thus, a global approach is proposed which considers a complete flat panel representative of the real configuration of an aircraft component: the composite, the lightning strike protection layer, and the paint. This approach decomposes the phenomenon into four events from the source: the lightning arc, its interaction with the lightning strike protection layer at the surface of the panel, the paint effect and the first composite ply, and finally the composite structure and the consecutive damage.

In order to support this global approach, several collaborations were necessary. The first one was between the two co-supervisors of this PhD who come from two very different academic fields: Mechanics and Plasma physics. This unprecedented collaboration was very fruitful in order to develop our understanding of the composite damage mechanism due to a lightning strike. Christine Espinosa from the "Institut Supérieur de l'Aéronautique et de l'Espace" (ISAE-Supaéro) and the "Institut Clément Ader" (ICA UMR 5312) of the Université de Toulouse brought her knowledge of numerical approaches to the fast dynamic loading of composite structures and damage creation. Jean-Marc Bauchire from the "Groupe de Recherches sur l'Energétique des Milieux Ionisés" (GREMI UMR 7344) of the Université d'Orléans contributed his knowledge in numerical and experimental approaches to plasma

physics and electrical arcs. These laboratories, ICA and GREMI, and ISAE-SUPAERO engineering school contributed to the development of this work by providing their numerical and test facilities but also the support of their teachers and technicians. Airbus, through EDIFISS, provided its experience and the material for sample manufacturing and funding of the project. This thesis report is organised as follow:

Chapter 2 presents the lightning phenomenon and the associated risk on the composite structure. Previous work performed in order to model the damage is also reviewed. Based on overview, the methodology of the present work is presented.

Chapter 3 focuses on the source, i.e. the lightning arc and its root. A study of the free arc is performed and then confronted with its behaviour in interaction with the lightning strike protection. The effect of the paint is investigated. In order to support this development, Matlab® and COMSOL® were used for electro-thermal models and arc models.

Chapter 4 presents the lightning strike protection behaviour under such solicitation, since the lightning current flowing into the protection will heat it so quickly that it generates an explosion. This overpressure is characterized as it is an important source of mechanical load on the composite structure. Dedicated tests were performed at the GREMI laboratory with their pulse generator but also with a lightning generator of 20kA provided by Airbus. The samples were manufactured at ISAE and the sensors for the pressure and strain measurements were provided by ISAE. The test results were compared to models created also in Matlab® and COMSOL®.

Chapter 5 studies the paint and its mechanical properties as it has a significant impact on lightning damage generation due to its mechanical confinement effect. For this purpose, original manufacturing procedures and normalized tests were designed and carried out to study this layer. This manufacturing was supported by the ISAE team and Airbus paint specialists. DMA tests were performed at ICA but also RESCOLL, a research company specialised in polymers. Tension and trouser tear tests were performed at ISAE. Finally, adhesion tests were done based on laser shock solicitation by SIMCHOC, a research company specialised in shock propagation in material. The mechanical model for the paint was built in Abaqus®.

Chapter 6 combines all the parameters studied in the previous chapters in order to create a complete mechanical model based on a mechanical solicitation, equivalent to the lightning strike, and a damage law. This model, built in Abaqus®, is confronted to lightning tests performed at DGA-TA in order to assess its validity and limitations in damage prediction. These final models required High Performance Computing (HPC) provided by a supercomputer Olympe at the computation centre CALMIP (UMS CNRS 3667) but also at Airbus. The damage measurements were performed by non-destructive ultrasonic but also destructive methods at ISAE.

Finally, chapter 7 concludes on the work performed and presents future perspectives.

Chapter 2

State of the Art

Objectives

This chapter describes the lightning strike phenomenon, its impact on the aircraft and the issues faced by aircraft manufacturers and airlines.

The damage generated by a lightning strike on the aircraft composite structures and the means to prevent it are presented. The studies carried out to understand lightning damage and the definition of the different contributors to damage are reviewed in this chapter. Different approaches are analysed and confronted with observations.

2.1. Lightning phenomenon

Lightning is a natural phenomenon that generates a high current and high voltage discharge [3]. This mechanism is due to the accumulation of electrical charges in clouds produced by movements of raindrops and ice particles leading to collisions and fragmentation. This produces an electrical field that can increase to the point that it ionises the air and generates a lightning discharge. This first starts with the polarisation of the clouds (positive or negative) that initiates an ionized channel of low current, called a leader. The leader propagates from the cloud in zigzag steps and possibly branches. In the vicinity of an area of opposite charges, such as a cloud or the ground, the electric field is intensified, initiating junction leaders from the opposite area (see Figure 2-1). When contact arises between the two leaders, it "closes" the circuit. The charges can propagate rapidly to discharge the cloud: this is the first return stroke.
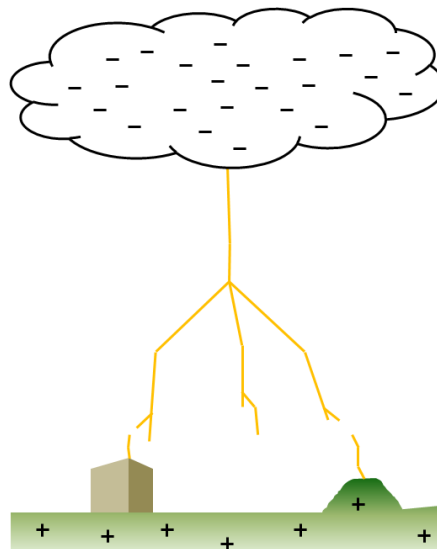
Figure 2-1 Lightning leader propagation for cloud to ground strike

Because of the presence of multiple centres of charges in the cloud, there will be a succession of discharges in the lightning event that are referred to as subsequent strokes. The first return strike is about 100kA and the subsequent strokes are lower current pulses but with still a few tens of kilo amperes. The rise time is extremely short, a few microseconds, and the decay time a few tens of microseconds. In between the different strokes, a lower current appears lasting a few milliseconds called an intermediate current. Finally, at the end of the lightning flash, a continuous current remains for a few hundreds of milliseconds. This is illustrated in Figure 2-2.

Most of the flashes to the ground are negative, with a downward leader coming from negatively charged cloud, but about 10% of lightning strikes can be positive with an upward leader, usually coming from mountains where no subsequent strokes are expected [3]. Still, the positive flash is usually more severe than the negative one, with a return strike of more than 200kA.
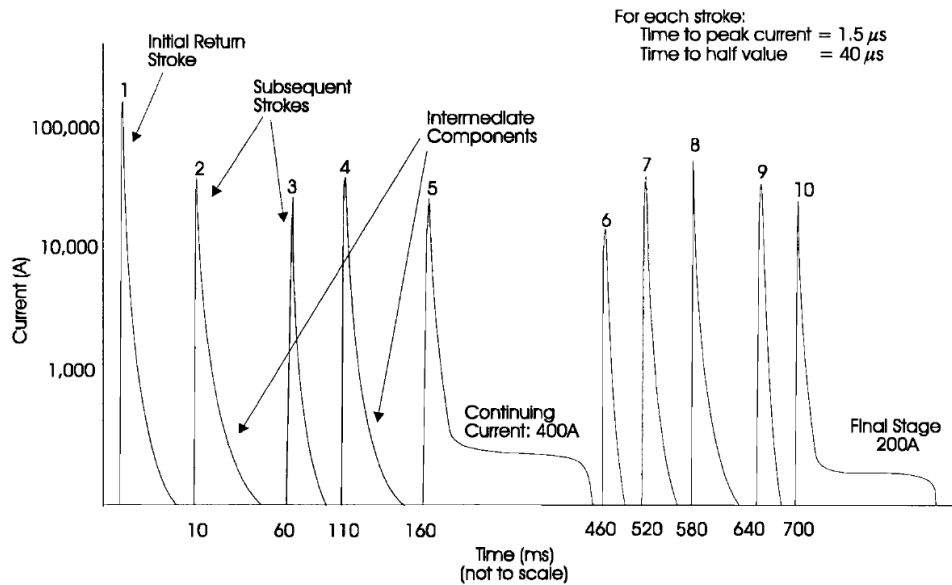
Figure 2-2 Lightning flash scenario [3]

In addition to cloud-to-ground lightning strikes which represent only 25% of lightning strikes worldwide, inter-cloud or intra-cloud flashes can arise. These lightning strike phenomena are usually less severe than the cloud-to-ground case. But whatever the origin of the leader initiation, there is one last lightning strike scenario that is due to the presence of an aircraft which is called triggered lightning. Due to the high electric field generated by the stormy conditions, the aircraft can initiate downward and upward leaders that can trigger a lightning strike that would not have occurred without the presence of the aircraft:
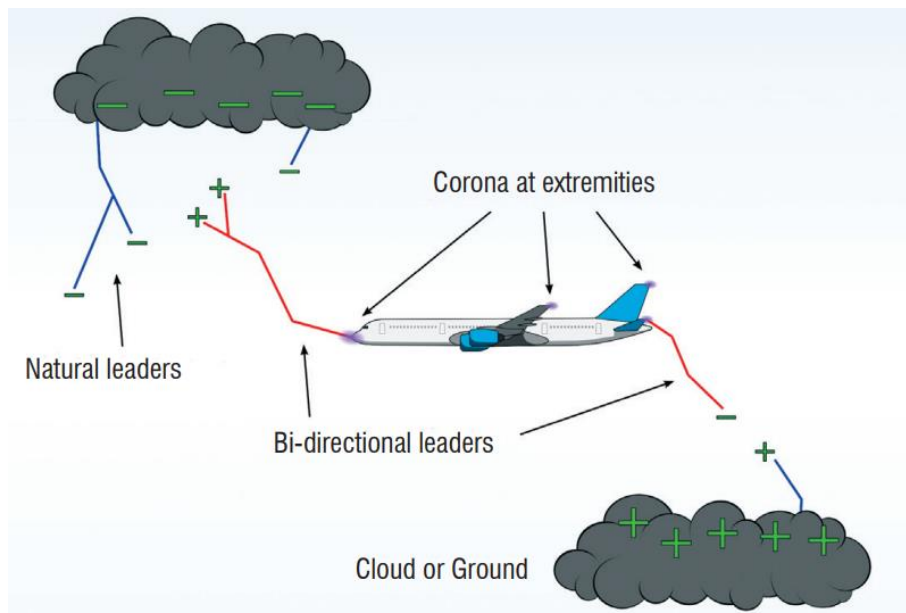
Figure 2-3 Aircraft triggered lightning [4]

These constitute the majority of the scenarios that concern aircraft and only 5 to 10% are intercepted lightning strikes, i.e. a natural lightning strike which would have occurred without the presence of an aircraft but that hits it as it flies into its column.

2.2. Lightning on aircraft

An aircraft is usually struck once to twice a year depending on its geographical location and its operability. A lightning strike on an aircraft is a risk that needs to be considered as it can endanger the safety of the flight if not properly managed. During the certification process, the aircraft design must be shown to be compliant with CS-25 regulation [5] to ensure that no catastrophic event can occur after a lightning strike. For this purpose, lightning threat standards have been established in order to define the different zones of the aircraft that will be impacted and their associated threat level.

2.2.1. Zoning & threat level

The first step in the lightning protection process is the definition of lightning zoning based on the ED-91[6] / ARP5414[7] recommendation defined by EUROCAE Working Group 31 and SAE Committee AE4L. This document is accepted by the certification authorities and the principle can be used by aircraft manufacturers to define the zoning. During a lightning flash, the aircraft will be struck several times as it moves during the phenomenon. The sharp areas of the aircraft will initiate the bi-leader where the return stroke will occur. Thus these areas are called zone 1 due to their high probability of lightning attachment. Then, the arc will sweep on the surface of the flying aircraft and the subsequent stroke will be discharged. The latter areas are called zone 2 as it is unlikely that a first return stroke will occur but the occurrence of a subsequent stroke is very likely. This will thus occur after the entry and the exit points, following the air flow direction:
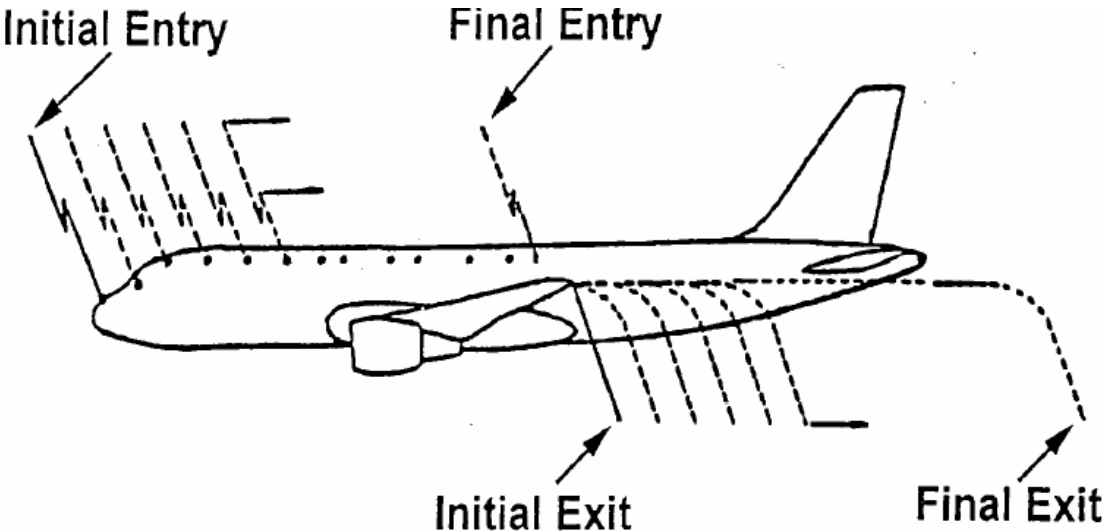
Figure 2-4 Lightning strike sweeping behaviour [6]

Outside these areas, it does not mean that a lightning attachment cannot occur but the probability is very low. Still, the lightning current can flow by conduction in the areas that are between the entry and the exit. These areas are referred to as zone 3. In addition to this high level zoning definition, it is necessary to consider for zones 1 and 2 the possibility of the arc moving (category A) on the structure or being maintained because it has reached the border of the structure (category B). Below is a zoning example:
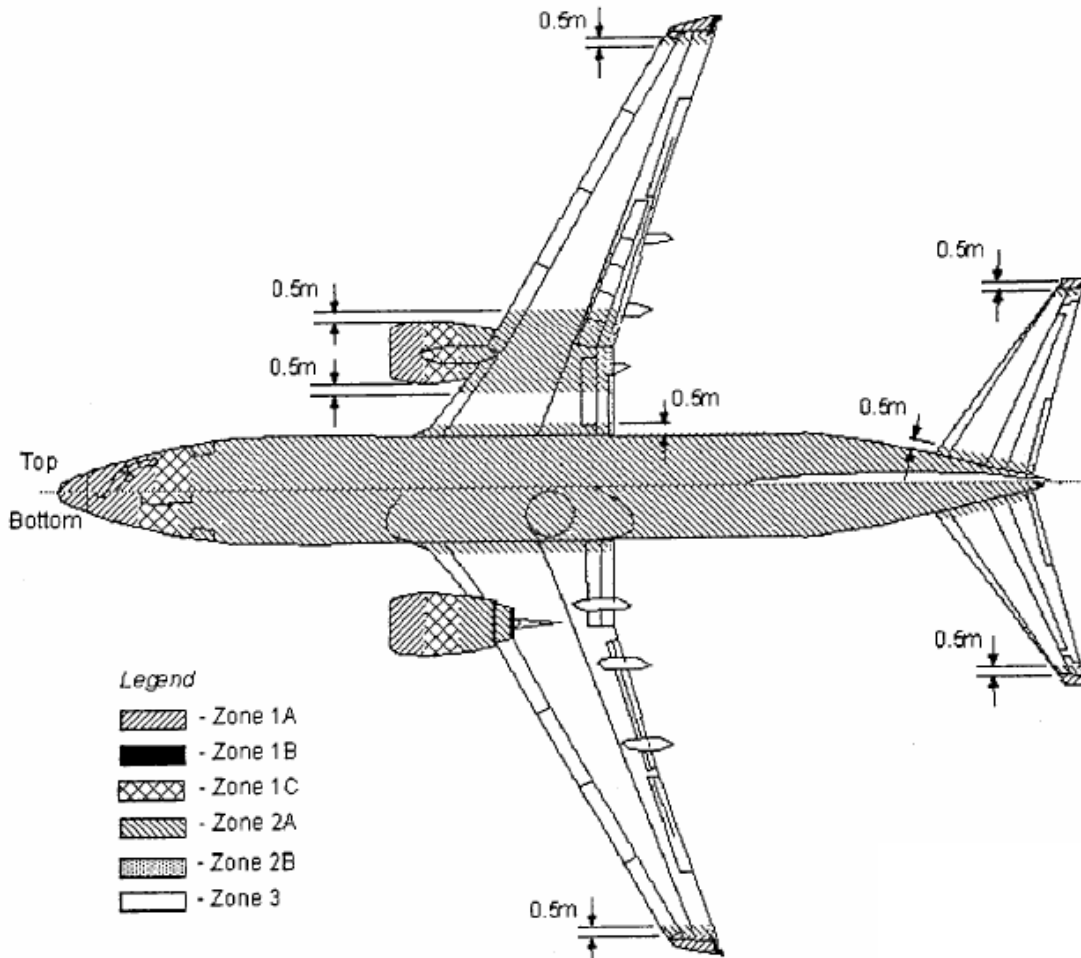
Figure 2-5 Aircraft zoning example [6]

Based on this zoning, it is then possible to associate a normalised lightning current composed of several waveforms in order to represent the strike behaviour as defined by ED-84[3]/ARP5412[8]:

Aircraft Zone	1A	1B	2A	2B	3 (Attachment)
Current Components	A+B+C*	A+B+C	D+B+C*	D+B+C	A/5+B+C*

Table 2-1 Lightning zoning and current components

With the different waveforms (WF):

- WFA: Very high current pulse (200kA) part of the first return strike
- WFD: High current pulse (100kA) part of the subsequent return stroke
- WFB: Intermediate current present between the pulses
- WFC*: Low continuous current (400A) of a few ms to represent the arc hang-on due to the presence of a dielectric (paint)
- WFC: Low continuous current (400A) of a few hundred ms to represent the arc hang-on due to its inability to move as it has reached a trailing edge

The main parameters are provided in Figure 2-6 below:

COMPONENT A (First Return Stroke)
Peak Amplitude	:	200kA (± 10%)
Action Integral	:	2 x 10^6 A^2 s (± 20%) (in 500μs)
Time Duration	:	≤ 500μs

COMPONENT B (Intermediate Current)
Max Charge Transfer	:	10 Coulombs (± 10%)
Action Integral	:	2kA (± 20%)
Time Duration	:	≤ 5ms

COMPONENT C (Continuing Current)
Amplitude	:	200 - 800 A
Charge Transfer	:	200 Coulombs (± 20%)
Time Duration	:	0.25 to 1s

COMPONENT C* (Modified Continuing Current)
Amplitude	:	400 A (± 10%)
Charge Transfer	:	18 Coulombs (± 20%)
Time Duration	:	≤ 45ms

COMPONENT D (Subsequent Return Stroke)
Peak Amplitude	:	100kA (± 10%)
Action Integral	:	0.25 x 10^6 A^2 s (± 20%) (in 500μs)
Time Duration	:	≤ 500μs

Figure 2-6 Lightning waveforms definition [3]

Based on this zoning and waveform definition, laboratory tests can be launched in order to assess the subsequent damage to a structure due to lightning. Using this information about the size of the damage zone, specific stress computations are also launched in order to demonstrate safe flight and landing.

2.2.2. Laboratory tests and procedure

As for the zoning and threat definition, there is a recommended procedure for lightning tests: ED-105[9]/ARP5416[10]. In order to limit the cost of a test, the sample considered is not a real aircraft component but a flat sample about 500 mm square with the minimum number of plies for the composite design to be validated. The lightning current is injected by an arc from an electrode placed 50 mm away from the panel, initiated by a metallic wire (≤ 100 μm).
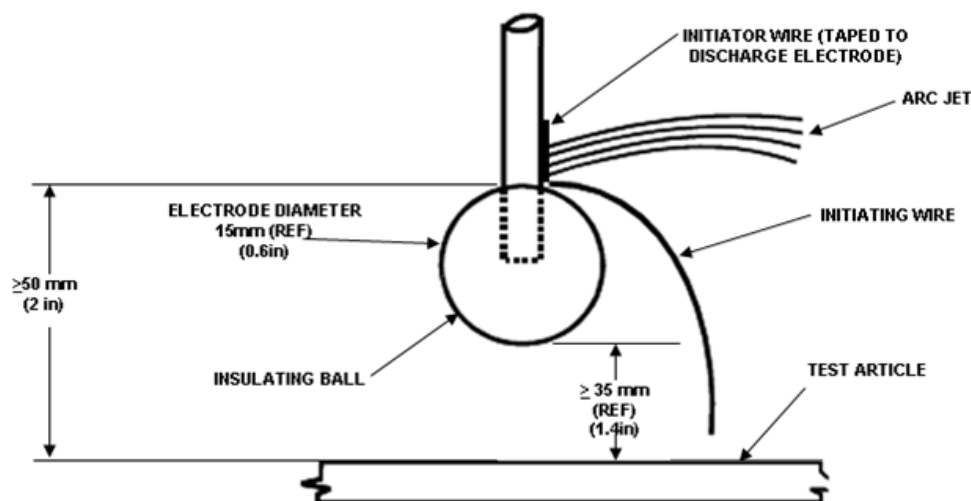
Figure 2-7 Arc injection set up [9]

As no fully standardised definition of the test setup yet exists, the mechanical clamping and the electrical bonding of the sample can vary from one lab to another. The return of the current is usually made by four bars around the sample in order to ensure a homogeneous

current distribution in the sample. Figure 2-8 below depicts an example of the setup for a test performed at DGA-TA (Direction Générale de l'Armement - Techniques Aéronautiques):

Figure 2-8 DGA-TA test set up example

After a lightning test, a NDT (Non-Destructive Test) is performed in order to measure the delamination area. The method used is generally an ultra-sonic scan. Such a test campaign is quite time-consuming and costly when the design definition and the manufacturing lead-time are taken into account in addition to the lab and manufacturing cost. Therefore, it should only be used for the certification of the design. Unfortunately, the lightning damage mechanism is quite complex and thus difficult to predict. For this reason, it is often necessary to perform tests during the development phase of the aircraft program in order to validate a design and its lightning protection.

2.3. Lightning direct effect: Damage

Among the different consequences of a lightning strike on an aircraft, the first one is the damage created at the arc attachment. The interaction of the arc and the damage is dependent on the structure.

2.3.1. Metallic

As explained in the introduction, the first generation of aircraft was made of aluminium skins. The damage on metallic structures is usually very low since only a small amount of energy is dissipated at the contact point [2]: the heat exchanged at the interface with the arc is very limited for a free arc, wandering over the structure, and it is conductive enough to divert the current with a limited increase in temperature. In this case, the damage is quite superficial with small burning marks and pitting:
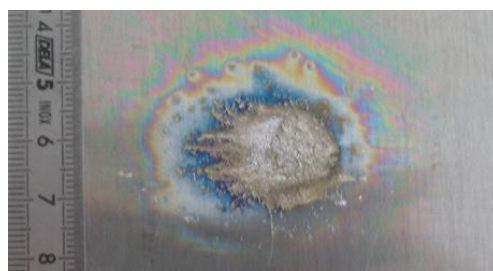
Figure 2-9 Bare metallic structure damage due to lightning [11]

But when the arc is concentrated and maintained in one location, which is the case for painted structures, the concentration of the energy leads to melting of the structure through its thickness; for thin skin this could lead to puncture (Figure 2-10).
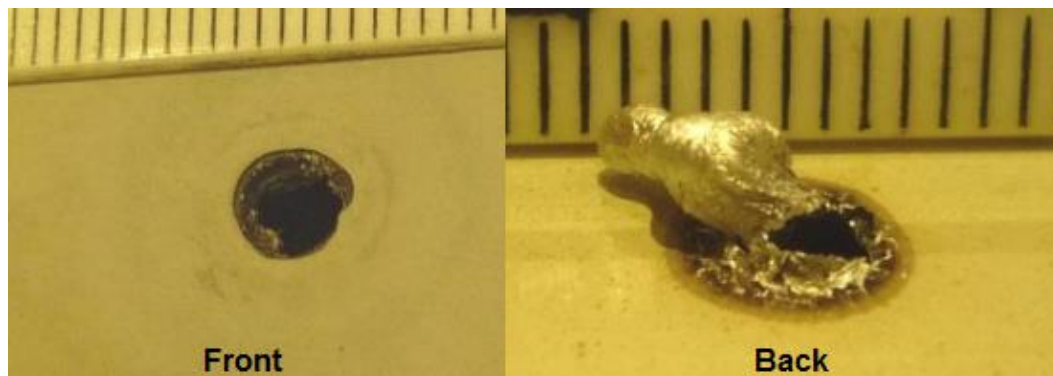
Figure 2-10 Painted metallic structure damage due to lightning [12]

The melting of a metallic skin is mainly dependent on the charge transferred by the lightning current which is contained by the waveforms B & C*. For an unpainted structure, the arc can move freely and will sweep quickly on the surface, transferring only the peak current and the intermediate current. For a painted structure, however, the arc is maintained in one point leading to a transfer of continuous current before jumping to the next point. The duration of this low level current depends on the thickness of the paint and aircraft speed. For certification, C* has been sized to consider thick coating as expected on aircraft. In any case, the puncture is very small ($\emptyset \leq 10$ mm) and is not a concern for the integrity of the structure. This is only an issue for the fuel tank area as it will ignite the vapour or for areas with systems installed very close to the skin. To avoid such a risk, the minimum thickness for aluminium skin is 2mm for civil aircraft. In addition to thermal constraints, panels are subjected to mechanical constraints due to the shock wave generated by the arc and to magnetic forces due to current flow but this has limited impact for metallic skins [13]. It has been demonstrated also that the vicinity of the strike to the clamping boundary conditions of the targets in laboratory tests, and the presence of paint on the rear face for measurement purposes, have an effect on the variability of the damage shape. The metal that has melted through the thickness can solidify again, thus maintaining closure, or be ejected, creating a complete hole.

The influence of the front face paint on aluminium structures was studied by Lago [14]. The deflection of the panel due to a lightning strike was measured using a digital image correlation method (DIC) with different paint thicknesses. Its detrimental effect was highlighted since the deflection increased with paint thickness for an identical sample configuration and lightning current amplitude.
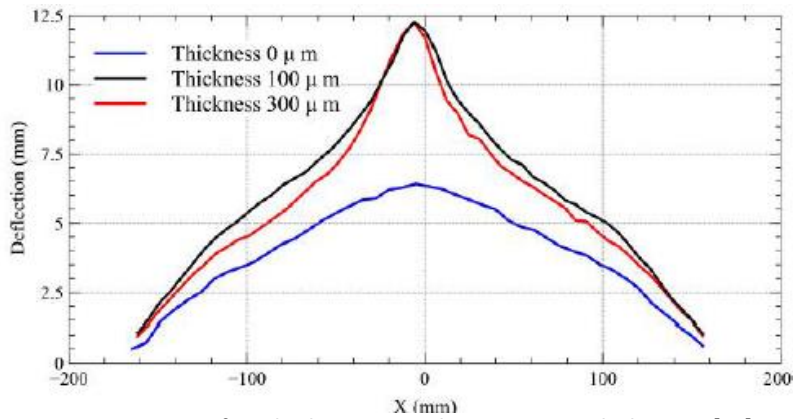
Figure 2-11: Rear face displacement with various paint thicknesses [14]

According to Lago, the front face paint thickness constrains the arc root which will increase the magneto-hydrodynamic pressure of the arc. He interpreted this increase in rear face deflection as a constriction of the arc root due to the paint that increases the magnetic and hydrodynamic pressure created by the arc.

2.3.2. Composite

2.3.2.1. Structure

Aircraft design is increasingly based on Carbon Fibre Reinforced Plastic composite structures (CFRP). Unfortunately, the low conductivity of this material compared to metal makes it very weak against lightning strike. The conductivity of the fibres is around 1000 times less than that of metal and the transverse conductivity (both in the plane and in the thickness of the laminate) is even poorer because of the resin matrix which is a dielectric. In order to better understand the damage mechanism in the composite, many studies have been performed ([15–19]).

The damage observed in the composite after lightning can be decomposed into three major post-mortem states:
- Fibre breakage and fibre damage (also called tuft)
- Resin deterioration
- Delamination of the composite

The first two modes can be related to surface damage and the last mode to core damage. For the first two, extreme temperatures are experienced due to the lightning arc interface and the high current concentration leading to Joule heating.

In this environment, **fibre breakage** [15] will certainly occur due to the lightning arc interaction and entry of current that will heat the fibres up to sublimation. Tufts of broken fibres are usually limited to the first plies but can go deeper if the arc is constrained. In addition, due to the very high temperature (up to 30000K) of the environment due to Joule heating of the fibres and the arc interaction, **resin deterioration** [15], [16] will occur as the temperature for the pyrolysis of the epoxy resin is about 300-600K. This deterioration could

lead to additional explosion with gas release. Finally, in the core of the structure, post-mortem **delamination** and ply damage have been observed. This damage is considered to be related to the shockwave and explosion on the surface that leads to a high overpressure. These processes are not independent and their interactions can lead to major damage, up to puncture.

The most visible damage is thus the damage occurring at the surface of the structure but the most extensive and detrimental damage is the hidden one: the core damage. Surface damage is usually limited to the vicinity of the arc injection, covering quite a small area of tens of square millimetres. Core damage, due to delamination, can be much wider than the visual damage and reach tens of thousands square millimetres. This defect will significantly degrade the mechanical properties of the structure, which may no longer be able to sustain flight loads. This could impact flight safety. Such damage can unfortunately only be measured by specific means, usually Non-Destructive Test devices (NDT) such as ultra-sonic scanning which defines the projected delamination of the panel. This is based on the measurement of the echo due to the reflexion of the ultra-sonic wave in the discontinuity produced by the air gap in the delamination area.
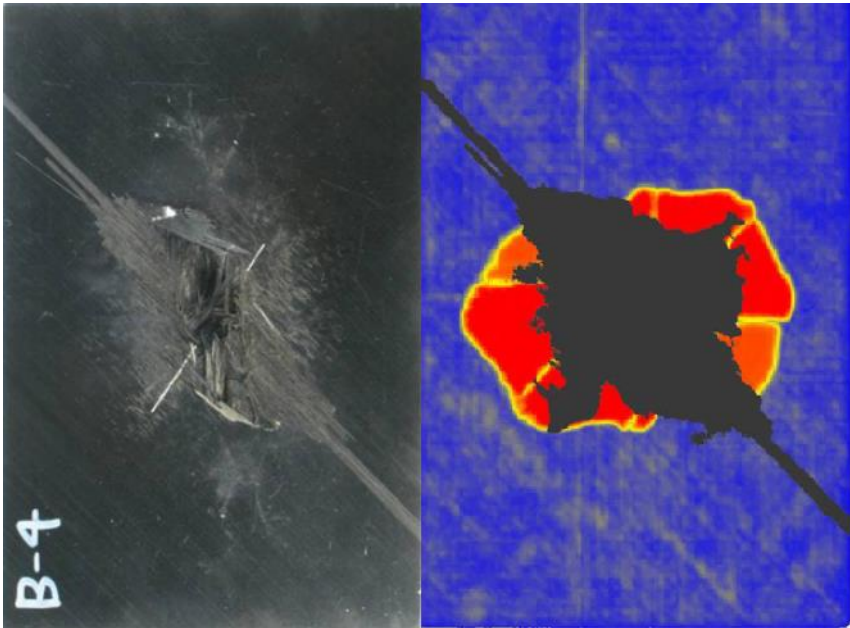
Figure 2-12: Lightning observable damage on a composite sample (left: Visual damage – right: Resin deterioration & delamination [15]

However, all the above-mentioned studies considered bare and unprotected composite, which is not representative of an aircraft design. First, as for metallic structures, the presence of a dielectric such as paint on the surface dramatically changes the damage signature. Within Airbus, several R&T investigations have been conducted to understand the damage due to composite structures. They have highlighted that the damage remains limited for bare CFRP but is increased with the paint thickness up to puncture (see Figure 2-13). As the arc cannot spread freely, it is concentrated in a local area and the current is more and more deeply injected due to the effect of the paint [20].
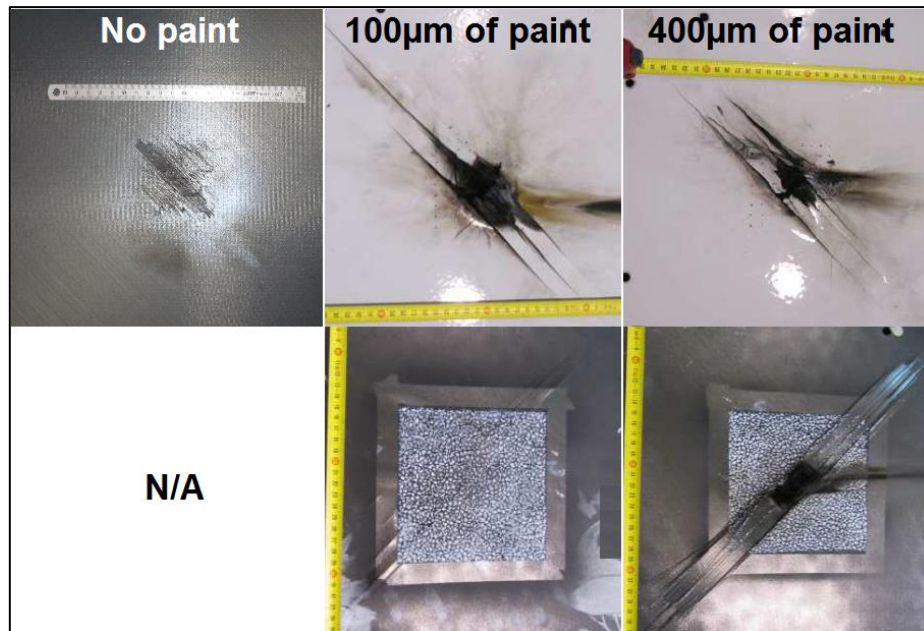
Figure 2-13 Unprotected composite damage evolution with paint, front view (top row) & back view (bottom row)

In order to limit the damage, aircraft manufacturers use a Lightning Strike Protection (LSP) applied on the external surface of the composite. This is a conductive sacrificial layer that is used to divert the lightning current from the CFRP. The layer is made of conductive material in order to act as the primary current path due to its low resistivity compared to CFRP. It is called sacrificial layer as it will be vaporised by the lightning current but since it is not part of the structure, this has no impact on flight performance. This technology and its principle are discussed in the next section.

2.3.2.2. Lightning strike protection technologies

Protecting the structure against lightning can raise several issues [21] for aircraft manufacturers, and several parameters need to be considered in order to choose the most appropriate solution:

- Efficiency of the lightning strike protection in preventing damage
- Additional weight penalty to the aircraft, considered per unit area (gsm)
- Adhesion properties to avoid peeling from the composite structure or the paint
- Compatibility with the composite (Galvanic corrosion risk)
- Cost of the lightning strike protection
- Manufacturability of the protection (process on complex shapes and cost)
- Reparability of the protection (process and cost)
- Resistivity for indirect effect of lightning (Faraday cage effect)

Many Lightning Strike Protections (LSP) [22] have been developed for the protection of composite structures against lightning damage. The most common technologies that fulfil the above requirements are expanded metallic foil such as Expanded Copper Foil (ECF) and metallic mesh such as Bronze Mesh (BM), as illustrated in Figure 2-14.
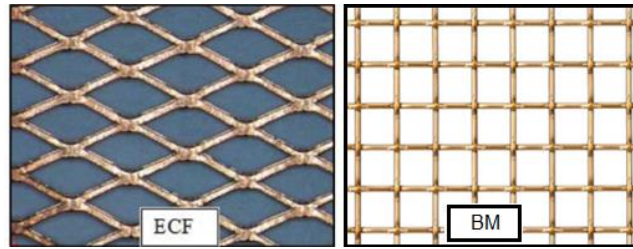
Figure 2-14 Common Lightning Strike Protection [20]

The difference between the mesh and the expanded foil is that the mesh is made of different wires that are meshed in a defined pattern and the expanded foil is made from a unique foil that has been punctured and then expanded to create its final shape. There is thus a contact penalty for the BM, making it less efficient compared to ECF of an equivalent weight.

The interest of a surface metallic protection is to divert the high lightning current from the structure as it is a highly conductive layer compared to the underlying composite structure. The current will therefore flow into the less resistive path and a very limited amount will be carried by the structure. The metal material is chosen for its high conductivity in regards to its density in order to limit the penalty on the design. Due to galvanic corrosion issues with the carbon, aluminium protections have been discarded in favour of copper protections.

Obviously, a continuous metallic foil is the best means of protection for lightning current dissipation as it facilitates the current flow and provides a complete "shielding effect" for the composite skin. There are two main drawbacks, however, with the implementation of this technology on aircraft. The first one is the drapability issue experienced during manufacturing. This kind of layer, for instance Solid Copper Foil (SCF), will be 10 to 20μm thick, making it very difficult to manipulate and also impossible to apply without wrinkles, which is not acceptable for structural and cosmetic reasons. The second one is the adhesion issue that leads to peeling problems with the paint and the lightning strike protection itself.
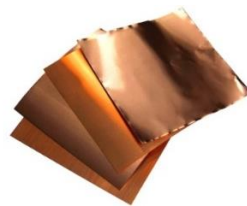
Figure 2-15 Solid Copper Foil (SCF)

In order to solve those manufacturing and operability issues, different technologies have been developed such as metallic deposition on a manufactured part. For example, thermal spray is based on the projection of a hot gas containing melted metallic particles on the surface of the composite. Another method is vacuum deposition, either Physical Vapour Deposition (PVD) or Chemical Vapour Deposition (CVD), in which a gas with the particles to be deposited is generated in the chamber where a layer will grow on the surface in interaction. Unfortunately, these technologies do not solve the adhesion issue and could be quite complex to implement in the production cycle (with the need for a vacuum chamber).

Finally, the easiest and cheapest way to ensure adhesion of the metallic protection to the composite is to create areas of attachment where there is no metal and the resin can flow. Expanded foils are based on this principle but other patterns of aperture could be studied.

Figure 2-16 Metallic foil with apertures
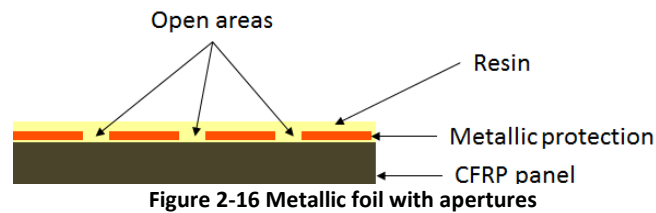
As the apertures decreases the efficiency of the protection, a compromise needs to be found to comply with protection efficiency, weight, cost, manufacturability or adhesion as illustrated in Figure 2-17, a continuous protection such as SCF provides a complete protection without damage to the CFRP even with a thick paint coating (400µm) compared to a discontinuous protection with open areas such as ECF where significant delamination can be observed.
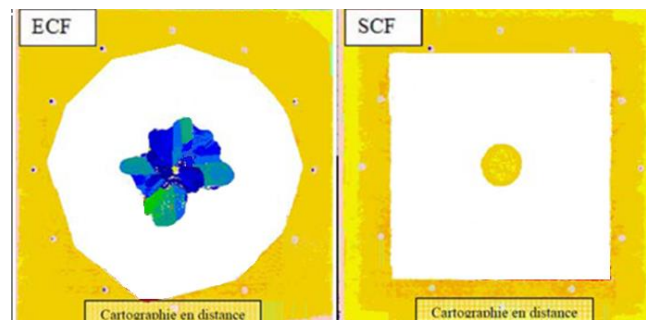
Figure 2-17 Damage comparison between continuous and discontinuous protection with WFD on identical CFRP panel

Another way to ensure the protection without adding a metallic layer is to introduce conductive fibres in the laminate itself either with metallic wires or by the conductive coating of the composite fibres. With this process, the conductivity of the first composite ply is increased with the aim of sustaining a lightning strike. Unfortunately, this protection is not as efficient as ECF since it does not prevent the injection of current in the CFRP.

On the same principle of developing a self-protection of the structure, transverse conductivity of the composite has been achieved by the addition of conductive particles in the matrix. Usually, the technology considered is based on carbon nanotubes (CNT), graphene, or metal particles [23–25]. The objective is to reduce the Joule heating created by the flow of current through the composite, by increasing the electrical conductivity of the material, or by reducing the electrical density, i.e. by distributing the current more evenly through the composite. By this mechanism, thermal damage is reduced. But, again, the efficiency of the protection has not been demonstrated and it usually impinges on the mechanical properties of the laminates, which is detrimental for the design [23]. Moreover, the manufacturing processes are usually quite expensive. Finally, the use of conductive paints has been considered by the addition of conductive particles in the polymer but the contact between the particles is not dense enough to be of use for lightning protection [21].

2.3.2.3. Real aircraft structure damage: Protection and paint effect

In the different developments of lightning protection technologies, one important parameter is seldom considered: the paint, which is considered as a merely cosmetic feature with no structural properties. However, lightning damage is highly dependent on the interaction from the arc to the structure. A free arc root will expand quickly in the air as a function of the conductivity of the surface: the lower the conductivity compared to the arc, the quicker the expansion is [26]. Since the lightning strike protection on the surface is more conductive than the underlying structure, the current will mainly flow in the external layer and most of the energy will be dissipated in this layer. In this respect, any lightning strike protection will be more efficient than a bare composite [27]. Obviously, aircraft are painted in order to protect the structure from the environment (UV, fluids, etc.) and also to respond to the airline's desire for customisation. In reality, however, the efficiency of a surface lightning strike protection decreases dramatically with the paint thickness. Below is an illustration of this mechanism for ECF195 protecting a 1.6 mm thick CFRP plate measuring 450 mm by 450 mm with a circular clamping of 370 mm in diameter (bolt hole visible on the picture):

Figure 2-18 Lightning damage evolution with paint (EDIFISS project)

Few studies have been reported on the influence of the paint in lightning damage [24]. Internal Airbus work showed during lightning laboratory tests that the paint was ejected by an underlying explosion. This phenomenon is assumed to be due to the Joule heating of the metallic protection, leading to its explosion. The confinement of the overpressure by the paint enhances the stress and increases the damage [28]. In addition, Lepetit [29] and Karch [30] were the first to consider the confinement effect of the paint as a simple mass which has an inertial effect on the overpressure occurring on the surface. Based on this approach, the density and the thickness of the paint are the only parameters that will affect the overpressure enhancement. A lighter or thinner paint will lead to a lower pressure and thus should decrease the damage.
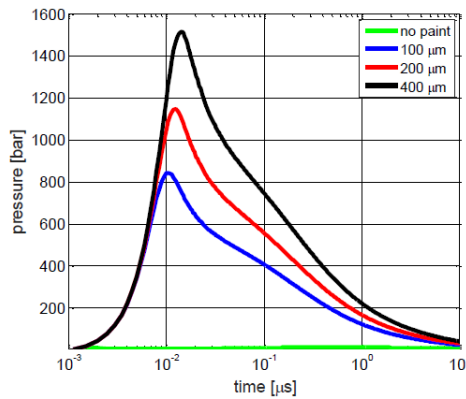
Figure 2-19: Effect of paint thickness on equivalent pressure to lightning strike [30]

The paint will constrain the arc root and with the vaporisation of the LSP, the concentrated arc will be forced to flow again into the underlying composite. The paint has an impact on the arc root, and therefore also on the current distribution and on the explosion that ensues. This theory was the first trial to provide a quantitative explanation of the impact of the paint. It needs to be enhanced, however, since it is only a 1D theory which considers the pressure in a central point only and simplifies the confinement to a mass effect.

Considering the entire system (CFRP, LSP and paint), the damage can be broken down into different elements:

- The **surface damage** that can be measured by a simple visual inspection:
  - *Cosmetic:* Vaporisation of the LSP and ejection of the paint (red)
  - *Structural:* Dry fibres (tufting) due to resin deterioration and broken fibres (green)
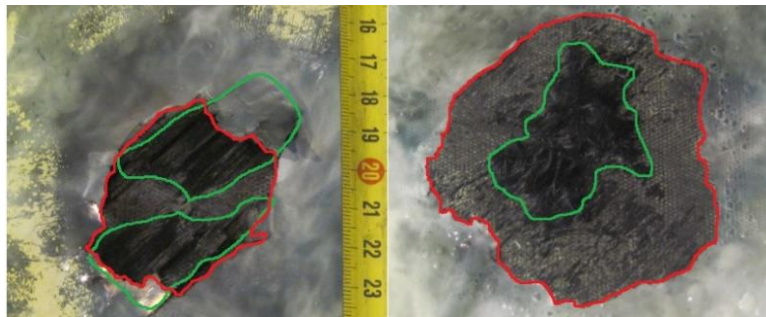
Figure 2-20 Surface Damage examples

This damage ([11], [29]) is mainly due to the electro-thermal effect of the lightning current in the LSP and in the composite.

- The **structural damage** which requires a specific inspection such as an ultra-sonic scan in order to measure the delamination, as shown in Figure 2-18. This type of damage is also called "core damage" ([11], [29])

There may also be thermal damage concentrated in the centre of the impact due to the increase in the current injection in the depth of the laminate with the concentrated arc, but the main issue is delamination which has a mechanical origin [11].
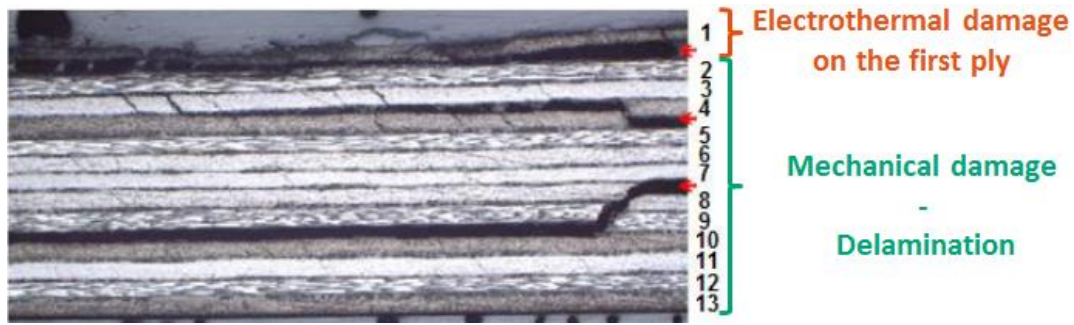
Figure 2-21 Lightning damage decomposition [30]

A lightning strike is a far more complex phenomenon than thermal damage due to current flow in the structure while it is partially composed of it [32,33]. The different forces that create the damage are defined and explained in the next section.

2.4. Lightning damage modelling

Modelling the damage mechanism is a complex problem that has been studied for many years. Models are derived from theories of damage processes. Many theories have been built and presented to the lightning community. The first and best-known theory is based on electro-thermal physics. Its purpose is to assess the increase in temperature in the composite due to the lightning current flow: Joule heating. The temperature is thus considered as a criterion for the damage in the laminate. In another approach, other theories have been developed in order to assess the lightning strike as a pressure applied on the surface. The damage, in this case, is considered to be based on mechanical criteria of the laminate with a composite damage model. In both approaches, the lightning arc is most of the time considered as a source of current with a local and fixed location of injection in the composite. The arc is thus independent from the structure. However, some researchers are starting to consider a more complex and coupled model of lightning damage. These different approaches are presented in the following sections.

2.4.1. Lightning forces & decomposition

It is difficult to quantify the importance of each of the different physical phenomena that are part of a lightning strike, least of all to quantify their interaction and coupling with one another. A representation of the possible physical constraints involved (thermal, electro, magnetic and mechanical constraints) is proposed on Figure 2-22 with a link to the observed damage on composite material impacted by lightning.

Currently, it remains difficult to predict the damage that could be generated by a lightning strike on a composite structure due to its complex phenomenology and the different constraints involved [34,35]. This is indeed a highly dynamic and multi-physics phenomenon. There is no fully validated theory on all the physics phenomena involved by the arc and its interaction with the structure or the associated chronology. Still, a proposal of the different constraints involved has been developed:
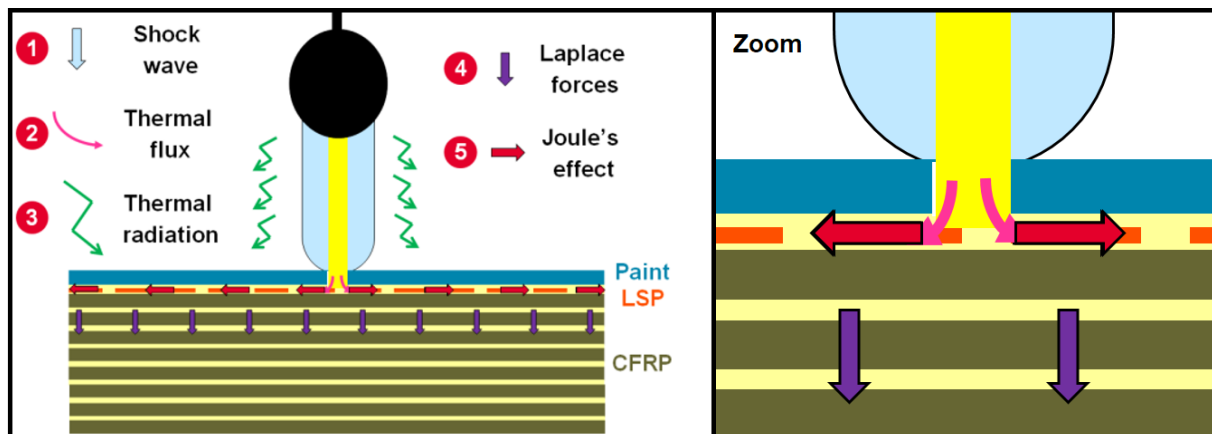
Figure 2-22 Lightning constraints generation in composite structures

We distinguish the following physical phenomena during a lightning strike on a protected and painted composite structure. The thermal constraints include:

- **Thermal flux:** This is related to the interaction of the plasma with the structure. Depending on the electron flux, and hence on the current density, and the conductive thermal flux to the material, it will generate a heat source to the structure that is dependent on the current, the arc radius and the state of the structure [34].
- **Thermal radiation:** This comes from the arc itself which is very hot. This is usually considered a negligible constraint on the structure compared to the other contributors [36]. The temperature increase in the material due to the heat transferred by radiation is a very slow process compared to the constraints generated during a lightning strike.
- **Joule effect:** Due to the lightning current flow in the metallic protection and the composite structure, its temperature will quickly increase up to vaporization which is in fact an explosion of the materials. The explosion of the LSP creates a shock wave that is transmitted to the structure. In addition, the upper fibres break and the resin disappears by pyrolysis [30], [37].

The mechanical constraints include:

- **Laplace forces:** The current flowing into the conducting elements, mainly the LSP, induces a magnetic field that interacts with the current to generate volume forces [30]. The electrical source is thus converted into a mechanical force on the structure, also called magnetic pressure.
- **Shock wave:** This is due to the rapid rise of the temperature in the plasma (up to 30000K in a few µs) that will rapidly increase its pressure. The plasma channel will expand rapidly, generating a shock wave that will propagate radially from the arc. The pressure will decrease rapidly with the propagation and only thunder will be heard. However, at the arc attachment the overpressure will be significant [38].

In addition to its complexity, this multi-physics phenomenon is not only dependent on the lightning current amplitude but also on the current distribution. The spatial and temporal distribution of the current will change the "weight" of each force and also the contributors

at stake. For example, Joule heating will not generate the same damage if the current flows only in the LSP or if it is also diverted into the underlying composite plies. The arc and its root are dependent on the structure it is in interaction with. And the presence of LSP and paint has a significant impact on the arc interaction. The arc constriction can be increased by the presence of a thick paint layer. It can change the current injection into the LSP and can lead to current injection into the first plies of the CFRP (Carbon Fibre Reinforced Plastic). The latter will then explode due to the Joule effect: the high concentration of current in the LSP leads to its rapid explosion, making the CFRP a contributor in the electrical return path since the conductivities are closer (10^4 S/m). On top of its constriction effect on the arc root, the paint has a confinement effect that enhances the overpressure generated by surface explosion. The ejection of the paint is a slower event compared to the explosion [29] and this changes the arc root shape and thus the current distribution.
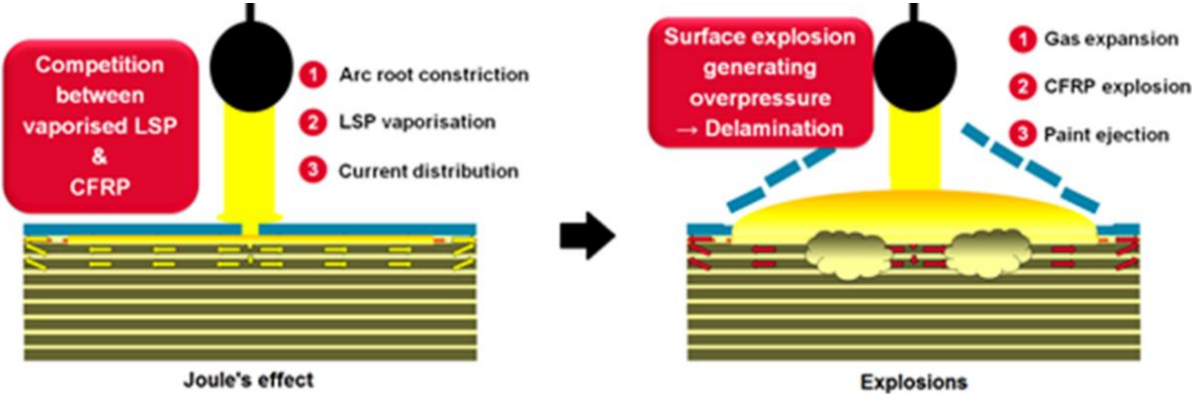
Figure 2-23 Lightning explosion

This leads to substantial delamination (Figure 2-18 & Figure 2-21) in the composite structure in addition to the thermal damage which is important to predict aircraft structure safety. The complexity of this phenomenon is enhanced by the fact that the damage is not only dependent on the structure configuration but also on the lightning strike protection and the paint thickness which are not part of the sizing of the composite structure against "nominal" stress loads, despite the fact that these two parameters are of major importance in the generation of surface explosion [20] and internal damage [39]. Finally, the model of lightning damage for an aircraft composite structure needs to be refined by considering the structure, the surface metallic protection and the paint with their temperature-dependent properties combined with an arc that is in interaction with this complete system.

2.4.2. Electro-thermal models

The different models developed over the last few years have mainly focused on electro-thermal constraints, i.e. Joule heating and sometimes heat transfer from the arc. The damage is assessed by considering first a temperature threshold for the composite fibre (over 3000°C) and/or the resin matrix (over 300°C). This type of damage should be related to the surface damage observed during a lightning test with tufting and resin deterioration [15]. Most of these studies considered only CFRP without any metallic protection [16,40],

and some assessed the impact of a surface protection but without experimental results to validate the model [19,41]. In order to assess Joule heating more accurately, electrical and thermal properties have been considered to be dependent on the temperature, based either on tables or on analytical laws [19,39,42,43]. This has a significant impact on the current distribution but also on the damage propagation. This dependency upon temperature cannot be neglected due to the high variation of the temperature in the material caused by rapid Joule heating. In addition, these models have also been made more complex by taking into account the pyrolysis of the resin, based mainly on the Arrhenius theory [19,43–47]. The pyrolysis models proposed are very complete and could help in understanding the current distribution in the depth of the composite laminate with the temperature dependence that could lead to additional explosion. Approaches based only on thermal constraints, however, are incomplete and unable to predict the whole damage, as highlighted by Murphy [48] who compared several results of the electro-thermal model presented in Figure 2-24. The damage criterion was based on the pyrolysis temperature of the resin or the carbon fibre vaporisation temperature. He found that the results differed depending on the thermal properties chosen in the composite and the conditions of the current injection. Nevertheless, the damage predicted by an electro-thermal model is much smaller than the damage measured by Hirano [15].
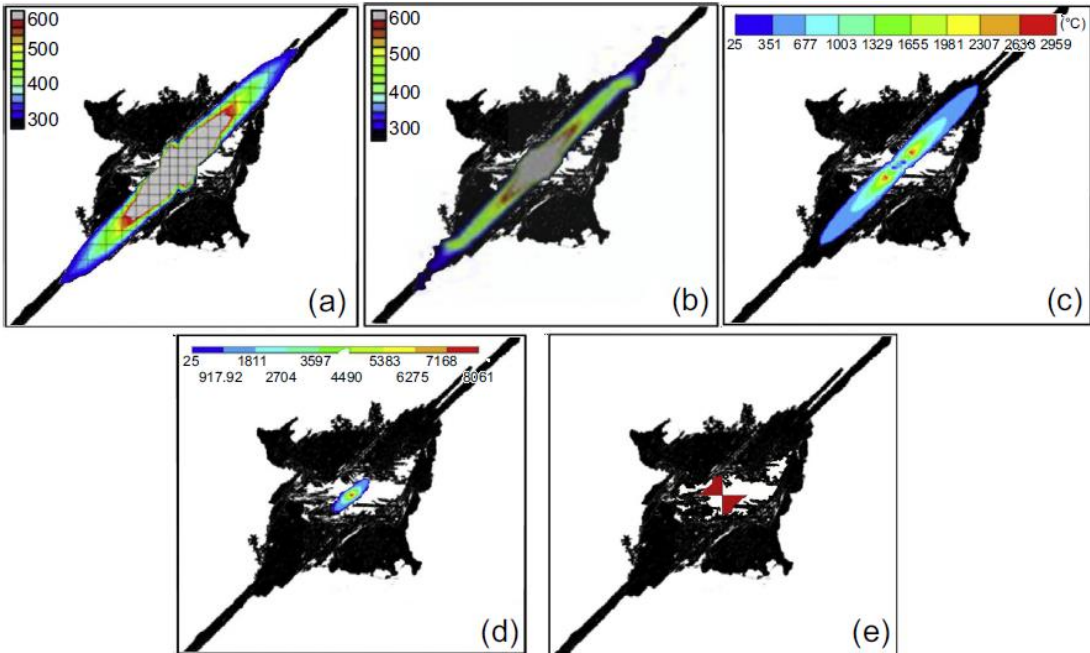
Figure 2-24 Comparison between thermal decomposition of the resin and modelled temperature distribution [48] (a: [44], b: [46], c: [49], d: [50], e: [19])

The first issue that could explain this gap is the difficulty of obtaining accurate values of the material properties' dependency on temperature since the range of temperature reached by the carbon and the resin (and also the metal when considered), is very high under lightning conditions and is not usually found in the literature. This becomes even more complicated when considering the phenomenon of pyrolysis since the rate of temperature increase has a strong impact on the model. The experimental method used to feed this model is based on

Thermogravimetric Analysis (TGA) in which the material is heated at a given rate (K/min) and the weight loss is measured. Performing this measurement up to high temperature (> 100 °C) is technically challenging, however, due to moisture evaporation. In addition, the temperature increase rate is far slower than that experienced by Joule heating due to a lightning current. This could lead to considerable inaccuracy in the material properties.

The second issue is the application of the lightning current. The arc is neglected in current electro-thermal models and is considered as a source of current applied to one point or on a fixed small radius (Ø 5 to 10 mm). The current injection profile has an impact, however, on the current distribution and thus the temperature increase as shown by Foster [39] and Millen [51]. A first approach was based on the free arc column theory considered by Braginskii [52] with a simplified hypothesis on the arc properties and considering a current linearly increasing with time (I=αt), as described by equation 2-1.

$$r = 0.93\rho_0{}^{-1/6}I^{1/3}t^{1/2} \qquad\qquad \text{2-1}$$

where r is the radius in mm of the arc column, ρ_0 is the air density at atmospheric pressure in g/cm^3, I is the current in kA and t is the time in μs from ignition. Even if the lightning current does not comply with the increasing condition, this theory has been considered to build a current load application with an increasing radius [53–55]. Still, this approach is not complete as the arc root is dependent on its interaction with the structure as shown by Tholin [56] and Lago [36].
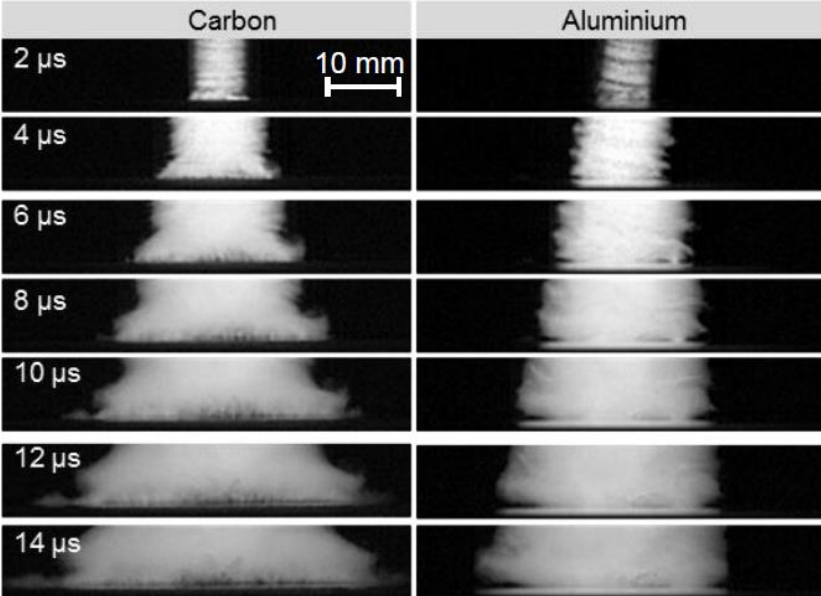
Figure 2-25 WFD Arc root interaction difference with Carbon and Aluminium interface (Bottom of each picture) [56]

A complete arc model, based on a Magneto-Hydro-Dynamic (MHD) approach where the electrodes are generally considered as boundaries, is quite complicated. This question will be discussed in greater detail in Chapter 3. In any case, even when a variable application of the electro-thermal load of the lightning arc is considered, the modelled damage is limited as an important contributor has not been considered up to now: the mechanical loads generated by the lightning strike. This approach is developed in the next section.

2.4.3. Mechanical load modelling

It is of course important to consider the electro-thermal damage due to the current flow in the composite but this is a limited view of the complete damage mechanism when we consider delamination as argued by Soulas [11,57]. The peak part (component A or D) of the lightning current generates strong mechanical forces as described in 2.4.1., such as the lightning shock wave, the magnetic pressure and the surface explosion. These mechanical loadings are considered as a resulting pressure applied on the surface of the composite. The assessment of the pressure from the arc and the current flow on the surface has been extensively investigated [30,34,57–60]. For the magnetic pressure, two areas are distinguished: the area below the arc root ($r \leq R_{arc}$), at injection, and the area outside where the current flows in the surface protection ($r > R_{arc}$). The pressure is assessed by integrating the magnetic force in the thickness of the surface protection and over the whole plate surface [30]:

$$
\begin{cases}
P_z(r,t) = \int_0^d f_z^V dz = \int_0^d \mu_r \mu_0 \left(\frac{I(t)}{2\pi r}\right)^2 \frac{z}{d_{LSP}^2} dz = \frac{\mu_0 r^2 I^2(t)}{8\pi^2 R_{arc}^4} \quad r \leq R_{arc} \\
P_z(r,t) = \int_0^d f_z^V dz = \int_0^d \mu_r \mu_0 \left(\frac{I(t)}{2\pi} \frac{r}{R_{arc}^2}\right)^2 \frac{z}{d_{LSP}^2} dz = \frac{\mu_0 I^2(t)}{8\pi^2 r^2} \quad r > R_{arc}
\end{cases}
\tag{2-2}
$$

The pressure is therefore dependent on the amplitude and waveform of the current but also on the arc root radius which increases the maximum pressure when it decreases in size. The maximum amplitude considered in the literature may thus vary depending on the hypothesis from 0.5MPa to 100MPa. This demonstrates again the importance of modelling the arc root and its variation in time as it is of prime importance in predicting the magnetic pressure. For the acoustic shock wave generated by the lightning arc, some theories have been developed [11,38,60,61] but there is no strong agreement on the pressure profile except that the pressure will quickly decrease when it propagates from the lightning channel. The theory has been mainly based on developments made by Lin [62] and Plooster [63]. In the strong shock wave approximation, thus in the vicinity of the arc, the pressure decrease is inversely proportional to the square of the distance [38,63]:

$$
\begin{cases}
\dfrac{P(t)}{p_0} = \dfrac{\gamma R_0^2}{2(\gamma+1)R_{shock}^2(t)} \quad R_{shock} \ll R_0 \\
R_0 = \sqrt{E_0/b\gamma p_0}
\end{cases}
\tag{2-3}
$$

where E_0 is the energy released per unit length at the start of the discharge, p_0 the ambient air pressure, b=3.94 and γ=1,4. In addition, Karch [64] defined the initial energy release by an arc from the following relationship equation 2-4:

$$
E_0 = 0.0045 \times I_{max}^{1.25}
\tag{2-4}
$$

Based on this approach, the maximum pressure is about 10MPa and decreases very quickly:
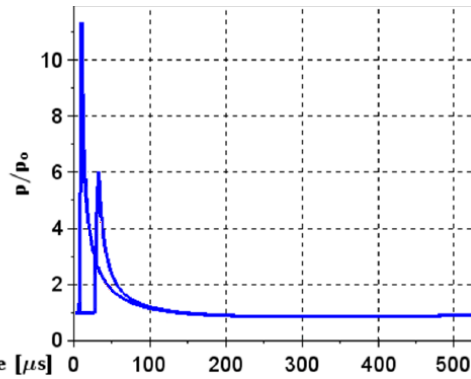
Figure 2-26 Shock wave pressure at 25 and 50mm from the lightning arc [38]

As argued by Munoz [60] or Lee [61], the damage generated by the stress wave and the magnetic pressure are negligible compared to the thermal damage due to Joule heating. The mechanical effects alone cannot explain the underlying severe delamination observed after a lightning strike on a composite structure.

Soulas [11] proposed an innovative approach by considering the lightning strike as a fully mechanical source, equivalent to the mechanical impact of a metallic ball. This was based on observation of the damage signature which presented similarities as regards delamination and matrix cracking which is the most detrimental effect for the structure.
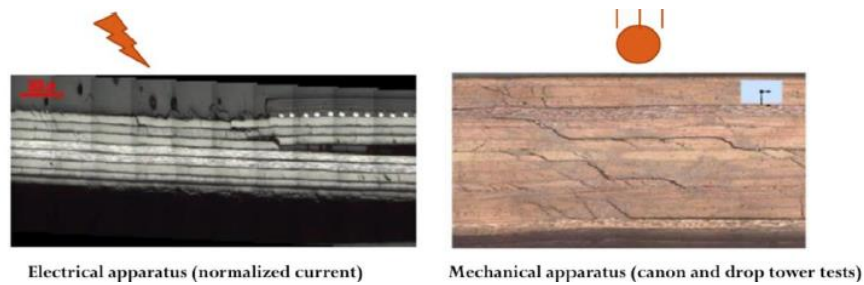
Electrical apparatus (normalized current)   Mechanical apparatus (canon and drop tower tests)
Figure 2-27 Lightning and pure mechanical damage comparison

However, as already observed, the application of the load from a lightning strike is variable in time and space, which is difficult to reproduce with a metallic ball impact. While the total delaminated area was correctly reproduced with a mechanical impact having the same impulse, the work by Soulas demonstrated that the distribution of delamination in the composite plate was not the same. Still, the deformation of the panel due to an overpressure with a validated model of delamination is of great importance in order to predict the whole damage in the CFRP, not only the thermal damage. The first attempts at modelling the evolving surface of pressure application due to the evolution of the vaporised LSP zone around the central point of injection were also done in this work. It was shown that the evolution of pressure in space changes the distribution of delamination in the thickness of the plate.

In addition to the fully mechanical approach based on the surface pressure, other studies proposed to consider Joule heating as a mechanical constraint due to the thermal expansion of the material [65–67]. However, the results obtained were again below those of lightning test measurements.

The parameter that has been lately studied is the explosion due to Joule heating in the composite. An innovative approach has been developed by Liu [50]. It proposes to couple an electrical-thermal analysis to assess Joule heating in a CFRP up to 3316°C (carbon fibre ablation) in order to trigger an explosion with a Blow-Off Impulse (BOI) based on the Jones-Wilkins-Lee (JWL) Equation Of State (EOS). This is the first time that this phenomenon has been compared to a surface explosion. An associated model of the panel to assess the deflection and the delamination of the CFRP due to a mechanical constraint is also proposed.

Following the same evolution of vaporized radius of the LSP layer given by Karch [30] and Lepetit [29] as Soulas [11], another approach has been developed by Espinosa et al.[68]. The proposed model uses a full electrical-thermal-mechanical analysis to compute the resulting pressure applied by vaporization of a copper mesh on the underlying composite structure. The LSP mesh used was coarse and results demonstrated that it is mandatory to model the detailed geometry to assess the mechanical shock properly. The study also demonstrated however that it is possible to compute the pressure from complex electro-thermal-mechanical phenomena arising in the LSP layer instead of applying separate cumulative effects.

The main parameters lacking in the different models analysed are the paint and the LSP. Even when considering only the CFRP, the phenomenon is of course already very complex, but a realistic aircraft model needs in addition to include these two parameters, as they have demonstrated their major impact. Lepetit [29] and Karch [35] proposed to take the mass effect of the paint into account since it has an impact on the overpressure generation and thus on the damage severity (Figure 2-19). These two models are the most complete since they took into consideration all the forces presented in 2.4.1 with the composite, its lightning strike protection and the paint. However, the lightning strike protection was considered as carrying the total lightning current, thus no Joule heating or associated thermal degradation (mechanical properties and pyrolysis) were considered. Also, as highlighted by experiment, the cohesion of the paint, and thus its mechanical properties, are even more important and need to be further investigated.

All the models presented have demonstrated the complexity of a lightning strike and the damage it can generate in the composite structure. Most of the approaches are based on a bare and unprotected composite in order to simplify the study of the phenomenon but this is not representative of a real aircraft structure. Moreover, coupling between the arc and the structure occurs, changing the different forces at stake in terms of amplitude, time and spatial distribution. It is thus very important to decompose each component of the lightning stress on the structure in order to understand their interaction and to finally define a complete scenario.

2.5. Conclusion

Lightning is a complex multi-physics phenomenon involving the coupling of many contributors such as electromagnetic, thermal, mechanical, shock physics… It is extremely difficult to predict the damage incurred by the composite structure since different types of damage occur: fibre tufting and resin decomposition on one hand, and delamination and matrix cracking on the other hand. The different forces and damages will have some influence on one another, which makes the damage model even more complicated. In addition, validation of the model is difficult since the extent of possible measurements during a lightning test is limited due to the rapidity of the phenomenon in which the damage is generated in the first microseconds (< 20 µs), and the intensity of the lightning arc which creates a strong electromagnetic field (100 kA reached in about 15 µs) and very high temperature source (up to 30000K [69]). In such a harsh environment, it is impossible to install sensors at the contact or in the vicinity of the arc.

Work performed in the past to simulate damage induced by a lightning strike, which can be found in the literature, was first based on a simple electro-thermal approach in which the current flow in the composite generates heat that will create damage. These models were subsequently refined by considering the degradation of the resin by pyrolysis. In many cases, the arc was modelled as an equivalent current source with a fixed injection area. It has been demonstrated, however, that the arc root interacts with the structure and that its injection is variable in time and space. Finally, this approach showed its limitations since it proved unable to predict the underlying delamination coming from a mechanical constraint. The damage predicted by models was always lower than the damage observed in laboratory lightning tests, even with a more complex current injection based on a simple hypothesis.

In order to assess delamination, which is the most detrimental effect for the sustainability of the structure, a model of the mechanical sources generated by the arc, i.e. the shock wave and the magnetic pressure, was introduced. However, the theory is not fully validated yet and the magnitude and distribution of these forces are highly dependent on the arc root interaction. This sensitivity makes it very difficult to weight these two contributors correctly. Even if a more accurate model could be developed, this would not suffice to predict the damage as the values of these forces that were determined were not high enough to generate significant stress in the composite.

This led some researchers to investigate the explosion effect of the composite but also the role of the metallic protection on the surface of the structure as the sudden and high lightning current flowing in the conductor leads to a rapid increase in temperature up to an explosion. The pressure and the mechanical impulse generated by this phenomenon is clearly not negligible and needs to be further investigated.

Finally, it is not enough to consider the different forces that can be generated by a lightning strike; it is also necessary to take into account the total system that will interact with these

forces. Of course, the composite structure where damage prediction is essential is part of it. But in addition, the lightning strike protection and the paint must be introduced in the model. Some studies tried to model the LSP behaviour but rarely compared it with test results, and only one group examined the contribution of the paint in their model through the added mass that has a confinement effect. This work is of paramount importance but needs to be further studied since it did not take into account the constraining effect of the paint on the arc and the confinement that is dependent on its mechanical properties and adhesion.

The research developed in this PhD aims to decompose the different parameters involved in the generation of lightning constraints and therefore the consecutive damage. Lightning is such a complex phenomenon that it is important to understand its contributors before building a complete approach to define the coupling between each of them and their associated weight and distribution. For this purpose, the study starts by studying the source which is the lightning arc itself and its interaction with the complete structure (LSP and paint) as it has been demonstrated that a fixed injection is limited. Based on this development, it will be possible to predict the explosion of the lightning strike protection on the surface which is an important contributor to the overpressure applied on the structure. Furthermore, the paint is characterized in order to understand its confining effect on the explosion of the LSP. Since this PhD also aims to predict the most detrimental damage to the structure, i.e. delamination, the modelled overpressure source that depends on the LSP and the paint will be injected into a mechanical model. The damage model developed by Soulas [11] is reused in order to assess delamination. The procedure followed in this PhD is summarized below in order to clearly highlight the different bricks that are studied individually in order to build a more complete lightning model for delamination prediction:
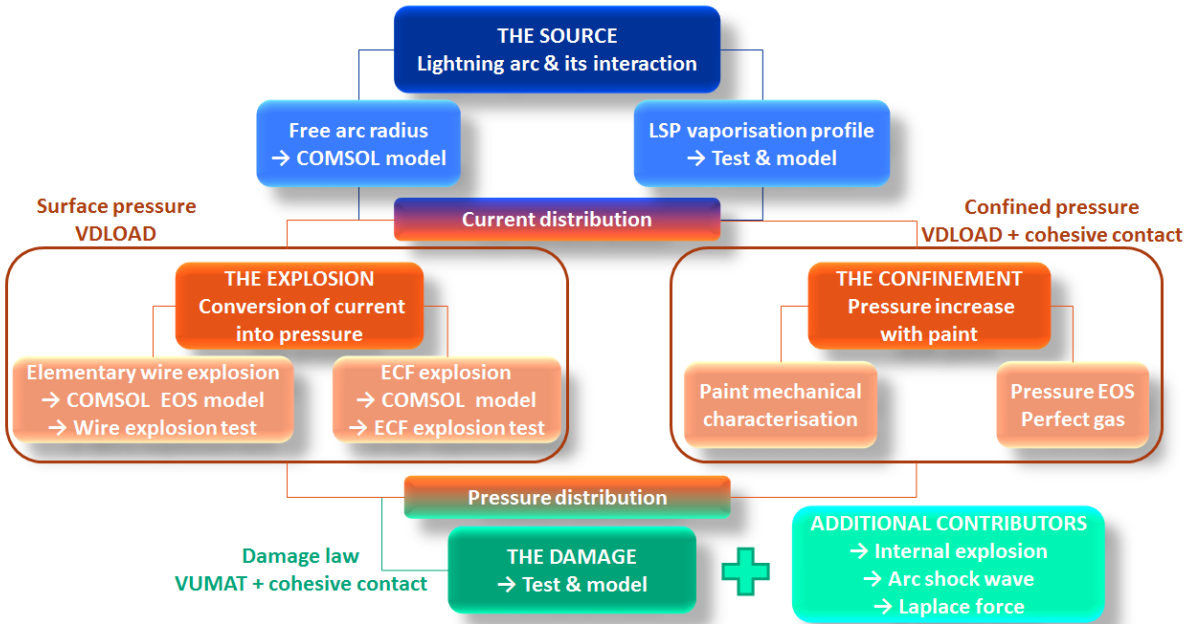
Figure 2-28 Lightning damage model and decomposition

Chapter 3

The lightning arc and its interactions

Objectives

The purpose of this chapter is to propose a model for the lightning arc and its interaction with the surface of the structure. This first step is of primary importance in order to define the current load distribution in time and space which will impact the weight and profile of the forces. To this end, the arc column was studied and then confronted with the arc root evolution when interacting with a surface Lightning Strike Protection (LSP) and then, constricted by the presence of paint.

Specific experimental tests were performed in order to study the arc root and to compare results with the models and propose a methodology to define the arc root space and time evolution with different surface configurations.
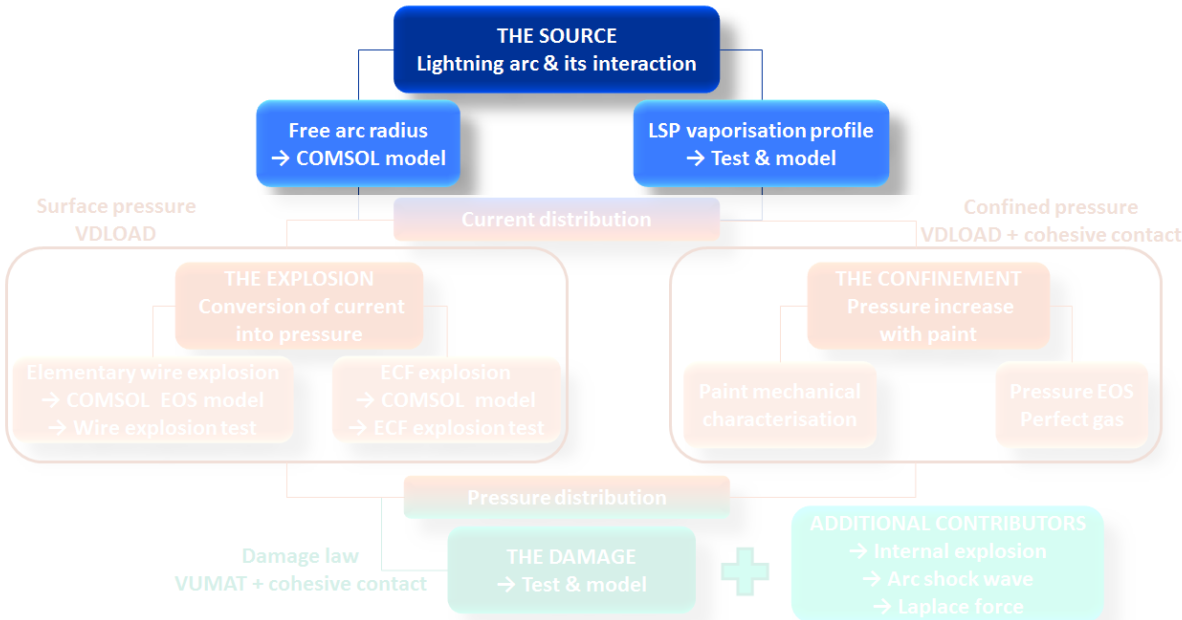
3.1. State of the art

Plasma is considered as the 4th state of matter after the solid, liquid and vapour states. It has been studied since the late 19th century and its behaviour is still difficult to predict as the physics involved are multiple and complex: Fluid mechanics, atomic physics, quantum physics, chemistry… Plasma is an ionised gas, and therefore contains a significant amount of electrical charges (ions and electrons) to become electrically conductive and create an electromagnetic field that will influence its behaviour. The ionisation of a gas usually occurs when the excitation of the atoms is sufficient to create a high rate of collisions that will free electrons. Nevertheless, a low-temperature plasma can be created with an external source of ionisation as in the ionosphere subjected to bombardment by solar particles where the aurora is its visual expression, or as in many industrial applications concerning sputtering or material deposition. Many different types of plasma exist in the universe with a wide range of temperature and charged particle density.
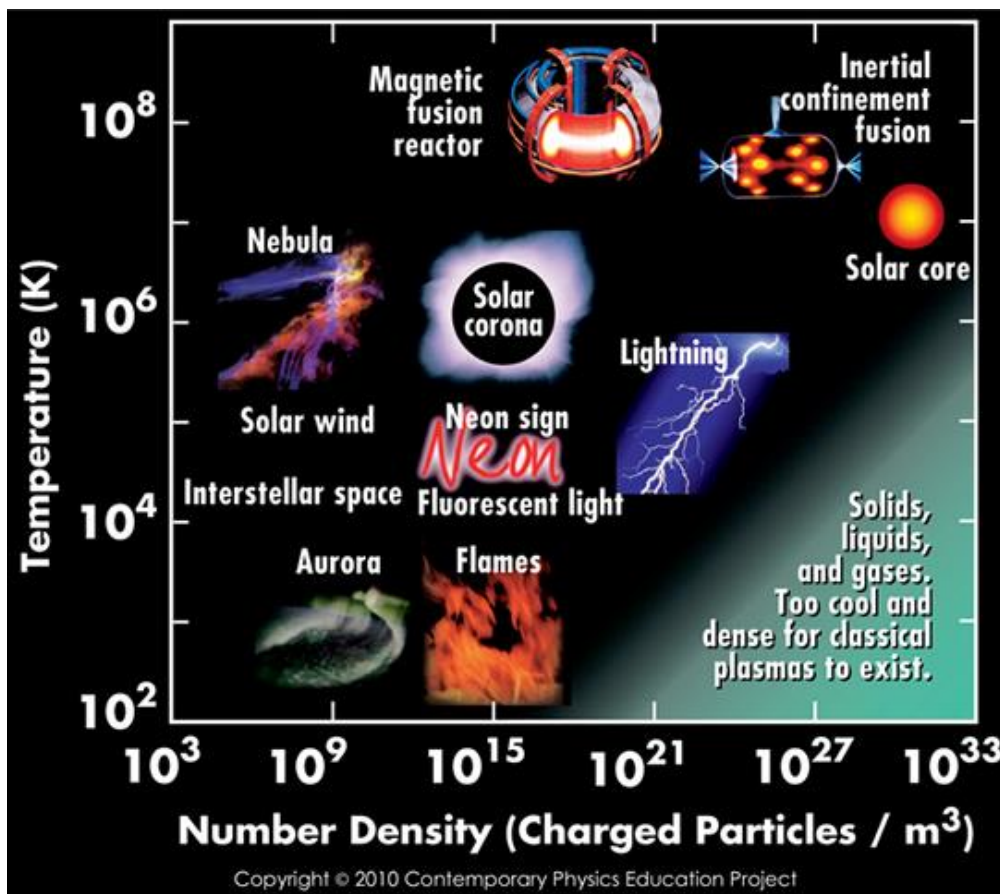
Figure 3-1 The different types of plasma classified by temperature and particle density

Among all these different types of plasma, one is of particular interest: Lightning. In the following chapters we will present the theories and models developed for an arc column and next, the latest development on the arc interaction.

3.1.1. Arc column

The lightning arc channel can be considered as a very hot plasma column since a lightning strike can reach a temperature of up to 40000K [26,70]. This ionized gas column is defined as thermal plasma which is a conductive fluid that will be influenced by an electromagnetic field. Therefore, the laws that will pilot the behaviour of an arc are based on a system of equations. Navier-Stokes equations for the fluid part, Maxwell's equations for the electromagnetic part and the energy conservation equation are coupled with thermal contributions such as Joule heating and radiative losses. The model of the arc physics is based on Magneto-Hydro-Dynamic (MHD) theory. The most usual simplification made is the hypothesis of Local Thermodynamic Equilibrium (LTE) [71]. This hypothesis, which is admitted for thermal plasma at atmospheric pressure, states that the electrons and the heavy particles (ions, molecules and atoms) are at the same temperature. This is an important simplification in modelling of the arc since the electron energy distribution is known. In all cases, the transport coefficients for the plasma in air, its thermodynamic properties and net emission coefficient need to be known.

MHD models have been widely developed for arc welding applications [72]. In this context, the current is continuous and limited to a few hundreds of amperes with a temperature that is therefore limited up to 15000 K. In addition, the arc is usually created in an inert gas (argon) environment. The simulation of these kinds of arc can be simplified and reduced to a stationary model. A lightning arc, however, is far more complex due to the range of current (100 kA) and its transient behaviour. The maximum current is reached in less than 20 µs and the arc is extinguished in less than 500 µs. The temperature reached is very high as well as the radiative losses. Furthermore, the thermodynamic and transport properties in air are required in a wider range of temperature and pressure. Fortunately, in the last decades, studies have been performed in order to provide the plasma community with this information [73]. The properties are now available from 0.01 to 100 atm and 50 to 60000K, which allow the modelling of lightning arcs.

Before considering the MHD model, some researchers [30,53,55,74] proposed to use Bragiinski's approach [52] in order to predict the arc radius. This is a simplified model for moderate current that is considered to increase linearly with time which is different from a lightning current based on a double exponential shape. The radius is expressed as follows:

$$r(t) = \sqrt{(4/\pi^2 \rho_0 \xi \sigma)^{1/3} \int_0^t I^{2/3}(\tau) d\tau} \qquad \text{3-1}$$

where ρ_0 is the air density, ξ is a gas constant equal to 4.5 for air, σ the electrical conductivity of the arc considered constant and equal to 22.2 kS/m, and I the current amplitude. Based on this equation, the maximum radius reached for a waveform D of 100 kA is about 33 mm [30]. This is a relatively simple approach that does not consider the dependency of the arc on pressure or temperature and neglects any losses.

MHD modelling is therefore necessary in order to predict the profile evolution of a free lightning arc. In a first step, 1D axisymmetric models were developed [75–77]. Further developments were performed by ONERA in order to validate this model based on experimental measurements [26,77], as shown in Figure 3-2.
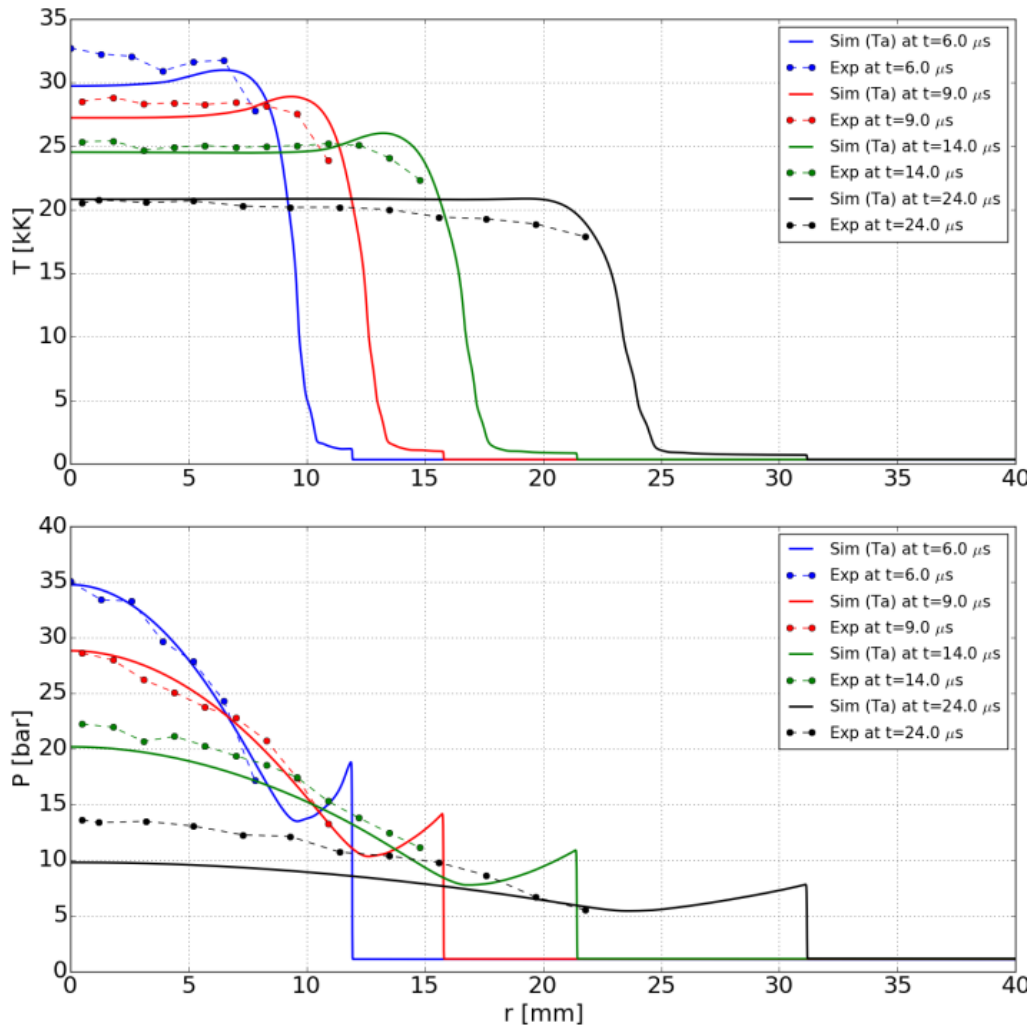
Figure 3-2 Pressure and temperature profiles of a lightning arc (100 kA) : Comparison between MHD calculations and experimental measurements [77]

The experimental work performed by Martins [26] highlighted that the ignition wire material will have an impact on the arc column propagation. This is an interesting point to discuss since lightning test laboratories use a conductive wire, usually metallic, in order to facilitate the arc trigger and orientation. In a metallic wire, the current will flow in the wire and vaporise it to create the plasma. However, the wire temperature does not change homogeneously along its section, as metal vapour but also liquid droplets are injected into the arc which will impact its behaviour (size, pressure, temperature, conductivity). For a carbon wire, due to its low electrical conductivity but also its high thermal properties, the arc seems to be triggered by ionisation around the wire which will not be destroyed by arc generation.
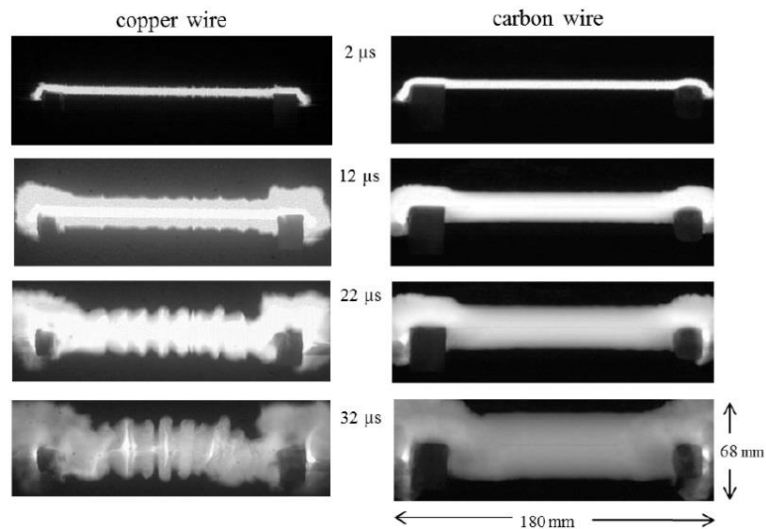
Figure 3-3 Lightning arc expansion dependence on wire material (Copper vs carbon) [26]

Triggering the arc with a metallic wire is less stable than with a carbon wire and this could impact the shock wave generated by the arc during a lightning test. Nonetheless, since it is a low contributor to the global overpressure applied on the composite structure, it should have a limited impact.

Besides these studies, it has been highlighted that the arc and its root are also impacted by the electrode shape and material.

3.1.2. Arc root

In order to model the arc and its interaction with its electrodes, it is necessary to increase the number of dimensions of the above-mentioned models. The first main drawback is that the LTE hypothesis is not applicable close to the electrode, which makes the model far more complex [78]. Originally, the electrodes were considered as a non-deformable boundary. Lago [36] developed a 2D axisymmetric MHD model for low level continuous current which was already a big step in the study of the arc behaviour. He considered the heat transfer and possible thermal degradation of the material due to Joule heating for an arc current. Moreover, he started the development of a 3D model in order to enhance the model's capability by considering anisotropic material for the anode. The objective was to investigate the degradation in the composite material due to the temperature increase but no ablation was possible.
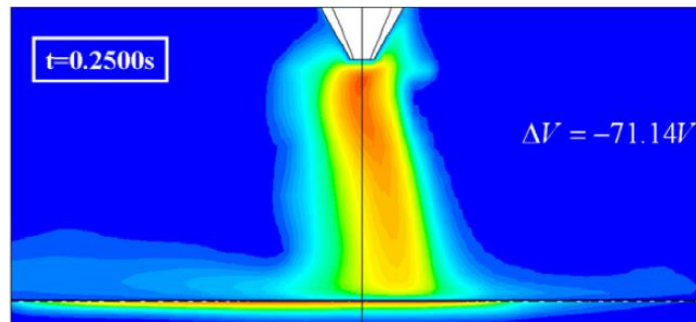
Figure 3-4 3D Continuous lightning arc model[36]

Chemartin [79] also developed a full 3D MHD model, again for low continuous current and aimed to predict the tortuous behaviour of the arc. He also studied the heating of metallic panels due to the continuous current.

These models are quite well advanced but have been validated only for continuous current in a static approach. However, the most important contributor to composite damage is the peak current. An additional step is therefore necessary: to introduce transient high-level current arc modelling. This work was undertaken by Tholin [56] by enhancing the 1D model developed by Peyrou [76]. He developed a 2D axisymmetric MHD model in which the conductivity of the substrate in interaction has an impact on the arc expansion and its root shape.
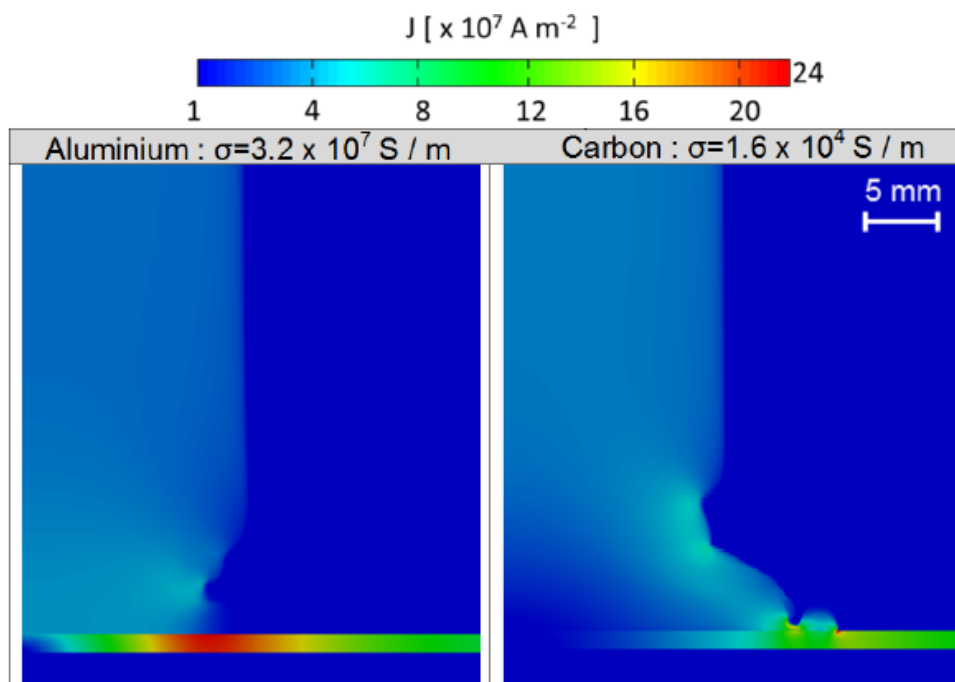
Figure 3-5 Lightning arc root comparison for different substrate conductivities at 26μs [56]

Considering an arc root electrical conductivity of 3×10^4 S/m, the substrate conductivity will constrict or expand its root if it is a higher or lower value compared to the arc itself. This is due to the lightning channel "choice" of the lowest impedance path. An aluminium panel will have a constriction effect in opposition to a composite panel that will expand the arc.

The electrical conductivity effect has been measured by high-speed camera on a bare composite sample [26]. Due to the anisotropy of a composite structure, the arc root expansion cannot be cylindrical and differs depending on its direction, i.e. along the ply or transversally. This effect is illustrated in Figure 3-6 where the expansion of the arc in interaction with CFRP is compared to the free arc column. The ply direction conductivity is 460 kS/m and the transverse conductivity is lower due to the resin matrix and the fibre contact: 4.6 kS/m [80].
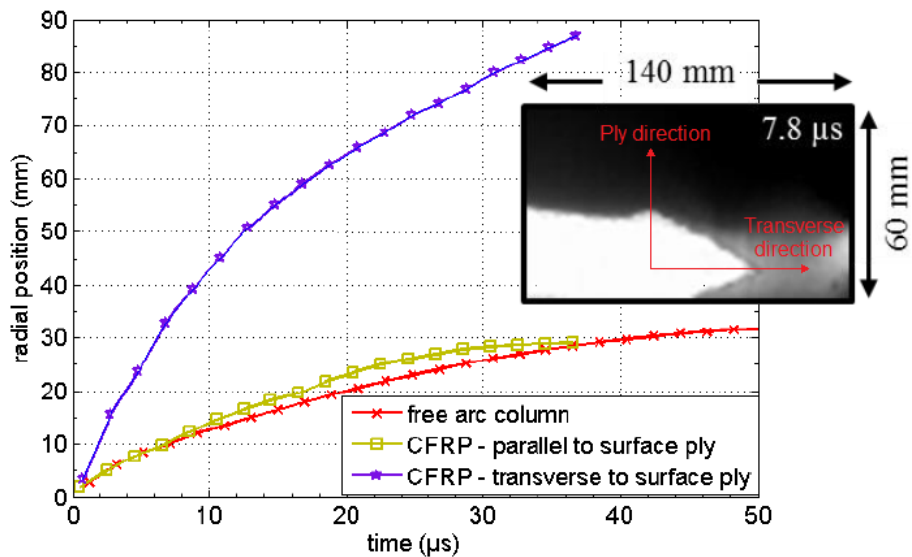
Figure 3-6 Arc root expansion on anisotropic material [26]

Since the conductivity of the substrate in interaction with the arc has a significant impact on the arc root expansion, the evolution of its conductivity with temperature needs to be considered, which is not the case in current MHD models. Moreover, due to the high current density injected into the surface metallic protection, it will rapidly heat up to vaporisation. This means that the surface material shape, in interaction with the arc root, changes during injection of the electric current. The conductive material (LSP) disappears in the central area and this area grows during the injection. Also, metallic vapour from the metallic protection is injected into the plasma and modifies its electrical and thermal properties. Indeed, what is usually observed is the disappearance of the lightning strike protection on the surface of the composite mainly due to Joule heating. Thanks to X-ray measurement, the area of missing metallic protection can be highlighted [30] as shown in Figure 3-7:
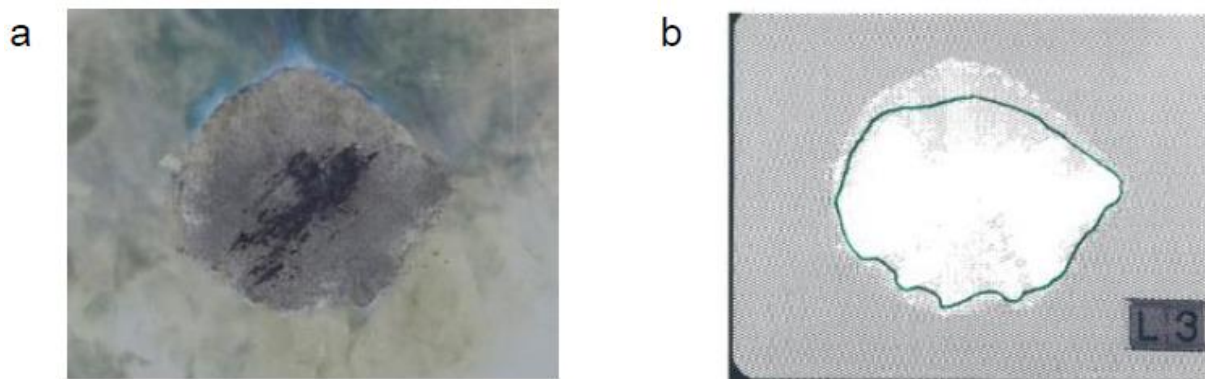
Figure 3-7 Visible damage (left) compared to X-ray measurement showing missing LSP (right) [30]

There will be a coupling effect between the creation of a hollow electrode due to the vaporisation of the LSP and the change of current injection in the LSP due to the change in the arc root profile. This additional phenomenon can be quite complex to model, making the prediction of the arc root evolution and therefore the associated current injection into the structure very difficult. The theory of the hollow arc was first proposed by Lepetit [37] and is illustrated below:
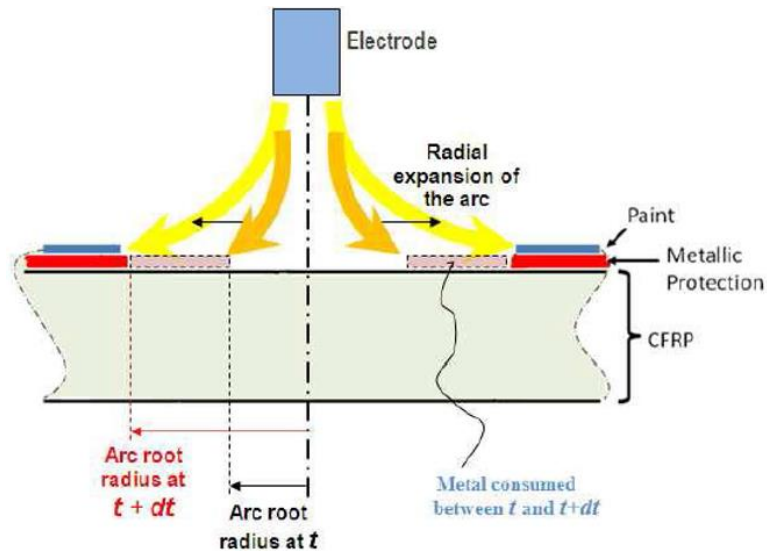
Figure 3-8 Hollow arc root expansion with vaporising surface protection [37]

Considering this approach, a lightning current injection model based on consumption of the metallic protection was proposed by Karch [30]. However, the model is based on an equivalent electrical conductivity with an asymmetrical model which is not adapted to the anisotropy of the LSP. The limitation of this approach is that the consumption of the metallic protection is not coupled with its change of state that will change the current distribution.

Finally, the presence of the paint will also disturb the arc root by creating a physical barrier to its expansion. Indeed, the lightning arc expansion is faster than the thermal effect it may have on the paint. This dielectric layer prevents the arc from attaching on the conductive substrate and will constrict its root. On a metallic panel, since it is thick enough to limit vaporization, the paint is maintained on the substrate and the arc root expansion is limited. This has been observed thanks to high-speed camera measurements [26]:
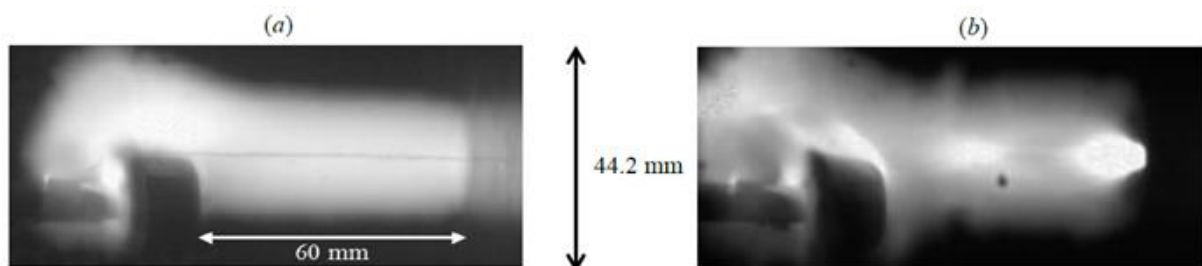
Figure 3-9 Arc root expansion at 15µs of lightning arc at 100kA: a) Bare aluminium panel vs b) painted aluminium panel (Jet electrode on the left and panel on the right)

On a composite panel, the paint is ejected only by the underlying explosion of the LSP as illustrated in Figure 3-10. The arc root constriction will thus change depending on the speed of paint ejection. The removal of the paint will thus be dependent on the type of lightning strike protection and its behaviour against Joule heating but it will also depend on the capability of the paint to sustain this underlying overpressure. The thickness of the paint and its mechanical properties will have a strong impact on its ejection and consequently on the arc root shape [20,29].
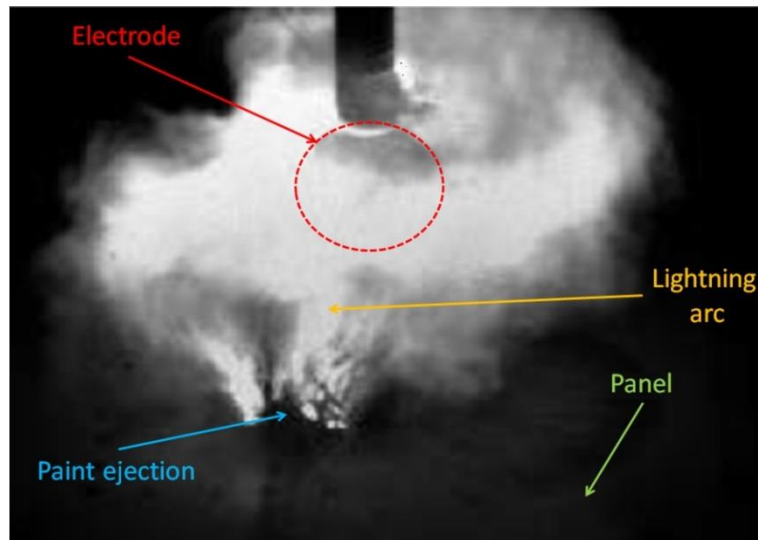
Figure 3-10 Paint ejection by underlying explosion after 32µs

3.1.3. Discussion

The development of a plasma physics model is highly complex but can be studied thanks to MHD theory. Simulation has been improved thanks to the progress in our computation capacity since such physics can be time consuming to solve but also thanks to the characterisation of the thermodynamic and transport properties of the plasma in a wider range of temperature and pressure. Starting with 1D axisymmetric MHD models on a low continuous current, the models have been enhanced to consider a 3D environment and higher current amplitudes with a transient effect. While these developments represent significant progress for lightning arc simulation, a further step is necessary: the introduction of the electrodes. A plasma will be influenced by its interaction with the electrode, especially for its root where the current is injected. The simplifying hypotheses taken for the arc column cannot be used in the vicinity of the interface since the thermodynamic equilibrium is lost. In a first approach, the electrodes were considered as a non-deformable boundary. Then, thermal transfer and Joule heating were studied for the electrodes in order to assess their damage but it has never been coupled to the arc root. This means that the removal of matter does not impact the boundary with the arc root and the matter is not injected into the plasma to study its change of state (temperature, species density, pressure…). Also, as observed experimentally, some simulations have demonstrated the impact of the electrical conductivity of the substrate on the arc root expansion compared to the arc column. But again, it has not been coupled to the change in the substrate conductivity due to thermal effects (mainly Joule heating). In addition to this highly coupled and complex modelling, the mechanical effect of the paint needs to be considered in order to fully study arc interaction with an aircraft structure. This dielectric layer has a constriction effect on the arc root which will again change its distribution. This complexity is increased by the underlying explosion of the metallic protection that pushes and ejects the paint, progressively freeing the arc. A complete model of an arc with its interaction with a composite structure, protected by a metallic LSP and covered by paint, does not exist today and would be very complicated to

develop due to the additional couplings and physics to consider. In order to cope with this difficulty, an innovative approach has been developed in order to study the arc root with the presence of paint and LSP and study its impact. The outcome of this study will be used to propose specific current injection profiles that take into account the impact of paint and LSP.

3.2. Lightning test: Vaporisation profile

The study of the vaporisation profile is important in determining the current injection distribution. The metallic lightning strike protection will divert the majority of the lightning current but its vaporisation, due to Joule heating, will change the interface between the arc root, the LSP and the composite. With an evolving current injection, this will significantly change the profile of overpressure applied on the composite structure and the thermal effect due to current injection. The previous hypothesis based on a fixed radius of current injection needs to be challenged in order to reproduce the loads due to a lightning strike.

The vaporisation of the lightning strike protection is first dependent on the current density and on the thermo-electric properties of the material. This mechanism will therefore also be disturbed by the presence of the paint, constraining the arc root.

Lightning strike is a sudden, very hot event that generates a strong electromagnetic environment. This situation makes it very difficult to perform some measurements, apart from the injected current during a lightning test in the laboratory and, usually, analyses are based on post-mortem observation of the damage (visually and in the laminate). Nevertheless, some researchers [17,29,30,81,82] have used a high-speed camera to observe the arc attachment and expansion on the front of the panel. In Figure 3-11, a sample image recorded by high-speed camera is presented. It was taken during Airbus R&T lightning tests.
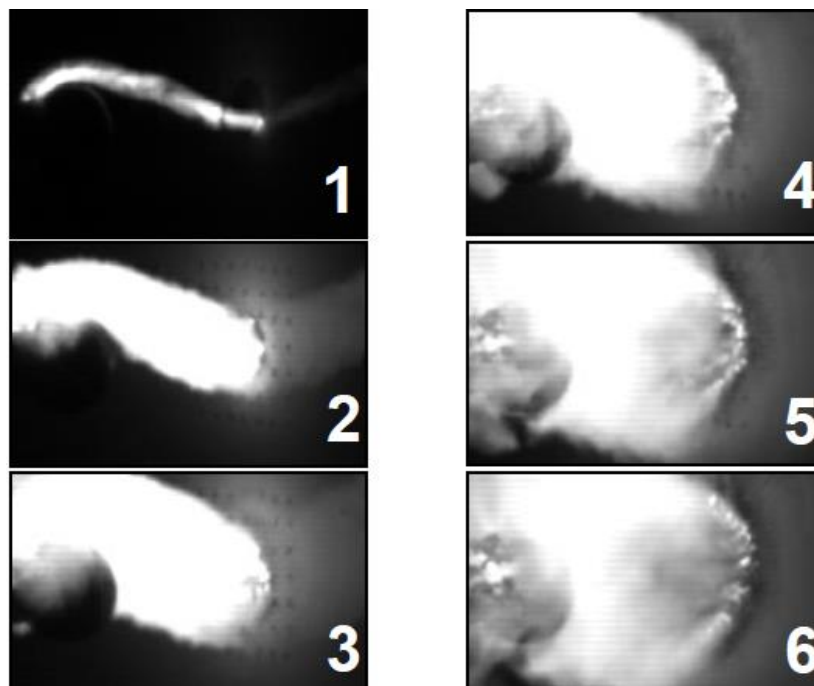
Figure 3-11 Lightning test - High speed camera measurement every 4.76 µs (Airbus R&T)

These observations are very interesting but provide mostly qualitative information that is difficult to interpret due to the ejection of paint that can mask the arc root and the high luminosity of the arc and hot gases that can saturate the camera. It has therefore been proposed to use the high-speed camera in a different way: Instead of recording the plasma evolution from the side, the camera is placed on the back of a transparent sample where the vaporisation profile can be easily measured.

There are several advantages with this approach. The first one is that it simplifies and decomposes the lightning damage mechanism since the use of a transparent panel instead of a composite (and black) panel will ensure that all the current is injected into the lightning strike protection. This will remove the uncertainty related to the distribution of current between the LSP and the CFRP panel since the transparent panel used is made of Glass Fibre Reinforced Plastic (GFRP) which is highly insulating compared to CFRP. As observed after a lightning test, the presence of dry fibre is evidence of current injection in the composite but it is difficult to determine the amount. This current diversion can modify the current distribution and add to the difficulty of validating an injection profile [83]. As shown in Figure 3-12 below, the vaporisation of ECF in the presence of an underlying CFRP panel that diverts part of the current is different from the case with an underlying GFRP panel. However, for SCF, which diverts the current completely, there is no influence of the underlying panel.
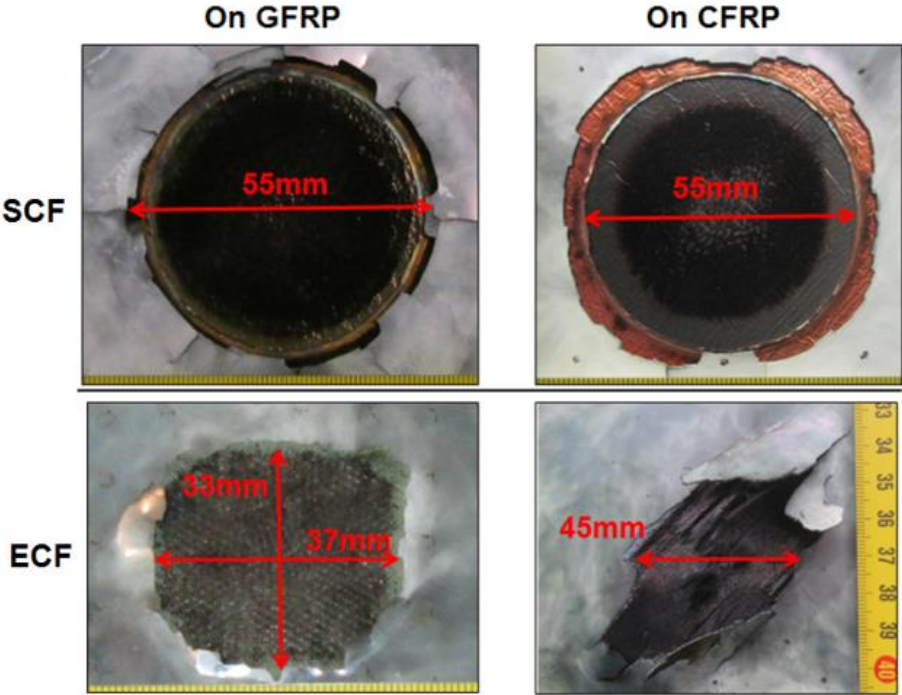
Figure 3-12 Vaporisation profile on CFRP vs GFRP

The second advantage of this method is that it enables the vaporization of the metallic protection to be observed without any disturbances due to the paint cover and the expanding arc column. The only focus is the arc root which is our interest in this study.

3.2.1. Test setup

Several lightning tests were performed in the DGA-TA laboratory (Toulouse, France) where a simulated lightning strike can be produced. This lightning current is based on the waveform D definition [3] with a maximum amplitude of 100 kA reached in 18 µs and a duration of about 80 µs. The transparent panels were made of 11 250 µm thick GFRP plies for the substrate. Several combinations of LSP (ECF195, ECF73 or SCF88) and paint thicknesses (200, 400, 800µm) were also manufactured.

A high-speed camera (Photron IS1M) was installed on the back of the sample in order to record the vaporization profile through the transparent panel since the vaporization of copper is brighter than the arc itself. The camera can record 100 pictures every µs with 312x260 pixels and a resolution of 96dpi. The setup is illustrated in the schematic below:
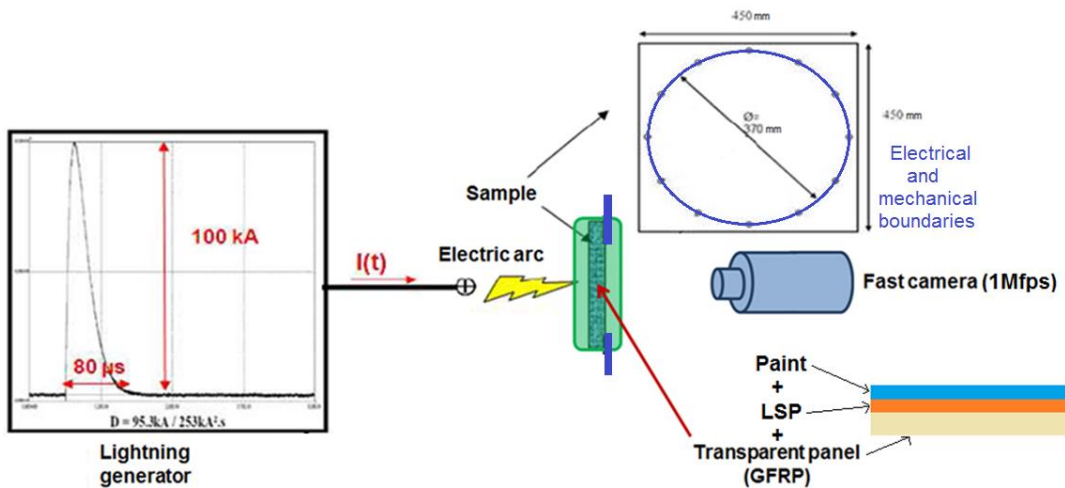
Figure 3-13 LSP vaporisation profile test set up

3.2.2. Test results & Interpretation

As explained above, the high-speed camera can record the light produced by the lightning arc through the transparency of the GFRP panel. The observation of the pictures is interesting as the arc root seems to be hollow and to expand with the vaporisation of the copper. The picture below shows the vaporisation profile of Solid Copper Foil which is circular since the conductivity of the protection is homogeneous and isotropic.
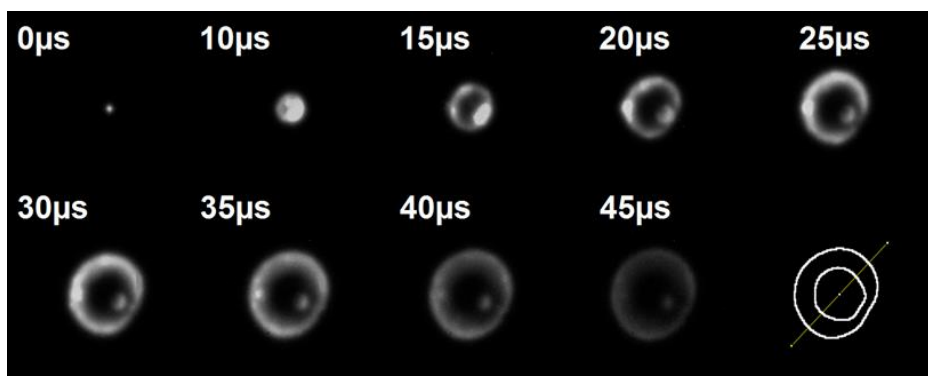
Figure 3-14 SCF vaporisation profile example with internal and external contour detection (bottom right)

After image processing with the software ImageJ, it is possible to extract the boundary of the light profile. This analysis was performed on the following configurations:

LSP type	Paint			
	0µm	200µm	300µm	550µm
ECF195	x	x	x	x
ECF73			x	
SCF88		x		x

Table 3-1 LSP vaporisation profile test matrix

It can be seen on Figure 3-14 that the detection of the vaporization profile is based on detection of the light corona profile. The intensity of the light is not constant during the test due to the decrease in current amplitude after 20 µs and the decrease in metal vaporisation. Therefore, the analysis of the pictures with a specific filter and binary conversion will lead to some uncertainty of measurement up to 2 mm. A high corona intensity will have a larger profile than a slightly luminous corona. This error is thus not constant along the measurement and with the camera settings. This is what we can observe on Figure 3-15 below: Between test campaign 1 and test campaign 2 in which the camera settings were different, the measured diameter is different. During campaign 2, the sensitivity was higher and the camera was slightly saturated which led to a value higher than the real SCF vaporisation: as the final diameter of SCF consumed was 55 mm, the vaporisation cannot be higher. This diameter was measured after the lightning test based on the missing copper area as shown in Figure 3-12. It was identical for all the different lightning tests performed with this SCF and is reported once in the graph below. It is also important to notice that the diameter decreases after a while which is due to the decreasing intensity of the light and therefore to the associated difficulty in processing the images with a good precision.
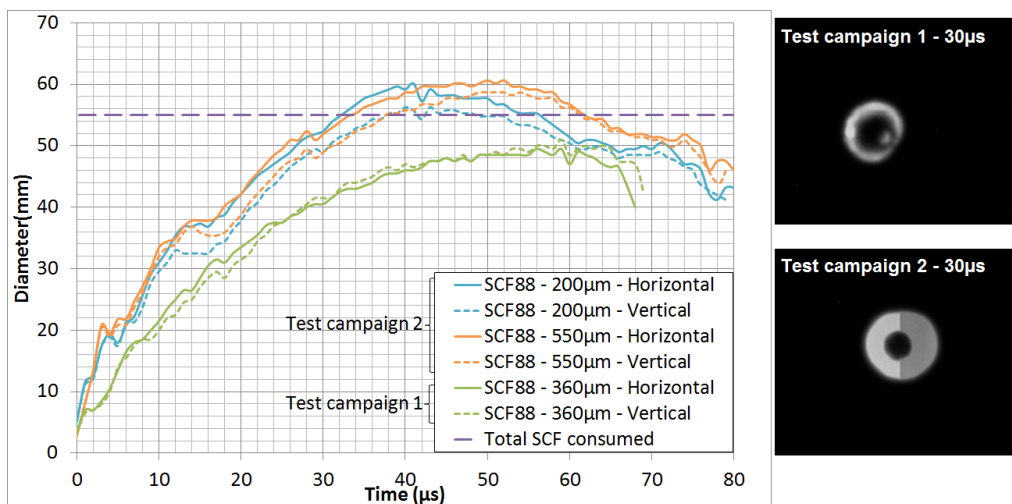
Figure 3-15 Measured mean vaporisation diameter in the case of isotropic protection (SCF88)

The important conclusion from this first configuration is the validation of the axisymmetric vaporization profile evolution of an isotropic protection since these horizontal and vertical profiles are identical. This will be useful to validate the Joule heating model developed in 3.3.2.

Another important observation is that the paint thickness has no impact on the consumption of metal. This is explained by the fact that the constriction cannot lead to a different current distribution since the electrical conductivity is isotropic therefore the impedance path is identical in all directions.

Moreover, the maximum value of the vaporization diameter of the first campaign, based on the light measurement on the back of the panel, is lower than the measured diameter of the total copper consumed recorded after the lightning test. This difference can be explained by the fact that the consumption of the metal is due to vaporisation but also to melting. Due to the gas expansion on the front of the panel, the liquid metal is ejected. Therefore, the final copper missing area, called the consumed surface, should be related to the melted area. This area is larger than the vaporised area that we associated to the light profile measured. This will be discussed in 3.3.2.

The metallic protection of interest is Expanded Copper Foil Figure 3-16 which is widely used in the aeronautical industry. Studying this protection presents a challenge due to the geometrical pattern that creates anisotropy in the electrical and thermal properties. We studied two grades of LSP: ECF73 and ECF195 which have exactly the same diamond pattern of 1.23 mm (SWD) by 2.54 mm (LWD) but with a different metal section per "wire".
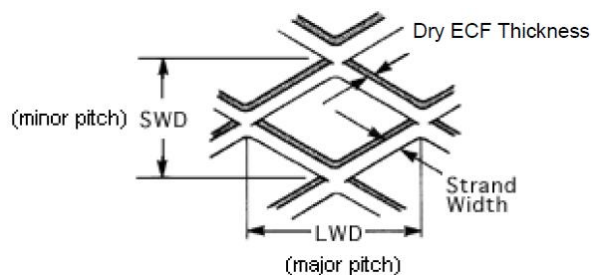
Figure 3-16 ECF pattern

For ECF195, the thickness is 76 μm and the strand width is 178 μm with a surface weight (w_{ECF195}) of 195 g/m² and for ECF73, the thickness is 51 μm and the strand width is 102 μm with a surface weight (w_{ECF73}) of 73 g/m². The data is detailed in Table 3-2:

	Surface weight (g/m²)	Thickness (μm)	strand width (μm)	SWD (mm)	LWD (mm)
ECF73	73	51	102	1.23	2.54
ECF195	195	76	178	1.23	2.54

Table 3-2 Expanded Copper Foil geometry parameters

Due to the metal pattern shape with a difference between SWD and LWD, the electrical conductivity of such a protection is anisotropic: the horizontal expansion of the vaporisation profile is greater than the vertical expansion since the conductivity is lower in this direction. For a lower density material, the vaporised area expansion is higher and quicker since a smaller section of metal is available to conduct the current. Considering the Joule heating law in a simplified approach, we can determine the total consumed mass ratio difference for these 2 ECF grades:

$$\int mC_p dT = \int Ri^2 dt \leftrightarrow \rho t_{eq} S_{vap} \int C_p dT = \frac{1}{\sigma 2\pi t_{eq}} \int ri^2 dt \qquad \text{3-2}$$

with m the mass of copper, C_p its specific heat, ρ its mass density, σ its electrical conductivity, R the electric resistance of the mesh, I the input current, t_{eq} the equivalent thickness of ECF (t_{eq}=w/ρ), S_{vap} the vaporised surface of ECF and r the radius from the current injection in the centre to the ground potential at the edge of the disk.

Based on this equation, we can define the mass ratio for the ECF vaporised surface:

$$\begin{cases} \dfrac{m_{ECF195}}{m_{ECF73}} = \dfrac{t_{eq}^{ECF73}}{t_{eq}^{ECF195}} = \dfrac{w_{ECF73}}{\rho} \times \dfrac{\rho}{w_{ECF195}} = \dfrac{73}{195} = 0.375 \\[4mm] \dfrac{S_{ECF195}}{S_{ECF73}} = \left(\dfrac{t_{eq}^{ECF73}}{t_{eq}^{ECF195}}\right)^2 = \left(\dfrac{w_{ECF73}}{w_{ECF195}}\right)^2 = \left(\dfrac{73}{195}\right)^2 = 0.14 \end{cases} \qquad \text{3-3}$$

This computed vaporised surface is compared to the consumed surface after a lightning test. This surface is associated to the area where the paint has been ejected. Indeed, the vaporisation of ECF creates a high pressure that pushes the paint away. The measured consumed surfaces for ECF195 and ECF73 are respectively 11.3 cm² (± 10 %) and 96 cm² (± 10 %), therefore the ratio is equal to 0.12 which is within the accuracy range in comparison to 0.14. This simple approach is possible only for an identical pattern. It will thus not work for SCF for which the geometry is different. For the SCF88 configuration, the consumed surface is 23.75 cm² and the total mass consumed is equal to that of the ECF195 configuration (0.212 g) but it is a coincidence. The shape of the vaporised area is close to an ellipse. We compare its horizontal and vertical diameter between the back light measurement and the front face consumed area in Figure 3-17:
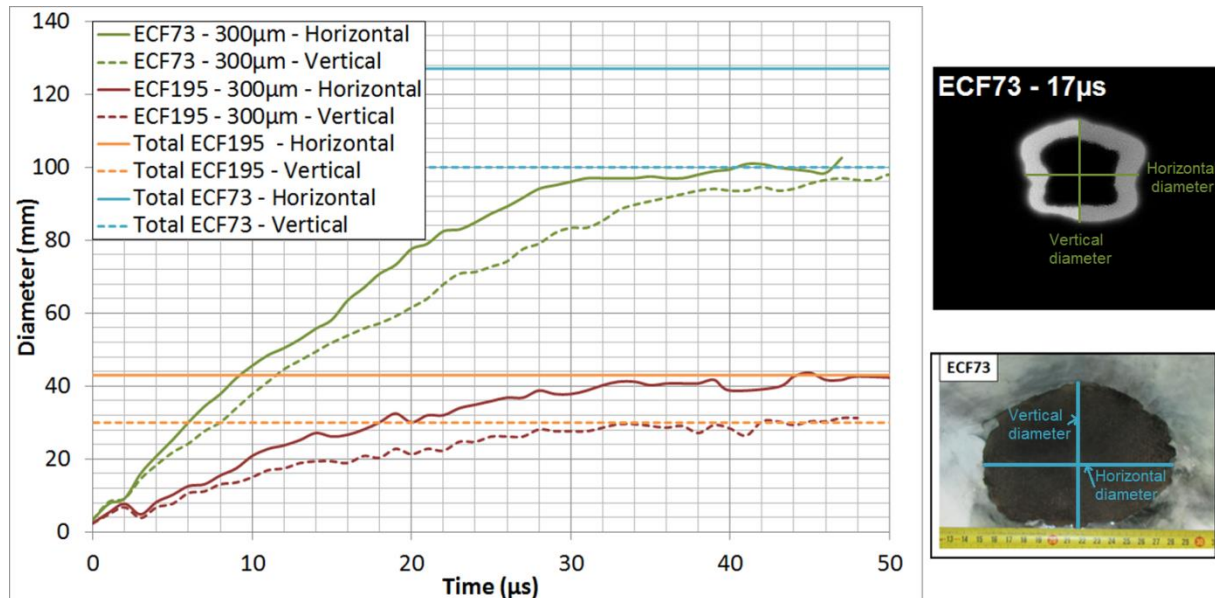
Figure 3-17 Measured mean vaporisation diameter in the case of isotropic protection (ECF73 and ECF195)

For ECF195, the comparison between the consumed horizontal and vertical diameters, measured after the lightning test based on the ejected paint surface, and the final diameters

of the light measurement from the back of the panel during the test, associated to the vaporisation profile, presents a good agreement. But this is not the case for ECF73 for which the horizontal light expansion seems to be constrained as can be observed in Figure 3-17. There is possibly a screen effect of the paint and the total consumed ECF is probably due to the subsequent melting which does not create any light.

The paint thickness has indeed a constriction effect as demonstrated in Figure 3-18. For a thin paint configuration, the consumption of the metal is close to a diamond shape, similar to its geometrical pattern. But, with the increase in paint thickness, the constriction of the arc root is more and more visible, leading to axisymmetric profiles of ECF vaporization. The horizontal and vertical diameters of the ellipse tend to be identical with increase in the paint thickness. In addition, based on the measurement of the arc column diameter from Sousa Martins [26], we can observe that the vaporisation profile is smaller than the arc column.
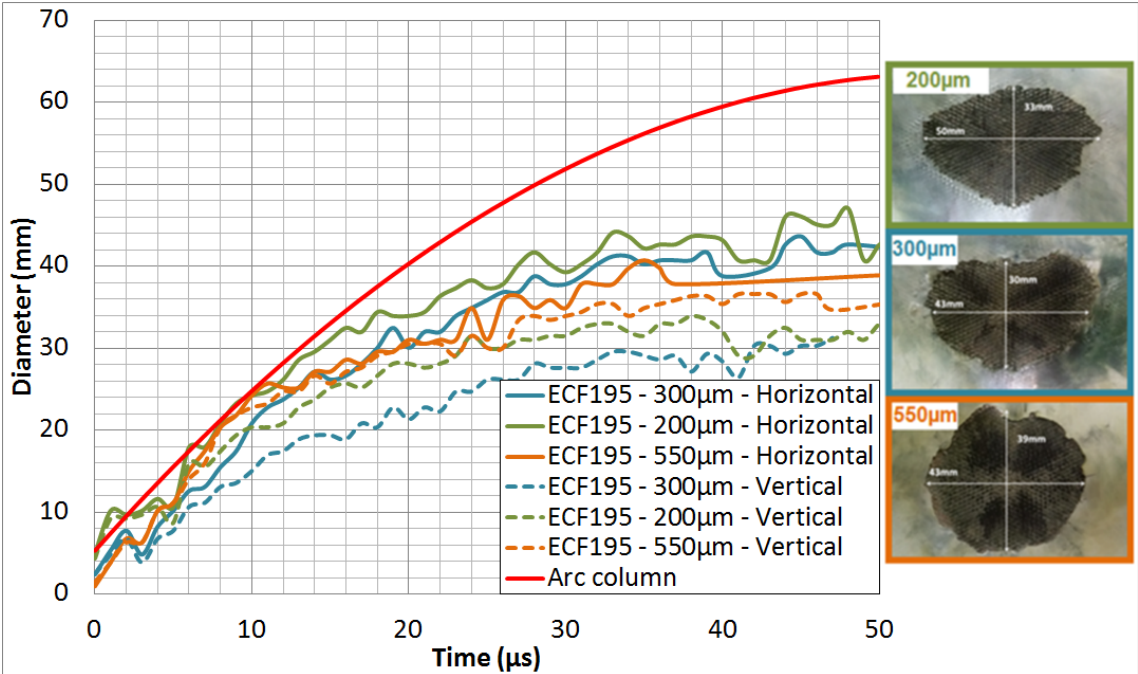
Figure 3-18 Paint impact on vaporisation profile of anisotropic protection (ECF195)

The total mass of copper consumed is the same regardless of the thickness of the paint. This result can be explained by the fact that in all cases the injected energy, related to the current density and material properties are the same. About 0.213 g is consumed for ECF195 with 200 and 300 μm of paint and it is slightly higher (0.245 g) for 550 μm of paint. This is the case if we consider only the ejected paint area, but there are some bubbles visible below the paint which are evidence of an underlying vaporisation. If we include this additional parameter, the areas are identical between all paint configurations, and therefore the mass of consumed metal as well. Yet, the contour is clearly different, as shown in Figure 3-19, which implies that the paint constriction effect is very strong on the arc root. The current injection profile in the LSP needs to be adapted depending on this constriction effect and the vaporisation profile as a consequence. The spatio-temporal distribution of the vaporisation is then used for the application of an equivalent overpressure in the next chapters.
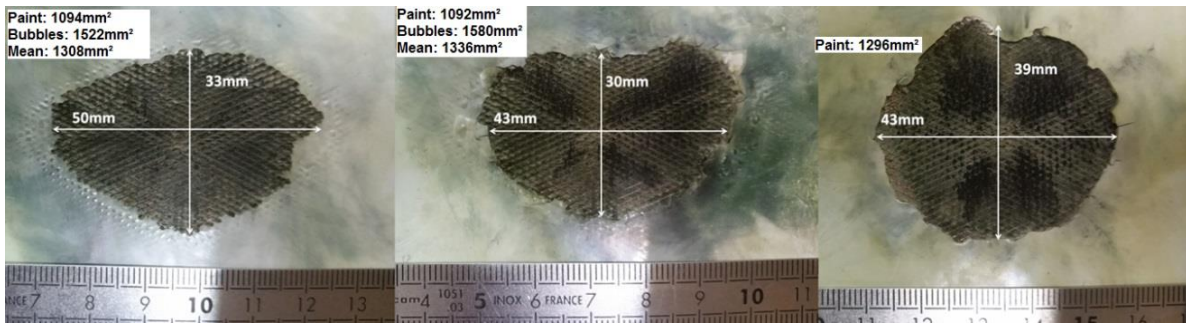
Figure 3-19 Paint impact on metal consumption (200µm/300µm/550µm)

In order to analyse this phenomenon, the arc can be decomposed into two areas:

- **The column:** The behaviour is that of a free arc column and the expansion is axisymmetric, if one neglects the influence of the tortuous movements of the column when it is long.
- **The arc root:** The behaviour depends on the LSP electrical conductivity and state (vaporised or solid). Its behaviour also depends on the presence of paint which prevents its expansion.

The column first goes through a phase of rapid expansion (Column Phase 1) before a stabilisation phase, and a recession with the decreasing current amplitude (Column Phase 2). The arc root has a first phase (Root Phase 1) with its expansion constrained by the paint, thus $\emptyset_{\text{Arc root}} \leq \emptyset_{\text{Arc column}}$. The expansion is dependent on the mechanical opposition of the paint to the axisymmetric expansion of the column, and consequently tends to be axisymmetric. Then, the Joule heating due to the current flow in the underlying LSP generates a sudden vaporisation which is, in fact, an electric explosion. This theory will be further explained in chapter 4. The explosion creates an overpressure that pushes and ejects the paint. The paint ejection depends on the explosion pressure profile and on the mechanical resistance of the paint to the underlying overpressure. Moreover, the explosion distribution, related to the vaporisation distribution, depends on the electro-thermal properties of the LSP as well as on the current injection distribution. If the paint is released quickly, the arc root expands as a function of the electric conductivity of the LSP which can be anisotropic. In that case the arc root diameter is higher than that of the arc column (Root Phase 2). The duration or even existence of this second phase will change with the mechanical resistance of the paint (linked to its thickness) and the LSP electric conductivity. This theory is illustrated in Figure 3-20:
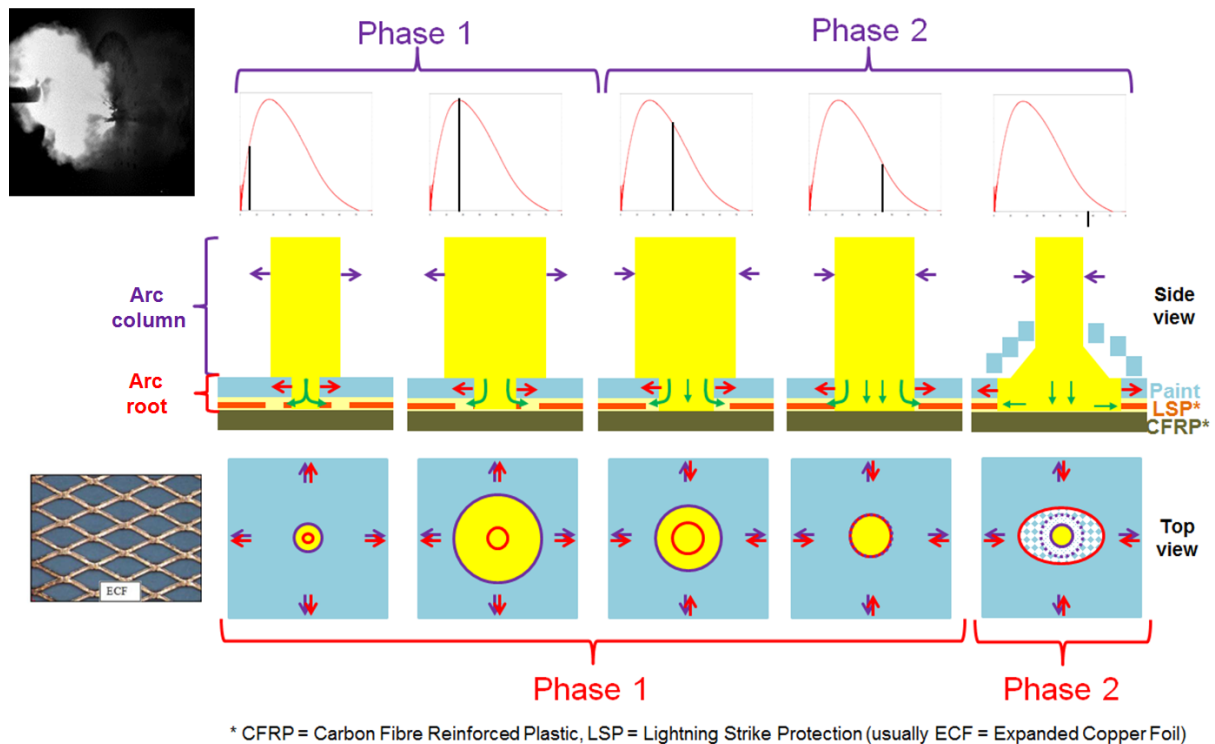
Figure 3-20 Arc expansion theory

For this reason, the vaporisation profile of ECF when there is no paint is close to a diamond shape as the arc root expansion is only dependent on ECF conductivity. This configuration has therefore no root phase 1 and is only in root phase 2. With the introduction of the paint, the root phase 1 is introduced and lasts longer due to the paint confinement effect. In this case, this is mainly related to the paint thickness for an identical coating. There is therefore a competition between root phase 1 and root phase 2 that will change the expansion profile and the shape of the metal consumption area.

The vaporisation temporal profile is based on the measurement of the light through the GFRP transparent panel. Several configurations of paint thickness were tested to assess its impact on the vaporisation profile of ECF195 subjected to lightning WFD. The results are presented in Figure 3-21 below. When the panel is painted, the deformation of the vaporisation profile with the thickness is clearly visible. For the bare panel, the measurement is more difficult since the panel is fully transparent and the arc column is visible. Still, the diamond shape is visible in the late stage of the vaporisation.
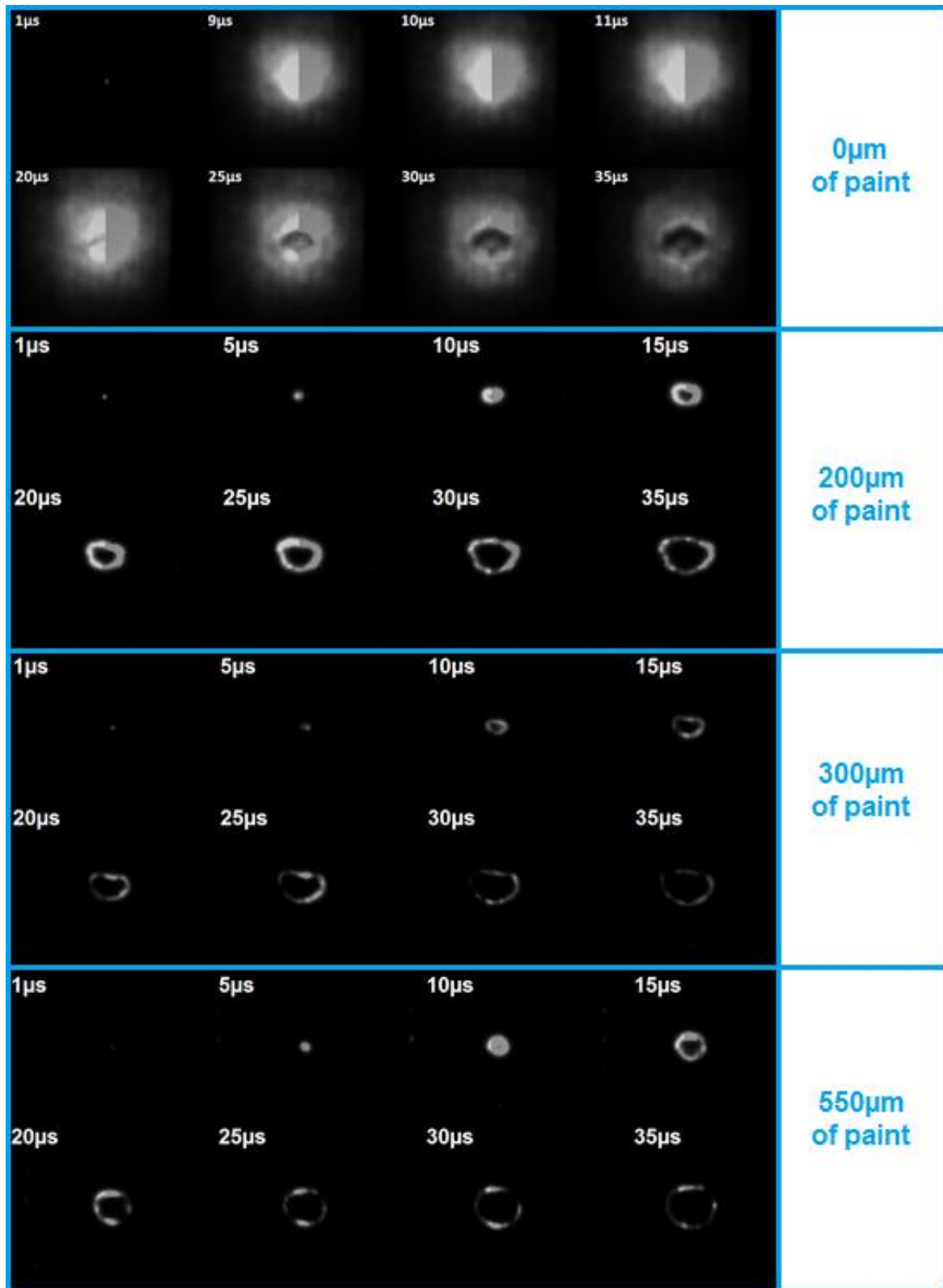
Figure 3-21 Vaporisation profile visualization vs time & paint thickness

The vaporisation profile is the consequence of the arc column and the arc root expansion due to LSP electro-thermal properties but also to the presence of paint. The mechanical resistance of this layer will modify the arc root expansion and, as a result, the current injection and the vaporisation profile.

3.3. Model

In the following section, the arc column and the vaporisation profile of the metallic LSP are studied. First, the arc column radius will be simulated in a 1D axisymmetric model. Then, the vaporisation profile of the SCF and the ECF are simulated considering first a fixed injection point, and then, with different injection profiles in order to assess their impact on the vaporisation profile. Finally, the two expansion profiles (arc column and LSP vaporisation) will be compared for the critical analysis of the theory developed above.

3.3.1. Arc column

We tried to predict the arc column expansion for a high amplitude transient current in a simple approach including however electromagnetic, heat and fluid equations. In COMSOL Multiphysics®, a 1D axisymmetric model was created to simplify the computation and save time since we consider a radial expansion only for the free column in a transient phase. The heat equation in the fluid is solved in 1D:

$$d_z \rho C_p \frac{\partial T}{\partial t} + \rho C_p \boldsymbol{u} \nabla T = \nabla.(d_z k \nabla T) + d_z Q + q_0 + d_z Q_p + d_z Q_{vd}$$

$$\nabla = \frac{\partial}{\partial r}$$

3-4

with d_z the thickness of domain in the out-of-plane direction (m), ρ the density (kg/m^3), C_p the specific heat (J/(kg.K)), T the temperature (K), $\boldsymbol{u}$ the velocity vector of translational motion (m/s), k the thermal conductivity (W/(m.K)), Q the heat sources (W/m^3) which are in this case the Joule heating and the radiation loss, q_0 the inward heat flux (W/m²), Q_p the pressure work (W/m^3) and Q_{vd} the viscous dissipation work (W/m^3). The pressure work and the viscous dissipation are defined as follows:

$$\begin{cases} Q_p = \alpha_p T \left(\frac{\partial p}{\partial t} + \boldsymbol{u}.\nabla p \right) \\ Q_{vd} = \tau : \nabla \boldsymbol{u} \end{cases}$$

3-5

with p the pressure (Pa), α_p the coefficient of thermal expansion $(-\frac{1}{\rho}\frac{\partial \rho}{\partial t})$ (K^{-1}) and τ the viscous stress tensor (σ=-p$\boldsymbol{I}$+τ).

The heat sources are computed following the relation:

$$Q = \boldsymbol{J}.\boldsymbol{E} - 4\pi Q_{rad} = \sigma E_z{}^2 - 4\pi Q_{rad}(T)$$

3-6

Since it is a cylindrical problem with a vertical current only, we can simplify the equation by considering only E_z homogeneous in the plasma of a computation domain radius r_{arc}:

$$E_z = \frac{I(t)}{2\pi \int_0^{r_{arc}} \sigma r dr}$$

3-7

This set of equations refers to material properties. These data for plasma in air were found in the literature up to 60000K [73]. The heat loss per radiation (Q_{rad}) was taken from the material database of COMSOL® and is also dependent on the temperature.

In addition to the heat equation, the fluid movement is solved using Navier-Stokes theory in 1D. In COMSOL Multiphysics®, it is introduced by a Partial Differential Equation (PDE). The conservation of movement quantity is associated to the mass continuity, the viscosity and the induced forces:

$$\rho r \frac{\partial u}{\partial t} + \rho r u \nabla u + \nabla . (-2r\mu\nabla u) + 2\frac{\mu}{r}u = r(F_{mag} + F_p) \tag{3-8}$$
$$F_{mag} = -\boldsymbol{j_z}.\boldsymbol{B_\theta} \ and \ F_p = -\nabla p$$

with ρ the density (kg/m^3), r the radius (m), u the radial velocity (m/s), μ the fluid viscosity (Pa.s), j_z the axial current density (A/m^2), B_θ the azimuthal magnetic field (T) and p the pressure (Pa). The components of the magnetic forces are defined below:

$$\boldsymbol{j_z} = \sigma \boldsymbol{E_z}$$
$$\boldsymbol{B_\theta} = \frac{\mu_0}{r}\int_0^{r_{arc}} \boldsymbol{j_z} r dr \tag{3-9}$$

Finally, the pressure will be considered to follow the perfect gas law:

$$p = \rho \frac{R}{M}T \tag{3-10}$$

with R the universal constant of the perfect gas (8,314 J/(K.mol)), M the molar mass (kg/mol) and T the temperature (K).

The objective of this model is to compute the radius of the free arc column. For this purpose, the Elenbaas-Heller equation [84] was used in order to obtain the temperature profile of the arc stabilised by the domain wall. For a domain limit smaller than the natural arc radius, the boundary conditions will influence the result of this equation. In order to assess the free arc column radius, it is necessary to consider the pressure F_p and the magnetic constriction of the arc F_{mag}. From the equation of movement quantity conservation, the speed u is computed and the influence of those forces is introduced as defined in equation 3-8. In a first step, the pressure in the arc is considered at equilibrium with the ambient environment: P=1bar.

Since an arc cannot be created from an ambient pressure and temperature, it is necessary to build an initial temperature profile. We therefore computed a temperature profile from a stationary configuration, considering 10% of the maximum lightning current waveform. Then, the temporal computation of the arc with a current of WFD, as applied during the laboratory test, and a maximum of 10kA was started at the time when this current waveform was assumed to reach 10% of its maximum.

Figure 3-22 presents the temperature profiles during the first fifty microseconds. As can be seen, the temperature profile seems usual but its values are too high for such a current (10kA). In addition, the result presented only considered a quarter of the speed contribution in the heat equation 3-4. Indeed, several computations were done with different speed weight contributions. With the total speed injected in the heat equation, the temperature profiles are very sharp and the temperature is even higher. This behaviour is explained by the magnetic constriction of the arc that is overestimated since it is not compensated by the internal pressure of the arc. This is due to our first simple hypothesis of the arc pressure at the ambient pressure and the plasma properties dependent only on the temperature and not on the pressure. However, it is mandatory to take into account the pressure gradient in the arc in order to obtain an acceptable temperature profile. This is not possible however with this hypothesis. Unfortunately, the next step is not straightforward since the pressure in the arc at its initiation is not well-known.
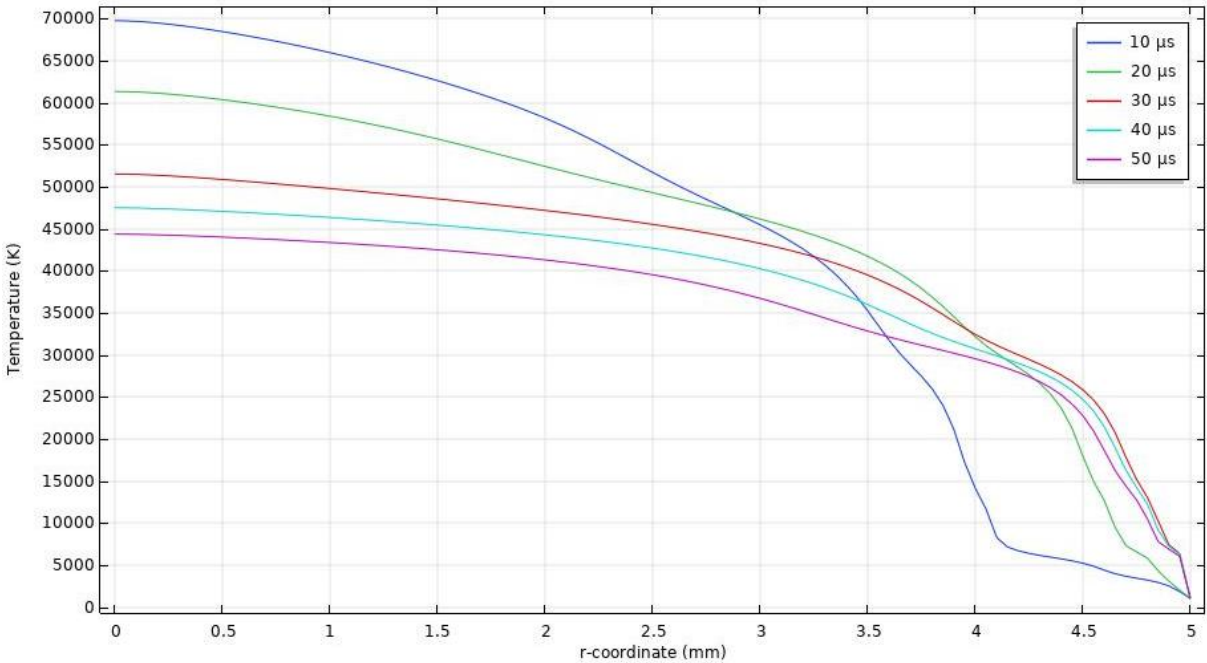
Figure 3-22 Lightning WF1 at 10kA: Arc temperature profile at different times (speed=0.25u)

Figure 3-23 presents the evolution of the temperature profile as a function of time at different radii in the domain. In addition, the current waveform is plotted in order to compare the result with the different current phases.
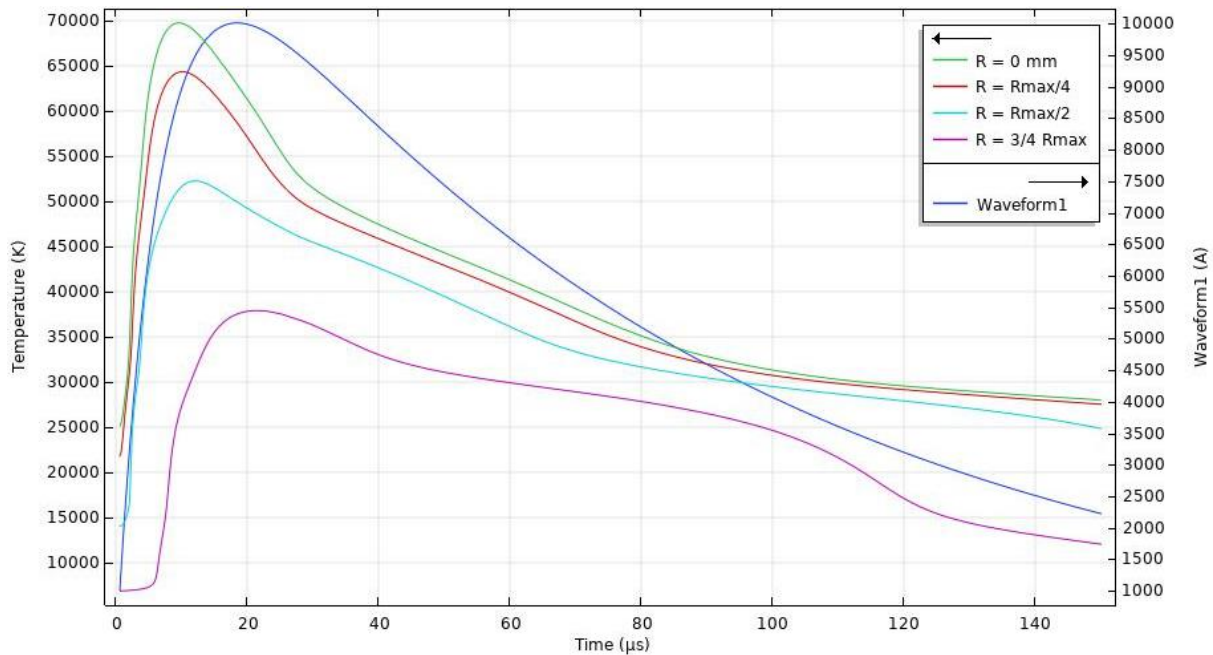
Figure 3-23 Arc temperature profile at different radii and synchronisation with the current waveform

Prior to the current peak, it seems that the temperature increases more rapidly than the current, which is unexpected. This overshoot of temperature is only due to the numerical equation solving and does not reflect the behaviour of the arc, as even with a change in the current waveform in order to assess the impact of the current increase in the temperature profile, there is a delay of about thirty microseconds before convergence to a consistent solution. This issue is purely numerical and has not yet been solved.

This first approach for the prediction of the arc column temperature is a good step reached in our study but it has to be improved in order to propose consistent results. For this purpose, it will be necessary to consider the arc pressure gradient with good initial conditions and plasma properties' dependency on both temperature and pressure. But it will also be mandatory to deal with the issue related to the numerical solver of COMSOL®.

Even if the arc column could not be predicted by our approach, we can still study the vaporisation profile of the LSP with an arbitrary fixed current injection. This next step, which is presented in the following section, is important to understand the parameters of the LSP involved in this phenomenon.

3.3.2. Vaporisation profile

In order to predict the vaporisation profile in the metallic LSP, Joule heating has to be computed. In COMSOL Multiphysics®, several configurations were simulated in order to assess our ability to manage LSP complexity. In a first step, SCF which is a uniform copper foil was studied. The interest of this configuration is its axisymmetric aspect which provides rapid results regarding the sensitivity to physical parameters. Then, a full 3D ECF model was considered and finally an equivalent foil with anisotropic properties was studied in order to facilitate the simulation. In the software, Joule heating was computed by the addition of the

"electric current" and "heat transfer" modules that are coupled with the "Multiphysics" module. The following equations, based on Maxwell's equations, will be solved for the first module:

$$\begin{cases} \nabla.\boldsymbol{J} = Q_j = -\dfrac{\partial \rho_e}{\partial t} \\ \boldsymbol{J} = \left(\sigma + \varepsilon_0 \varepsilon_r \dfrac{\partial}{\partial t}\right) \boldsymbol{E} + \boldsymbol{J}_e \\ \quad \boldsymbol{E} = -\nabla V \end{cases} \qquad \text{3-11}$$

with J the current density in the material (A/m²), Q_j the current source (A/m^3), ρ_e the electric charge density (C/m^3), J_e the externally generated current (A/m²) which is equal to zero in our case, σ the electrical conductivity (S/m), ε(=$\varepsilon_0\varepsilon_r$) the permittivity (F/m), and E the electrical field (V/m) related to the gradient of electric potential V (V).

And, in the second module, the heat equation will be computed:

$$\begin{cases} \rho C_p \dfrac{\partial T}{\partial t} = \nabla.(k\nabla T) + Q + Q_{ted} \\ \quad Q_{ted} = -\alpha T : \dfrac{dS}{dt} = 0 \end{cases} \qquad \text{3-12}$$

with ρ the density (kg/m^3), C_p the specific heat (J/(kg.K)), T the temperature (K), k the thermal conductivity (W/(m.K)), Q the heat source (W/m^3) and Q_{ted} the thermoelastic damping which was set to zero. The coupling was achieved by the equation of the heat source which comes from the resistive heating in the material due to the current flow:

$$Q = \boldsymbol{J}.\boldsymbol{E} = {J^2}/{\sigma} \qquad \text{3-13}$$

3.3.2.1. Isotropic configuration: SCF

With the Solid Copper Foil, it is possible to run a 2D axisymmetric model with a rectangle of a length (equivalent to the radius) of 50 mm and a thickness of 10 μm. A total of 7144 elements were meshed for this case. The current is injected on the top face and, in a first step, is fixed to a disk with a radius of 1mm as shown in Figure 3-24:

Figure 3-24 2D axisymmetric model: Electrical boundary conditions

Since it is not possible to use the arc column model as an input for the current injection, an arbitrary choice of a fixed injection area as presented above was made. For our baseline configuration, we considered fixed properties of the copper at room temperature except for the specific heat C_p and the electrical conductivity σ for which a temperature dependency

law was introduced as defined in Appendix B. We can compare the simulation result with the lightning test performed on SCF during the first campaign with the measurement of the light from the back of the impacted panel, interpreted as the vaporisation profile. Also, after the lightning test, observation of the panel on the front provides information regarding the missing metal which is related to the melting of the copper. Due to the explosion occurring on the surface, the liquid metal is blown away, therefore the final missing metal area is similar to the melted area. Moreover, we can observe a smaller black disk within the melted area which is interpreted as the final vaporisation profile. The vaporisation of the copper could increase the temperature of the plasma and could burn the GFRP panel resin on its surface. This is presented in Figure 3-25:
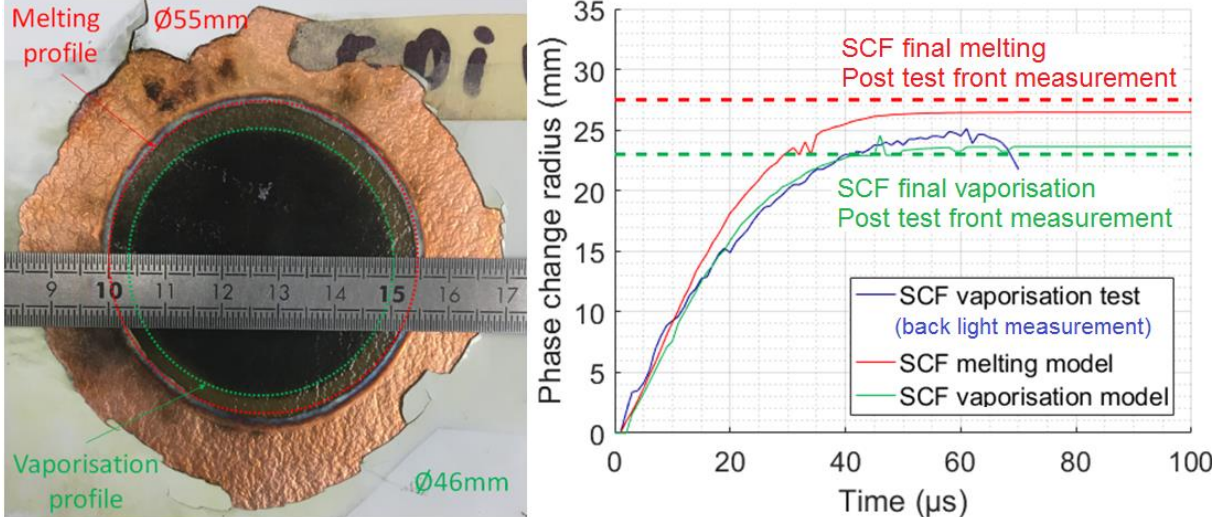
Figure 3-25 SCF melting and vaporisation profile comparison

This first model is in quite good agreement with the experimental result. The simulated vaporisation profile (T = 2835 K) is close to the measurement of the dynamic vaporisation profile presented in 3.2.2. Also, a comparison of the post-test measurement of the final melting and vaporisation profile and the simulation show that the latter predicts the results well. The simulation is performed during 100 μs since the heat source due to the lightning current stops at 70 μs and no data are available on the heat exchange from the LSP to the air in order to predict the cooling of the material. This might be the reason why the simulated melting profile is slightly lower than the measurement.

Additional analyses were performed to study the sensitivity of the melting profile (T = 1357 K) to the material parameters. The results are presented in Figure 3-26.
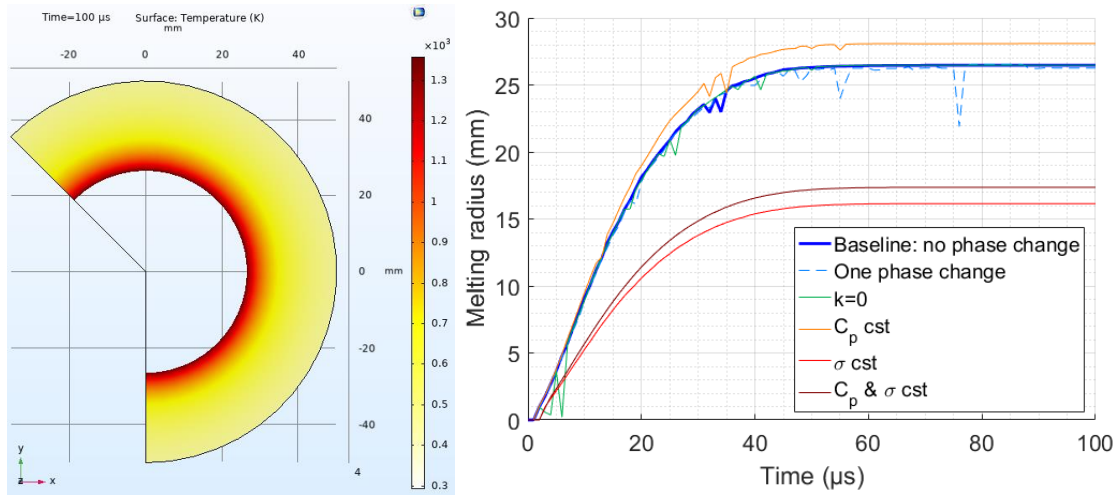
Figure 3-26 Melting profile - Material parameter sensitivity analysis

Compared to the baseline without any phase change which has C_p and σ dependent on temperature but a constant density and thermal conductivity, the most important parameter to define is the electrical conductivity. A constant conductivity will limit the heat generated in the material since the conductivity is 6 times lower at melting temperature compared to room temperature and the heat source is inversely dependent on σ. There is also a linear dependency with the specific heat but the parameter only increases by 30 % up to the melting phase therefore its impact is more limited. In addition, the thermal conductivity has no impact on the melting profile since the Joule heating speed is related to the electrical current which is very fast and lasts only 70 µs compared to the thermal conduction which is a far slower process, close to the order of a millisecond. Finally, the phase change from solid to liquid has a negligible impact since the fusion energy is very low compared to the total energy injected into the system:

$$\begin{cases} E_{total} = \int \dfrac{j^2}{\sigma} dt = 5{,}8.\,10^{10}\ [J/m^3] \\ E_{melt} = \rho \Delta H_{melt} = 1{,}8.\,10^9\ [J/m^3] \end{cases} \qquad 3\text{-}14$$

with $\rho = 8960\ [kg/m^3]$ and $\Delta H_{melt} = 2{,}058.\,10^5\ [J/kg]$.

Based on the validation of the melting and vaporisation profile developed on the SCF, we can now increase the complexity and consider the ECF configuration.

3.3.2.2. Anisotropic configuration: ECF 3D model

In a first step, ECF was modelled in 3D, considering its global geometry. Due to the small size of an ECF pattern, it leads quickly to a high number of elements for the global model. For this reason, in order to limit the computation duration, only a square 75 mm by 75 mm was built instead of a whole disk of Ø 370 mm as in the lab test configuration. The current injection is fixed on a central area in a diameter of 6 mm and each side of the square is set to the ground potential (V=0). The model is presented in Figure 3-27. The total number of elements is 252000.
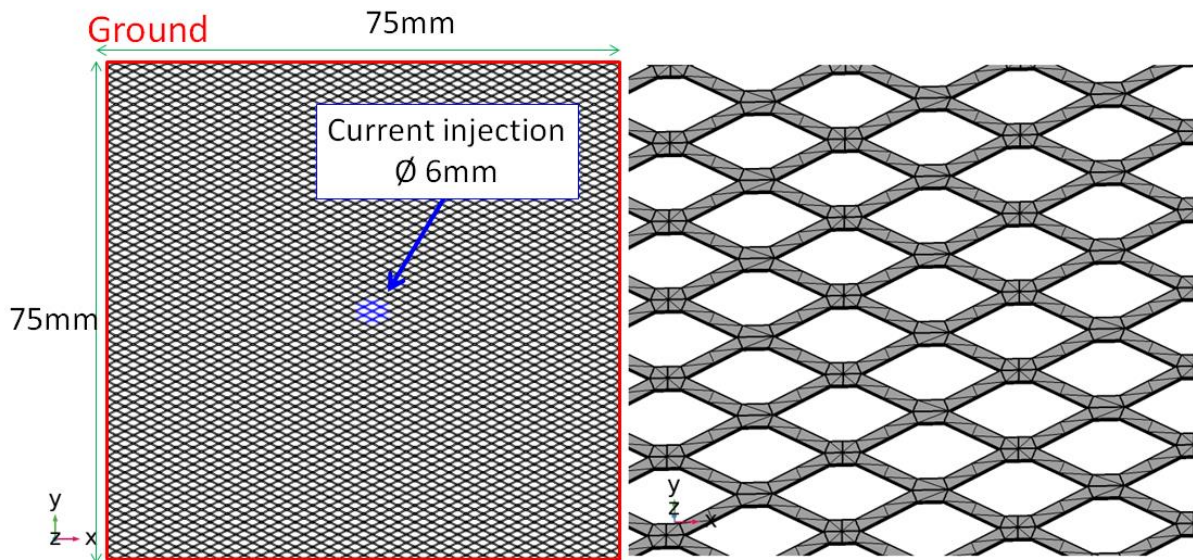
Figure 3-27 ECF 3D model mesh and electric boundary conditions

Since the phase change has almost no impact on the total melted or vaporised area, it was not considered in this configuration in order to limit the computation time. The temperature and current are computed during 100 µs and a result is available every µs. The total computation time for this case was 32h 18'. The comparison of the total melted area for the ECF195 configuration between the test results on a free ECF subjected to 100 kA (WFD) and this model presents good results as shown in Figure 3-28. Since the current injection lasts about 70 µs, the melting profile is stabilised long before 100 µs and there is no need to prolong the computation. For the test result, the melted area contour is highlighted with a green line and for the model result, the melted area is visible in blue.
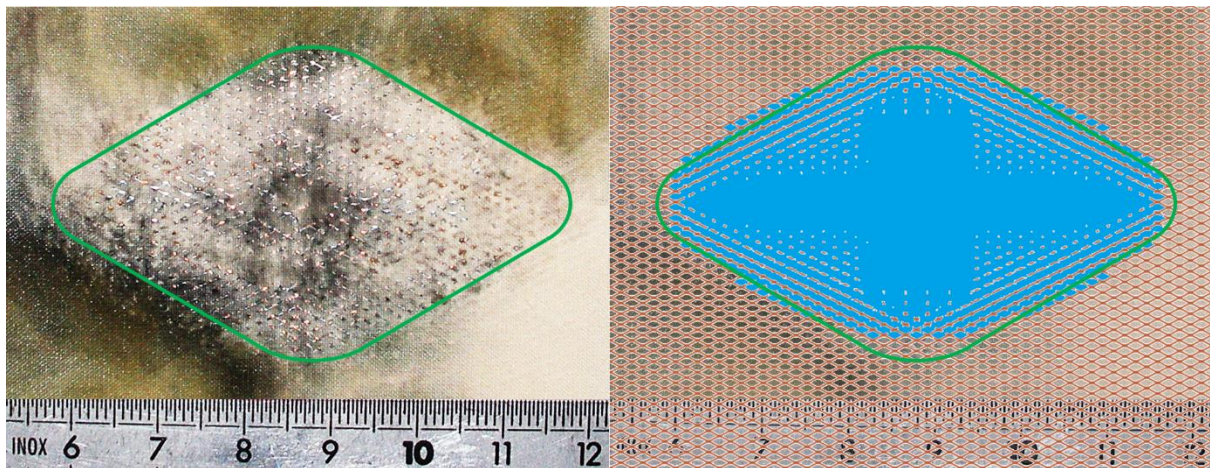
Figure 3-28 Total melted area for ECF195 subjected to WFD: Comparison between 3D model and test on a free surface

For a free arc root injection, i.e. no paint layer, a fixed current injection on a small diameter is enough to predict the final melted area with this 3D model. Still, it is necessary to be able to predict the vaporisation profile in time in order to support the explosion model and to consider the impact of a different current injection due to the paint constraint. Since this model is very time consuming, an equivalent layer was considered in order to facilitate the study.

3.3.2.3. Anisotropic configuration: ECF 2D equivalent model

In this second step, instead of the ECF geometry an equivalent foil was modelled with an anisotropic electrical conductivity and the other material parameters isotropic. The interest of such a model is to save computation time. In addition, given the symmetry of this equivalent foil, only a quarter of it was modelled. Finally, the number of elements of such a configuration was 25247 which is ten times less than the complete 3D ECF model. The computation time was about 38 s. The thickness of the solid foil was chosen by considering the surface weight of the protection and metal density:

$$t_{eq} = \frac{w_{ECF}}{\rho_{copper}} = \frac{195 \ g/m^2}{8.96 \ g/m^3} \approx 21.8 \mu m \qquad \text{3-15}$$

For the electrical conductivity σ in the different directions, the sheet resistance R_s is considered since it can be easily measured on a sample of LSP by measuring the electrical resistance R across a sample of length L, width W and thickness t:

$$\begin{cases} R_s = R\frac{W}{L} \ and \ R = \frac{L}{Wt} \times \frac{1}{\sigma} \\ \\ \sigma = \frac{1}{R_s t} \end{cases} \qquad \text{3-16}$$

Based on the measurements provided by the supplier in the specifications of ECF195, the values of the sheet resistance in both x and y directions are respectively 1.1 mΩ.sq and 3.6 mΩ.sq. The measurement principle explained above was used to assess the sheet resistance of the ECF195 modelled in the previous chapter and is 1.1 mΩ.sq for the x direction and 2.6 mΩ.sq for the y direction. Comparisons are made between melting and vaporisation profiles with the values of sheet resistance highlighted with a black line and the 3D complete model in blue. As presented in Figure 3-29, with the supplier values (1.1 and 3.6mΩ.sq), the profiles are in good agreement with the model values. This better agreement compared to the modelled equivalent resistance are due to manufacturing defect not included in a perfect model. This question is further studied in 4.3.1.3.
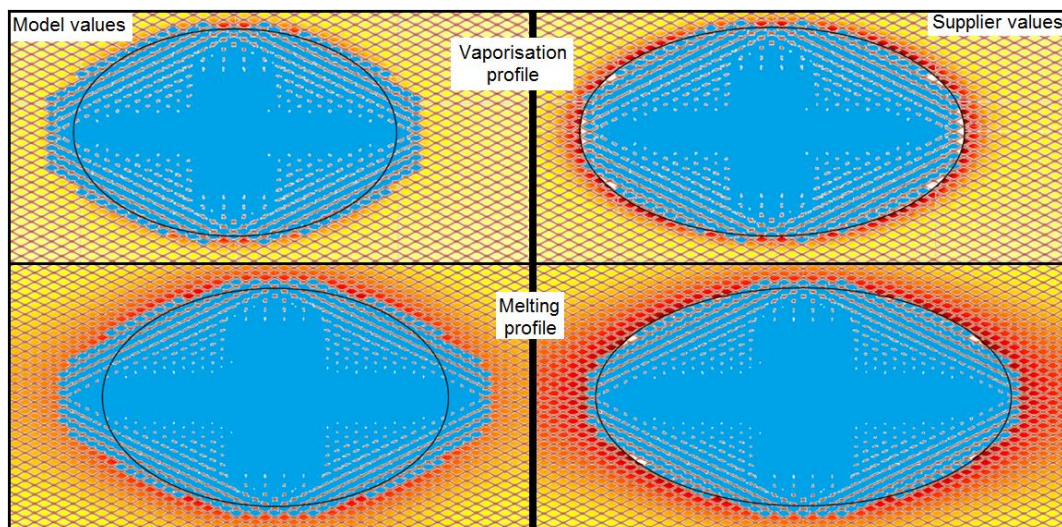
Figure 3-29 Melting and vaporisation profile comparison with different resistive sheet values

As shown in Figure 3-21, the vaporisation profile of an unpainted panel was not consistent because no paint could filter the light from the arc column. Therefore, this modelled profile will be used to study the overpressure generated by a free ECF195 which has a different spatio-temporal evolution to the painted configurations.

The next step would be to consider a current injection profile changing with time and space due to the presence of paint that constrains the arc root since the vaporisation profile is different with the paint thickness, as shown in Figure 3-18. This difference is the consequence of a different current injection profile due to the arc root constriction.

3.4. Conclusion

The objective of this chapter was to propose a model to describe the interaction between the lightning arc and the surface of the structure in order to model the LSP vaporisation profile. The overpressure generated on the surface of the composite structure is the consequence of the explosion of the Lightning Strike Protection which will damage the laminate. The origin of this explosion is the sudden vaporisation of the metallic protection due to Joule heating. It was therefore necessary to understand how the current from the lightning arc is injected into the protection system material and how the protection system material is vaporised. For this reason, the arc column was studied and then confronted with the arc root evolution when interacting with a surface Lightning Strike Protection (LSP) and constricted by the presence of paint in order to understand the mechanisms related to arc injection.

The main issue in the study of lightning strike on a composite is the difficulty related to measurement. The development of a theory or a model needs to be confronted to real test data to support its validation. But the intensity of such phenomena as the light, temperature or magnetic field makes it almost impossible to conduct any measurements due to the disturbances that it could generate on a sensor. In our case, it was necessary to measure the LSP vaporisation profile but this is fully hidden between the composite plate, the paint and the lightning arc column. We therefore developed a specific test setup in order to observe this phenomenon. The use of a transparent GFRP panel in order to record the light through it was very beneficial for observing the vaporisation during the test. We were thus able to demonstrate the influence of the paint on the vaporisation profile and therefore on the arc root.

In addition, an attempt was made to model the arc column in order to confirm our theory regarding the different phases of the lightning column and root that are in competition. An innovative approach has been proposed in order to model the lightning arc in the temporal domain. However, the high amplitude and the transient aspect of the current led to serious convergence issues. Moreover, it is necessary to integrate the dependency on the arc pressure in order to complete the model.

Finally, for the prediction of the vaporisation profile, we developed an original electro-thermal model. In order to validate it, we performed a sensitivity analysis on a simple configuration, a homogeneous protection such as metallic foil. We then progressively increased the complexity in order to take into account all the parameters related to an Expanded Copper Foil and proposed a configuration in order to save computation time.

The definition of vaporisation distribution in time and space is an important input that will be used for the definition of a mechanical load, equivalent to the lightning constraints, in order to assess the damage in a composite structure. With the work performed in this chapter, several profiles were established for different paint thicknesses and LSP which will support the development of equivalent mechanical load profiles. To this end, it is necessary to combine this spatio-temporal profile with a pressure profile due to the explosion of the LSP. This next step, i.e. the explosion pressure, is studied in the following chapter.

An important step has been reached in the understanding of the influence of the paint and the LSP on the arc root. The lightning arc cannot be considered as a simple current injection in one point or a fixed area. On the contrary, it is mandatory to consider an injection that will grow in time and space. Its contour is dependent on the coupled paint and LSP behavior. In order to fully predict the vaporisation profile and lightning forces, this work needs to be finalised and combined with the electro-thermal model developed.

Chapter 4

Lightning strike protection explosion

Objectives

This chapter presents the development of the electric explosion theory in metallic lightning strike protection in order to predict the shock wave generated by the sudden vaporisation of the metal. Thanks to this work, it is possible to relate the current density flowing into the LSP to a shock pressure amplitude. Associated to the work developed in chapter 3, a space and time distribution of the surface overpressure can be defined and used to determine the mechanical load on the composite structure.

The Lightning Strike Protection (LSP) was decomposed into elementary wires in order to simplify the study of the electric explosion. Specific tests were developed in order to measure the shock wave of an exploding metallic wire and were confronted with simulation. The complete LSP was then studied in order to validate the integrated pressure model.
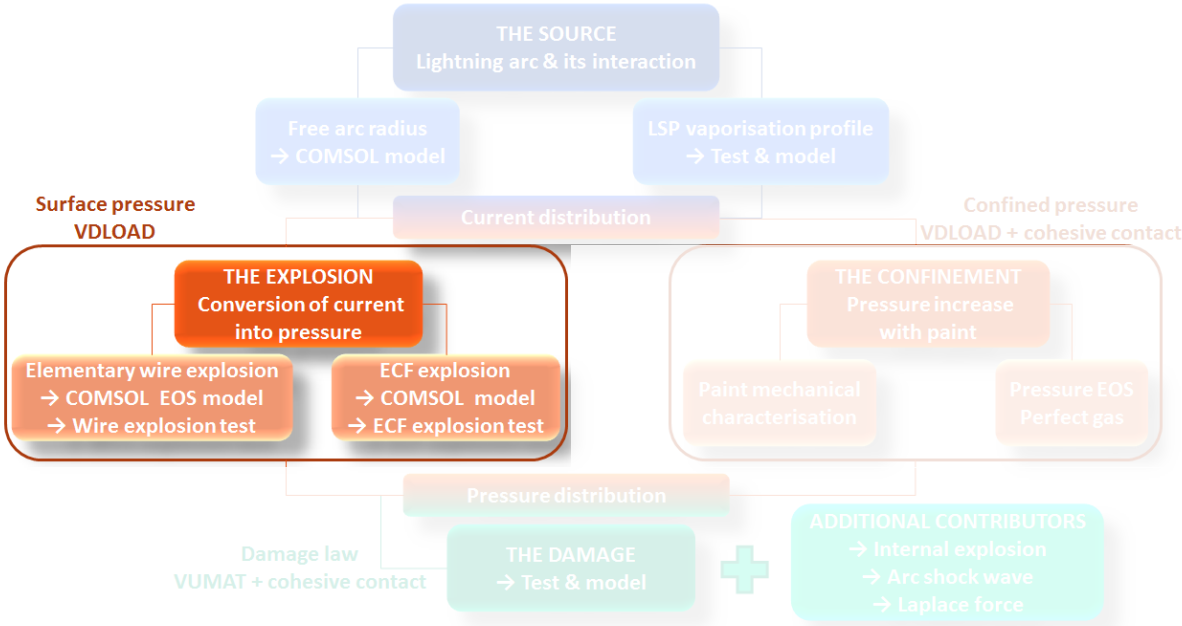
4.1. The surface explosion theory

During a lightning strike, there are several forces at stake, as explained in section 2.4.1. Among them, Joule heating should not be considered as a thermal source only, for the following reason. The lightning current reaches a significant amplitude (100 kA) in a very short time (less than 20 µs), flowing into a very small section of metal since the LSP is a few tens of microns thick. Therefore, the current density in the protection is very high and the increase in temperature is so rapid and so high that the LSP will vaporise, generating a plasma. This sudden change of state and temperature will generate a shock wave. As the metallic protection is on the surface of the composite panel, this will create what we will call a surface explosion.

4.1.1. The surface explosion: Observation

Experiments demonstrated that an explosion occurred on the surface due to the rapid vaporisation of the LSP and possibly the CFRP [29]. This has been highlighted thanks to high speed camera measurements of the front face of the impacted sample where it can be seen that an underlying explosion pushes the paint away. In Figure 4-1, an example of a test performed during the EDIFISS test campaign illustrates the expansion of the lightning arc and hot gases, which are quite bright at the beginning of the test, the shock front propagation from the lightning arc and the ejection of pieces of paint.
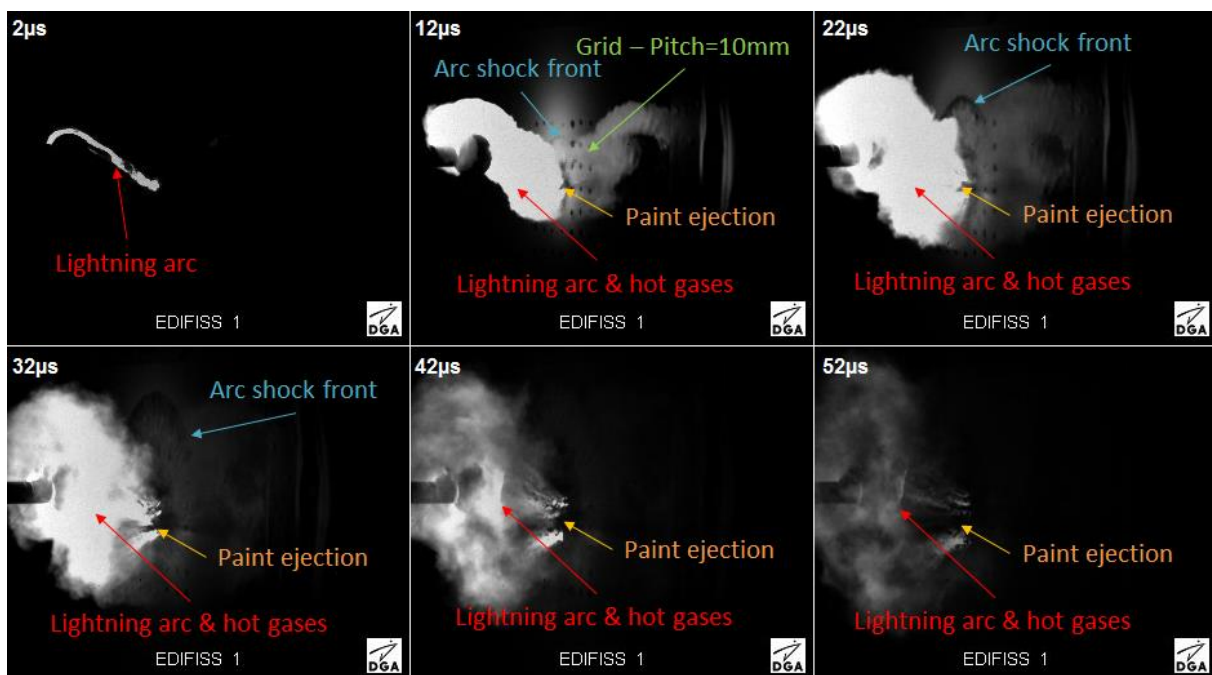
Figure 4-1 Lightning arc (WFD=100 kA) on protected and painted CFRP sample face - High speed camera record front view

A similar assumption is also supported by Liu [50] who proposed a Blow-Off Impulse (BOI) model caused by resin pyrolysis and fibre decomposition. Like many researchers, he considered an unprotected panel and therefore no explosion due to the metallic LSP. But this theory has also been postulated by other researchers regarding the metallic protection

and its explosion due to Joule heating [29,35]. In order to develop a theory of this vaporisation due to Joule heating and the associated explosion, it is important to understand the physical phenomenon and to build the real overpressure and temperature profile in time and in space. In previous research, the pressure P related to the explosion overpressure was simply related to the Joule heating energy E by a linear relationship: $\alpha E=3/2P$ [29], but the phenomenon created by the sudden vaporisation of the metal is far more complex and cannot be related solely to the energy by a simple empirical ratio.

4.1.2. Discussion: Lightning strike protection decomposition

The main lightning strike protection used for aircraft composite structures is based on the expanded foil principle and from past applications, i.e. a mesh. LSP technologies are similar to a web of elementary wires as illustrated in Figure 4-2 and detailed in section 2.3.2.2. This metallic protection is embedded in a resin matrix, forcing the current to flow in the metal without any arc in between the different wires.
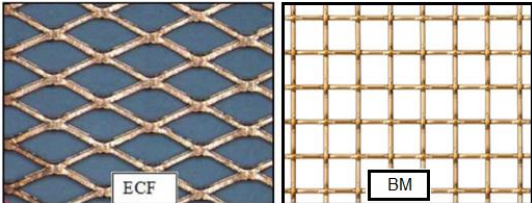
Figure 4-2 LSP technologies – Wire web

Since the resin is highly electrically insulating and the metallic wires are interconnected, no arc can occur to fill the gap between the wires. In addition, the resin around the metal is barely affected during the lightning peak current injection. This is because the Joule heating in the metallic protection, even if very intense, is extremely rapid. Therefore, the explosion of the metal occurs well before any deterioration of the resin. This was observed by Guo [27] thanks to electron microscope images presenting a close view of the surface of a protected CFRP plate with ECF after a lightning test with a WFD. Several areas of the surface are shown in Figure 4-3:
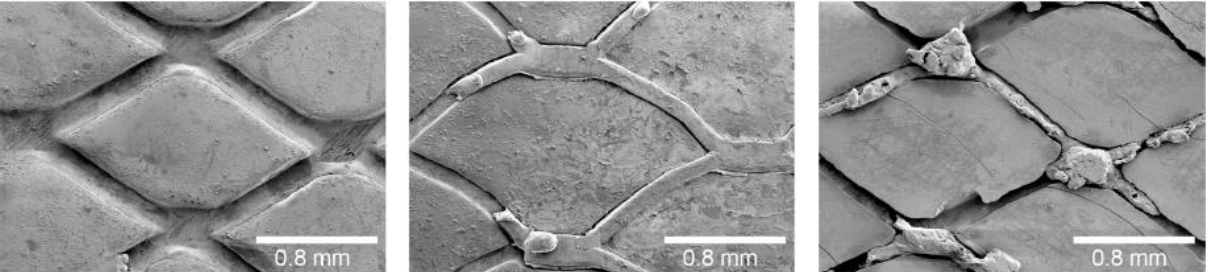
Figure 4-3 Microscope view of vaporised LSP after a lightning test [27]

The pattern of the ECF is visible in the resin which means that the metal vaporised and pushed away the resin on the top. The main factor in the overpressure created on the surface comes from the explosion of the metal and the contribution of the resin pyrolysis can be neglected. Based on this hypothesis, the global overpressure profile can be decomposed into elementary explosions due to the sudden vaporisation of each wire in the

LSP, producing a cylindrical shock wave. The distribution of the explosion in time and space will be dependent on the current injection into the LSP. From Chapter 3, we know the lightning arc current distribution that we can confront to the ECF pattern in order to define the current in each wire as illustrated in Figure 4-4:
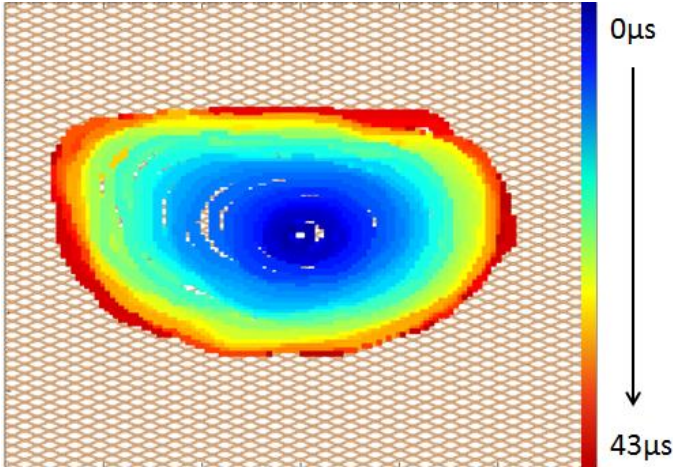
Figure 4-4 Time distribution of the vaporisation profile distribution in ECF pattern

It is therefore necessary to relate the current amplitude flowing into a given metallic wire with the shock wave pressure amplitude.

Several theories of the shock wave generated by Joule heating in metal have been mainly studied by the "electric explosion" community through experiments and models for different applications such as thermonuclear fusion, solid-state and plasma-chemical physics, X-ray sources due to Z-pinch effect, rockets... More specifically, Electrical Explosion of Wire (EEW) developments are of great interest and can be applicable to the lightning current field and metallic protection system understanding and design.

4.1.3. Electric explosion – State of the art

An electric explosion is due to the rapid heating of a conductor by a high-power current pulse [85]. The rate of energy deposited into the conductor is high since it will allow the creation of an unstable state where liquid conducting droplets are ejected by the surrounding vapour and a dense plasma forms instead of a smooth change of state from solid to liquid and then to vapour. There is currently no consensus in the community regarding the physics behind this phenomenon as it involves very complex thermodynamic physics. The EEW depends on many parameters such as the wire properties: Diameter [86], length [87,88], material physical properties [89], but also the electrical characteristics of the current injection [90] and lastly the surrounding medium [91]. Moreover, the complexity is enhanced by the change of the wire and medium properties during the current injection. Joule heating will significantly modify the temperature, and hence the electrical conductivity [92], as well as other material properties (density, specific heat, thermal conductivity…) will change related to this increase in temperature. In addition, it is difficult to measure the

temperature in the wire and in the surrounding medium, which leads to additional uncertainties.

All these parameters influence the total energy deposited into the wire prior to the creation of the arc. When a plasma is created, it is through the exploding wire and part of the energy deposition is diverted into the shock wave propagation. A resistive heating stage occurs before the breakdown that will generate the plasma. This phase is important as it will change the energy deposited into the system: the longer it lasts, the more powerful the shockwave will be. But this phenomenon does not occur because of the ionisation of the metal vapour. In fact, the change of state in the metallic wire is not homogeneous and several phases can coexist before the explosion and a plasma can also be created around the wire. For this reason, the rate of energy is important since it will allow the deposition of more energy before breakdown if high enough. According to Grinenko [93], the pressure of the explosion is dependent on the square of the density multiplied by the derivative of the electrical power:

$$\begin{cases} P = \beta \sqrt{\rho \dfrac{dN}{dt}} \\ N = RI^2 \end{cases} \tag{4-1}$$

with P the pressure, β a constant, ρ the wire density and N the electrical power, as a function of the wire electrical resistance R and the electrical current I. This relationship described in equation 4-1 is not fully validated but it gives an empirical trend of the pressure increase with the speed of power deposition and density. This electrical energy source is dependent on the electrical circuit and thus the current waveform with its maximum amplitude and time to peak but also the electrical conductivity of the wire and its section. Since the conductivity of the wire depends on the temperature, the parameters involved in the Joule heating equation will impact its time evolution as it will impact the temperature rate increase and thus the maximum pressure generated. These parameters are the density, the specific heat and the current density in addition to the electrical conductivity.

As experimented by Pikuz [94], Ivanenkov [95] and Romanova [89], there are two main classes of conductor:

- "Classical" conductors such as copper, aluminium, bronze… which are the main components of lightning strike protection
- "Refractory" conductors such as tungsten but also carbon which is the main component of our composite laminate

The main difference between these two types of conductor is their ability to sustain high temperature without any change of state. This is mainly visible by assessing their melting temperature: when it is higher than 2000°C, the material can be considered refractory. Depending on the type of conductor, the phenomenon that will generate the shock wave is different, as shown in Figure 4-5:
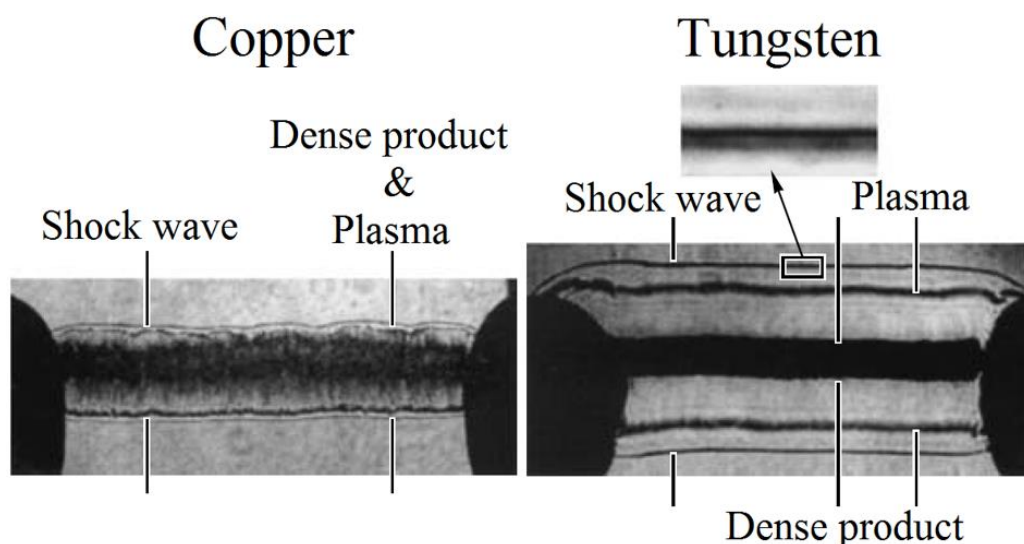
Figure 4-5 Electric explosion and shock wave profile: Copper vs Tungsten (Wire length = 12mm) [94]

For the first family, the melting and vaporisation temperature are quickly reached and the explosion of the dense product will occur and consecutively a plasma will be generated in it. Therefore, the plasma is filled by dense matter and the shock wave is due to the rapid expansion of the explosive wire. All the energy is deposited in this dense product area, even after breakdown.

For the second family, a shunting current breakdown occurs around the wire since the material can sustain high temperature before changing state. In this case, a high ionisation of the medium around the wire is created and a plasma is generated along its surface. Therefore, a more limited amount of energy is injected into the metal and is diverted into the plasma. The shock wave comes, in this case, from the wire explosion but also from generation of the plasma.

Nevertheless, the current is injected into this system in both cases after the explosion and will contribute to the shock wave propagation. Therefore, the current waveform and its decay shape can have an impact on the total overpressure generated but to a more limited extent.

This shunting phenomenon will be impacted by the surrounding medium. In a confined medium, as experimented by Sinars [91], the resistive heating will last longer as it prevents the breakdown from occurring. It will therefore delay the plasma creation that will shunt the wire and generate the shock wave but as more energy has been deposited, it will make it more powerful. This is an important conclusion as it is fully applicable for LSP confined by resin and paint.

The study of the current and voltage can help us to identify the different states of the wire during the electric explosion [90]: Solid state, melting, liquid state, vaporisation, collapse and finally plasma state. According to this definition, we can consider different energies deposited in the wire that will impact the shock wave amplitude. First, energy E_1 is deposited in the metallic wire during its solid, melting and liquid phases. The current and the

voltage are quite stable during the solid phase. Then, due to the increased resistivity of the wire during the liquid phase, the voltage starts to increase and the current decreases slightly compared to its theoretical pulse waveform, and starts to collapse. Then, during the vaporisation phase, energy E_2 is deposited in the field. As this medium is very poorly conductive, the voltage increases dramatically up to its maximum which ends the vaporisation stage. Since the generator still needs to evacuate the pulse energy, ionisation of the channel occurs and consequently the voltage collapses. The current continues to decrease up to the creation of the plasma. During this collapsing phase, energy E_3 is deposited in the gaseous medium. Finally, the arc is created and the current starts to flow again significantly. Since the plasma is a conductive medium, the voltage decreases continuously and the current returns to its theoretical value. Energy E_4 represents the energy deposited from the end of the voltage collapse to the end of the first current pulse in the plasma.
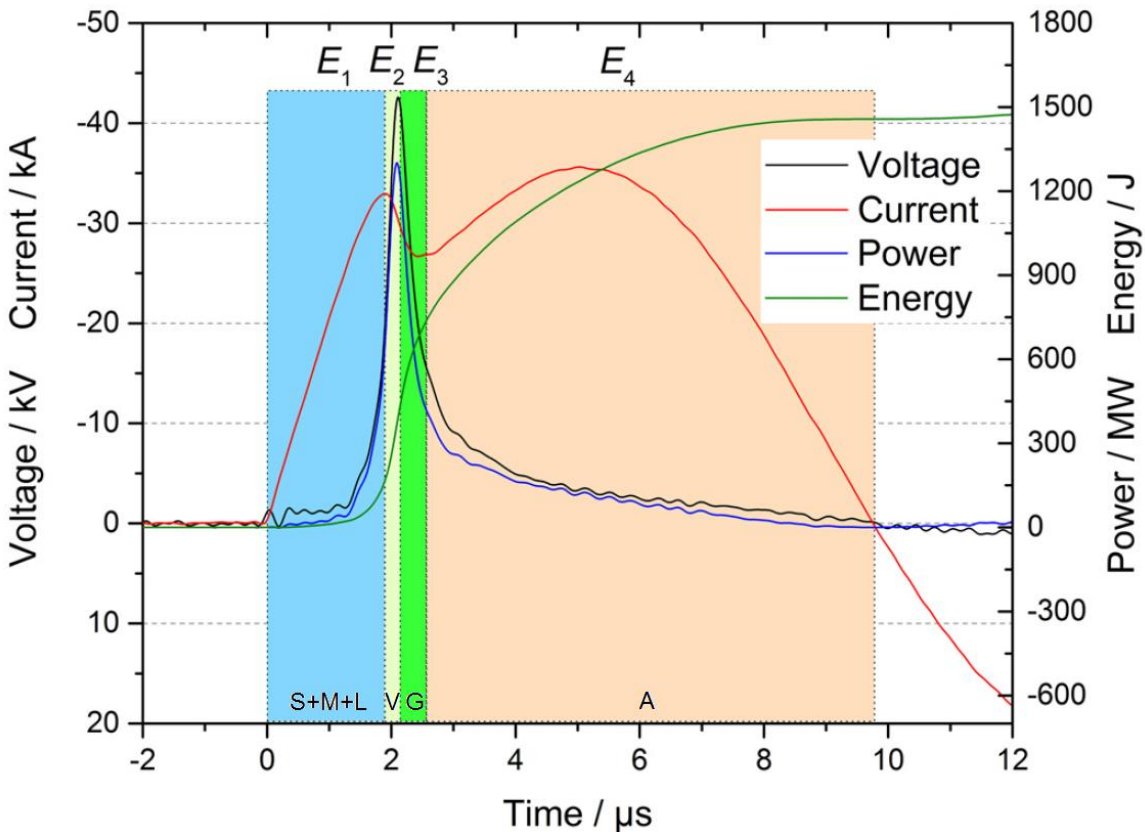
Figure 4-6 The different stages of the electric wire explosion [90] with state identification addition (S=Solid/M=Melting/L=Liquid/V=Vaporisation/G=Gas/A=Arc)

The shock wave is created by this shunting phase and it might be thought that only the energy deposited (E_1+E_2) prior to this phase would play a role in the pressure amplitude. In fact, it seems that the energy deposited after this phase also has an impact. Indeed, this phase is also important since it feeds the plasma and its propagation that will impact the shock wave before its detachment.

In addition to the shunting phenomenon that will impact the occurrence of an explosion, magneto-hydrodynamic instabilities can also generate an explosion that will be less efficient [96]. This is the case for what is called slow mode, where the current is slower and/or of lower amplitude. The conditions of equilibrium between the conducting liquid metal and the surrounding medium are impinged by instabilities in the system that have time to develop. The most dangerous MHD instability is the mode m=0 also known as the sausage instability which creates waists as illustrated below:
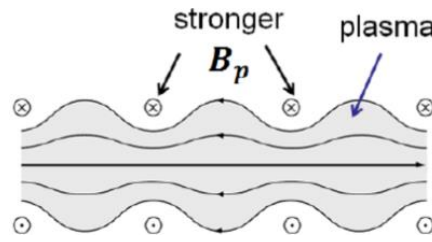
Figure 4-7 Sausage instability [83]

The non-uniformity created by the waists will lead to non-uniformity of temperature in the wire. The system will therefore collapse due to overheated local areas. The characteristic time for this instability development is related to the Alfven wave:

$$\begin{cases} t_A = {}^r/_{W_A} \\ W_A = {}^H/_{\sqrt{4\pi\rho_l}} = {}^I/_{2\pi r\sqrt{4\pi\rho_l}} \end{cases} \rightarrow t_A = {}^{2\pi r^2\sqrt{4\pi\rho_l}}/_I \qquad\qquad 4\text{-}2$$

In order to produce a wire explosion without any instabilities, the explosion must occur before this instability has time to develop, which imposes a minimum value of the current for a given wire configuration.

In contrast, superfast modes can also impact the energy deposition. In this configuration, the current increases so quickly that the skin effect is significant and the energy is concentrated on the external layer of the wire. The condition for the skin effect is defined by:

$$\delta = \frac{1}{\sqrt{\mu\pi\sigma f}} \qquad\qquad 4\text{-}3$$

δ is the skin thickness with μ the metal permeability, σ its electrical conductivity and f the signal frequency. The concentration effect is the highest at the maximum frequency. The normalised WFA and WFD defined in ED-84 [3] for laboratory lightning tests present a very fast time to peak, respectively 6.4 µs and 3.18 µs. For the lightning tests that we performed in the GREMI laboratory with the results presented in this chapter, the theoretical waveforms WF1 and WF5A, also defined in ED-84, were slowed down due to the high impedance of the element tested. The shape of the waveforms is detailed in 4.2.1.1. With a time to peak greater than 15 µs, the signal spectrum for the current waveforms tested (GREMI WF1/WF5A) is limited to 25 kHz as illustrated in Figure 4-8. In this case, for copper, the skin thickness is higher than 400 µm. It is therefore not necessary to consider such a mode for the wire analysed (Ø<125 µm).
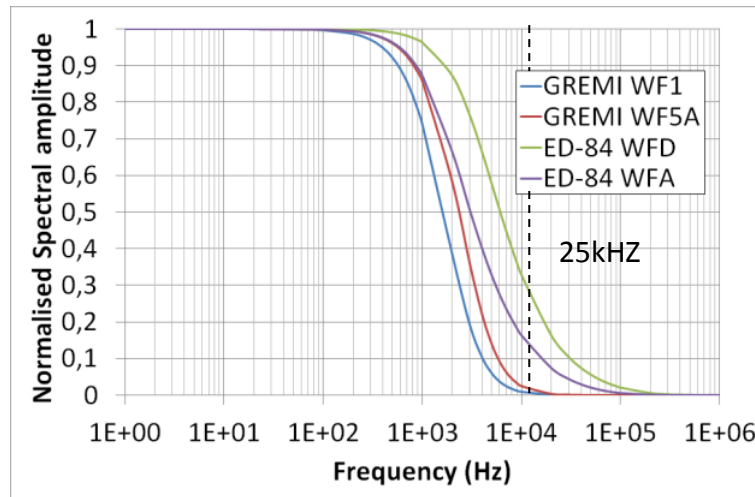
Figure 4-8 Lightning spectral amplitude of normalised and tested current waveforms

Due to the magnetic field created by the current flow, the liquid core of the wire is compressed [97]. Therefore, it delays the boiling conditions and the equilibrium pressure with liquid and vapour is higher than the vapour saturated pressure. With the increase in temperature, the critical point can be reached and the vapour will be instantaneously dispersed into vapour mixed with liquid droplets which is the explosion.
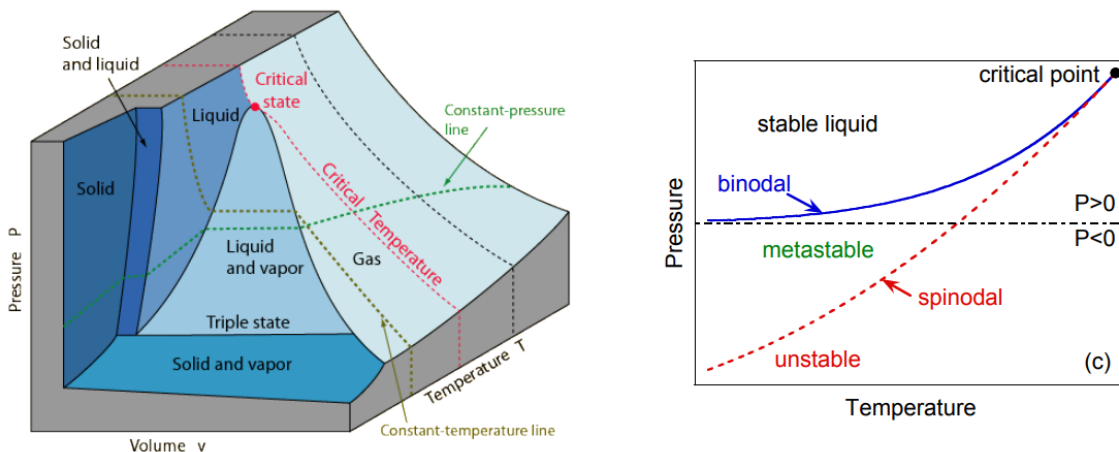
Figure 4-9 Thermodynamic state of the matter [98]

Finally, for this physical phenomenon, the Equation Of State (EOS) is key as it will support the determination of a pressure and energy profile as a function of the temperature and density. This will describe the shock wave generated by this rapid change of state and allow the change of material properties with the temperature. In this approach, Luo [99] considered the Burgess EOS to describe the explosion but Le Blanc [100] preferred to use the Gray EOS which seems more appropriate for a rapid and energetic pulse similar to lightning. In both cases, the theory was developed for a foil configuration. The most fully developed theory adapted to metallic wire explosion was proposed by Chung [101] based on QEOS (Quasi Equation Of State) corrected by Ray [102] in order to better tackle the liquid-vapour transition which is key in the explosion phenomenon.

A good characterisation of the explosive behaviour of our LSP is thus extremely important in order to validate a shock wave model. For this purpose, we developed specific tests in order to assess the shock wave generated by the wire explosion.

4.2. Electric explosion test

In order to study the explosion of the metallic lightning strike protection, specific tests were performed. In a first step, elementary metallic wires were studied. The interest of this approach is to remove the complexity due to the geometry with a simple 2D asymmetrical case. The vaporisation can be simply studied in a homogeneous environment and an electro-thermal model can be validated. With this configuration, it is possible to measure the shock wave pressure considering a cylindrical propagation of the front. In a second step, the complete LSP system was studied in order to finalise the validation of the model previously developed and analyse the effect of the ECF geometry. For this purpose, 4 test campaigns were performed in the "thermal plasmas" group at the GREMI laboratory:

1. Copper wire explosion with slow waveform
2. Copper wire explosion with fast waveform and feasibility test for LSP dumbbell sample
3. Complementary metallic wire explosion with fast waveform (Aluminium, Copper and Tungsten)
4. LSP dumbbell explosion test

4.2.1. Wire explosion test

In order to simplify the study of the explosion of ECF, it was first studied on metallic wires. With this approach, it is possible to consider it as a 2D symmetrical problem instead of a complex 3D problem. There were 2 main objectives for this specific test. The first one was to assess the onset of vaporisation and our ability to predict it based on a simple electro-thermal model. It was necessary to launch this test campaign because, due to Joule heating, the wire will change state from solid to liquid and then to vapour; in the context of a lightning current, however, the heating is so fast that it could even lead to sublimation with additional phenomena. The second objective was study the shock wave, and thus the pressure generated by this rapid vaporisation. In order to convert the explosion of the ECF due to the current flow in it into a pressure profile, it is important to be able to assess the pressure amplitude. With these test campaigns, we aimed to build a law that relates the current density in the metal to a shock wave pressure, due to the metal explosion.

4.2.1.1. Test setup

In order to study the vaporisation profile, a 40 mm long copper wire was bonded between 2 electrodes with a coaxial return to ensure homogeneity as presented in Figure 4-10.
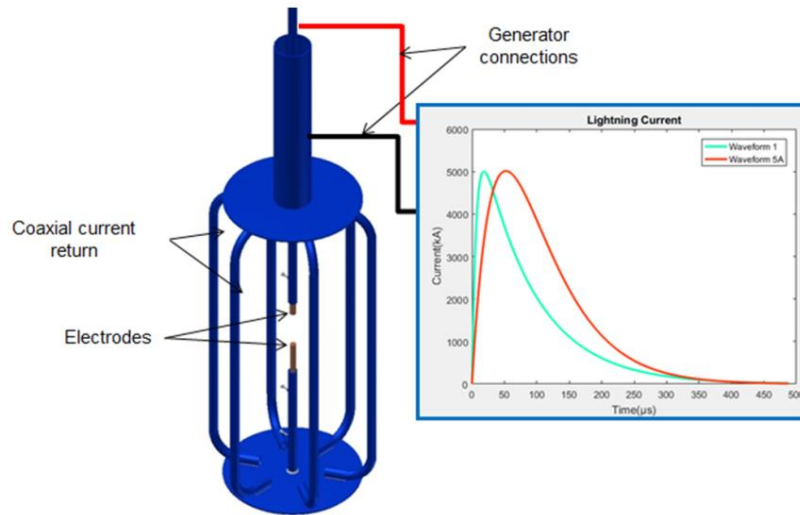
Figure 4-10 Wire explosion - Test setup

In order to validate the principle of the vaporisation profile, a slow current waveform with a peak current at 5ms was first considered before studying lightning waveforms with a peak current reached in a few μs. This first waveform is half of a sine curve with a time to peak of 5 ms generated by a pulse generator installed at GREMI, aimed to simulate a short-circuit on a home power circuit. Then, two lightning waveforms were considered: WF1 and WF5 ([ED-84]). These currents were generated by a pulse generator at Airbus, aimed to assess a conducted lightning threat on an aircraft internal system. The first one, WF1, has a time to peak of 18 μs, instead of 6.4 μs, and a time to half the peak of 84 μs. The second one is WF5A with a time to peak of 54 μs, instead of 40μs, and a time to half the peak of 142 μs. These waveforms are slower than in the ED-84 standard due to the impedance of our test setup. It is illustrated in Figure 4-11 below:
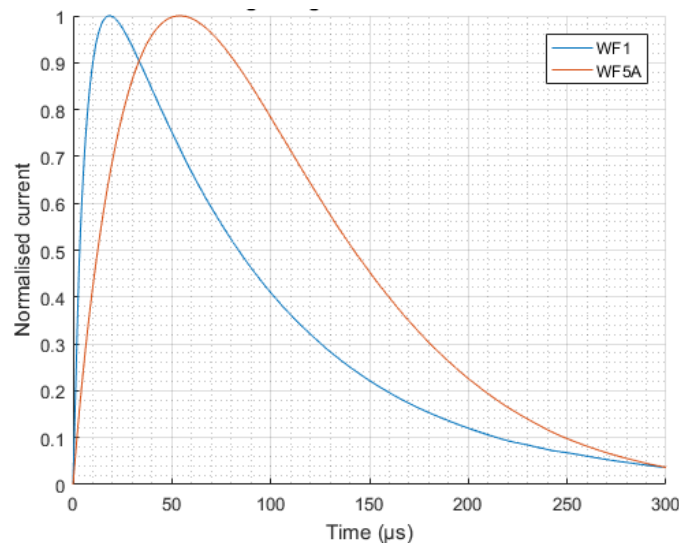
Figure 4-11 Lightning current waveforms

To support the objectives of the study, several measurements were performed: the electrical characteristics of the wire, before, during and after the explosion; the current and the voltage, respectively with a current probe Pearson Electronic Model 5664 and a voltage probe Testec TT SI 9010 and recorded with a Lecroy WaveRunner HRO 66Zi 600MHz 12bit. Also, thanks to a high-speed camera Photron SA5 operating at 300 kfps, we attempted to use the Schlieren method in order to follow the shock wave expansion. But due to the high brightness of the arc, the necessary space to implement it and the quality of the mirrors and camera required, we could not perform this measurement. Nevertheless, pictures of the electric explosion, thanks to a high-speed camera Photron IS1M operating at 1Mfps and an ICCD camera iStar Andor, were taken that provided very interesting information on the discharge mechanism and enabled the interpretation of the current and voltage measurements to be validated. Finally, two pressure sensors were installed perpendicular to the wire, in its centre, assuming a cylindrical distribution of the shock wave. Several distances were considered in order to assess the damping effect of the propagation of the shock wave in air and to be able to reconstruct the pressure amplitude in the vicinity of the wire. The installation is presented in Figure 4-12. The sensor mounting does not allow the measurement of the incident blast wave but a part of the reflected pressure against its sensitive surface before being disturbed by lateral wave refraction. The pressure sensors used were the PCB model 113B23 capable of performing a measurement up to 10 kpsi (68.95 MPa) with a sensitivity of 74.17 mV/MPa, an uncertainty of ± 1% and a resonant frequency higher than 500kHz. The conditioner for signal acquisition was the PCB 482C05.
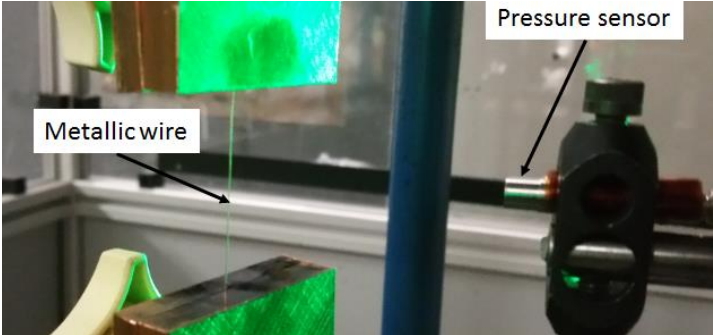
Figure 4-12 Pressure sensor setup – side view

Due to the high electromagnetic field generated by the lightning current and the generation of the arc, we added a metallic braided sleeving around the sensor wire in order to limit the disturbances in the measurement as shown in Figure 4-13:
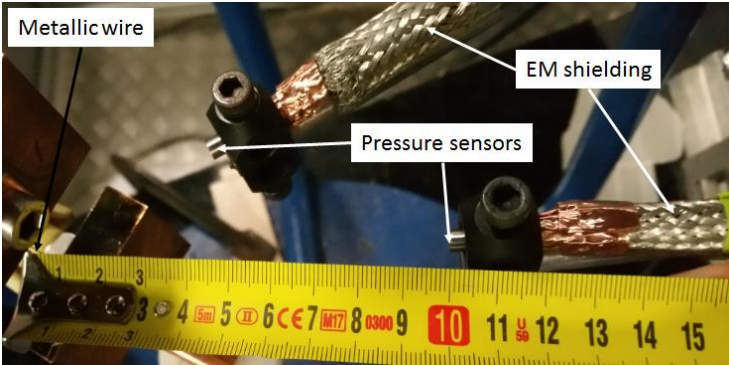
Figure 4-13 Pressure sensor setup - top view

4.2.1.2. Test configurations

The usual lightning strike protection is Expanded Copper Foil (ECF) which exists in several grades. The most common ones are the low grade: ECF73 and the medium grade: ECF195. As explained above, if we consider the ECF as a web of copper wires, we need to consider a wire diameter of an equivalent section. Figure 4-14 below presents the ECF pattern for which 73 gsm and 195 gsm have the same minor and major pitch but different thicknesses and strand widths.
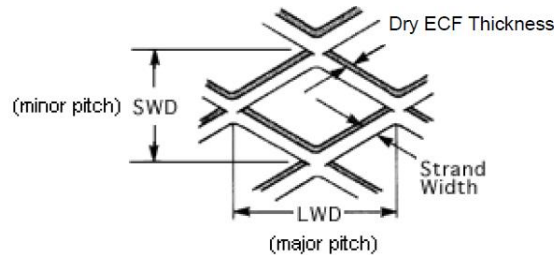
Figure 4-14 ECF pattern

For ECF195, the thickness is 76 μm and the strand width is 178 μm, thus an equivalent wire of 131 μm in diameter, and for ECF73, the thickness is 51 μm and the strand width is 102 μm, thus an equivalent wire of 81 μm in diameter. Due to market availability, we used copper wires of 125 μm and 75 μm of diameter respectively for ECF195 and ECF73.

In order to assess not only the impact of the section in the explosion mechanism, we also considered two other metals: aluminium with a wire diameter of 125 μm which has lower thermal properties (such as melting temperature) and tungsten with a diameter of 100 μm which is a refractory material and is thus very resistant when the temperature increases due to Joule heating.

In total, 4 wire configurations were thus considered:

Rationale	Heavy ECF: ECF195 type	Light ECF: ECF73 type	Low melting temperature	Refractory behaviour
Material	Copper	Copper	Aluminium	Tungsten
Diameter (μm)	125	75	125	100

Table 4-1 Wire test configuration

4.2.1.3. Test results

4.2.1.3.1. Slow waveform

In order to assess our ability to predict the vaporization time of the wire based on a simple electro-thermal model, as detailed in 4.3.1.2, we first considered a slow sine waveform with a maximum current reached in 5 ms. Three levels of maximum current were used for this campaign: 3 kA, 9 kA and 15 kA. It can be seen in Figure 4-15 that the current measured in the wire is equal to the theoretical injected current at the beginning, then with the increase in resistance in the wire, a detachment compared to its theoretical value is visible. When the wire enters its liquid phase, current collapse occurs. Then, a current disruption can be detected which helps in the observation of the vaporisation since at vaporisation, the resistance increases dramatically which leads to a current shutdown before the arc creation.

When we observe the voltage, the different phases of the copper wire are also visible. During the solid phase, the voltage increases almost linearly with the current increase since the resistance is quite stable. Then, there is a rapid increase due to the phase change to a liquid phase which is much more resistive. This phase is followed by a different shape of the voltage increase due to the resistance increasing with the vaporisation. Finally, there is a voltage peak at the end of the phase change. The voltage collapse is due to the state of ionisation of the gas prior to the creation of a plasma: the arc. One can observe these mechanisms in Figure 4-16 for one configuration (ECF195, Imax = 9kA); they are in good agreement with the theory given at the beginning of this chapter [90]. Since the current injection increase during this test is far slower than the theory illustrated in Figure 4-6 (Time to peak = 5 ms vs 5 µs), there are more disruptions in the current during the liquid state and vaporisation phase that are likely linked to the instabilities that can occur in a slow mode, as illustrated in Figure 4-7.
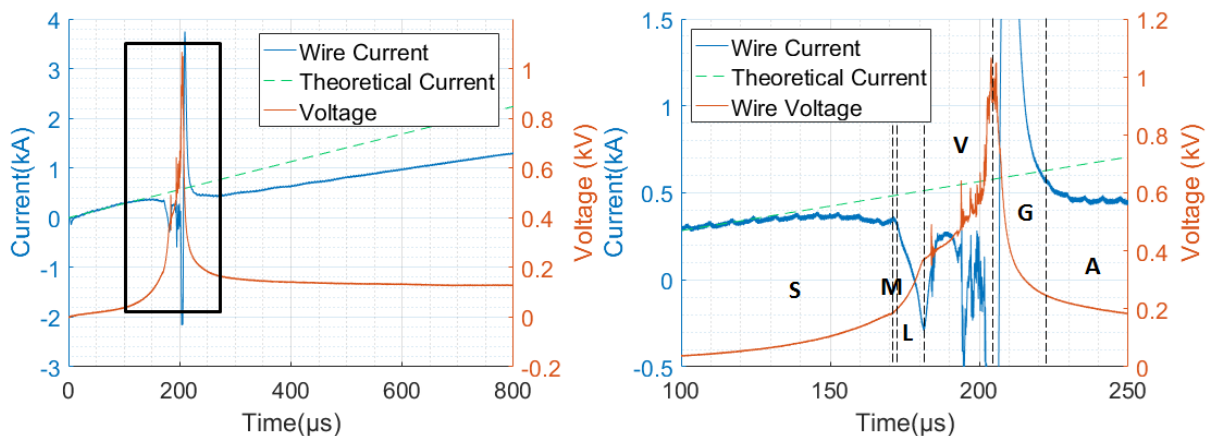
Figure 4-15 Slow waveform - Current & voltage evolution (ECF195, Imax = 9kA) with state identification addition (S=Solid/M=Melting/L=Liquid/V=Vaporisation/G=Gas/A=Arc)

The results are summarized in Table 4-2 below:

Type	Maximum injected current (kA)	Vaporisation moment (µs)	Current before disruption (A)	Peak voltage (V)
Ø 125 µm (ECF195)	3	406	260	>600
		390	276	>600
		390	265	670
	9	215	365	>700
		196	354	/
		200	380	1060
	15	150	420	1080
		146	420	1080
		146	*420*	*1080*
		144	440	1080
Ø 75 µm (ECF73)	3	215	130	630
	9	110	120	1080
		110	120	1080
		110	120	1100
	15	80	120	/
		80	120	1080
		79	135	1060

Table 4-2 Slow waveform - Test summary

As expected, the vaporisation moment, which corresponds to the voltage peak, occurs more rapidly with the current increase and also with the decrease in the wire section, as shown in Figure 4-16. For an identical metal, here copper, the vaporisation moment can be predicted with a power law with an identical exponent for different wire sections. The relationship between the vaporisation moment and the current is not only dependent on the maximum current, as explained in 4.3.1.

$y = 423.54x^{-0.616}$

$y = 778.98x^{-0.615}$
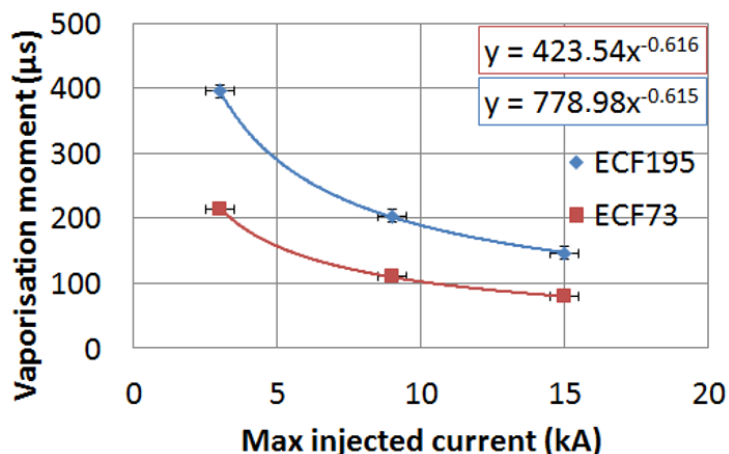
Figure 4-16 Arcing moment vs maximum injected current

Because of the strong solicitation, the wire starts to be distorted due to Lorentz waves [103] and instabilities are visible in the copper wire. Figure 4-17 shows that the wire is distorted, thus longer, at the moment of vaporisation and dense copper matter with disruption, i.e. fully vaporised metal, is visible along the wire. This phenomenon is probably related to the

sausage instabilities presented in 4.1.3 and could impact the vaporisation mechanism which is not predicted in a simple Joule heating model. Indeed, the models developed in 4.3 are based on a macroscopic electro-thermal approach, coupling the heat equation to an electrical power source. The metal is a homogeneous material in which the temperature increases identically with the current density. The prediction of such instabilities would require a more complex model based on MHD. Since the temperature is not homogeneous along the wire but locally higher, vaporisation could occur more quickly than predicted in our model.
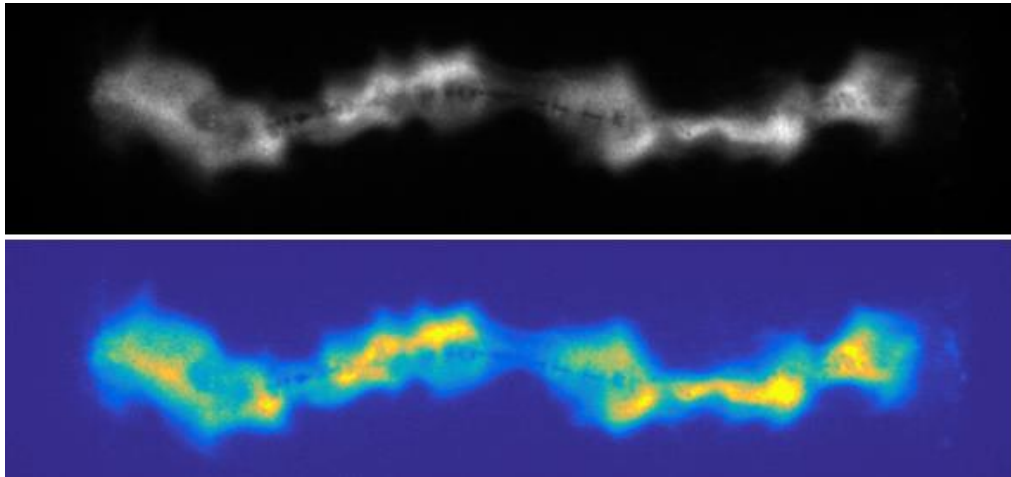
Figure 4-17 Snapshot at vaporisation moment with ECF195 at 3 kA (ICCD Camera, TTL = 1 µs, top view = original picture & bottom view = colorized picture)

This first campaign demonstrated the feasibility of vaporisation detection thanks to the current and voltage disruption. We can now study the fast lightning waveform.

4.2.1.3.2. Lightning waveform

The detection of the different states of the metallic wire depends on the speed of the electrical energy injected into the wire. In theory, the energy to vaporise a given mass of metal is constant. This value depends on the resistance of the wire, thus its resistivity and cross-section, and the integration of the square of the current. For a metallic wire of a defined cross-section, the time to reach this energy will depend on the current shape, i.e. its maximum and waveform. This speed is thus dependent on the current derivative at the beginning of the phenomenon but also on the current decay if the derivative is not high enough to reach vaporisation before the current peak. Therefore, we will differentiate the detection of the end of the melting and vaporisation phase considering two modes: slow and fast. For example, we consider a fast mode for a copper wire of 125 µm diameter that will vaporise in less than 5µs with a 10 kA WF1, well before the current peak, whereas with a 1 kA WF1, vaporisation will occur after 50µs, long after the current peak which is associated to a slow mode. This result will be different for another current waveform. With the current impulse at the beginning of the test and the arc creation, a strong electromagnetic field is created which disturbs the signal acquisition. For this reason, oscillations can be visible.

For the slow mode, different material states can be identified when studying the current waveform. Melting is still identified by the shutdown of the current but it is now possible to differentiate the vaporisation from the arc creation. The onset of vaporisation is identified by the change in current slope during the decrease. The arc corresponds to the current restart. The current detachment from its theoretical shape is related to the significant increase in resistance with the temperature close to the melting phase. It was unfortunately not possible to measure the voltage due to the high increase in resistance prior to vaporisation. The voltage surge generated by this phenomenon is so great that it breaks the probe protection, leading to a high current flow in it which fully destroys the probe. This first detection method is illustrated in Figure 4-18.
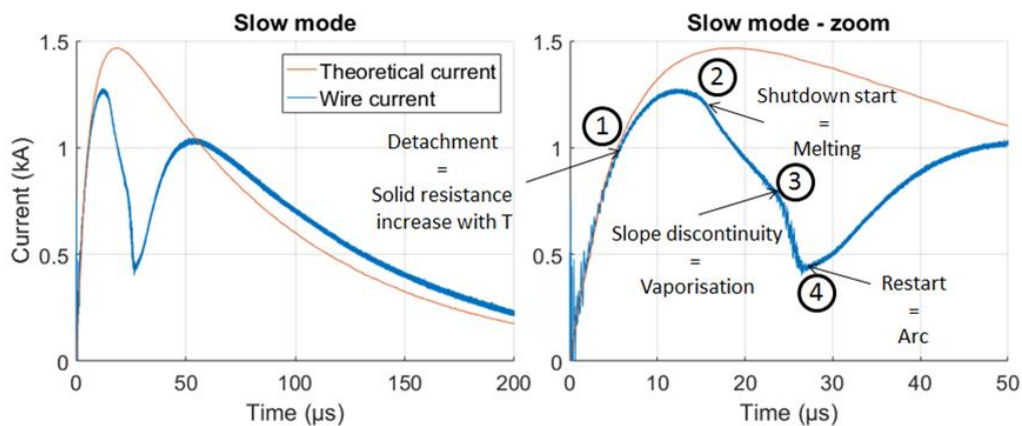
Figure 4-18 Typical wire state changes identification with current measurement – Slow mode

There is a delay between the end of vaporisation and creation of the arc due to the time necessary to sufficiently heat up the channel containing metallic vapour and to ionise the column.

A different behaviour in the slow mode was also observed for refractory material. As presented by Pikuz [94] and illustrated in Figure 4-5, the plasma is generated around the dense matter of the wire for tungsten and not in the metallic gas as for copper. The metallic vapour might be maintained as a dense area where a small current could flow up to complete ionisation and arc creation around the wire. Therefore, a current plateau is observed during this transition phase, as illustrated in Figure 4-19:
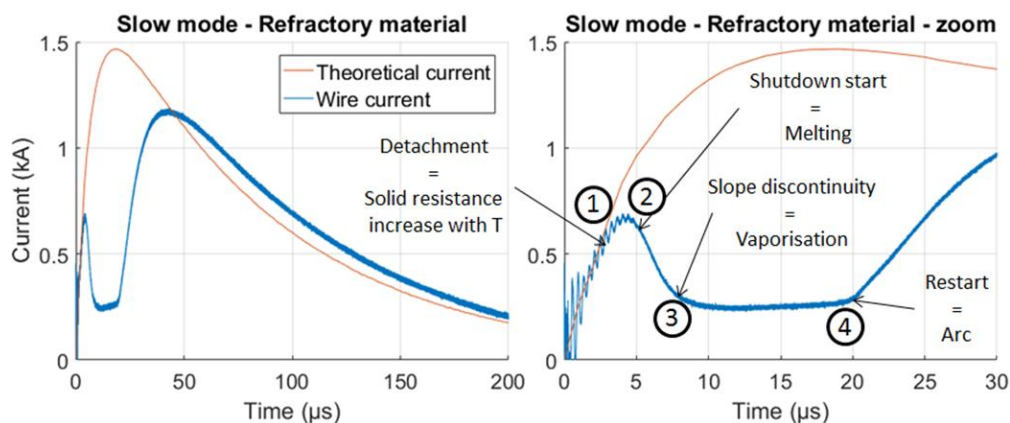
Figure 4-19 Typical wire state changes identification with current measurement – Slow mode – Refractory material

For the fast mode, the identification of the different wire states is difficult due to the constriction of the duration of each phase. As a result, only 2 steps were identified. The detachment of the current from its theoretical injection is considered as the end of the melting phase, where the resistance increases significantly. For this mode, a disruption is visible with high peak noise which is considered as the almost simultaneous occurrence of arc creation and the end of vaporisation. This second detection method is illustrated in Figure 4-20.
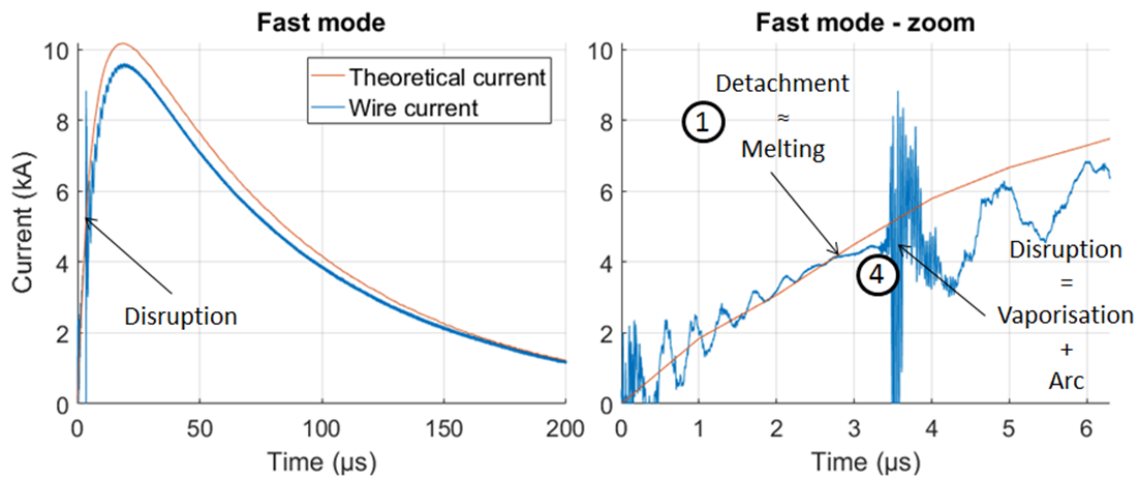
Figure 4-20 Typical wire state changes identification with current measurement – Fast mode

The study of the detachment and the disruption for all the configurations is summarised in Table 4-3 below with the different phases identified:

Current type	Current amplitude (kA)	Wire type	1 (µs)	2 (µs)	3 (µs)	4 (µs)	Wire type	1 (µs)	2 (µs)	3 (µs)	4 (µs)
WF1	10	Copper Ø125µm	2.6/0	/	/	3.5/0	Copper Ø75µm	1.7/0	/	/	1.7/0
	5		3..6/0.1	/	/	6.2/0.1		2.4/0.2	/	/	2.9/0.1
	3.57		4.5/0.3	/	/	8.2/0		2.8/0	/	/	3.9/0.1
	2.27		5/0	9.2/0	12.7/0.3	14/0		-	-	-	-
	1.47		6.4/0.4	14.5/0.3	23/0.6	25.3/0.7		3.3/0.1	5.9/0.1	8.7/0.3	10/0
	1		7/0	26.7/1.5	46/0	52.3/6		-	-	-	-
	0.81		8/0	37.3/1.5	58.3/2.9	78.3/4		4.1/0.2	10.4/0.5	20.2/2.3	26.8/2.9
	0.8		8.5/0	39/0	62.7/3.1	75.7/3.1		-	-	-	-
WF5A	10		6/0	/	/	7.6/0		-	-	-	-
	5		9/0.5	/	/	12.6/0.2		4.7/0.3	/	/	6.5/0.1
	3.57		10.2/0.3	/	/	16.5/0.4		-	-	-	-
	1.47		17.3/0.4	25.9/0.8	32.6/1.1	34.6/1.5		9/0	12/0	/	16.3/0.2
	0.81		24/1.4	43.5/1.4	55.6/1.8	64.2/1.6		13/0	19.2/0	21.2/5.8	17/0
WF1	10	Alu Ø 125µm	2.5/0	/	/	2.5/0.02	Tungsten Ø 100µm	1.5/0	/	/	1.5/0
	5		3.5/0	/	/	4.3/0.08		2/0	/	/	3.5/0
	1.47		4.5/0.5	9/0	13.7/0.6	16.2/1		3.0/0	5.0/0	9.5/0.7	20.4/4.3
	0.81		8.0/0	16.3/0.3	22.0/0	35.8/2.4		2.8/0.2	9/0	17.7/5.5	92/20.8
WF5A	10		3/0	/	/	5.5/0.05		3/0	/	/	3.6/0
	5		6/0	/	/	9.3/0		4.5/0	/	/	7/0
	1.47		12.8/0.4	17.5/0	21.5/0.7	23.5/0		5.5/0.7	11/0	17.0/0	26/0
	0.81		12.5/3.5	29.2/0	39.0/0	42.8/0.4		7.0/0	16/0	28.5/2	96/1.4

Table 4-3 Lightning waveform - Test summary (*: Mean Value/standard deviation)

The results are quite stable for high current values but less so for current values close to the limit of vaporisation. For example, the minimum current value that has to be reached in order to vaporise a copper wire Ø 125 µm with a WF1 is 650 A. With the current decrease, the duration of the melting phase and of the vaporisation phase increases. And in this case, another phenomenon could prevail such as an arc creation in air, along the surface of the wire. Such a phenomenon is clearly less stable and could occur during this phase as one enters a slow mode for the electric explosion as explained in 4.1.3.

The different phase changes are of course faster for the copper wire with a smaller section but the behaviour is similar. As for aluminium wire which has properties fairly similar to those of copper, it is in the same family. Only the tungsten wire tends to maintain the melted phase as it has quite significantly different properties. The currents recorded are summarised in Figure 4-21 where the different configurations are presented. The star with 4 branches represents the melting phase and the one with 5 branches, the arc creation where the plasma phase begins:
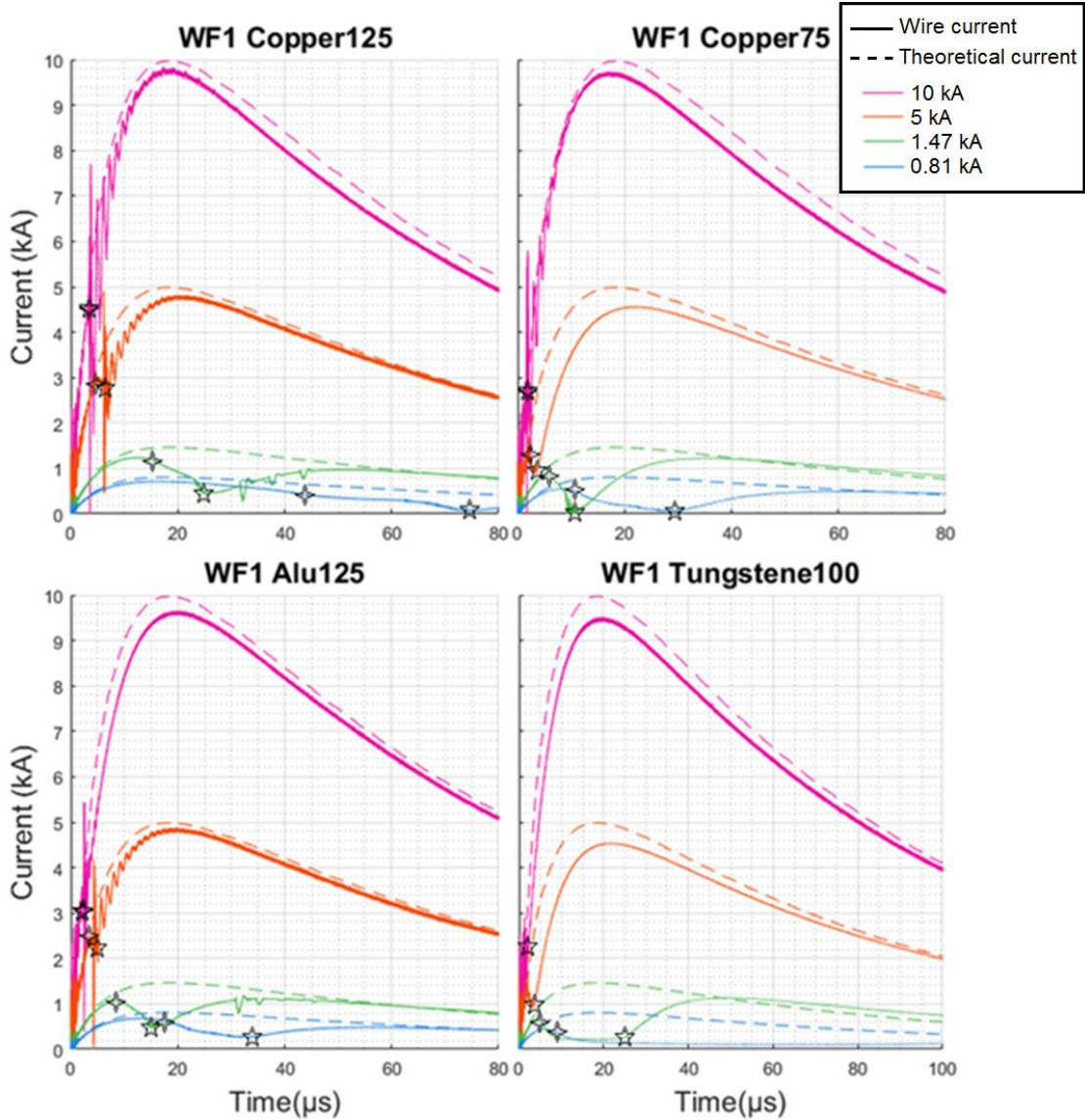
Figure 4-21 Wire melting and vaporisation detection

As the energy deposited in the wire as a function of time is impacted by the waveform shape, it will change the vaporisation time at the same current amplitude. WF1 is a faster waveform but less energetic than WF5A. Even if current cannot be directly related to the phase change, as explained in 4.3.1, some trends per waveform and wire configuration can be discerned. This is illustrated in Figure 4-22 where it can be seen that the waveform shape impacts the power coefficient of the time decay with the current. Again, copper and aluminium belong to the same family of metals and thus, their behaviours are similar, in opposition to tungsten for which the arc creation mechanism is very different as explained in 4.1.3. Still, this material is interesting to study the phase change and vaporisation detection since its thermodynamic properties are very different from those of aluminium and copper. This is useful to increase confidence in our electro-thermal model detailed in 4.3 where different configurations are necessary.

The curves in the left graph are labelled:
$y = 50.473x^{-1.279}$
$y = 17.328x^{-1.073}$
$y = 26.284x^{-1.062}$
$y = 50.816x^{-1.595}$

The curves in the right graph are labelled:
$y = 50.443x^{-0.846}$
$y = 22.542x^{-0.778}$
$y = 34.246x^{-0.804}$
$y = 57.181x^{-1.257}$

Legend: Cu125, Cu75, Al125, W100
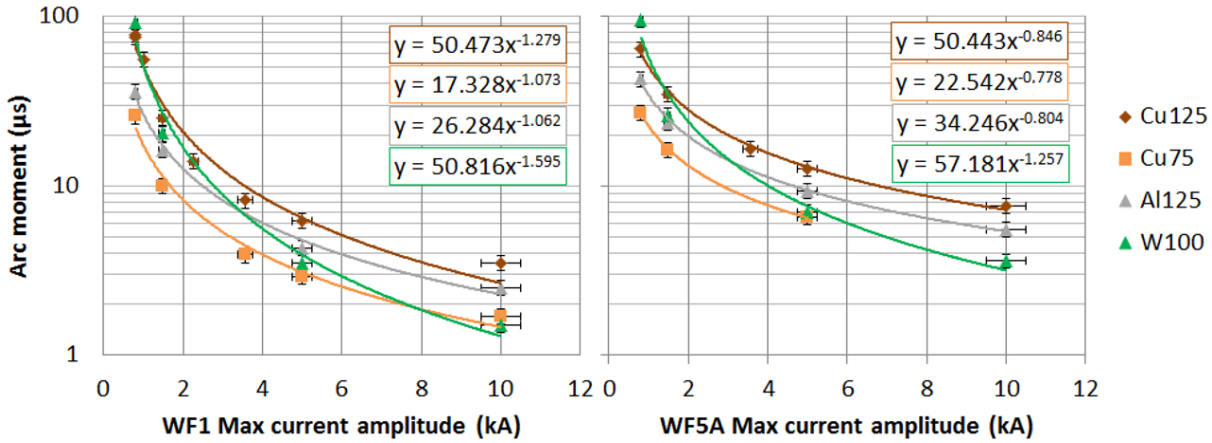
Figure 4-22 Vaporisation time comparison

With a faster waveform, the wire is less distorted prior to explosion but it can still be observed that the expansion is not fully homogeneous (Figure 4-23). As depicted by Pikuz [94], arc creation is very different between copper and tungsten. For tungsten, a refractory material, dense matter is visible in the centre of the arc and the wire is practically not distorted or disrupted. This seems to confirm the theory of creation of the plasma around the vaporised wire for tungsten and not through the vaporised metal as for copper.
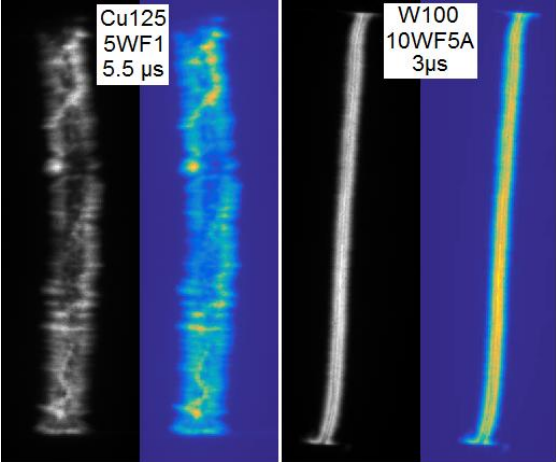
Figure 4-23 Snapshot at vaporisation time with fast waveform (ICCD camera – TTL=1 µs) (Original and colorized pictures)

In addition to the current measurement to detect the vaporisation time, we performed pressure measurements in order to assess the shock wave generated by the wire explosion since the rapid change of state of the wire is not a mere melting and vaporisation but an explosion that creates a strong shock wave. An example of measurement is presented in Figure 4-25 where it can be seen that the sensors are highly disturbed during the first 20 µs and that the pressure amplitude quickly decreases due to the damping effect of air.

The analytical fittings shown in Figure 4-25 come from expression 4-4, which is the Friedlander equation, considering that the profile of the measured pressure is related to a shock wave with a rapid pressure increase (ΔP+) and an exponential decay (dt+) following the equation for the positive overpressure:

$$P(t) = \Delta P^+ e^{-(t-t_0)/dt^+} \times \left(1 - \frac{(t-t_0)}{dt^+}\right) \qquad \text{4-4}$$

with:

- Time of arrival (t_0)
- Maximum positive overpressure (ΔP^+)
- Positive phase duration (dt^+)
- Positive pulse (I^+)

These parameters are also illustrated in Figure 4-24 below:
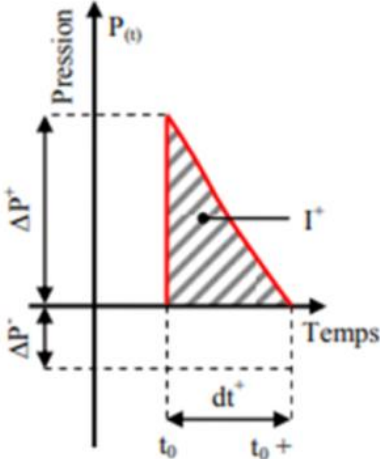
Figure 4-24 Shock wave pressure waveform

Still, the pressure measurement is quite disturbed as the value measured is low: between a few kPa to a few hundreds of kPa. The sizing of the pressure probe was based on a similar experiment performed in water [101], but the damping effect of air is significantly higher than the one expected in water. We need to consider 10% of error in the assessment of this value, in view of the fact that the pressure before the shock is not constantly zero and a threshold effect is considered.
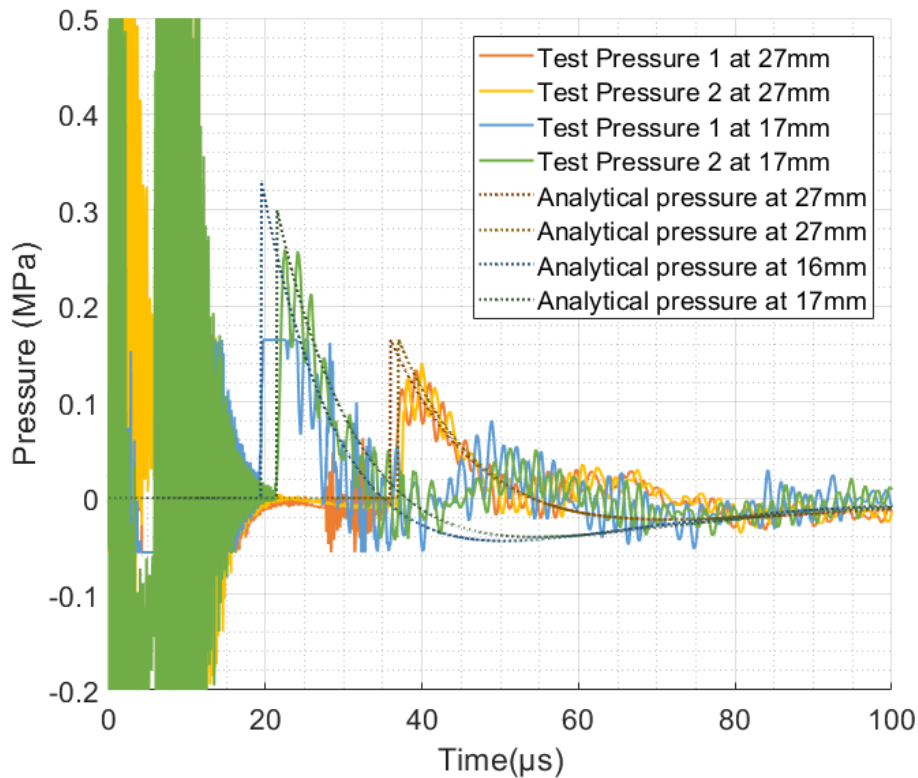
Figure 4-25 Shock wave measurement and analytical fittings (Cu125 at 5kA)

The following results in this section concern Cu125 but all the pressure measurement results are presented in Appendix A.

As expected, the shock wave time of arrival decreases with the current increase for an identical current waveform as it changes the amplitude of the explosion pressure as shown in Figure 4-26. With a different waveform or a different type of wire (material and diameter), the pressure created by the explosion will be different. Indeed, if we refer to Equation 4-1 the power deposition speed in the wire will change, which impacts the maximum pressure created by the wire explosion.
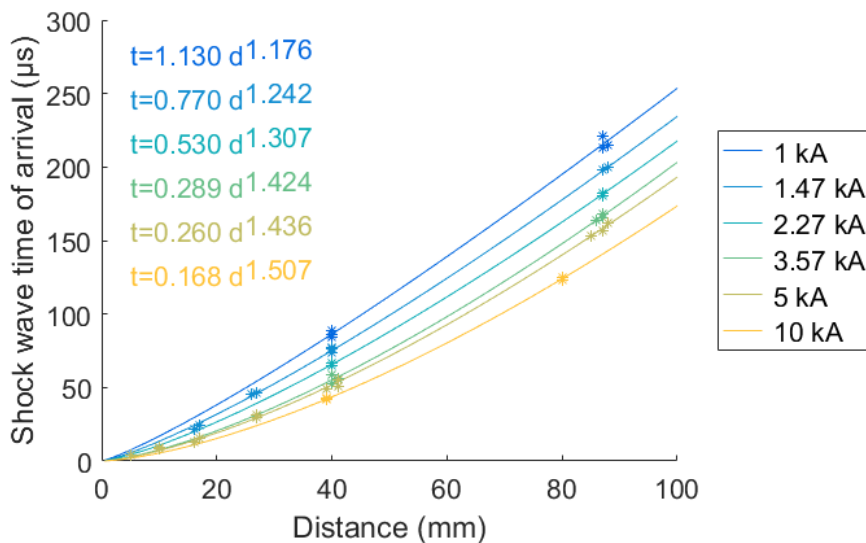
Figure 4-26 Shock wave time of arrival (t_0) dependency with current for WF1 & Cu125

For the decay time, it is very difficult to quantify the damping effect of air; even if it seems to increase with the distance, the shock wave front expands and its amplitude decreases, making it increasingly difficult to detect the front. It should also be noted that it is increasingly difficult to measure this parameter as the amplitude is very low. This measured decay time in shown in Figure 4-27 for the case of waveform WF1 and a Cu125 wire.
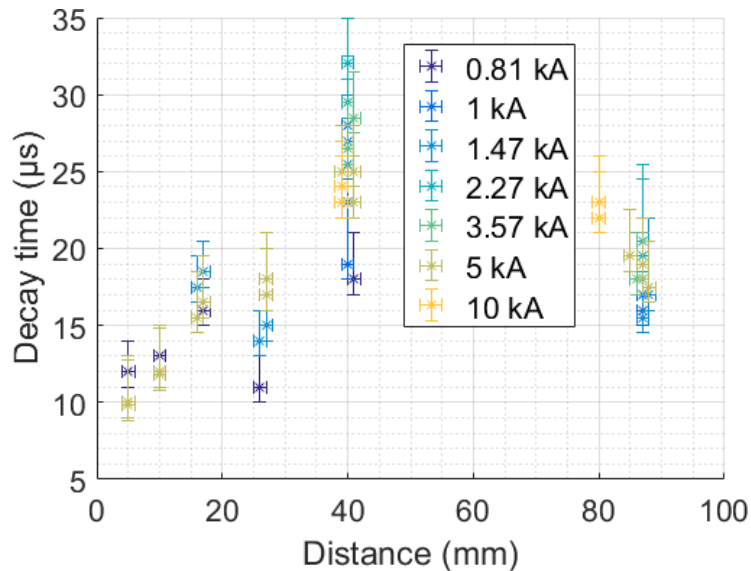
Figure 4-27 Decay time (dt$^+$) dependency with current for WF1 & Cu125

As the metal properties and section change the energy deposition mechanism that will lead to the wire explosion, a simple law that will characterise the pressure amplitude as a function of the current (amplitude and waveform) cannot be defined. For this reason, we first developed a phenomenological model for the Cu125 configuration with WF1 prior to a more complex explosion model. This configuration was chosen as it represents the most widely used LSP, i.e. ECF195 with the laboratory lightning shape. This model is detailed in the following section.

4.2.1.4. Phenomenological model

The first step is to assess the peak pressure generated at the wire boundary. For this purpose, we considered the pressure measured at several distances and defined a decay law in order to extrapolate the wire pressure. As the pressure amplitude changes with the energy, and hence the amount of current and its shape, we normalised the amplitude, considering the value measured at 40 mm as the reference. Only high currents were considered as they presented less variability and higher pressures are easier to measure. The results are shown in Figure 4-28:
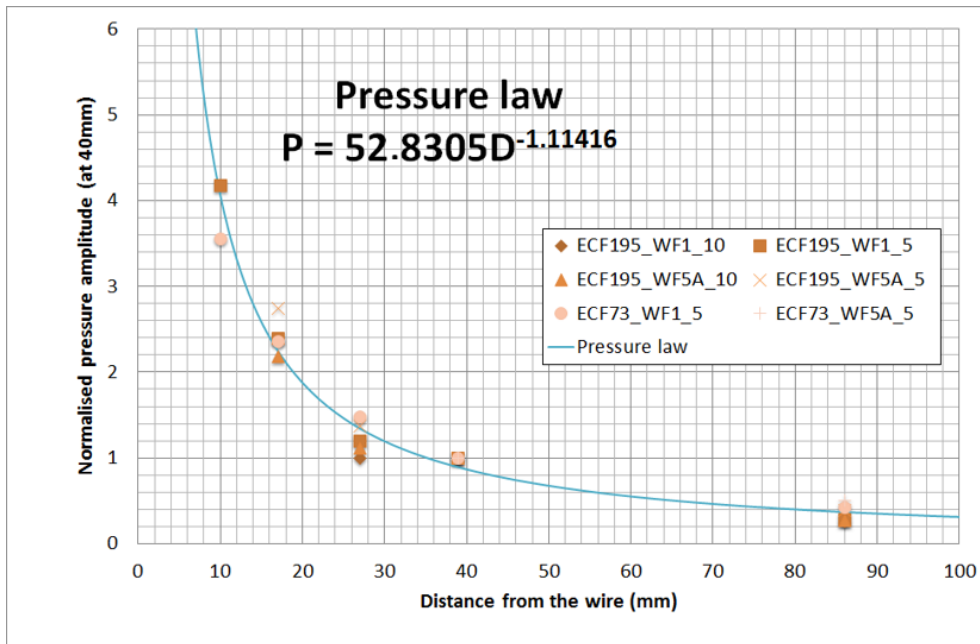
Figure 4-28 Normalised pressure decay law for Copper

Based on this law, we can deduce the pressure at the wire boundary knowing its radius and the pressure amplitude measured 40 mm from the wire.

	Pressure at the wire (MPa)					
	WF1 10kA	WF1 5kA	WF1 1.47kA	WF1 0.81kA	WF5A 10kA	WF5A 5kA
ECF195	290	160	45	4	218	127
ECF73	157	138	40	N/A	N/A	61

Table 4-4 Shock wave pressure vs current & wire section

The law presented in Equation 4-1, which relates the pressure to the power deposition speed, could not be used directly because of two issues. The first one is that it was not possible to measure the voltage during the test, and therefore the electrical power deposited in the wire prior to its explosion could not be computed. The second one is that even if this maximum pressure is impacted by the power deposition prior to the wire explosion, the part deposited after the explosion also seems to change the maximum pressure amplitude, possibly because it will "feed" the shock front propagation differently depending on the current waveform. We therefore created an empirical law that relates the pressure at the wire to the current amplitude for ECF195. For this configuration, we need a minimum of 650 A in WF1 to reach vaporisation and thus, possibly, create a shock wave. This is, therefore, the start point (0 MPa) for the law. With this hypothesis and the values provided in Table 4-4, we obtain a power as described below:

$$\Delta P^+ = a \times I_p{}^b + c \qquad \text{4-5}$$

In this configuration, a = 80.3 (MPa.A^{-b}), b = 0.64 and c = -62.88 (MPa).

This pressure law will then be used for the pressure profile application in the VDLOAD in chapter 6 for the calculation of structural damage in CRFP.

4.2.2. Dumbbell-shaped LSP explosion test

After the study of the wire explosion, representing an elementary component of the LSP, we then needed to study the complete lightning strike protection. For this purpose, we injected a conducted lightning current in a layer of lightning strike protection with a dumbbell shape in order to concentrate the current density in the centre and create the explosion in this area only. The first objective was to confirm our ability to predict the electro-thermal effect, and therefore, the chronology of the explosion. The shape of the lightning strike protection could increase the complexity of the electro-thermal effect. This is why we need to analyse the Joule heating within this wire web in order to confirm that we can transpose our hypotheses made for the wire as a 2D asymmetrical problem to a 3D problem. The second objective was to understand the overpressure effect of a global protection explosion taking the confinement effect into account. As has already been observed, the deflection of a composite panel subjected to a lightning strike is enhanced by the presence of the paint. One of our hypotheses is that the paint confines the gas coming from the explosion and increases the overpressure applied on the panel. With this conducted current test, we remove the contribution of the arc and its associated effects such as the shock wave and the current distribution dependency with the paint confinement.

4.2.2.1. Test setup

The same setup presented in Figure 4-10 was used for the injection of current in the sample but instead of the metallic wire, a dumbbell-shaped LSP sample was installed. This shape was chosen in order to ensure a good injection of current in the sample at each extremity and to concentrate the current density in the centre where the cross-section is smaller. The size of the sample is presented in Figure 4-29:
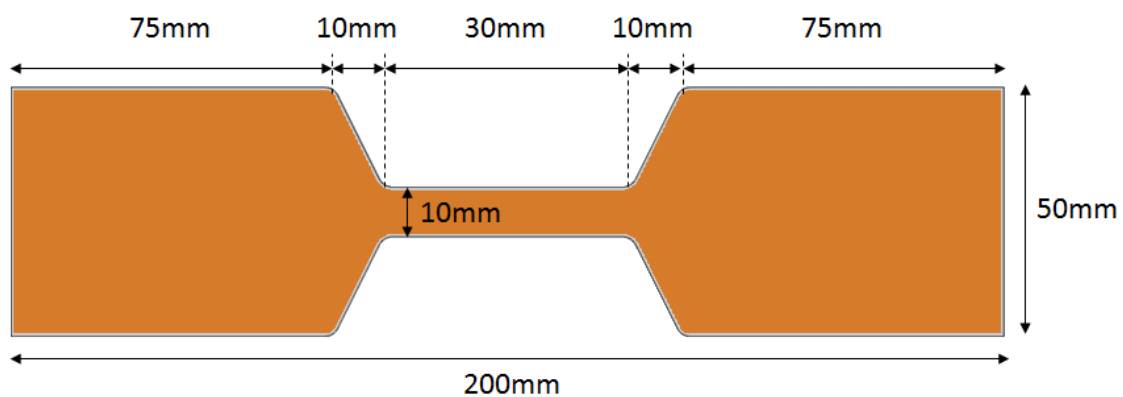
Figure 4-29 Dumbbell-shaped sample dimensions

In order to assess the Joule heating and the vaporisation time, the current and the voltage were measured. The high-speed camera IS1M (1Mfps) was installed on the front of the sample in order to visualise the vaporisation. Moreover, the LSP sample was co-cured (on the back side) with a GFRP rectangular panel in order to measure the deflection due to the surface explosion. As the pressure is too complex to interpret with the confined

configurations, the high-speed camera SA5 operating at 300kfps was installed on the side of the sample in order to follow the deflection profile. Lastly, a strain gage was installed on the back of the panel. Due to the strong electromagnetic environment, however, it was impossible to interpret the measurements as the sensor was disturbed during 400 μs. Figure 4-30 presents the installation of the sample.
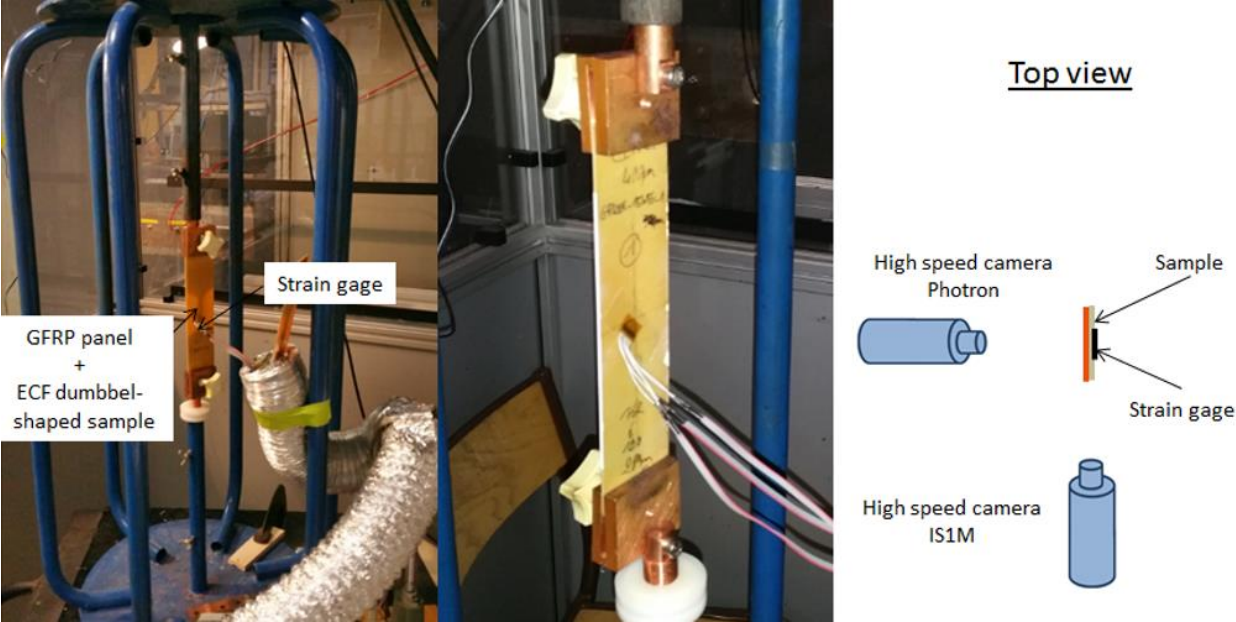
Figure 4-30 Dumbbell-shaped sample installation

4.2.2.2. Test configurations

In a first step, in order to assess only the vaporisation time, the dumbbell-shaped LSP were tested without any GFRP panel. For this analysis, two configurations were considered: ECF195 and SCF88. Even if ECF is the lightning strike protection of interest, it is useful to study the SCF configuration as it presents homogeneous properties and is easier to analyse with the model. In a second step, the two LSPs were tested in different configurations on the GFRP panel: Free, with paint on the front side and with a GFRP panel also on the front side. The first configuration was used as a reference for the overpressure generated by the LSP only. The ECF tested is a cured prepreg and not the raw material which means that resin surrounds the ECF layer as shown in Figure 4-31. prepreg is the usual form of the material sold for manufacturing. The second configuration was used to assess the impact of confinement by the paint, while the third configuration was used as an extreme case of confinement. Altogether, 8 wire configurations were thus considered:

Rationale	Vaporisation time		Free explosion		Confined explosion with paint		Extreme explosion confinement	
LSP type	ECF195	SCF88	ECF195	SCF88	ECF195	SCF88	ECF195	SCF88
Confinement	None		None		Paint		GFRP	
Support	None		GFRP					

Table 4-5 Dumbbell-shaped sample test configuration

In Figure 4-31, an example of the tested configuration with different views is given. The LSP was sanded on each side at the extremities of the sample in order to remove the resin and ensure a good contact for the current injection.
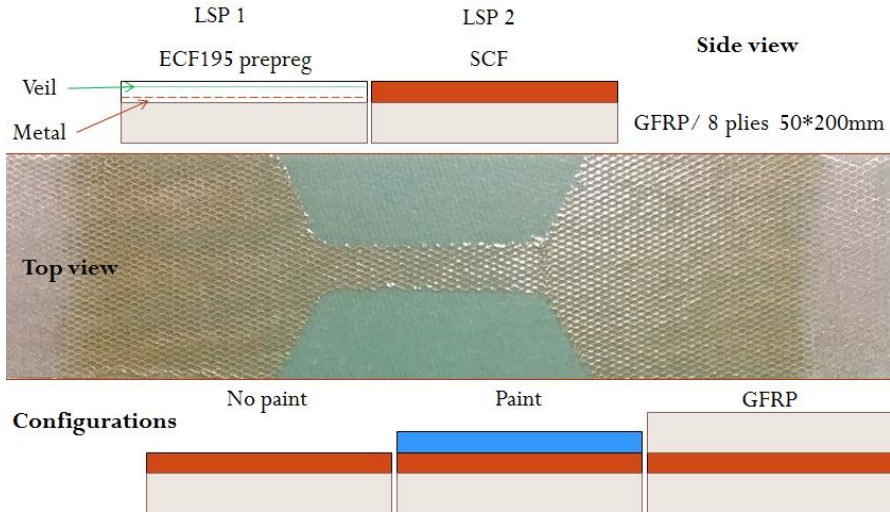
Figure 4-31 Illustration of dumbbell-shaped configurations

In this picture, the ECF is longitudinally oriented with respect to current propagation but this configuration wastes more material. Therefore, all the tested configurations were manufactured with a transversal installation of the ECF which fits better with the material roll provided. In this case, the path is more resistive.

4.2.2.3. Test result

In a first step, configurations without the GFRP support were tested in order to measure the vaporisation time and identify the parameters that impact the result. As expected, for an identical waveform and amplitude, ECF vaporised more quickly than SCF. Indeed, the sheet resistivity (=$1/\sigma d$) is twice as high for ECF (3 mΩ.sq) as for SCF (1.7 mΩ.sq), which means that the ECF equivalent thickness is half the thickness of SCF. Therefore, since both LSPs are made of copper, the Joule heating will be greater in ECF in this transverse direction due to the smaller section available for current flow. Also, a higher current amplitude will accelerate the vaporisation time as the time to peak decreases, shorter for WF1 (18 µs) than WF5 (54 µs), since the energy to reach the vaporisation state will be deposited more quickly. These first results are summarised in Table 4-6:

Type	Confinement	Maximum injected current	Waveform	Melting moment	Arc creation moment	Melting voltage	Arc voltage
SCF88	Free	10 kA	WF1	17.5 µs	24 µs	1.05 kV	6.4 kV
		15 kA	WF1	10.9 µs	14.1 µs	1.3 kV	9.4 kV
		15 kA	WF5A	21.5 µs	26.4 µs	1.5 kV	8.6 kV
ECF195	Prepreg	10 kA	WF1	5.7 µs	6.1 µs	2 kV	7.5 kV
		15 kA	WF1	4.2 µs	4.5 µs	3 kV	>7.6 kV
		15 kA	WF5A	9.3 µs	9.8 µs	2 kV	7.4 kV

Table 4-6 Free LSP melting and vaporisation time

As described in the literature and visible in Figure 4-6, the different stages of the LSP electric explosion can be determined by observing the current and voltage shapes. The two LSPs present the same electric explosion signature with a different speed due to the difference in metallic section available. The current detaches from its theoretical waveform since the resistance increases during the melting phase. Another clue to this increase in resistance is the voltage increase, clearly visible for the SCF configuration. The vaporisation is detected at the voltage peak. Then, the voltage collapses and the current returns to its theoretical value since an arc has been created and the conductivity of the path is restored. The results are quite repeatable as shown in Figure 4-32:
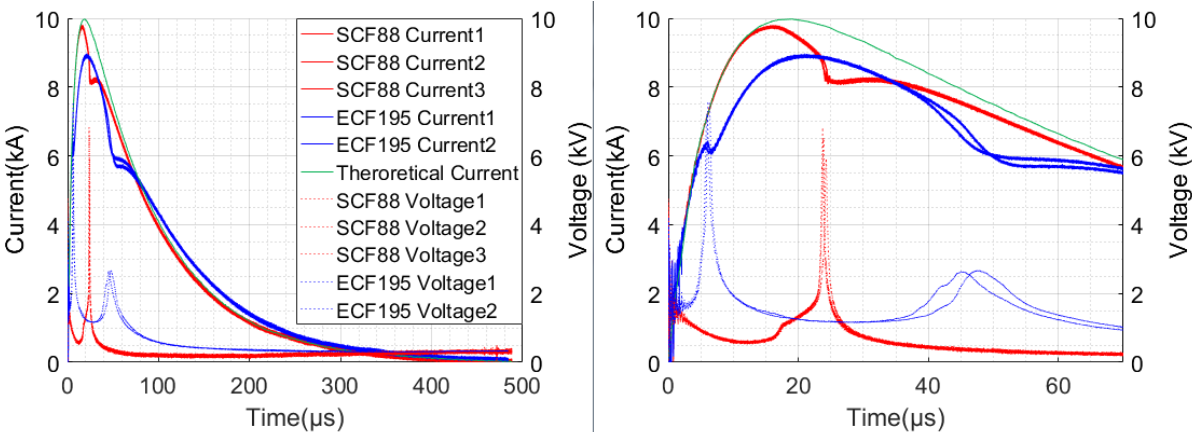
Figure 4-32 Voltage and current during electric explosion for ECF195 & SCF88 (zoom on right figure)

Still, a second voltage peak (45 μs) is visible for the ECF configuration at a lower level which does not exist for SCF. At this second peak, there is again a current collapse which is the demonstration of a high increase in resistance. This phenomenon was not observed for a low current value such as 6 kA but is present for all waveforms at 10 and 15 kA. The analysis of the vaporisation signature after the test provides an explanation for this second peak. Indeed, parallel lines of vaporised metal can be observed on the large area of the sample in the 10 kA test but not at 6 kA. No vaporisation was expected on this area due to its higher section available, sufficient to limit Joule heating. But possibly, the presence of micro-cracks in the ECF structure during the stretching of the protection to create the diamond pattern may have led to local discontinuities which concentrate the current. Since the current density is lower in this area, vaporisation will occur later than in the central area. Also, the local vaporisation and not the total section of metal limits the increase in resistance, therefore the voltage peak is lower. Possibly, this mechanism would not occur with a longitudinal orientation of the ECF since the cracks would be parallel to the current flow. Apart from this specific phenomenon, it is important to note that the presence of paint does not change the consumption of metal, which depends only on the current amplitude and waveform. The results are illustrated in Figure 4-33 below.
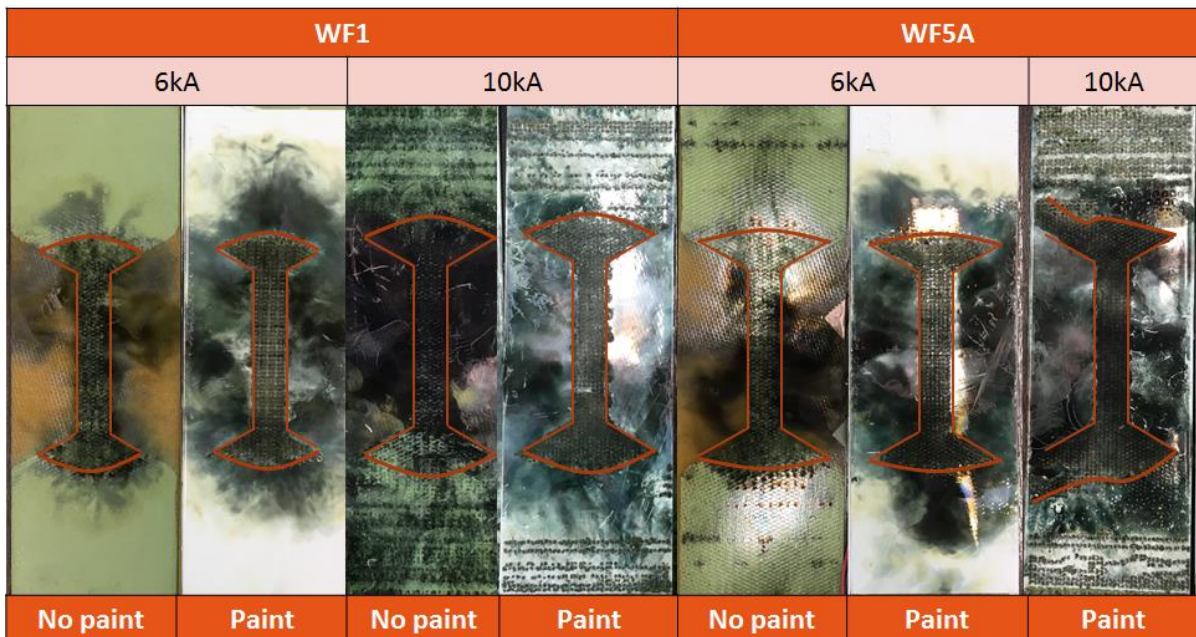
Figure 4-33 ECF post-lightning test vaporisation profile

In the same way, the presence of paint did not impact the metal consumption even if part of the metal layer was pulled off when the paint was ejected. The adhesion of SCF is lower than that of ECF since there is no resin plot to maintain it on the substrate.
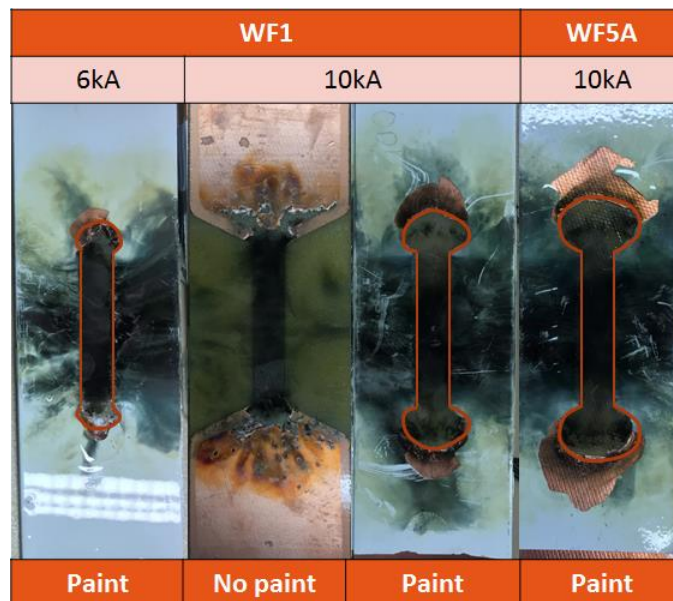
Figure 4-34 SCF post-lightning test vaporisation profile

Observation of the current confirms that the presence of paint or high confinement does not impact the melting and vaporisation process. As for the free LSP study, the vaporisation time is shorter for higher current amplitudes and faster waveforms. The results are summarised in Table 4-7:

Type	Confinement	Maximum injected current(kA)	Waveform	Melting moment (µs)	Vaporisation moment (µs)
ECF195	GFRP	6	WF1	8.5	12
	GFRP+100µm Paint			9.3	12.5
	GFRP+400µm Paint			9	12.5
	2 GFRP			10.2	14.8
	GFRP	10	WF1	6	7
	GFRP+100µm Paint			6.1	7.5
	GFRP+400µm Paint			6.5	8
	2 GFRP			6.7	8.7
	GFRP	6	WF5	19	21.5
	GFRP+100µm Paint			20	22
	2 GFRP			22	24.6
SCF88	GFRP+100µm Paint	6	WF1	46	68.5
	GFRP+400µm Paint			45	66
	2 GFRP			48	67
	GFRP	10	WF1	18	26
	GFRP+100µm Paint			18	25
	GFRP+400µm Paint			18	27.5
	2 GFRP			20	25
	GFRP+100µm Paint	10	WF5	30	40
	GFRP+400µm Paint			28	37

Table 4-7 LSP melting and vaporisation moment

However, the confinement has an impact on the current collapse and arc creation. The vaporised metal prior to arc creation is highly resistive, which could shut down the current if no arc breakdown occurs and generates a conductive plasma. The confinement delays the creation of this shunting current and the collapse is more pronounced as the pressure is increasingly maintained with an increased confinement. This higher pressure requires a higher temperature to ionise the channel and create the plasma [73]. This is visible for the ECF195 configuration in Figure 4-35.
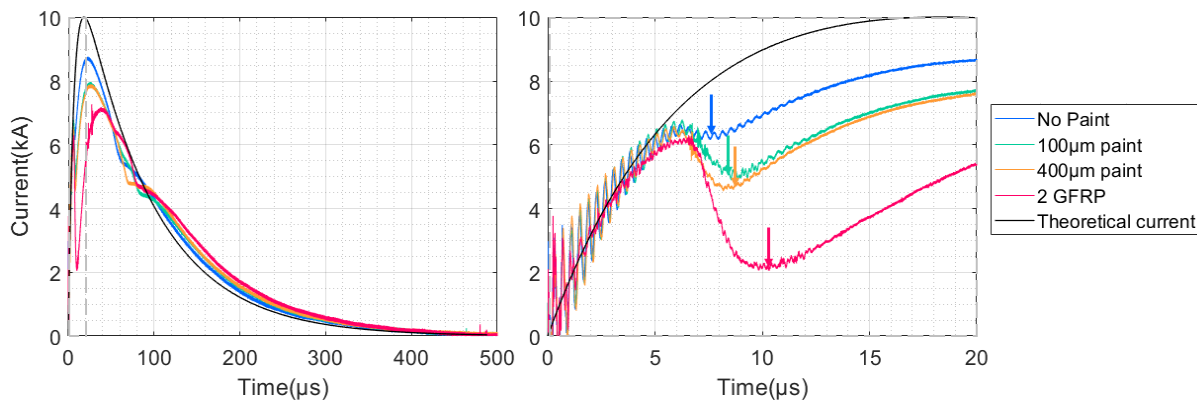
Figure 4-35 Confinement impact on voltage and current for ECF195 (zoom on right figure)

This mechanism can also be clearly observed for the SCF88 configuration as shown in Figure 4-36.
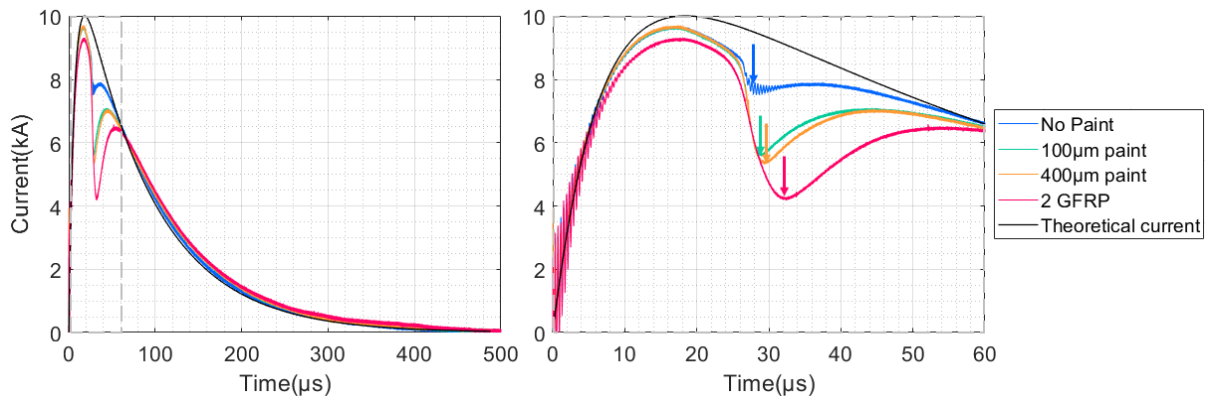
Figure 4-36 Confinement impact on voltage and current for SCF88 (zoom on right figure)

Lastly, observation of the deflection of the GFRP substrate with the high speed camera placed on its side provides interesting information regarding the confinement effect of the explosion. Three different confinements were compared: Free surface, painted sample with 400 μm of paint and high confinement with a GFRP plate. For the unpainted surface, the expansion of the explosion is free and no movement of the substrate can be recorded. With a painted surface, however, a deflection is visible. A maximum is reached at frame 376, i.e. after 1250 μs, and then oscillation of the sample occurs due to the reflexion of the mechanical wave to the boundary of the sample. Finally, the high confinement of the ECF explosion provided by a GFRP plate, identical to the substrate, leads to a deflection that is so high that its maximum cannot be measured due to the limited picture size that the camera can record. In this case, the two plates are fully separated by the explosion, ejected from their mechanical boundaries and broken in two parts. This is the demonstration of the confinement effect of the paint which will significantly increase the overpressure profile applied on the surface of a composite structure by lightning. The interest of this configuration is the absence of an electrical arc perpendicular to the surface that generates a shock wave and can be constrained by the presence of the paint at its root, changing the distribution of the current and the associated forces. In this specific test procedure, there is only conducting current, therefore the deflection is due only to the surface explosion and its overpressure. In all configurations, the magnetic forces will be identical since the confinement does not change the current distribution. For this reason, the absence of movement when the explosion is not confined confirms the limited contribution of Laplace forces in the observed overpressure compared to the confined explosion. The different deflection records are illustrated in Figure 4-37 below. The wires that are visible on the picture come from the strain gage installed on the back of the sample.
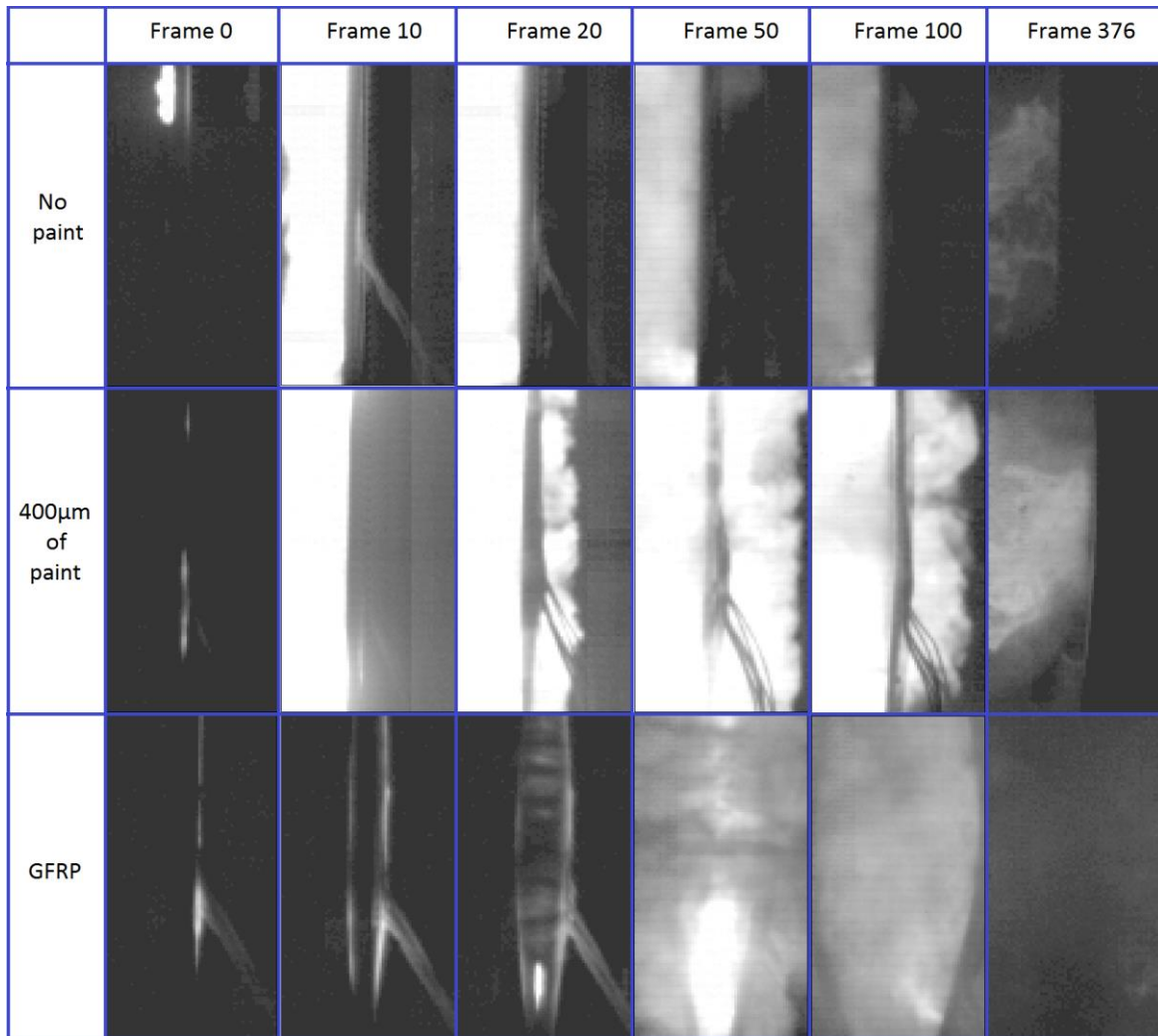
Figure 4-37 High-speed camera (300kfps) - Side view of ECF195 explosion on GFRP with different confinement configurations

Figure 4-38 below presents the impact of the confinement of the average speed of deflection. For the painted configuration, it represents the maximum deflection divided by the time when it is reached. For the fully confined configuration (GFRP), since the maximum deflection is not visible on the picture, this speed value represents the distance from the centre of the sample to the border of the picture divided by the time when the border is reached. Clearly, the confinement increases the speed and the maximum deflection, and hence the maximum overpressure and impulse generated on the substrate. As for the wire, a higher amplitude leads to a higher overpressure and the waveform shape has a more limited impact on the explosion shock wave amplitude. The explosion generated by ECF is slightly higher than that generated by SCF. This point will be further studied in Chapter 6.

Figure 4-38 Average speed of deflection

4.3. Numerical modelling

4.3.1. Vaporisation prediction: Electro-thermal model

4.3.1.1. Theory

In order to predict the vaporisation of the lightning strike protection, we first consider only the Joule heating generated by the flow of the lightning current in the metal. This is the main contributor to the heating of the protection [35] that leads to its explosion. Considering the first law of thermodynamics, we can relate the internal energy (U) with the work (W) and the heat supply (Q):

$$dU = \delta W + \delta Q \qquad \text{4-6}$$

In our case, we will consider that there is no variation of volume, thus $\delta W = 0$ and $dU = dH$ with H, the enthalpy. The heat supplied to the system comes from the electrical contribution P and the conductive heat flux $\overrightarrow{J_Q}$. The latter contributor depends on the thermal conductivity λ of the system and the temperature gradient $(\overrightarrow{gradT})$. But due to the extreme rapidity of the heat generated by the electrical contribution, thermal diffusion can be neglected. In this case, the electrical energy is converted into heat and can be expressed by the following heat equation 4-7:

$$dH = \delta Q \leftrightarrow \iiint_V \rho \, C_p \frac{\partial T}{\partial t} dVdt = \iiint_V P \, dVdt \qquad \text{4-7}$$

with:

- Density of metal (ρ)
- Specific heat of metal (C_p)
- Electrical Power (P)
- Temperature (T)
- Time (t)
- Volume (V)

The electrical power P can be expressed by the product of the current density $\vec{J}$ and the electrical field $\vec{E}$. Also, the electrical field and the current density can be related to the electrical conductivity σ of the metal. Thus:

$$P = \vec{J}.\vec{E} = \vec{J}.\frac{\vec{J}}{\sigma} = \frac{J^2}{\sigma} \qquad\qquad 4\text{-}8$$

With the heating due to the Joule effect, the metal will change state from solid to liquid and to vapour before being converted into a plasma. The properties of the metal need to be considered in each of its states as they will vary greatly with the change in temperature. Moreover, during the phase change, the energy supply is used to change the volume from one state to the other.

$$dH = \delta Q \ \leftrightarrow \ \iiint_V \rho\,\Delta H_{1\to 2}\frac{\partial x}{\partial t}dVdt = \iiint_V P\,dVdt \qquad\qquad 4\text{-}9$$

x is the mass fraction which has changed state and $\Delta H_{1\to 2}$ is the enthalpy of the phase change. We can now define the heat equation for each phase:

$$\begin{cases} \rho C_{ps}(T)\dfrac{\partial T}{\partial t} = \dfrac{j^2(t)}{\sigma_s(T)} & : T < T_{melt} \\[2mm] \rho\Delta H_{melt}\dfrac{\partial x}{\partial t} = \dfrac{j^2(t)}{\sigma_{s\to l}} & : T = T_{melt} \\[2mm] \rho C_{pl}(T)\dfrac{\partial T}{\partial t} = \dfrac{j^2(t)}{\sigma_l(T)} & : T_{melt} < T < T_{vap} \\[2mm] \rho\Delta H_{vap}\dfrac{\partial x}{\partial t} = \dfrac{j^2(t)}{\sigma_{l\to v}} & : T = T_{vap} \end{cases} \qquad\qquad 4\text{-}10$$

For the wire model, this set of equations was implemented in Matlab® by considering the heat equation in the wire by the current density j through the section of metal wire S and a constant density ρ. Each phase and phase change are managed by the function ode45 to solve the differential equation. The time step was adapted in order to monitor the temperature increase correctly (or the mass fraction for the phase change) and to sequence each equation based on the phase change temperature (or respectively the mass fraction equal to one). In order to start the modelling of the wire vaporisation, we need the physical properties of the metal in each phase. A bibliographic study was performed in order to obtain these properties for the different materials considered. In addition, an investigation of different electrical conductivity laws as a function of the mass fraction x was carried out for the phase change (melting and vaporisation) as a constant average value did not provide satisfactory results. The properties and their functions are summarised in Appendix B. The

equations of the material properties' dependency on the temperature were added to the Matlab® code and were changed at each time step. The lab currents were recorded and fit functions were created in order to remove the variability of noisy current measurements. The computation lasts less than 10s per configuration studied.

For the dumbbell model, a 2D approach is necessary and cannot be covered by the Matlab® code developed (0D). Therefore, COMSOL® Multiphysics software was used. In addition to the principal module, AC/DC and heat transfer in solid modules were added and coupled in order to solve the Joule heating problem defined above. The same material property functions were used for the solid and liquid phases. However, the phase change is fully managed by the software and cannot be modified by the user. The principle of the phase change management is illustrated in Figure 4-39. The phase change is not performed at a constant temperature but a ΔT needs to be defined in order to compute the mass fractions θ_j and modify the material properties in proportion.
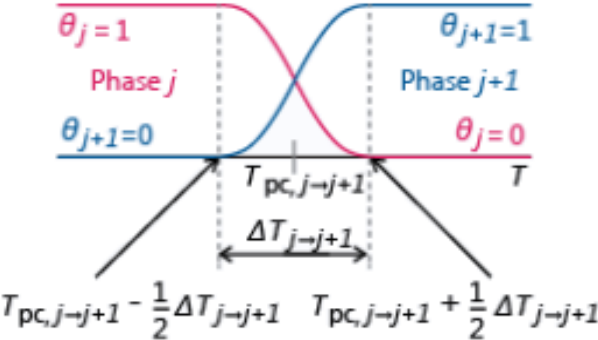
Figure 4-39 COMSOL® phase change law

Further details regarding the model implemented are presented in 4.3.1.3.

4.3.1.2. Wire model

4.3.1.2.1. Slow waveform

The slow waveform is half of a sine curve with a frequency f of 50 Hz:

$$I(t) = I_0 \sin(2\pi f t) \qquad \text{4-11}$$

In a first step, only the melting phase was considered. The model was used to study the Joule heating in ECF73 and ECF195 equivalent wires and an example is presented in Figure 4-40. The prediction of the vaporisation is quite good compared to the test, with a maximum difference of 14%. As expected, the model provides a faster vaporisation time since only the melting change phase was considered. The vaporisation phase will be introduced in a second step for the fast waveform.
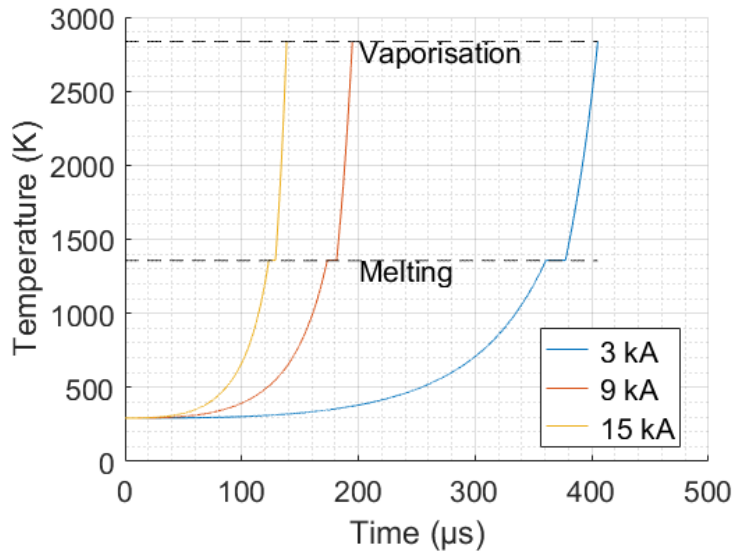
Figure 4-40 Slow waveform – ECF 195 modelled temperature

The results are summarised in Table 4-8 below:

Results	I=3 kA		I=9 kA		I=15 kA	
	Test	Model	Test	Model	Test	Model
ECF195	395	405	204	195	147	138
ECF73	215	205	110	98	80	69

Table 4-8 Vaporisation comparison between test and model with the GREMI sine waveform

4.3.1.2.2. Lightning waveform

The normalized lightning waveforms called WF1 and WF5A can be expressed with the following equation 4-12:

$$I(t) = I_0(e^{-\alpha t} - e^{-\beta t}) \qquad\qquad 4\text{-}12$$

with the following values:

	I_0 (A)	α (s^{-1})	B (s^{-1})
WF1	1.3612	$1.208.10^4$	$1.482.10^5$
WF5A	$2.5977.10^4$	$1.9112.10^4$	$1.9114.10^4$

Table 4-9 Lightning current variables

Since the test current injected into the exploding wire is not identical to the theoretical lightning waveform, we constructed a fitted waveform that represents the test current when a shutdown occurs without noise measurement. The two currents are illustrated in Figure 4-41:
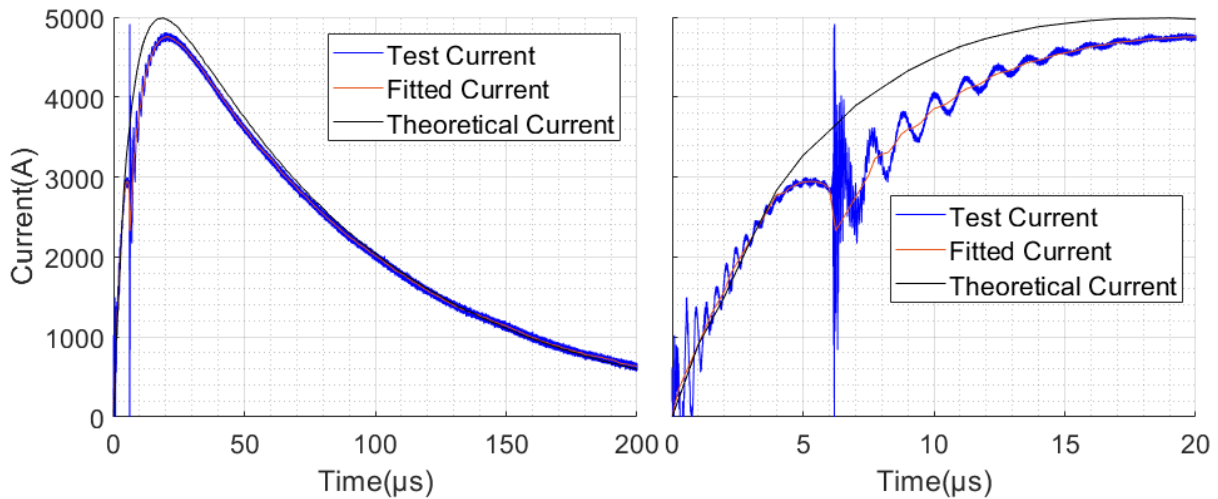
Figure 4-41 Theoretical and fitted current definition

The comparison with the lab result demonstrates a greater difficulty in predicting the melting and vaporisation of the metallic protection accurately with the current decrease, as illustrated in Figure 4-42.
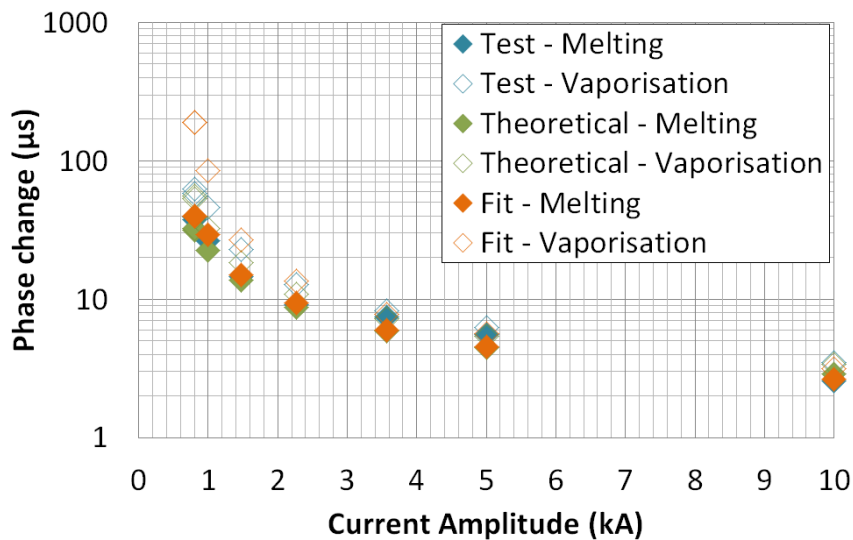
Figure 4-42 Example: Copper 125 wire vaporisation model with WF1: Comparison with lab test

The use of a waveform fit leads to a worse prediction, especially for low current where the current shutdown is enhanced, leading to a greater difference with the theoretical current that would be injected in a stable conductor. Unfortunately, since the voltage could not be measured during these test campaigns, it is not possible to validate the electrical resistance law with temperature based on the electrical energy injected into the wire. This means that our model underestimates the increase in resistance, especially during the vaporisation phase. The differences between calculations with the fitted current and experimental results are presented in Table 4-10 below. They were computed based on the following equation 4-13:

$$Err = \frac{Simulation - Measurement}{Measurement} \times 100$$

4-13

WF type	Current (kA)	Wire type	M	V	Wire type	M	V	Wire type	M	V	Wire type	M	V
WF1	10	Copper Ø125µm	2%	-10%	Copper Ø75µm	-31%	-14%	Alu Ø 125µm	-29%	-2%	Tungsten Ø 100µm	-13%	49%
	5		-19%	-9%		-10%	-12%		-13%	3%		29%	44%
	3,57		-19%	-6%		-2%	-11%						
	2,27		2%	6%									
	1,47		4%	17%		-2%	-7%		1%	72%		250%	254%
	1		10%	84%									
	0,81		6%	224%		-4%	7%		9%	181%		566%	
	0,8		2%	201%									
WF5A	10		-2%	-7%					38%	6%		4%	34%
	5		10%	-5%		1%	-11%		17%	8%		20%	32%
	3,57		28%	-3%									
	1,47		-1%	2%		-6%	-13%		-1%	43%		51%	130%
	0,81		5%	55%		-5%	15%		3%	88%		256%	

Table 4-10 Fitted current - Model error (M=Melting moment/V=Vaporisation moment)

The use of the theoretical waveform seems to compensate this effect and the predictions still remain very good for low current (<20%) as presented in Table 4-11. This is of interest since the theoretical form of the current is known but not the shutdown shape of the fitted current which needs to be measured. The use of the theoretical current for the prediction of explosion time for more complex metallic shapes such as ECF can be achieved with a limited error, decreasing with the current increase.

WF type	Current (kA)	Wire type	M	V	Wire type	M	V	Wire type	M	V	Wire type	M	V
WF1	10	Copper Ø125µm	11%	-4%	Copper Ø75µm	-26%	-12%	Alu Ø 125µm	-24%	6%	Tungsten Ø 100µm	-9%	31%
	5		-20%	-13%		-10%	-14%		-12%	-1%		20%	-4%
	3,57		-21%	-12%		-2%	-18%						
	2,27		-4%	-14%									
	1,47		-5%	-20%		-10%	-26%		-9%	-7%		10%	-12%
	1		-16%	-29%									
	0,81		-15%	-8%		-15%	-45%		-7%	26%		4%	-12%
	0,8		-17%	-12%									
WF5A	10		0%	-7%					42%	3%		6%	20%
	5		9%	-8%		1%	-13%		-18%	-14%		10%	-1%
	3,57		25%	-9%									
	1,47		1%	-1%		-4%	-17%		-3%	14%		9%	2%
	0,81		6%	9%		-5%	5%		-4%	8%		19%	1%

Table 4-11 Theoretical current - Model error (M=Melting moment/V=Vaporisation moment)

For lower current, the calculated delays to reach any phase changes are higher. At 800 A, the lowest current tested, the vaporisation limit is reached while it was estimated at around 650 A of the WF1 for a 125 µm diameter copper wire. The decrease in current tends to put the electric explosion increasingly into a slow mode as presented in 4.1 with instability along the wire that is not simulated in this simplified model. Indeed, the physics modelled in our approach are independent from the wire length. Moreover, the cross-section is only a factor used to compute the current density in the wire. Therefore, the temperature is fully homogeneous in the whole wire section and along its length. Looking at the shape of the wire at the time of the explosion, the sausage instability becomes more and more visible for copper wires when the maximum current decreases. The temperature evolution and associated phase changes are therefore less and less homogeneous, which would explain the difference with the model. This sausage effect and the wire torsion are visible for copper and aluminium configurations in Figure 4-43. Tungsten wire presents a very different behaviour without any visible sausage instability, possibly related to its refractory properties which confer on it a higher stability up to high temperature.
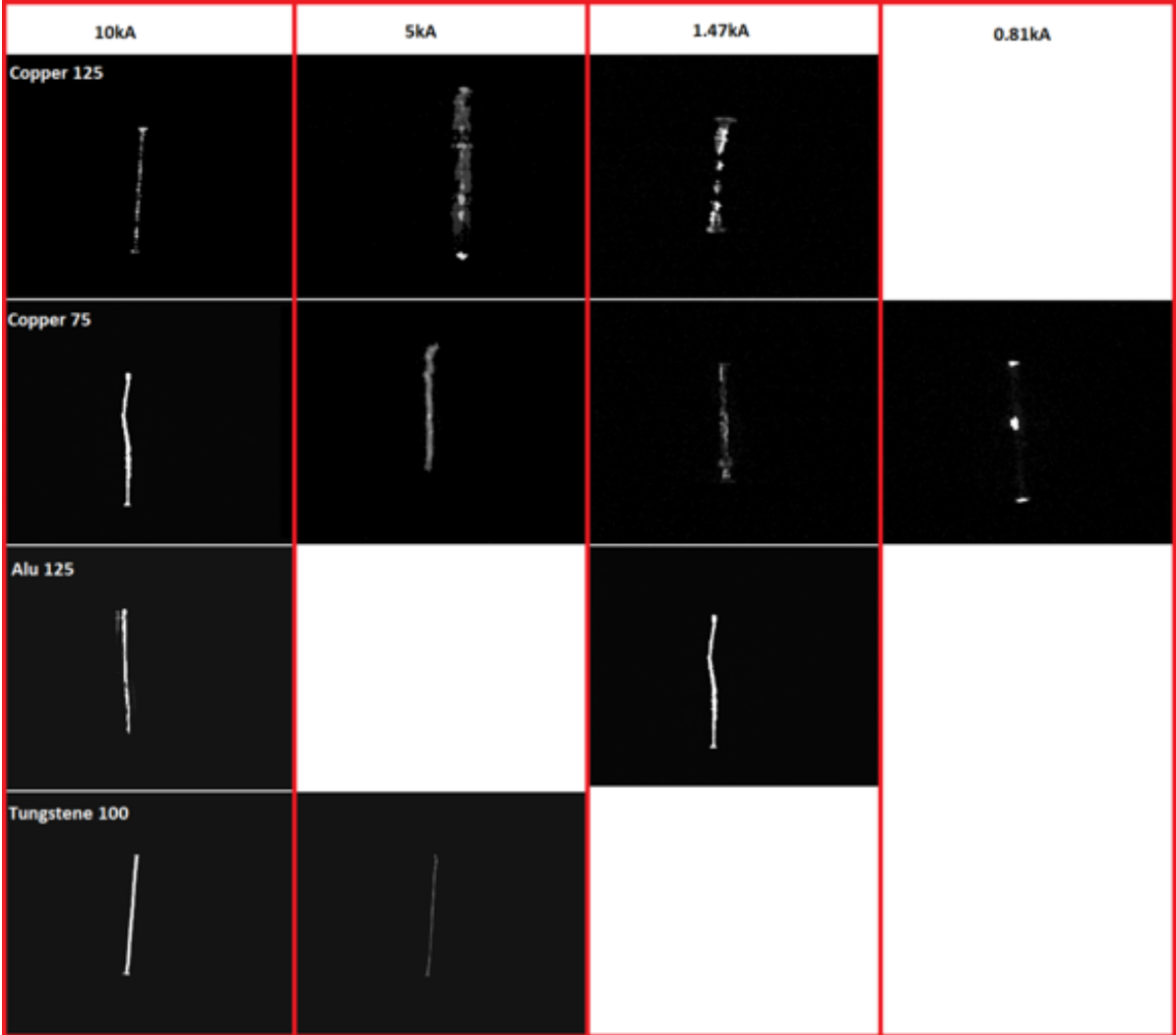
Figure 4-43 Wire pictures close to explosion for different metal configurations

4.3.1.3. Dumbbell model

Now that the electro-thermal model has been validated for an elementary configuration, the wire, we need to assess its applicability to a more complex configuration such as the ECF. A 2D model was therefore built in COMSOL®, as introduced in 4.3.1.1. As a reminder, the manufacturing principle of ECF is based on a copper sheet which is slit and then stretched in order to create the pattern as shown in Figure 4-14. The sheet can also be flattened in a final step. Before studying the vaporisation of the dumbbell sample, we analysed the electrical resistance of this protection without thermal dependency by considering a low level DC current. One of the objectives was to validate the impact of the geometry on the global layer resistance. In a first approach, we considered the ECF as a perfect copper material with the theoretical pattern as described in the specifications. In this study, only the AC/DC module needed to be implemented in COMSOL® with constant copper electrical properties. The current was injected on one side and the opposite side was grounded as illustrated Figure 4-44. In order to measure the resistance in both directions, 2 cases were studied with a current injection in x and Y direction. For this configuration, the mesh consists of 2146 2D elements.
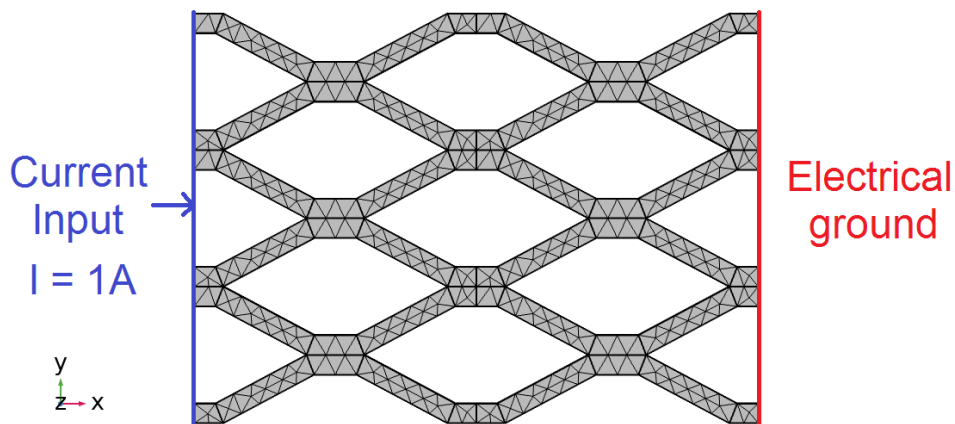
Figure 4-44 Resistance analysis model (x injection example)

As explained in 3.3.2.3, based on the values of the sheet resistance R_s in both x and y directions, we can build a layer with anisotropic properties that will be equivalent to a 3D configuration. In Figure 4-45, the two configurations are illustrated where a small sheet has been modelled (5.08 x 3.63 mm).
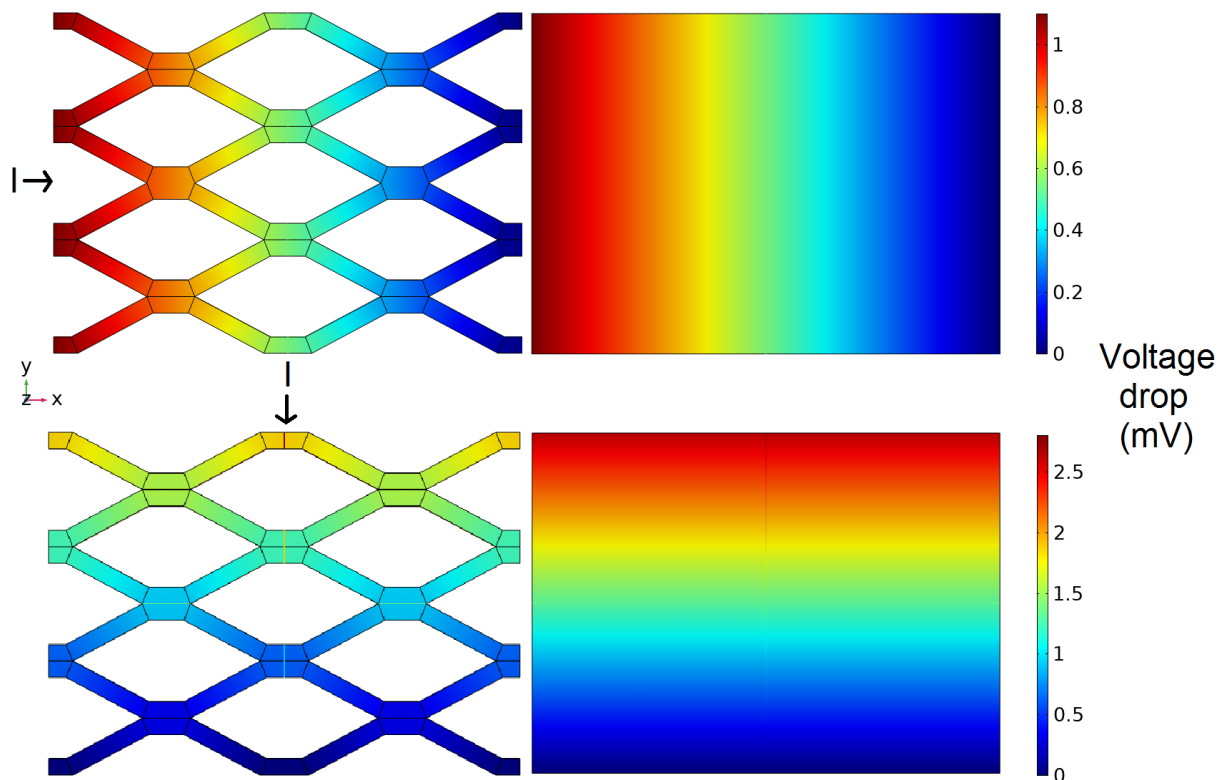
Figure 4-45 ECF195: 3D geometry and equivalent layer voltage drop (Top: x-direction – Bottom: y direction)

Looking at the voltage drop across the sample in both directions with 1 A of injected current, we can observe a significant difference in the y-direction but none in the x-direction. In order to find an explanation for this difference, we examined it under the microscope and discovered a discontinuity in the sheet, possibly due to the stretching process (Figure 4-46).
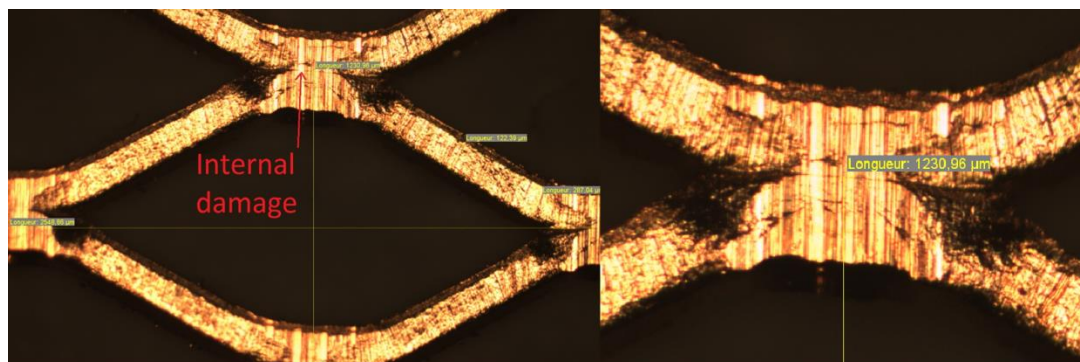
Figure 4-46 ECF microscope observation (zoom on right hand side)

The section is thus reduced at the node in the y-direction but not in the x-direction which could explain this difference in voltage, and consequently in resistance. We therefore introduced this damage in the ECF geometry as illustrated in Figure 4-47. For this configuration, the mesh number increased up to 11609 elements.
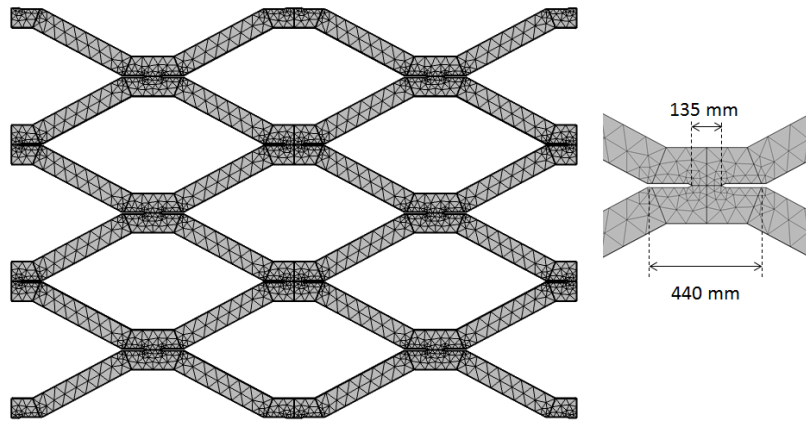
Figure 4-47 ECF with internal damage

With this new pattern, the voltage drop is very similar to the one obtained with the supplier protection values as shown in Figure 4-48. The discontinuity in the voltage drop value for the 3D configurations is due to the discontinuity of the geometry.
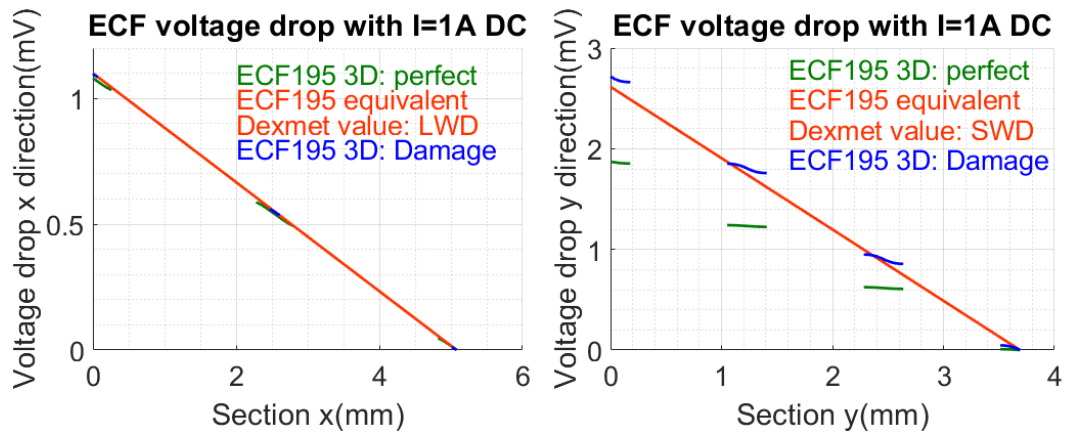
Figure 4-48 ECF voltage drop study (x and y directions)

This pattern, which represents ECF internal damage due to the manufacturing process, was used for the study of the vaporisation performed on the dumbbell samples. For this analysis, the mesh pattern has to be completely modelled, which could lead to a heavy configuration if the full dumbbell sample is meshed. Therefore, only 2 rows of the ECF pattern in the central area were modelled as illustrated in Figure 4-49:
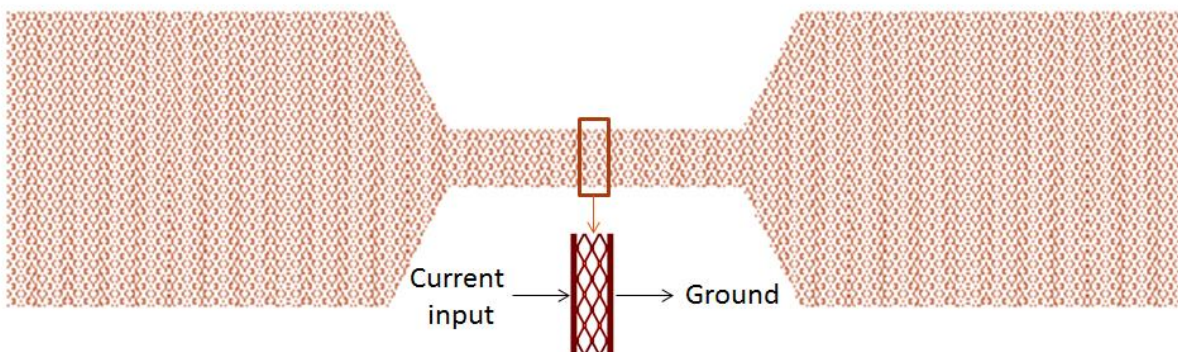
Figure 4-49 Dumbbell simplified model

The melting and vaporisation moment were recorded for the test based on the electrical current shape modification on the same principle as the wire test. For the model, the moments for the phase change were observed on the node where the current density is the highest. This node is where the damage was introduced by the manufacturing process. This area was the driver of the phase change detection during the dumbbell test and not the wire vaporisation which occurs much later than node vaporisation as shown in Figure 4-50. With 10kA of a WF1 for an ECF195 dumbbell sample, the end of vaporisation occurs at about 6μs in the node area and after 15μs in the wire area.
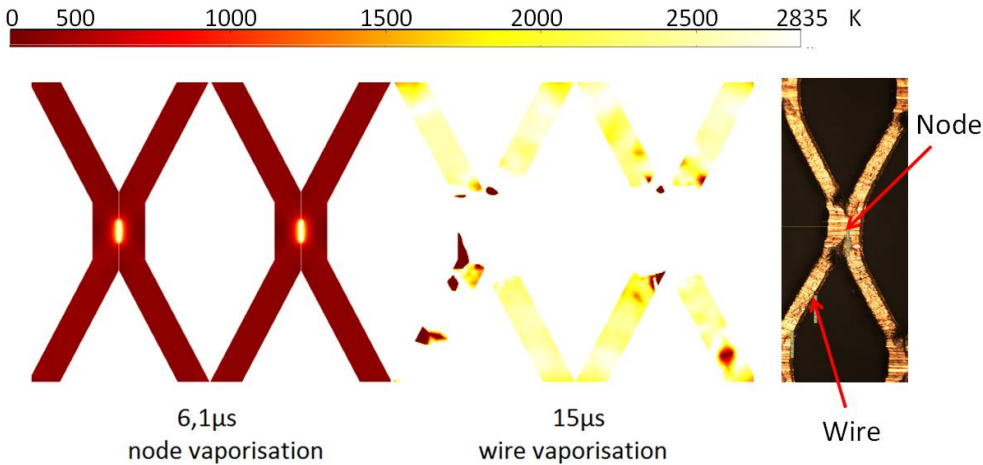
Figure 4-50 Vaporisation comparison between wire and node section (ECF195, 10WF1)

Indeed, the width of the node is 135μm which is 25% less than that of the wire: 178μm.

The comparison between the test and the model for the melting and vaporisation for both a homogeneous layer such as SCF and an anisotropic layer such as ECF presents fairly good agreement. The results are depicted in Figure 4-51.
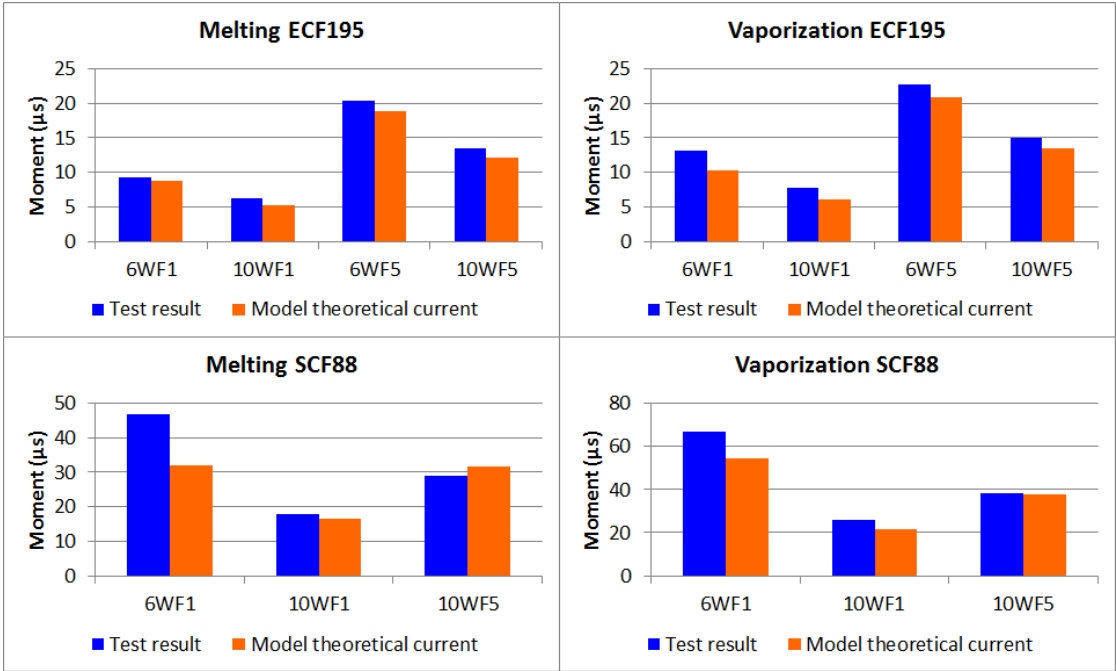
Figure 4-51 Dumbbell sample analyses: Test and model phase change moment comparison

The model results are slightly in advance compared to the test, possibly due to the phase change computation performed in COMSOL® software which is different from the previous model solved with Matlab® as summarised in 4.3.1.1. The phase change in COMSOL® is made by considering a linear weight distribution between phase 1 and phase 2 for the contribution in the heat equation. In the Matlab® model, a specific relationship was defined based on a polynomial law which slows down the contribution of phase 2.

Finally, based on this 2D model, we have demonstrated our ability to predict the explosion time of a protection based on a good description of the real protection structure: The dependency of its thermo-physical properties on temperature and the manufactured geometry.

4.4. Conclusion

The objective of this chapter was to predict the overpressure generated by the sudden vaporisation of the lightning strike protection due to the flow of lightning current. Based on our observation of a panel subjected to a lightning strike with a high speed camera, we have highlighted that the paint layer covering the composite panel is ejected by an underlying overpressure. The lightning current is mainly diverted by the metallic lightning strike protection which vaporises due to Joule heating. But this is not just a change of state to a gaseous phase. In fact, a high amount of energy is injected in the LSP in a very short amount of time leading to what we have defined as an electric explosion. The study of this phenomenon in the literature helped us to understand the parameters that influence the explosion intensity (wire diameter, wire physical properties, the electrical characteristics of the current injection and the surrounding medium) and how to identify its different phases based on the analysis of the current. The hypothesis of an explosion of the LSP due to the lightning current flow concurred with our test observations and needed to be characterised. In addition, observation of the surface of a panel tested after a lightning strike showed that the imprint of the ECF, the protection focused on in the present work, was visible in the resin. This demonstrates that the metal explosion is the main contributor to the overpressure since the resin remains almost intact except where it has been ejected by the LSP explosion.

In order to simplify the study of the LSP explosion, we have proposed to decompose the protection into an elementary wire that can be studied independently. This approach is possible for ECF protection due to its specific shape. Moreover, from chapter 3, the vaporisation of the LSP can be located at each moment during the lightning current injection. By comparing the vaporisation profile obtained in the previous chapter, we can assess the current density in each wire in intersection. Then, with the aim of defining the explosion produced by an elementary wire of ECF with different lightning current amplitudes, specific laboratory tests were defined. The principle of these tests was to inject

a pulse current through a wire and to study its phase change and shock wave creation. First, we demonstrated our ability to predict the different phase changes of the wire up to its explosion. A clear identification of the different states of the wire during the test was key in order to create a consistent test result matrix. This was made possible through our understanding of the lightning current deformation associated to the metal state. In parallel, we developed a model in Matlab® that was able to solve the system of differential heat equations. Since the explosion mechanism can be influenced by the type of wire and the current waveform, we chose to consider additional configurations in order to confirm our ability to predict the melting and vaporisation of a metallic wire no matter what the current waveform or wire properties were. Then, since the wire pressure itself cannot be measured, the shock pressure in the air was measured at several distances from the exploding wire in order to get to the source of the explosion. Based on this campaign, we were able to build a phenomenological model that relates the peak overpressure to the maximum current amplitude for the laboratory lightning waveform. This method is very interesting since it could be applied to other types of LSP based on the same construction principle as ECF in order to build a pressure law.

Before considering the complete LSP subjected to a lightning arc which is quite complex, we performed an intermediate step by studying the LSP electric explosion due to a conducted lightning current. To this end, we designed a dumb-bell shaped sample made of LSP in which the current density is well known. On the same principle as for the wire study, we validated our ability to predict the vaporisation of such a protection. We thus built a new model with COMSOL® to compute the Joule heating in a 2D configuration. Results highlighted that the manufacturing process has an impact on the properties of the LSP that will influence the vaporisation mechanism. Therefore, a close study of its structure is necessary before developing any more complex model. The study of the overpressure created by its explosion could not be performed as for the wire, since its complex geometry generates a shock wave that is not cylindrical, preventing the original overpressure at the LSP. We observed however the displacement of the plate on which the LSP was placed. Even if not a quantitative result, this highlighted the significant influence of the paint confinement in the overpressure that builds up on top of the panel, since a free explosion of the LSP led to a negligible displacement involving a limited overpressure.

The work performed in this chapter that provides a pressure law dependency with the lightning current amplitude for ECF195 will be combined with the spatio-temporal vaporisation profile built in the previous chapter. From this combination, we are now able to build a spatio-temporal pressure profile for the mechanical loading of a composite panel. This is an important outcome that will be used in our final chapter 6 in order to replace the lightning solicitation by a mechanical load and predict the consecutive damage in the composite laminate.

In addition to the specific objective of this PhD, this work provides a preliminary framework for the study of electric explosion in a complex geometry such as ECF. The instabilities observed in the metal prior to its explosion need to be studied in greater depth in order to be able to better model the temperature distribution but also the energy deposited in the metal. Predicting the distribution of energy prior to and after the explosion needs to be improved as it has an influence on the pressure shock wave amplitude. For this purpose, the theory proposed by Chung [101] which couples MHD equations with copper EOS should be developed. It would replace the phenomenological model defined in this chapter to relate the explosion pressure with the current and could be expanded to more complex configurations.

Chapter 5

Paint

Objectives

The purpose of this chapter is to study the mechanical properties of the paint and to propose a numerical model for this top layer. The confinement effect of the paint needs to be quantified but the limited amount of data regarding this material led us to develop and perform specific tests for its characterisation.

Comparisons between the characterisation tests and the numerical model are made in order to assess the validity and limit of this model prior to its integration in the global lightning model.
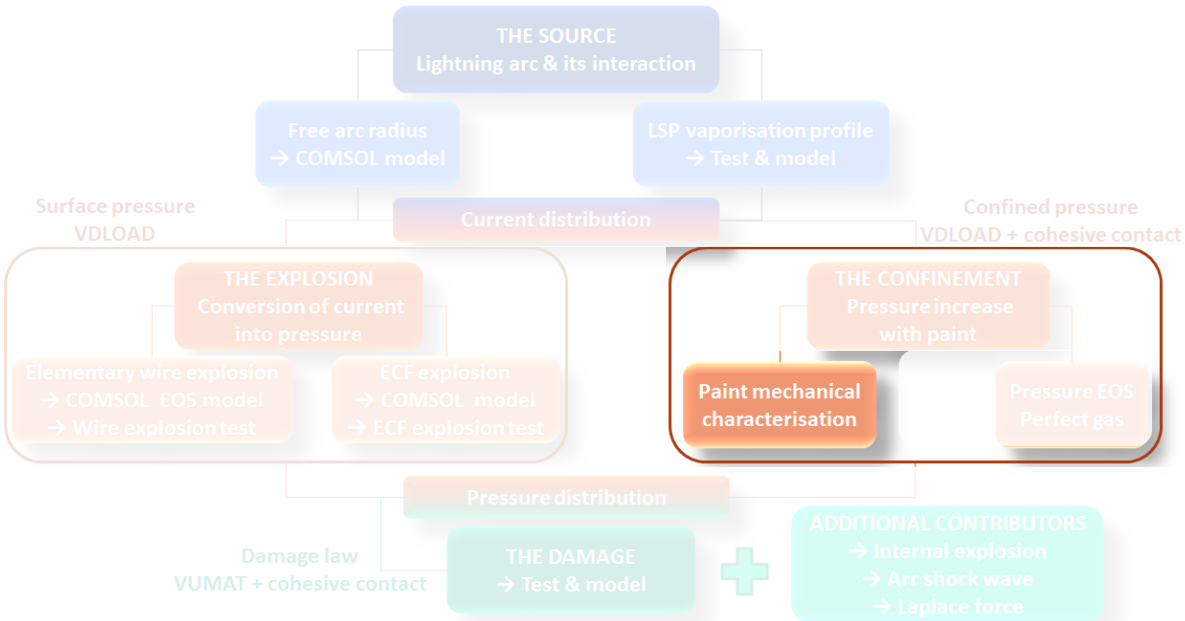
5.1. Paint impact on lightning damage

5.1.1. Introduction

Several forces are involved in a lightning strike and the presence of the paint adds a further complexity to this mechanism. Its presence will have 2 effects:

- Constriction of the lightning arc and modification of the current injection. This effect was studied in Chapter 3.
- Confinement of the surface explosion due to Joule heating in the LSP. The slow ejection of the paint compared to the explosion propagation in the LSP will enhance the overpressure applied on the composite panel and lead to additional damage.
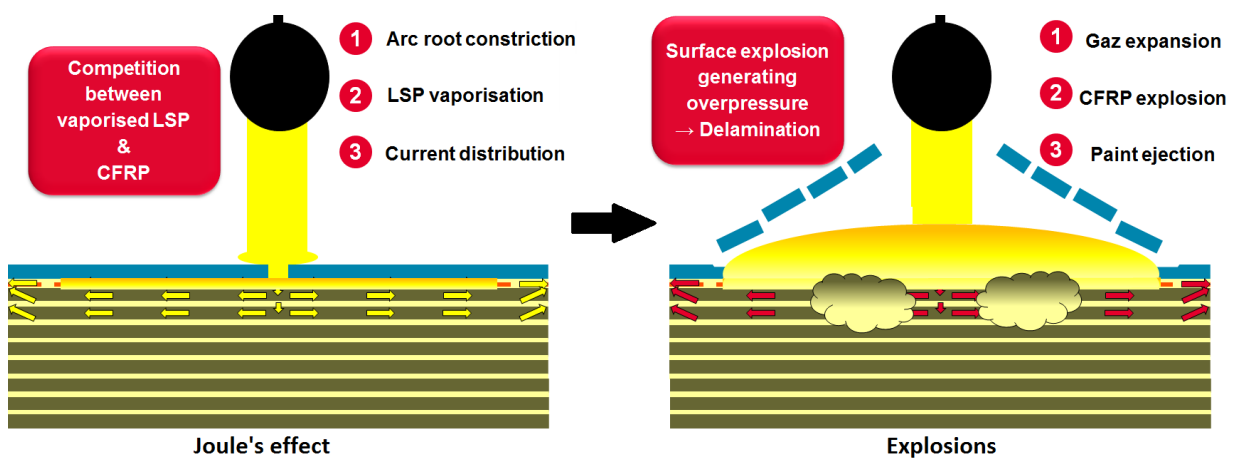
Figure 5-1 Paint impact during a lightning strike

Up to now, very few researchers have considered the paint in their investigations on composite damage due to lightning strike. Its effects were observed by Chemartin [34], especially on the arc root. In an attempt to assess the effect of an overpressure due to the presence of paint on the damage suffered by the composite, Espinosa et al. [28] used thermomechanical numerical simulations and simulated the paint confinement contribution as an equivalent pressure of 5MPa, which is not significant on the stress level suffered by the composite plate in the case of a SCF protection. The first models on a general and physically based computation of the confinement effect due to the paint on the overpressure were developed by Lepetit [29] and then used by Karch [35]. In their approach, the paint is considered as a mass that will have an inertial effect over the explosion and comparison with the test is based on panel deflection only. This 1D approach based on laser shock separates the phenomenon into two phases: a first step in which the shock wave due to the explosion of the LSP propagates into the paint and the composite panel, as shown in Figure 5-2, which lasts less than 1µs due to the propagation speed expected in the medium; followed by a second phase, in which the reflections occur, leading to a momentum in the acceleration of the gap opening.
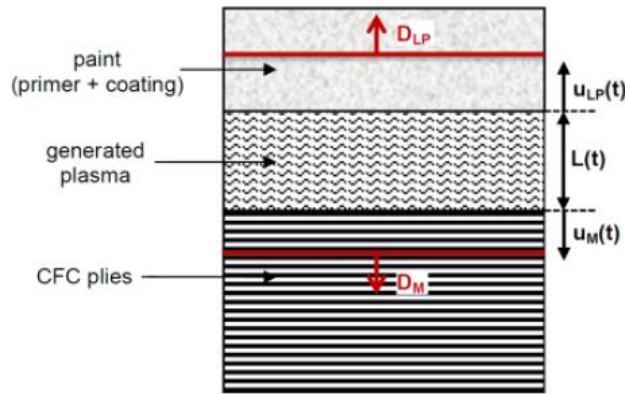
Figure 5-2 Gap opening caused by the explosion

 This approach is interesting but needs to be further developed to consider the physical properties of the paint and not only its mass as they will have an influence on the confinement and associated overpressure. This is examined in the following section.

5.1.2. Lightning test observations

Several lightning tests were performed in order to identify and separate the different effects of the paint in the generation of lightning damage. The first important observation is global and made "post-mortem": The damage in the composite increases with paint thickness, even with a lightning strike protection. Without any paint, the LSP fulfils its function perfectly and is only vaporised by Joule heating. In this configuration, there is no damage to the composite structure. With the presence of paint, damage in the composite can be observed and increases with the paint thickness [104]. Figure 5-3 presents the visual damage and the evolution of delamination with the increase in paint thickness. The total projected delaminated area is provided for each configuration.

	No paint	250µm	400µm	1000µm
Visual				
NDT	No Damage			
	0 cm²	40.2 cm²	119.6 cm²	411.6 cm²

Figure 5-3 Lightning damage evolution in protected composite with paint thickness

In the central area, thermal damage due to the current flow in the composite is visible but the most detrimental and extensive damage is delamination which has a mechanical origin, as shown in section 2.3.2.3. Therefore, if the mechanical damage is increased by the layer of paint on the top surface of the composite, it is expected that it will increase the overpressure generated on the panel and that it will be a significant reason for an increase in damage. There are several possible sources for this enhanced overpressure:

1. Arc constriction leading to an increasing current injection in the composite:
   —> More explosion of the top layers of the composite due to an increase in Joule heating
2. Arc constriction leading to plasma concentration:
   —> Higher temperature and pressure in the arc due to increased current density generating higher thermal and mechanical arc forces (Thermal flux and Laplace forces) applied locally on the panel
3. Surface explosion confinement leading to an increased overpressure:
   —> The metallic gas and composite pyrolysis products cannot expand freely in air due to the presence of the paint on the top. This will slow down the pressure decay and globally increase the spatiotemporal overpressure profile.

In order to assess the weight of these different sources, specific lightning tests were performed.

For the first source, i.e. the CFRP explosion (1), since we cannot measure the pressure generated by a lightning strike, we measured the displacement of the back of 11 GFRP ply (2.75mm) panels protected with LSP, with or without a CFRP ply (127µm) in between, thanks to the DIC method, and painted with 400µm of typical aeronautic white paint. As for other lightning strike tests, the panels were 450mmx450mm square plates clamped on a circular window with a diameter of 370mm using 12 bolts. The added contribution of the explosion of the underlying composite ply to the total overpressure generated by the explosion of the metallic protection was limited: Rear face deflections measured without and with the underlying CFRP ply on top of the GFRP substrate were very similar. First, for the SCF configuration, the amplitudes and shapes of the measured displacement profile around the rear face centre at different instants after the test strike were quasi-identical with or without the CFRP ply. In this configuration, there was no current flowing into the LSP in opposition to ECF, therefore the overpressure was due only to explosion of the LSP. The presence of dry fibre is visible with ECF but not with SCF with 400µm of paint as illustrated in Figure 5-4.
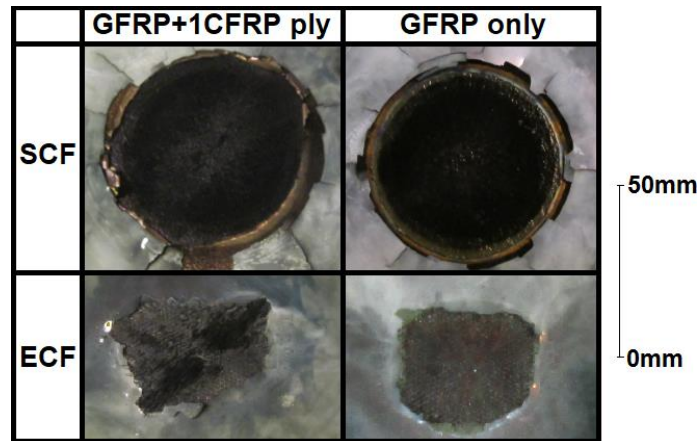
Figure 5-4 Visual damage observation between ECF and SCF with or without underlying CFRP ply

The deflection is not changed by the presence of the CFRP ply. Indeed, the equivalent bending modulus from the laminate theory [105] of the GFRP panel with an additional CFRP ply at 45° is very similar to the reference GFRP panel. If we consider, in a simple approach, an equivalent shell, we can define an equivalent elastic bending modulus E_{fx} in x direction for the composite laminate:

$$E_{fx} = \frac{12}{h^3} \times \bar{E}I_{11}$$

5-1

With h the laminate thickness and $\bar{E}I_{11}$ the laminate equivalent elastic stiffness. From the laminate theory explicated by Gay [105], this elastic stiffness of a balanced laminate can be calculated from the bending stiffness factors C_{ij}:

$$\begin{cases} \bar{E}I_{11} = C_{11} - \dfrac{C_{12}^2}{C_{22}} \\ C_{ij} = \displaystyle\sum_{k=1^{st}ply}^{n^{th}ply} \bar{E}_{ij}^{\ k} \dfrac{(z_k^3 - z_{k-1}^3)}{3} \end{cases}$$

5-2

The factor C_{ij} is dependent on the laminate distribution, ply orientation and property $\bar{E}_{ij}$ of each ply. The location of the ply k in the laminate depth is identified by z_k and z_{k-1}, respectively the top and bottom height positions of the ply in the laminate with the origin located in the medium plane. This stiffness coefficient $\bar{E}_{ij}$ (i,j=1..3) is a projected value of the ply coordinate system (l,t) in the global coordinate system (x,y) of the ply elastic modulus as presented below:

$$\begin{Bmatrix} \sigma_x \\ \sigma_y \\ \tau_{xy} \end{Bmatrix} = \begin{bmatrix} \bar{E}_{11} & \bar{E}_{12} & \bar{E}_{13} \\ \bar{E}_{21} & \bar{E}_{22} & \bar{E}_{23} \\ \bar{E}_{31} & \bar{E}_{32} & \bar{E}_{33} \end{bmatrix} \begin{Bmatrix} \varepsilon_x \\ \varepsilon_y \\ \gamma_{xy} \end{Bmatrix}$$
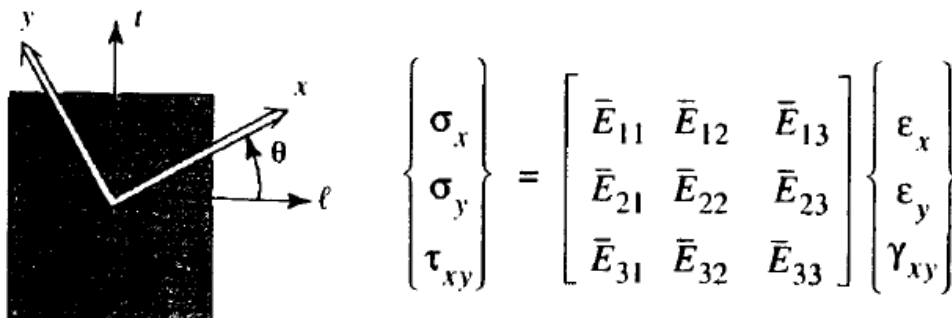
Figure 5-5 Elastic relationship projection in the global coordinate system [105]

For the assessment of the equivalent elastic bending modulus E_{fx}, we need to compute the factors ($\bar{E}_{11}$, $\bar{E}_{22}$, $\bar{E}_{12}$) for each ply orientation θ :

$$
\begin{cases}
\bar{E}_{11} = c^4 \bar{E}_l + s^4 \bar{E}_t + 2c^2 s^2 (\nu_{tl} \bar{E}_l + 2G_{lt}) \\
\bar{E}_{22} = s^4 \bar{E}_l + c^4 \bar{E}_t + 2c^2 s^2 (\nu_{tl} \bar{E}_l + 2G_{lt}) \\
\bar{E}_{12} = c^2 s^2 (\bar{E}_l + \bar{E}_t - 4G_{lt}) + (c^4 + s^4) \nu_{tl} \bar{E}_l
\end{cases}
\qquad \text{5-3}
$$

with $\bar{E}_l = E_l/(1 - \nu_{tl}\,\nu_{lt})$, $\bar{E}_t = E_t/(1 - \nu_{tl}\,\nu_{lt})$ and c=cos θ , s=sin θ.

If we neglect that the laminate is not fully balanced with the addition of the CFRP ply on the GFRP substrate, we can calculate the bending modulus with the same approach. The GFRP plate presented a bending modulus of 24GPa and the addition of the CFRP ply change the modulus to 27GPa which is only 12% higher. The assessment of the laminate behaviour based on the flexion is limited but it provides a first framework of comparison to study the influence of such a configuration. A similar approach was used by Soulas [57] considering an equivalent bending stiffness factor, as the mean value of C_{11} and C_{22}, in order to compute an equivalent impulse.

For the ECF configuration, the influence of the presence of a CFRP layer changes the maximum amplitude of deflection slightly but also the span. The maximum deflection is lower, possibly because part of the current has been diverted to the CFRP which decreases the explosion pressure of the LSP in this area. This is illustrated in Figure 5-6 below on the right hand side.
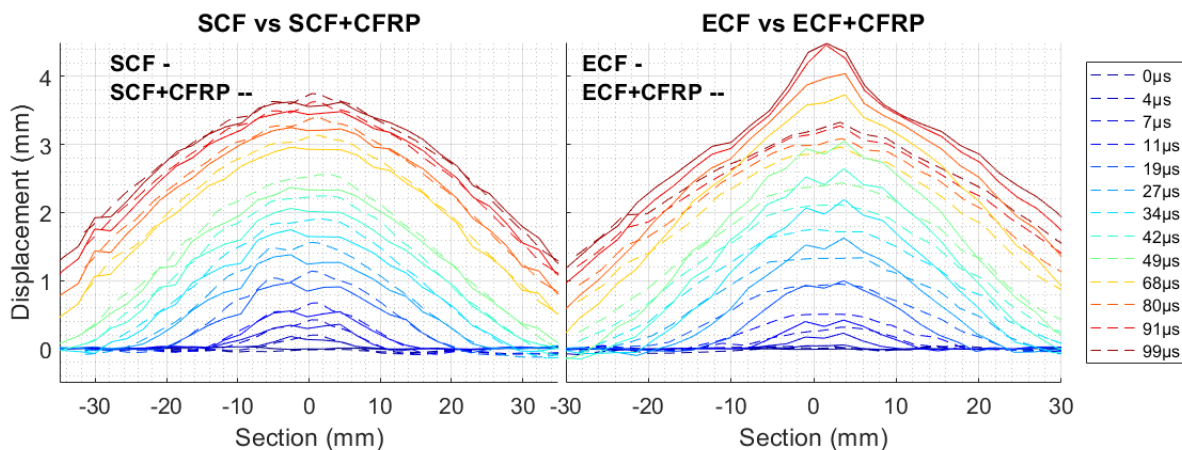
Figure 5-6 CFRP explosion influence on total deflection (Bump due to stereocorrelation defect during test)

With these test results, we can generally, in a first stage, neglect the contribution of the CFRP explosion (1) in the overpressure generation that will contribute to the mechanical damage. In addition, we neglect the internal damage of the CFRP due to Joule heating.

Regarding the second source which is the increased mechanical forces due to the concentrated arc (2), its influence is considered negligible. No specific tests were performed due to the difficulty in differentiating this contributor from the other ones. Therefore, a theoretical analysis is proposed. The magnetic forces are negligible (<1MPa) compared to the explosion due to the LSP, as shown by Karch [35]. The expected maximum overpressure

peak due to ECF explosion, empirically quantified in 4.2.1.4, is more than 100MPa. Therefore, an increase in the magnetic pressure from the arc will have a limited influence compared to the LSP explosion. Likewise, the pressure in the arc is a few MPa as shown by ONERA [77] and illustrated in Figure 3-2, which is also negligible compared to the explosion.

With these observations, we can also neglect the contribution of the arc forces (2) in the overpressure generation that will contribute to the mechanical damage. In addition, we neglect the internal damage of the CFRP due to direct heat transfer from the arc.

Lastly, the confinement effect of the LSP explosion by the paint (3) was assessed by testing panels made of GFRP. The main interest of glass material is that it is highly insulating, therefore no lightning current will flow in this layer and internal explosion is thus avoided. The influence of the paint is clearly visible in Figure 5-7 showing the out-of-plane rear face displacement at the centre of the panels for a top painted (400μm thick) and an unpainted panel protected with ECF195.
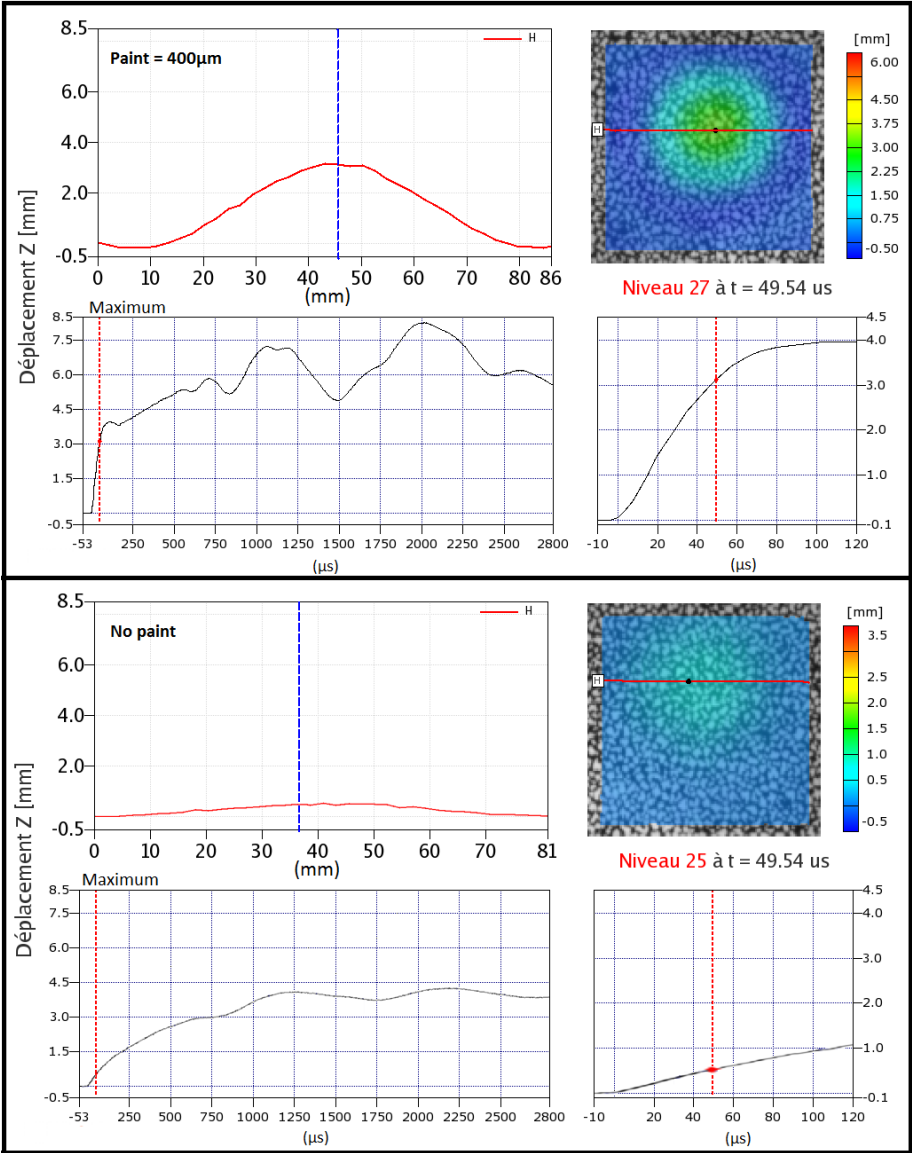
Figure 5-7 Image correlation data at 49μs: comparison between painted and unpainted panels (GFRP+ECF195)

The comparison during the first 100μs highlights even more the difference in behaviour due to the presence of paint, since the maximum displacement when there is no paint (below 1mm at 100μs) can be considered as almost negligible, whereas the painted sample presents a "sharper" displacement history with a higher acceleration. The maximum amplitude of displacement reaches almost 4mm at 100μs. Free oscillations of the panels can be seen from 750μs, with about the same frequency of about 1140Hz for both panels, but a higher amplitude for the painted panel (about 2mm) compared to the unpainted one (about 0.25mm). This appreciable difference in the displacement testifies to higher pressure profile amplitude that could be mainly due to the confinement of the explosion and induced effects.
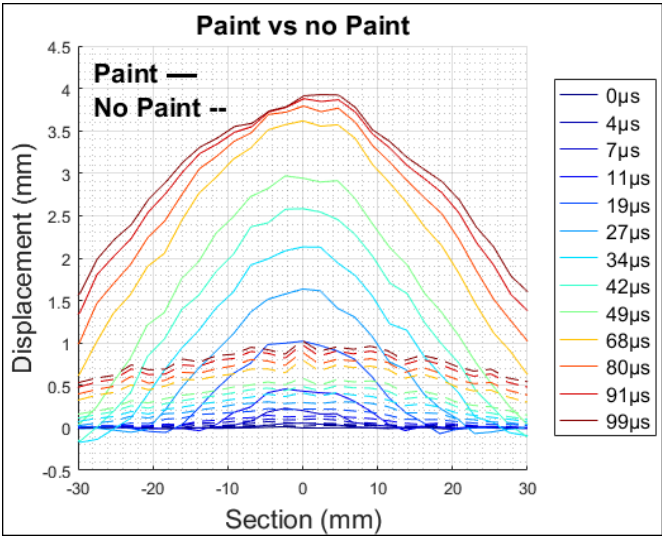
Figure 5-8 Displacement profile comparison: Paint vs no Paint

It is therefore very important to understand this confinement of the explosion but it can unfortunately not be tackled as solely a mass effect of the paint. The study of the influence of different coatings instead of paint revealed very different behaviours. The materials considered are presented in Table 5-1:

	Paint	Tufnol ®	Sticker	PVC
Density (g/cm^3)	1.44	1.36	1.3	1.38
Material	Polyurethane	Synthetic Resin Bonded Fabric	Polyurethane	PVC
Literature Young's Modulus (GPa)	0.04-0.6 [106]	6.3 [107]	0.04-0.6 [106]	3 [108]

Table 5-1 List of coating materials

These materials were chosen because of their similar density but different apparent mechanical and thermal properties. Aeronautical paint is quite soft, easily bended and torn. The sticker is quite similar but melts at a lower temperature and seems softer, whereas Tufnol® material is quite rigid and brittle. Lastly, the elastic property of PVC is intermediate between that of paint and Tufnol. The thickness of all the coatings in the configurations tested was 400μm. The panels are 450x450mm² panels clamped using 12 bolts on a 370mm diameter metallic rigid window. As presented in Figure 5-9, the damage resulting from a

lightning strike on identical 13-ply CFRP composite panels, protected with ECF195, was very different in severity as regards delamination but also surface thermal damage. Yet, the mass of the different coatings during the tests was of the same order of magnitude, because of the same densities and thicknesses. C-scans were taken from the rear face only because of the high thermal damage on the front face. They were compared with pictures of external damage. Black frames were added on the C-scans to help comparisons, taking into account the fact that C-Scans should be right-left reversed to be set in the top view of the pictures.
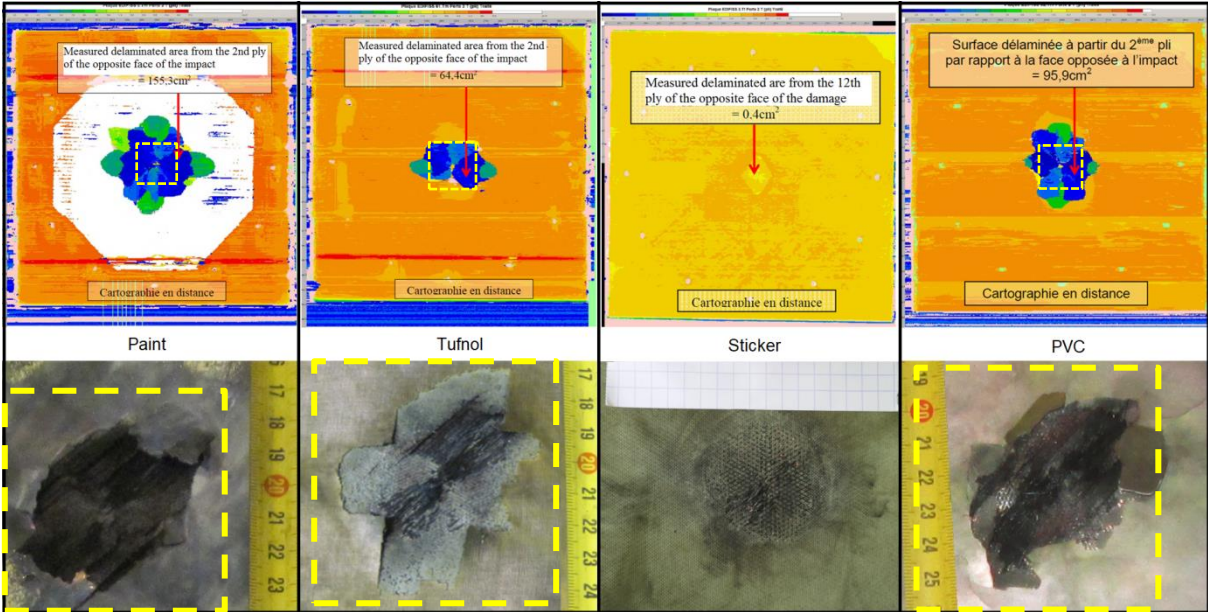
Figure 5-9 Coating type influence on lightning damage with front picture of the visual damage and reverse C-scan pictures

The damage distribution is summarised in Table 5-2:

	Paint	Tufnol ®	Sticker	PVC
Shape of area	Ellipsoid	Cross	Circle	Ellipsoid with flakes
External Dimensions	3.9x6.3	2.9x7.8 X 2.5x6.4	N/A	3.7x6
Ejected or burned area of layer (cm²)	77	32	N/A	70
Total delaminated area (cm²)	155.3	64.4	0.4	95.9

Table 5-2 Summary of coating type influence on lightning damage

The ejection of the paint has a strong influence on the release of the arc root (1 & 2) and on the confinement of the surface explosion underneath (3). This ejection is dependent on the mechanical properties of the coating, i.e. its ability to sustain the underlying overpressure before breaking, but also on its adhesion on the substrate apart from the vaporised layer. For this purpose, the mechanical characterisation of the paint is necessary and is presented in the following section.

5.2. Paint characterisation: State of the art

For aircraft applications, an extensive set of material specifications is defined [109]. The paint is made from 2 components: the base and the hardener. The first part of the specifications concerns the physical and chemical properties of the individual components of the paint such as the density, the water content, acid, amine and hydroxyl indices, flash point, viscosity, etc. The second part concerns the physical properties of the liquid paint before application: drying time, viscosity, pot life, volatility, etc. A final part concerns the dry film properties with cosmetic requirements such as colorimetry or surface roughness, but also many tests to assess its resistance to the aeronautical environment (water, hydraulic fluids, solvents, kerosene, toilet fluid, humidity, salt spray, cycling temperature…), as no blisters or cracks should be produced. Very few specifications concern the mechanical properties of the paint. As explained above, it is important to define these properties of the paint in order to assess its confinement effect. Unfortunately, as its main function is cosmetic, only qualitative tests are required to qualify the paint for aeronautical applications. The adhesion is estimated empirically following ISO 2409 [110]. An adhesive tape is applied on the paint that has been previously crosscut with a grid pattern. The tape is then removed from the paint, and if there are no loose parts, the test is passed. The procedure is shown on Figure 5-10:

Figure 5-10 Paint crosscut test

The resistance to impact is assessed based on ISO 6272 [111] where an indenter is pushed by a falling tube and impacts the paint. It is therefore assessed if any cracks occurred. The resistance to scratch is also measured with ISO 1518 [112] where the test is passed if no penetration occurred with the scratch stylus loaded with 1500g. Finally, the flexibility (ISO1519 [113]) is tested by the progressive bending of a cylindrical mandrel where no peeling or cracks should be produced. All these tests are useful to determine the durability of the paint in a highly constraining environment but none provide quantitative values for its mechanical or adhesive properties.

5.3. Properties and the corresponding tests chosen

The bulk properties of the paint need to be assessed in order to build an adapted model for its behaviour under lightning solicitation. In a first approach, a DMA (Dynamic Mechanical

Analysis) test was used to assess the paint properties. As will be detailed in 5.4.1, this procedure is useful to determine the elastic and inelastic Young's moduli on a wide range of temperature with a dynamic constraint. Polymers, like the paint, can have several glass transition phases which can greatly influence their strength. It is therefore also important to assess the stability of the mechanical properties with temperature.

In addition, tension tests were performed. These are developed for stickers which have, of course, different applications, but it is the closest configuration existing for which some quantitative tests are defined. In order to assess the tensile properties, the ISO 527 [114] norm defining a tension test with a dumb-bell specimen are of great interest for paint. An example of the specimen is shown in Figure 5-11:
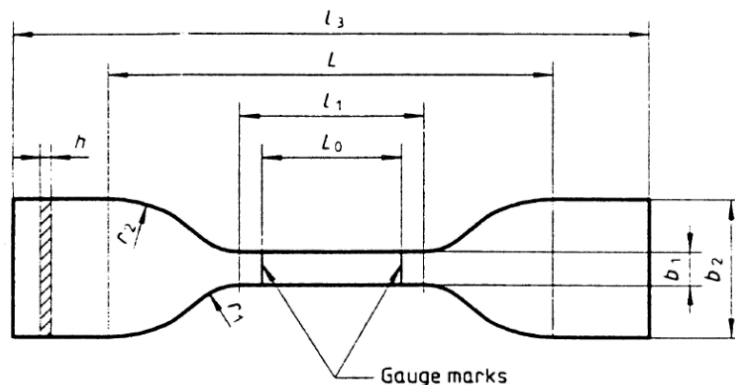
Figure 5-11 Dumb-bell specimen

With this tension test, it will be possible to determine the macroscopic tensile Young's modulus, Poisson's ratio and axial ultimate stress and strain at rupture. These data are also very useful in order to build a stress-strain relation for the paint which is expected to be of a hyperelastic kind [115,116] since aeronautical paints are based on polyurethane which is an elastomer with a visco-hyperelastic behaviour. The paint might thus also present a viscous behaviour, which means that the stress will be dependent on the strain rate. Unfortunately, there is no machine either for tension or DMA that reaches the level of solicitation (up to $1mm/10\mu s=6.10^{5}mm/min$) created by the underlying explosion below the paint, as can be estimated from figures 5.4 to 5.6. Therefore, this parameter was not measured.

In addition, during a lightning test, the paint is torn into several pieces. It is thus interesting to measure its tear resistance which is the force necessary to propagate an existing crack. A test method based on ISO6383 [117] for sheets was used for the paint measurement.

An important point to attend to is the fact that the mechanical properties of thin films may be nonlinear with the thickness. It was therefore important to manufacture samples with different thicknesses and consider them as different materials.

Another important parameter to study is the adhesion of the paint on the substrate, as this could change the kinematics of its removal during a lightning strike. The adhesion of the paint above the exploded LSP is not under question since there is no substrate for it to stick

to anymore; however, as it is pushed by the underlying explosion of the metallic protection, the paint could be disbonded in the front of the explosion instead of breaking into small pieces, which could change the confinement. The following norms were used to determine the peel resistance for high strength adhesive bonds: ISO4578 [118]. Figure 5-12 shows the principle of the test:
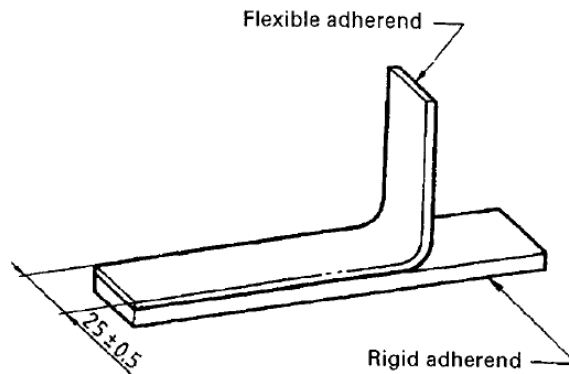
Figure 5-12 Adhesion test

Due to the difficulty of manufacturing a paint layer with a pre-existing crack from its substrate without deforming the dry layer, this test method was not used, and another method to measure the adhesion was investigated, based on the double lap shear joint test. The principle of this method is to double lap the composite sample with paint at the joint. However, the low viscosity of the paint prior to its polymerisation makes manufacturing of such samples difficult with a poor paint matter quality at interfaces. The paint film high flexural compliance made also very difficult the reproducibility of crack initiation at the paint interface. The stiffer and more brittle composite substrate leads to considerable variability in the results as its interfaces were the first broken. Instead, we used a high speed solicitation which is closer to our problem. A shock wave was generated by a laser on the bare composite sample and the disbonding of the paint applied on the opposite side was measured. This method is detailed in 5.4.5.

5.4. Mechanical tests

5.4.1. Manufacturing

A key challenge for the mechanical characterisation of the paint is to manufacture a free paint film as the paint is made to be applied on a substrate and is highly adhesive. The substrate usually has a high stiffness compared to the paint and this will interfere with determining the mechanical properties of the paint itself. Therefore, a specific manufacturing procedure needs to be used in order to be able to strip the paint film from its substrate. The preparation of the different paint layers followed the procedure defined in ASTM D4708 [119] where the use of a release film is proposed to ensure paint stripping when dried. The type of film needs to be chosen to ensure that the paint will uniformly cast on the film without any defects. In our case, we used film made for unmoulding composite

plate. A minimum quantity of paint must be applied for the surface to be sufficiently wetted. If not, the paint will generate localised drops.

Another challenge when manufacturing the paint film is the uniformity of the thickness and its control. The paint is sprayed with a gun by sweeping above the surface to be covered; the speed of the gun, the number of passes of the gun, its delivery rate and the viscosity of the paint will influence the final thickness of the film. Also, the thickness of the dry film will be different from the wet film due to the release of volatile compounds during polymerisation. Several methods are proposed in ASTM D823 [120] in order to ensure a constant thickness but many are based on expensive tools. Thus, manual application (referred to as practice D in the standard) was used. It is difficult, however, to maintain a constant sweeping speed and delivery rate during the spraying of the paint, and as a result, the paint thickness is variable along the film.

5.4.2. DMA test

In order to characterise polymers, Dynamic Mechanical Analysis (DMA) is classically used as it is well adapted for viscoelastic behaviour. This test method measures the complex Young's modulus E^*, and the shear modulus G^*:

$$\begin{cases} E^* = E' + iE'' \\ G^* = G' + iG' \end{cases}$$

5-4

with $E'=E^*.\cos(\delta)$ and G', the storage moduli, $E''=E^*.\sin(\delta)$ and G'' the loss moduli.

It is also possible to obtain the phase angle δ which gives the limit between a pure elastic behaviour where the stress is proportional to the strain ($\delta=0$ and $\sigma=E\varepsilon$) and a pure viscous behaviour where the stress is proportional to the strain rate ($\delta=\pi/2$ and $\sigma=Kd\varepsilon/dt$). During the DMA test, a sinusoidal stress σ is applied on the sample and the strain ε is measured.

$$\begin{cases} \sigma(t) = \sigma_0\sin(\omega t + \delta) \\ \varepsilon(t) = \varepsilon_0\sin(\omega t) \end{cases}$$

5-5

with t the time and ω the excitation frequency.

The tangent of the phase angle is therefore determined by the ratio of the loss modulus E'', which represents the viscous part where the energy is dissipated as heat, and the storage modulus E', which represents the elastic part where the energy is stored in the material: $\tan\delta=E''/E'$.

Another interest of DMA is to determine the glass transition temperature T_g. Polymers can present several transitions with the temperature where the stiffness of the material decreases dramatically and the viscosity is increased. This is important information in order to know the stability of the behaviour in the temperature range studied. The temperature can be slowly swept in order to determine this transition.
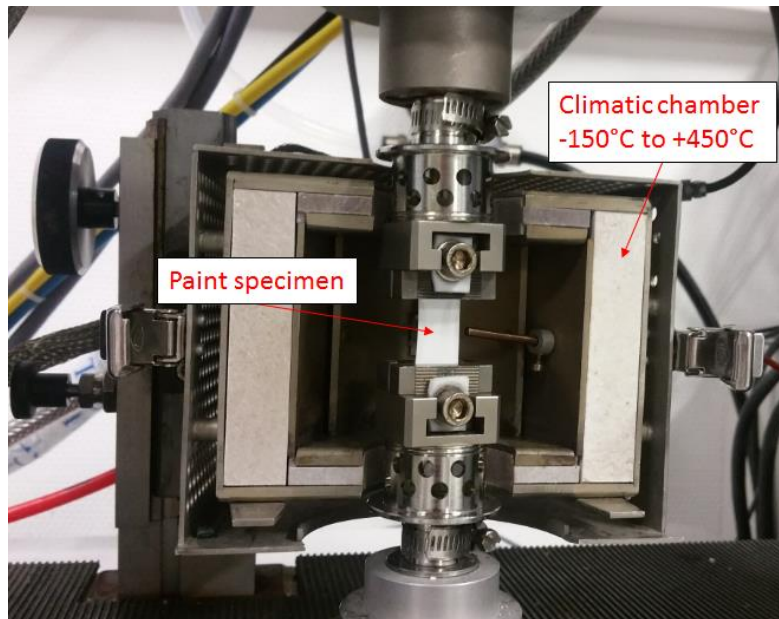
Figure 5-13 DMA test set up

In this test campaign, a Metravib DMA+ 150 was used to perform tension tests controlled in displacement. The size of the sample is provided in order to deduce the strain and the stress from the force and displacement measurement (30 mm x 5 mm). The test conditions used to characterise the paint are given below:

- Temperature range: -60°C (Aircraft environment lowest temperature) to +150°C (Instrument limit)
- Ramp temperature: 2°C/min (In order to ensure a stabilised temperature for the measurement)
- Frequency: 10Hz (Maximum solicitation possible with DMA)
- Displacement amplitude: 5µm

In order to assess the influence of paint thickness, several thicknesses were tested: 100, 300, 400, 500 and 900µm. For each configuration, 3 samples were tested.

As expected, the behaviour differed with the different film thicknesses but the differences cannot be attributed only to this parameter. The final properties of the paint can be influenced by the environment (Temperature, pressure, air humidity…) during the manufacturing and curing process since it can influence the chemical content of the dry film through solvent evaporation. Also, even if the usual curing process lasts 7 days at 23°C, solvent evaporation is not over and curing continues. Therefore, mechanical properties can be modified [121]. Even for identical paint and film thickness, differences were observed which makes a final assessment of the mechanical properties difficult. Still, the trend is the same for the different paint films:
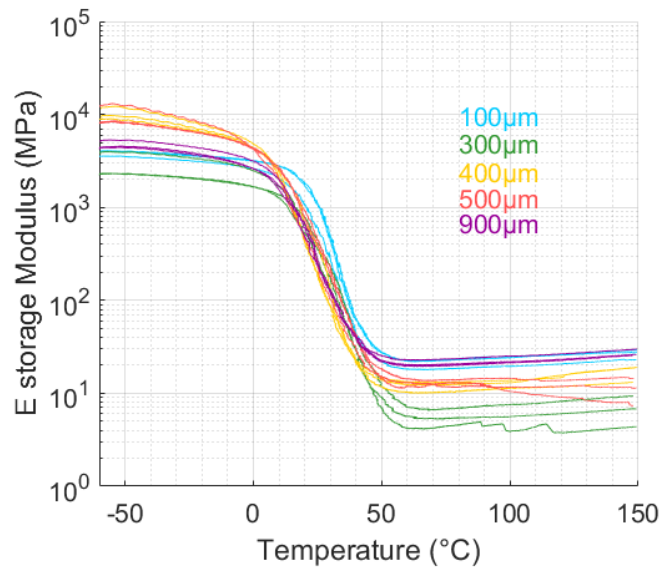
Figure 5-14 Paint storage modulus vs temperature

Unfortunately, the glass transition occurs close to room temperature which means that the paint properties change significantly in this range. Measured Tg is around 36°C±10% but the phase transition is not sharp and starts at about 10C°, ending at about 60°C (Figure 5-14). It is also illustrated by the evolution of tanδ versus temperature, where the maximum indicates the glass transition temperature. It is also noticeable that except for 300µm thick samples, the tanδ peak seems to decrease when the thickness increases.
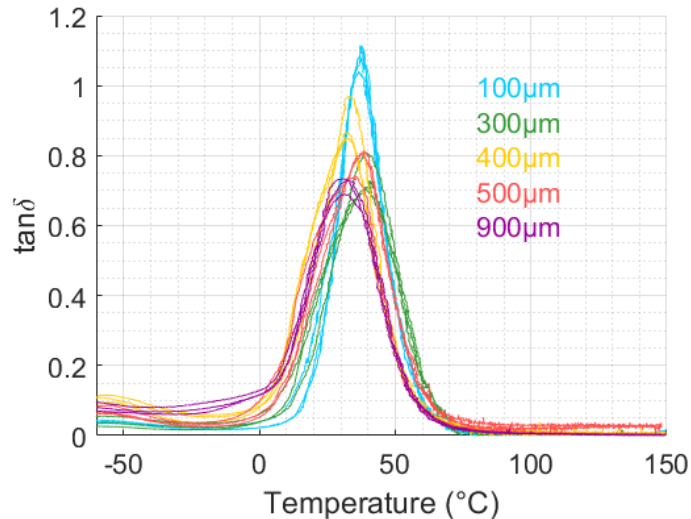
Figure 5-15 Phase angle tangent vs temperature

In a lightning laboratory hall, the temperature is not fully regulated and, depending on the season, can vary between 18 to 30°C.

This variability of more than ±50% could explain some of the differences observed after a lightning test with identical properties and lab test procedure.
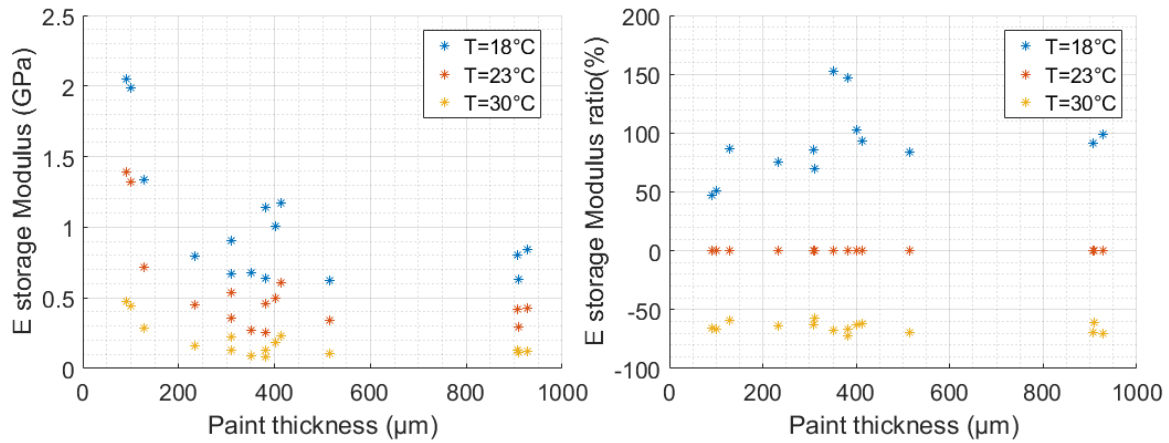
Figure 5-16 Storage modulus variation at room temperatures

During a lightning test on the contrary, the arc and the LSP vaporisation produce a high and fast temperature rise but due to the fast paint ejection, it is considered that the heat transfer is slow compared to the mechanical physics. Consequently, it should be pointed out that the paint properties have no time to change significantly before the ejection of paint flakes, and so the properties of the paint can be considered at room temperature, and the paint is assumed to have no time to behave in a viscous way.

5.4.3. Tension test

In order to characterise the strain/stress at break but also to analyse the behaviour of a polymer film in tension, a tensile test is usually performed on a dumb-bell shaped sample. The principle of the test defined in ISO 527 ([114,122]) is to elongate the sample at a constant speed until its failure. During the test, the elongation and the load are measured. Engineering stress and strain can be simply deduced with the use of an extensometer. The principle of the extensometer is to measure the length evolution from the measurement of the distance between two gauge marks chosen in the narrow portion of the sample. The recommendation in the ISO standard for the shape of the sample is to consider type 5 for material with high strain at break, which is what is expected for polyurethane paint.

b_1	Width of narrow parallel-sided portion: 6 mm $\pm$ 0,4 mm
b_2	Width at ends: 25 mm $\pm$ 1 mm
h	Thickness: $\leqslant$ 1 mm
L_0	Gauge length: 25 mm $\pm$ 0,25 mm
l_1	Length of narrow parallel-sided portion: 33 mm $\pm$ 2 mm
L	Initial distance between grips: 80 mm $\pm$ 5 mm
l_3	Overall length: $\geqslant$ 115 mm
r_1	Small radius: 14 mm $\pm$ 1 mm
r_2	Large radius: 25 mm $\pm$ 2 mm
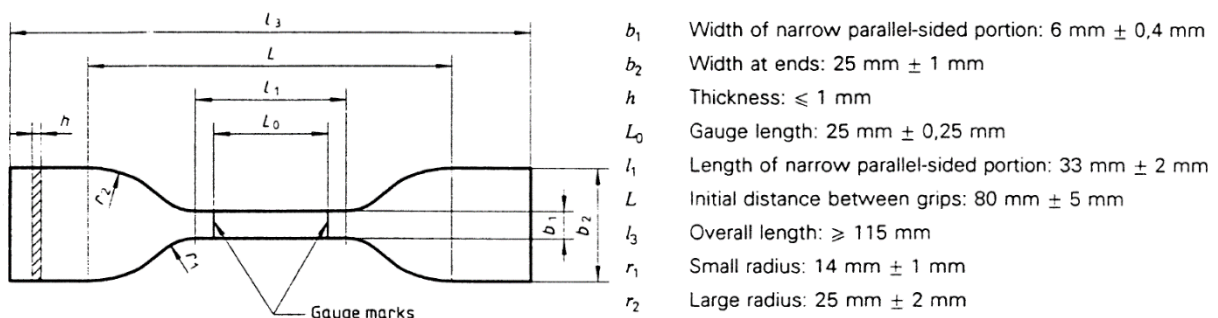
Figure 5-17 Type 5 specimen

Therefore, the longitudinal engineering strain ε and stress σ can be defined as follows for small perturbations:

$$\begin{cases} \sigma_{ing} = F/S_0 \\ \varepsilon_{ing} = \Delta L/L_0 \end{cases}$$

<div align="right">5-6</div>

with F the measured force (N), S_0 the initial cross-section of the specimen (mm²), L_0 the initial length between the gauge marks (mm) and ΔL the gauge length increase (mm).

Since the elongation is large, we need to consider the section modification which is not negligible in order to get true strain and stress. In this case, the true strain is the integration of the tiny displacements at all points along the path:

$$\varepsilon = \int_{L_0}^{L_f} \frac{dl}{l} = ln\left(\frac{L}{L_0}\right) = \ln\left(\frac{L_0 + \Delta L}{L_0}\right) = ln(1 + \varepsilon_{ing})$$

<div align="right">5-7</div>

If we consider the strain in a constant volume, therefore $S \times L = S_0 \times L_0$. Based on this hypothesis, the true stress is defined as follows:

$$\sigma = \frac{F}{S} = \frac{F}{S_0} \times \frac{L}{L_0} = \sigma_{ing} \times (1 + \varepsilon_{ing})$$

<div align="right">5-8</div>

In this test campaign, an Instron 5900R was used to perform a tension test controlled in displacement. A measurement cell for 10kN was used for the load with an error of ±0.25%. In addition, two cameras with different viewing angles were installed in order to measure the strain in the sample thanks to DIC.
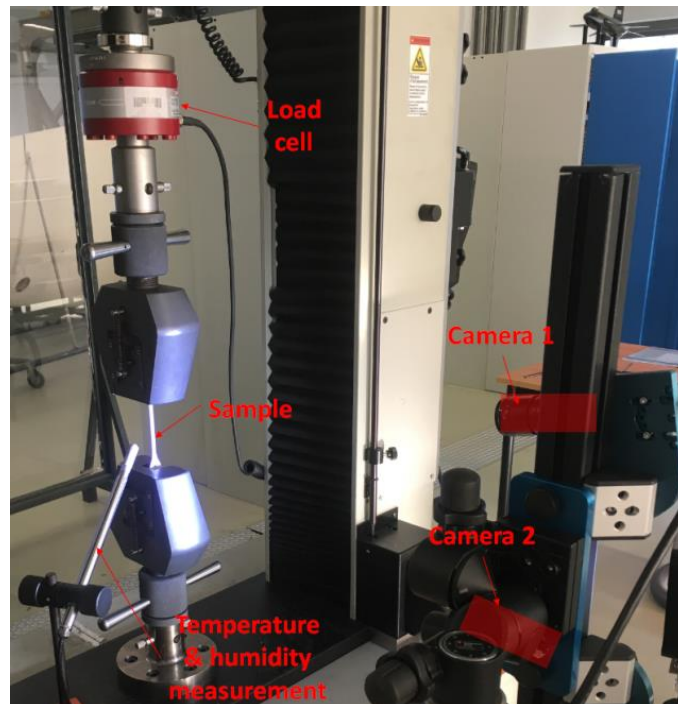
Figure 5-18 Traction test set up

For this purpose, a random pattern made of Indian ink was rolled out on the paint sample as shown in Figure 5-19 below:
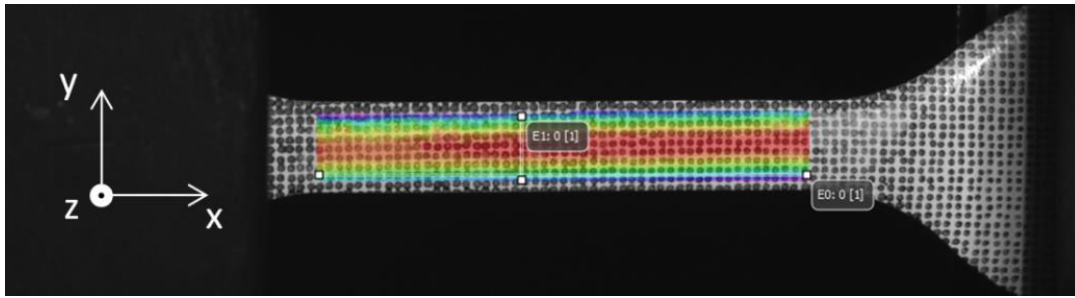
Figure 5-19 Image correlation pattern and measure of Z deformation using VIC 3D (0 to 160μm)

In order to assess the influence of paint thickness, several thicknesses were considered: 100μm, 160/200μm, 350/400μm and 450/500μm. For each configuration, around 10 samples were tested, creating what we have called a family. In addition, two speeds for the prescribed displacement were tested: 4mm/min and 10mm/min.

Within a family, the behaviour was quite similar except for the force at rupture, the latter being possibly explained by small defects in the samples. Force-displacement curves were different between families which can be partially explained by the difference in thickness, except if we consider families 3 and 4. Indeed, with an increased thickness, the resulting force is increased for the same displacement. Engineering stresses and strains were then computed using the classical formula 5-6.
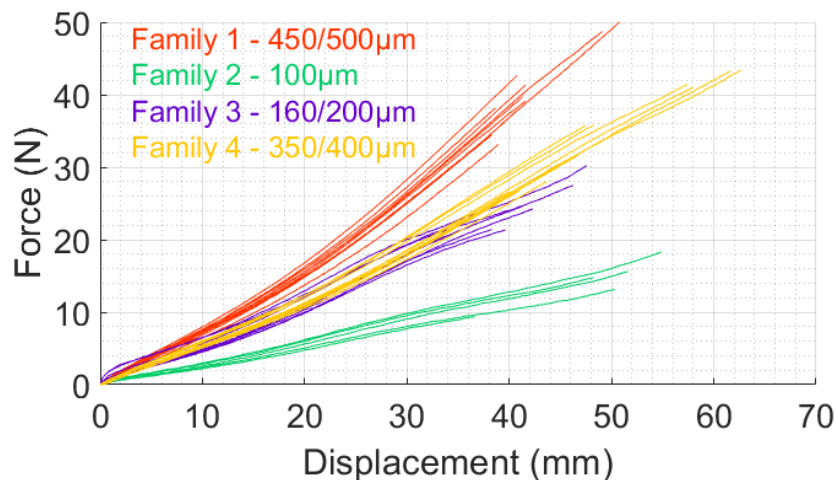
Figure 5-20 Instron measurement - Force vs displacement

Using these measurements, the axial strain is obtained thanks to the extensometer function proposed in VIC-3D DIC system which supports the analysis of the image correlation pictures. But it was not expected to have different stress-strain laws as is visible in Figure 5-21. This means that, as observed with the DMA test, the manufacturing process can lead to some variability in the final structure of the polymer. Indeed, Families 1 and 2 were cured at room temperature as is usual for aircraft painting, and Families 3 and 4 were cured in an oven at 75°C during several hours. In addition, the thickness of the paint might have an influence on the homogeneity of the sample after the curing process. Still, the behaviour is similar between the families and can be identified as hyperelastic behaviour.
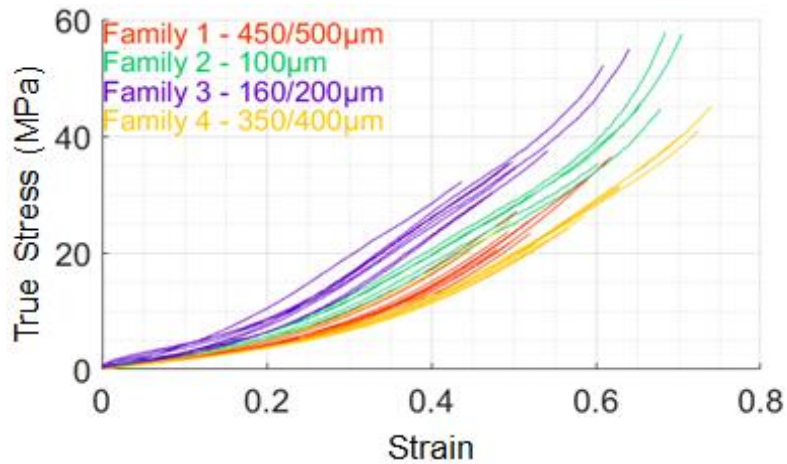
Figure 5-21 True stress vs strain

For the development of our model, only Families 1 and 2 were considered since their manufacturing process is the closest to the one used in industry.

Furthermore, the change of speed for this tension test has a negligible influence in this range, which tends to support our choice not to consider the viscous behaviour of the paint.

Lastly, the maximum stress and strain at rupture present some variability due to sample defects. For family 1, which is our targeted thickness for lightning tests, the mean values at rupture (simple mean over the values in the family) are respectively 26.5MPa (±30%) and 0.52 (±30%).
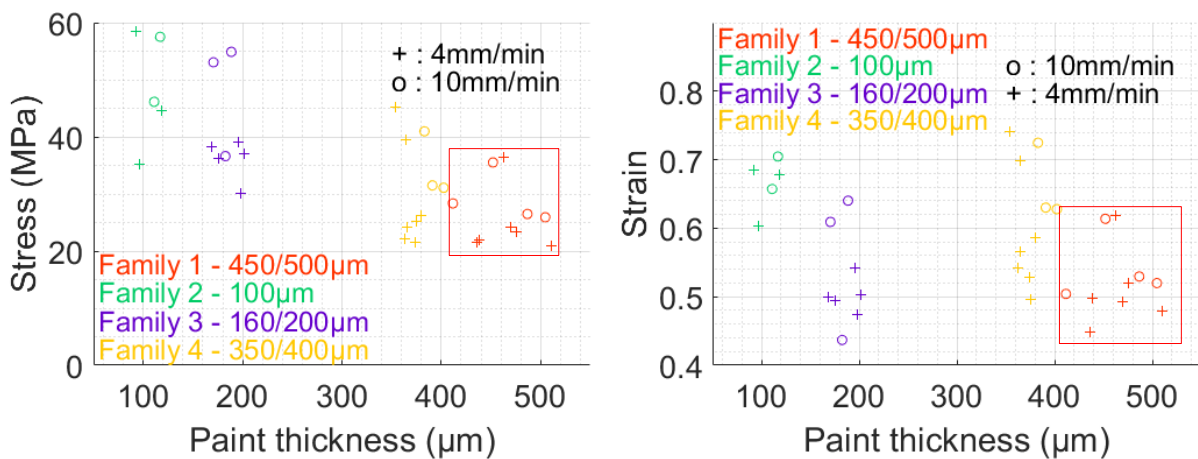
Figure 5-22 Ultimate stresses and strains at rupture in tension

During paint drying time, it was observed that the film was not flat and this was even more visible on the dumb-bell shape samples for the tension tests. Indeed, the drying process is not homogenous in the thickness since the top face is free and the bottom face is on the substrate. This difference will lead to the relaxation of residual stresses after separation of the paint from its substrate first, and then after cutting the samples. A curvature is observed in the tested area. This residual curvature decreases with increasing the thickness as shown in Figure 5-23 for sections in the width, perpendicular to the tensile direction. It is suspected to be due to the flexural rigidity of thicker samples:
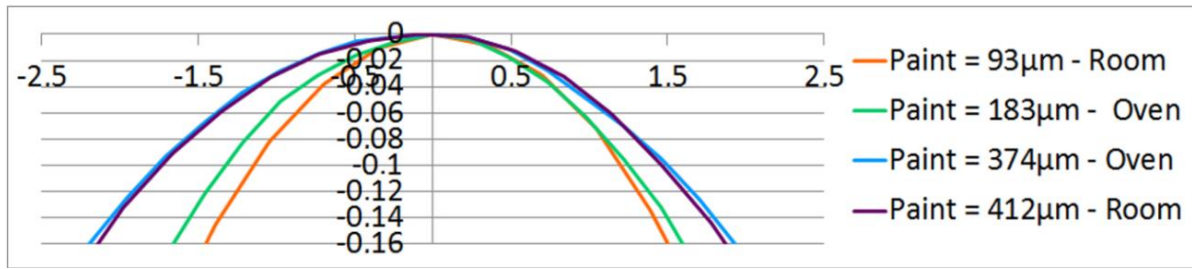
Figure 5-23 Curvature effect with paint thickness

In order to evaluate the influence of this deformation during the tests, we measured the evolution of the curvature. It was concluded that the influence of the curvature is limited, since this curvature did not significantly change during the tests, as shown in Figure 5-24 which shows a section in the width of the sample, perpendicular to the tensile direction. Therefore the stress distribution remains uniform:
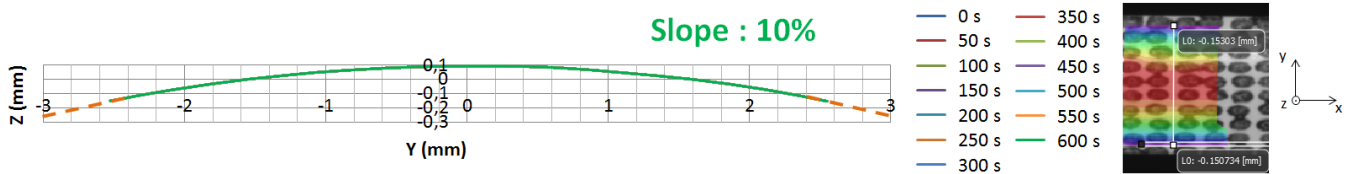
Figure 5-24 Sample curvature

In addition, the image correlation data demonstrate that the strain is stable within the tested central area of the dumb-bell sample all along the tensile test as presented in Figure 5-25 below where the value is constant in the transverse (Y-direction) and relatively constant in the longitudinal (X-direction) i.e. the tensile direction:
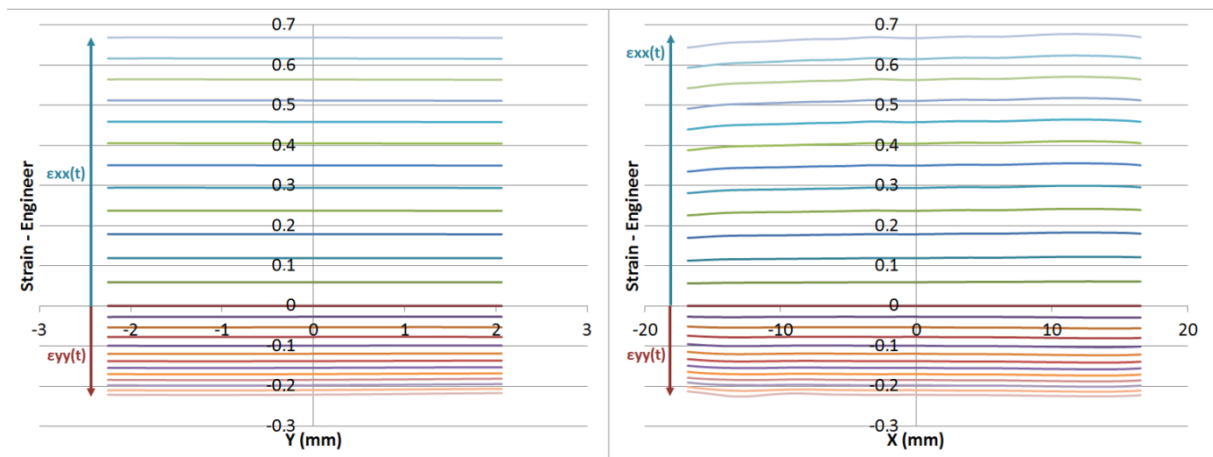
Figure 5-25 Strain homogeneity along x & y direction

It is therefore considered in the rest of the work that the stress is homogeneously distributed in the cross-section of the sample after relaxation and during the tests. Differences between samples are mainly due to differences in manufacturing and to the thickness effect during the drying period.

5.4.4. Trouser tear test

In order to characterise the crack propagation in the paint that will impact the arc release process, we performed a trouser tear test as per ISO6383[117]. The principle of the test is to perform a tension test on trouser legs made by a slit in the middle of the sample. The average force necessary to tear the sample along its whole length is used to assess its tear resistance. The shape of the sample is illustrated in Figure 5-26 below:
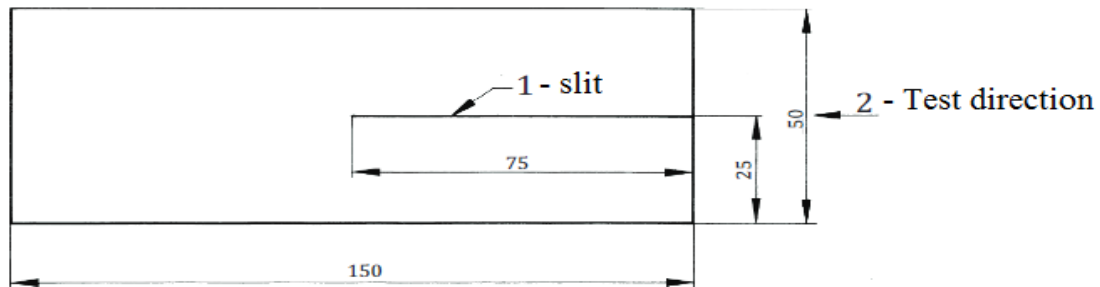
Figure 5-26 Trouser tear sample

The thickness of the sample was measured all along the propagation path of the slit prior to the test in order to check the homogeneity of the thickness and to assess the tear resistance which is the force divided by the sample thickness. The speed of displacement for the traction test was set at 200 mm/min. The force used to compute the tear resistance is the average force measured after the first 20 mm torn and before the last 5 mm to the complete tear of the sample. The setup is presented in Figure 5-27:

Figure 5-27 Tear trouser test set up (Left: Before test/Right: During test)

A first set of data was obtained with a sensor made for a 10kN test for which the sensitivity was not high enough to detect the paint tear resistance. A second set of data was therefore measured with a sensor for 250 N and 1/100 kN of accuracy. An example of force measured during the test is presented in Figure 5-28 where 2 plateaus are visible: the first one before the start of the slit propagation and the second one during the slit propagation.
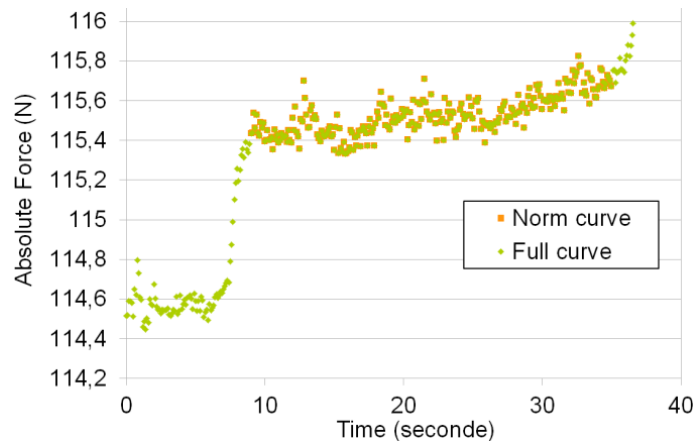
Figure 5-28 Tear trouser test result example

Several films with different paint thicknesses from 200 µm to 500 µm were measured. As for the traction test, the manufacturing process is visible through the results: in the same film extraction, the results are very similar and the paint thickness has a limited impact on the results. About 4 families with 3 to 5 samples each were tested with respective thicknesses of 245/14 µm, 510/28 µm, 240/25 µm and 210/10 µm. From this test campaign, the tear resistance (Force/thickness) obtained for the polyurethane paint was 3.8 N/mm (Standard deviation = 0.25 N/mm) and the propagation stress (Force/thickness*slit propagation length) was 11.5 MPa (Standard deviation = 0.8 N/mm). These very low values demonstrate that the paint will be easily torn once a crack has been created. The results are summarised in Figure 5-29 below:
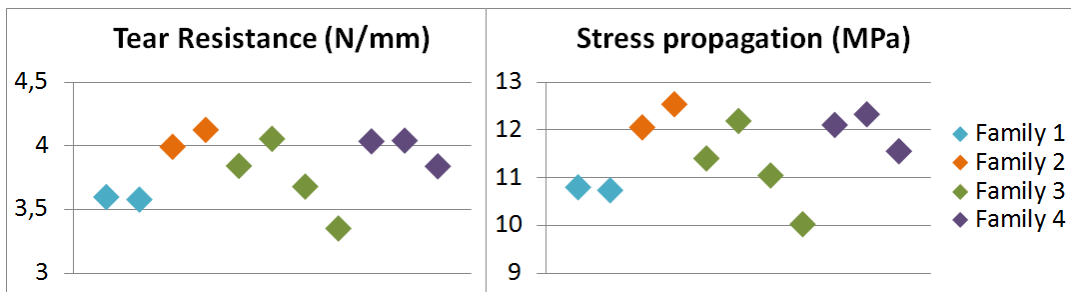
Figure 5-29 Resistance propagation results

5.4.5. Laser test: Interface

The interface between the paint and the substrate, made of CFRP plies and LSP on its external face, is put under a shock solicitation that could break this interface. The adhesion of the paint layer could play a role in the confinement of the LSP explosion. The metallic protection does not explode at one unique time, but it should be considered as a source of multiple explosions which are triggered sequentially from the centre of current injection. Therefore, when the adhesion of the paint layer is poor, it can be disbonded by a lever arm effect from the nearby explosion. In this case, when the underlying protection explodes, it is less confined since the paint is already ejected. The influence of adhesion is illustrated in Figure 5-30 below:
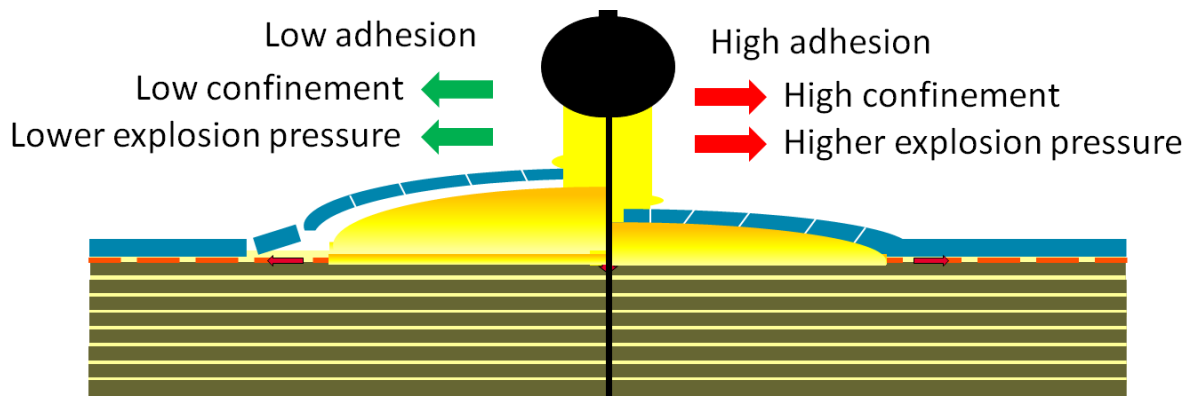
Figure 5-30 Paint adhesion influence on confinement

For this reason, we used a laser in order to generate a shock wave in the laminate and characterise the stress necessary to break the adhesion. This method has been presented by Arrigoni [123] for the characterisation of bonded interface under shock. The propagation of a shock wave in the thickness of a substrate and its reflection at the boundaries will create several shock fronts. The crossing of those fronts will create internal tensile stress that could break the substrate. Figure 5-31 below illustrates this principle for a substrate (right) subjected to a shock from a mechanical impactor (left).
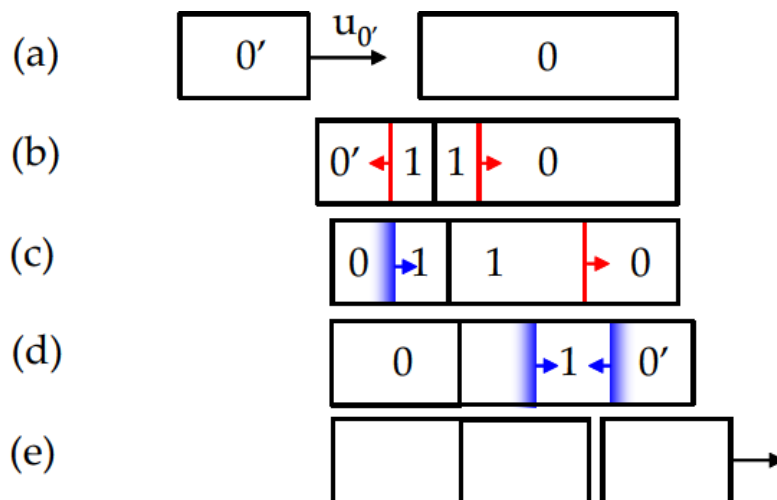
Figure 5-31 Shock propagation with mechanical projectile[124]

This principle can be used similarly to generate traction stress at the interface between the substrate and the paint with a LASer Adhesion Test (LASAT) as illustrated in Figure 5-32 :
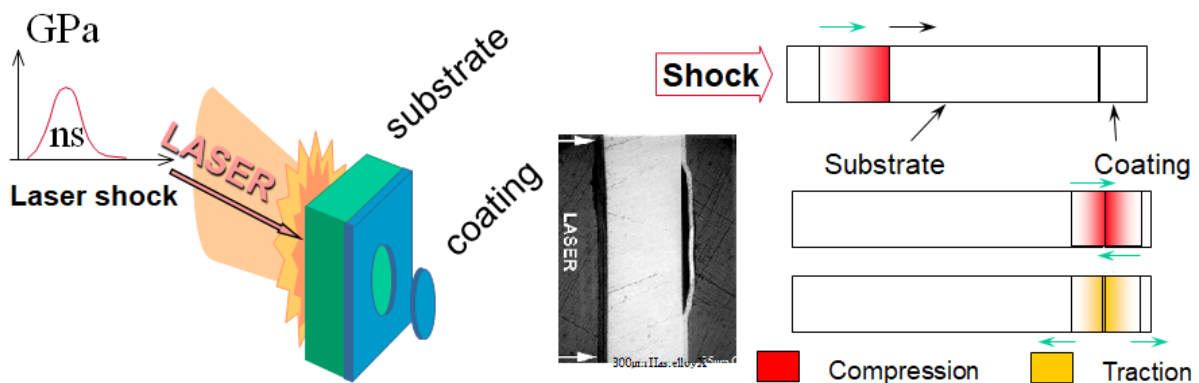
Figure 5-32 LASAT principle [125]

Based on the Rankine–Hugoniot conditions which describe the relationship between the states on both sides of a planar shock wave, it is possible to predict the thermodynamic state of the material after the shock front [125,126]. These conditions, based on the conservation of mass, momentum and energy combined with the Mie-Grüneisen equation of state, are defined by this equation system:

$$\begin{cases} \rho_0 \times (D_{01} - u_0) = \rho_1 \times (D_{01} - u_1) = m \\ p_1 - p_0 = \rho_0 \times (D_{01} - u_0) \times (u_1 - u_0) \\ E_1 - E_0 = \frac{1}{2}(p_1 + p_0) \times \left(\frac{1}{\rho_0} - \frac{1}{\rho_1}\right) \\ D_{01} = c_0 + su_1 \end{cases} \qquad 5\text{-}9$$

with ρ the material density (kg/m³), D the shock front speed (m/s), u the material speed (m/s), P the material pressure (Pa), E the material energy (J), c the material sound velocity (m/s) and s the material constant for the equation of state. The state 0 is before the shock front and the state 1 is after. The shock front propagation is illustrated in Figure 5-33 below:

Figure 5-33 Shock front propagation [125]

With the knowledge of the pressure load on the front and the speed in the back of a sample, it is possible to reconstruct the propagation and reflections of the shock wave in the sample, detect the crack initiation and assess the stress in the material thanks to a shock diagram methodology as illustrated below:

Figure 5-34 Shock diagram [125]

Thanks to the SimChoc company, a laser adhesion test was performed on small square samples (50x50mm) made of different configurations with a composite substrate (CFRP or GFRP), with or without ECF and paint. The laser impacted the carbon face and the speed was intended to be measured on the paint side. The test setup is illustrated in Figure 5-35 below:
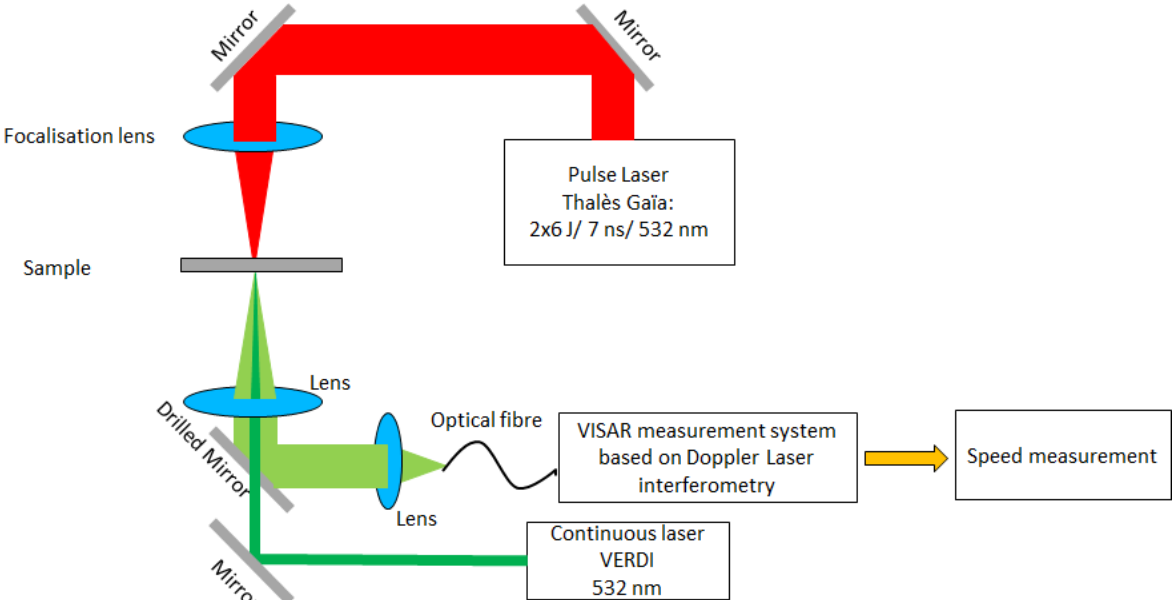
Figure 5-35 Laser test setup scheme from SimChoc

The laser was focused on a disk 4.9 mm in diameter and a layer of water was present on the sample surface in order to confine the laser and increase the pressure load. For some configurations, a trial was done with an aluminium tape on top of the composite surface in order to obtain a more usual interface. The laser flux was set at 7.8 GW/cm² and progressively decreased in subsequent tests in order to find the threshold where there was no disbonding of the paint. The results of the different shots on a configuration of CFRP with ECF195 and paint are illustrated in Figure 5-36 below. The complete detachment of the paint layer occurred for shots 1, 2 and 3 with a laser flux higher than 3.58 GW/m². With shots 4 and 5 at 2.51 and 1.51 GW/m², the paint was slightly disbonded. Finally, below 1.07 GW/m², no detachment could be observed.

Figure 5-36 LASAT test results on CFRP+ECF+Paint(EDIFISS51)

As explained above, several configurations were tested in order to assess the paint adhesion. A summary of the results with paint is presented in Table 5-3 below:

Substrate	ECF	Total sample thickness	Laser focal diameter (mm)	Lowest Laser flux for total paint detachment (GW/m²)	Lowest Laser flux for paint disbonding (GW/m²)	Highest Laser flux for paint adhesion (GW/m²)
CFRP	X	2.1 mm	4.9	1.51	1.07	0.51
		2 mm	4.9	2.52	1.05	0.51
GFRP	X	3.05 mm	4.9	3.57	2.5	1.49
	X	3.05 mm	**2.35**	7.77	5.24	3.03

Table 5-3 LASAT result for paint adhesion

The detachment threshold was identified as the lowest laser flux for slight disbonding. This threshold was identical for a CFRP substrate with or without ECF in between. This can be explained by the fact that the interface with the paint is the same: both CFRP ply and ECF are embedded in resin. This test therefore characterises this interface. However, the threshold is different with the GFRP substrate even if the resin is still the material at the interface with the paint. The increased thickness will absorb the shock front more, therefore a higher laser flux will be needed to generate the same stress at the interface. But the material properties could also influence the absorption of the shock front. Finally, the focal diameter has a linear influence on the threshold: dividing the diameter by two multiplies the threshold by two.

In order to fully analyse these test results, it is necessary to convert the laser flux and focal diameter into a pressure load. The temporal profile of the pressure due to a laser shock on a substrate is dependent on its interaction with the substrate. A preliminary step is therefore necessary to perform additional tests with the substrate only in order to calibrate this pressure profile. For example, a profile for an aluminium substrate was defined, based on the work done by Peyre [127]:
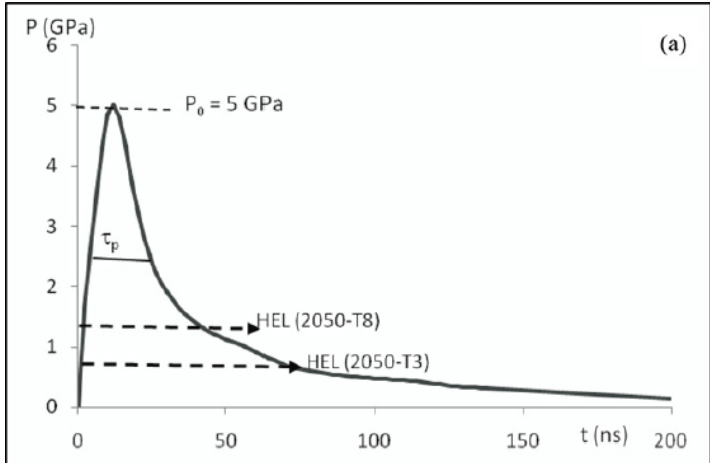
Figure 5-37 Laser pressure profile on aluminium

The maximum amplitude (Pa) can then be related to the laser flux (GW/cm²) as defined by Courapied [128]. For the composite, this will be difficult since the material is not

homogeneous and the resin is consumed during the laser injection, which will disturb the power deposition. An investigation was done with an aluminium tape applied on the sample to reproduce the pressure profile as calibrated for aluminium plate. This would need further work in order to validate the process. Therefore, the pressure load is not yet defined.

Finally, essential information in order to assess the stress at the interface was the speed on the back of the test sample with the method defined above. Unfortunately, the shiny finish of the paint highly disturbed the VISAR measurement and the result could not be used. It is necessary to find a way to obtain a mat surface finish and allow accurate measurements.

The feasibility of this characterisation has been demonstrated and a qualitative approach is possible. In order to obtain quantitative results, it is essential to calibrate the pressure load obtained from the laser shock and to accurately measure the speed on the back of the sample. With this test result, a first analytical approach with a shock diagram would provide an assessment of the stress at break for the interface. In order to take into account the spherical propagation of the shock wave in the material, which is more representative, a 3D mechanical model should be developed with the right material properties of the composite laminate for the Mie-Grüneisen equation of state.

5.5. Model

Aeronautical paints are based on polyurethane, a thermosetting polymer. This type of material has a behaviour similar to that of the rubber family. Therefore, a simple elastic law cannot represent the mechanical response of the paint. Indeed, polyurethane is composed of long chains and a certain amount of crosslinking. Depending on the balance between the two components, the behaviour of the material will change significantly. Long chains with low crosslinking allow very high strain (up to 1000%) since the unfolding segment length is high, whereas short chains with high crosslinking give a very rigid polymer. There are thus as many polyurethanes as chemical compositions for this polymer. For this reason, it is important to develop a specific model for this polyurethane paint. For such a polymer, a non-linear elastic behaviour with incompressibility, strain rate dependency and isotropy is considered. These non-linearities can be explained by the physical deformation of the chain webs in the polymers [115]. Looking at the uniaxial response of polymers, instead of a linear curve in the case of a perfect elastic behaviour, we can observe an S-curve with 3 parts, as illustrated in Figure 5-38:

- A first slope with a small strain (l/l_0) due to the reorganisation of the polymer where the chains' orientation is aligned to the traction direction.
- A second, softer slope where the chains are unfolded thus a small stress is necessary to stretch the material.
- A third and last steep slope where the stiffness is increased since the chains have almost reached their maximum size.
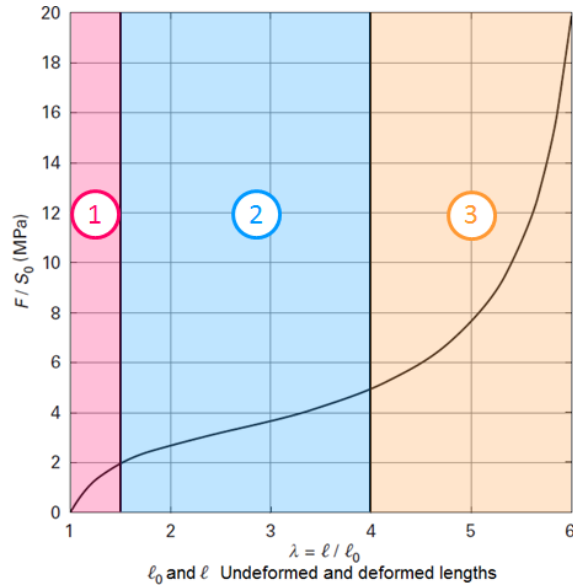
Figure 5-38 Stress-strain curve of uniaxial tension test [115]

The principle of the hyperelastic law is to define a stress-strain relationship from a function of the strain energy density W(F):

$$P = \frac{\partial W(F)}{\partial F}$$

<div align="right">5-10</div>

with **F** the tensor of the deformation gradient and **P** the stress tensor.

There are several forms for this function available in Abaqus® for incompressible isotropic elastomers [129]: the Arruda-Boyce form, the Marlow form, the Mooney-Rivlin form, the neo-Hookean form, the Ogden form, the polynomial form, the reduced polynomial form, the Yeoh form, and the Van der Waals form. For the complete characterisation of those laws, several test data are necessary: uniaxial, biaxial, planar and volumetric tests, performed in tension and compression, as illustrated in Figure 5-39.
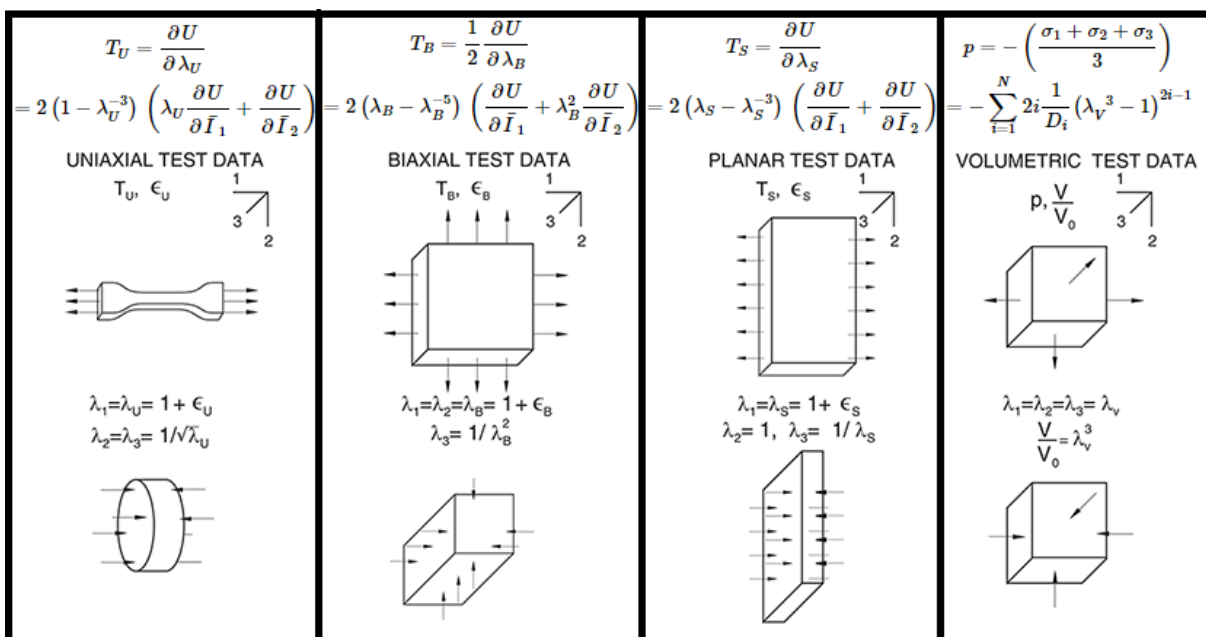
Figure 5-39 Hyperelastic characterisation tests [129]

On this figure, T and ϵ are respectively the stress and the strain tensors. The small deformation stretch in a given direction is given by $\lambda_i = l_i/l_0 = 1 + \varepsilon^{inj}_i$ with ε^{inj}_i the engineering strain.

Apart from the uniaxial tension test performed in 5.4.3, such tests can be very complicated to implement for a paint film, especially for the compression constraints. Therefore, only one type of test data is available for the characterisation of the law and its coefficients.

We studied in greater detail three different laws for the paint mechanical behaviour: the Marlow form, the Ogden form and the reduced polynomial form. The other forms presented unstable answers for small strain values with the paint tension test data extracted from experiments and were discarded.

Before explaining these three different forms, it is important to define the baseline of the mechanical laws. First, there are three invariants in the deformation tensor: I_1, I_2 and I_3.

$$\begin{cases} I_1 = tr(\boldsymbol{C}) = \lambda_1{}^2 + \lambda_2{}^2 + \lambda_3{}^2 \\ I_2 = \frac{1}{2}[tr(\boldsymbol{C})^2 - tr(\boldsymbol{C}^2)] = \lambda_1{}^2\lambda_2{}^2 + \lambda_2{}^2\lambda_3{}^2 + \lambda_3{}^2\lambda_1{}^2 \\ I_3 = det(\boldsymbol{C}) = \lambda_1{}^2\lambda_2{}^2\lambda_3{}^2 \end{cases} \qquad \text{5-11}$$

These parameters I_1, I_2 and I_3 represent respectively the geometry change in 1D, 2D and 3D. Indeed, if we consider the transformation of an infinitesimally small cube, I_1 is proportional to the sum of the squares of the diagonal in the transformed cube, I_2 is proportional to the sum of the squares of its surfaces and I_3 is proportional to the square of its volume change. I_1 and I_2 are related to the changes in the cube shape, i.e. to the deviation of the matter, while I_3 is only related to the volume change. Here, **C** is the Cauchy-Green strain tensor.

In our case, only the first deviatoric strain invariant and the volumetric invariant were considered for the following forms:

$$\begin{cases} \overline{I_1} = \overline{\lambda_1}^2 + \overline{\lambda_2}^2 + \overline{\lambda_3}^2 \ \ with \ \overline{\lambda_i} = J^{-1/3}\lambda_i \\ J = \lambda_1\lambda_2\lambda_3 \end{cases} \qquad \text{5-12}$$

If the material is fully incompressible with no energy dissipation, then $J = I_3 = 1$.

Then, thermal expansion for hyperelastic material is defined by its elastic volume ratio called J^{el}. It is the ratio of the total volume ratio J and the thermal volume ratio J^{th}, dependent on the linear thermal expansion strain.

$$\begin{cases} J^{el} = J//J^{th} \\ J^{th} = (1 + \varepsilon^{th}) \end{cases} \qquad \text{5-13}$$

In our case, since we did not perform any temperature study for this expansion, $J^{el} = J$.

The **Marlow** form of the strain energy per unit volume of reference is:

$$U = U_{dev}(\overline{I_1}) + U_{vol}(J^{el}) \qquad \text{5-14}$$

The deviatoric part of the potential U_{dev} is defined based on the uniaxial test data provided in our study but another test could be used instead (biaxial or planar). The volumetric part is defined from the Poisson's ratio when no volumetric test data are available. This form is recommended when only one set of test data is provided since it will reproduce the test data (stress-strain curve) and will provide a reasonable behaviour for the other deformation modes.

The **Ogden** form of the strain energy per unit volume of reference is:

$$U = \sum_{i=1}^{N} \frac{2\mu_i}{\alpha_i} \left(\overline{\lambda_1}^{\alpha_i} + \overline{\lambda_2}^{\alpha_i} + \overline{\lambda_3}^{\alpha_i} - 3 \right) + \sum_{i=1}^{N} \frac{1}{D_i} (J^{el} - 1)^{2i} \qquad \text{5-15}$$

N is a material parameter that can be chosen from 1 to 6. α_i, μ_i and D_i are material parameters that can be temperature dependent. This form provides the most accurate model to fit the results when multiple test data are provided. The initial shear modulus μ_0 and bulk modulus K_0 are given by:

$$\mu_0 = \sum_{i=1}^{N} \mu_i \ and \ K_0 = \frac{2}{D_1} \qquad \text{5-16}$$

The **reduced polynomial** form of the strain energy per unit volume of reference is:

$$U = \sum_{i=1}^{N} C_{i0} (\overline{I_1} - 3)^i + \sum_{i=1}^{N} \frac{1}{D_i} (J^{el} - 1)^{2i} \qquad \text{5-17}$$

N is a material parameter than can be chosen from 1 to 6. C_{i0} and D_i are material parameters that can be temperature dependent. This form performs less well than Ogden but provides a reasonable behaviour. The initial shear modulus μ_0 and bulk modulus K_0 are given by:

$$\mu_0 = 2C_{10} \ and \ K_0 = \frac{2}{D_1} \qquad \text{5-18}$$

Apart from the Marlow model for which no coefficient is defined since the test data are directly used to characterise the strain energy potential, the material coefficients are determined thanks to a least-squares fit procedure in order to minimize the relative stress error E_{rr} for an experimental set of stress-strain with n data.

$$E_{rr} = \sum_{i=1}^{n} \left(1 - \sigma_{ing_i}^{th} \Big/ \sigma_{ing_i}^{test} \right)^2 \qquad \text{5-19}$$

$\sigma_{ing_i}^{test}$ is the engineering stress data from the test compared to the simulation result: $\sigma_{ing_i}^{th}$. The error is minimised up to the best fit.

In Abaqus®, the determination of the coefficients is provided based on the program for the nominal (engineering) stress-strain data of the uniaxial test and the unit is set in MPa. The material coefficients, stability and the simulation results for the different types of test are provided in order to support our choice. For the Ogden form, complete stability is reached only for N=3 and the coefficients of this form are defined below:

i	μ_i (MPA)	α_i	D_i (MPA^{-1})
1	-342.824997	-2.23588148	2.719731511E-03
2	160.596987	-0.944732817	0
3	189.606271	-3.63172020	0

Table 5-4 Ogden coefficients with N=3

For the reduced polynomial form, N was set equal to 5 with the coefficients listed below:

i	D_i (MPA^{-1})	C_{i0} (MPA)
1	3.070665320E-03	3.26751494
2	0	-0.918974432
3	0	6.36503201
4	0	-6.02129393
5	0	1.86979083

Table 5-5 Reduced polynomial coefficients with N=5

Even if the simulation is considered stable by Abaqus®, it is necessary to analyse the results provided by the code. In this evaluation, uniaxial, biaxial and planar results are presented in tension but also in compression. Looking at Figure 5-40, the fit to the uniaxial tension test data is very good for all the different forms. But as advised by Abaqus®, it is the Marlow form which gives the most stable answer in all the different solicitations. The reduced polynomial form diverges in compression for planar and biaxial tests and, for the Ogden form, the stress increases very quickly for all the solicitations apart from the test fit. Therefore, considering the test inputs that can be provided, we chose the Marlow form in order to limit the stress in compression.
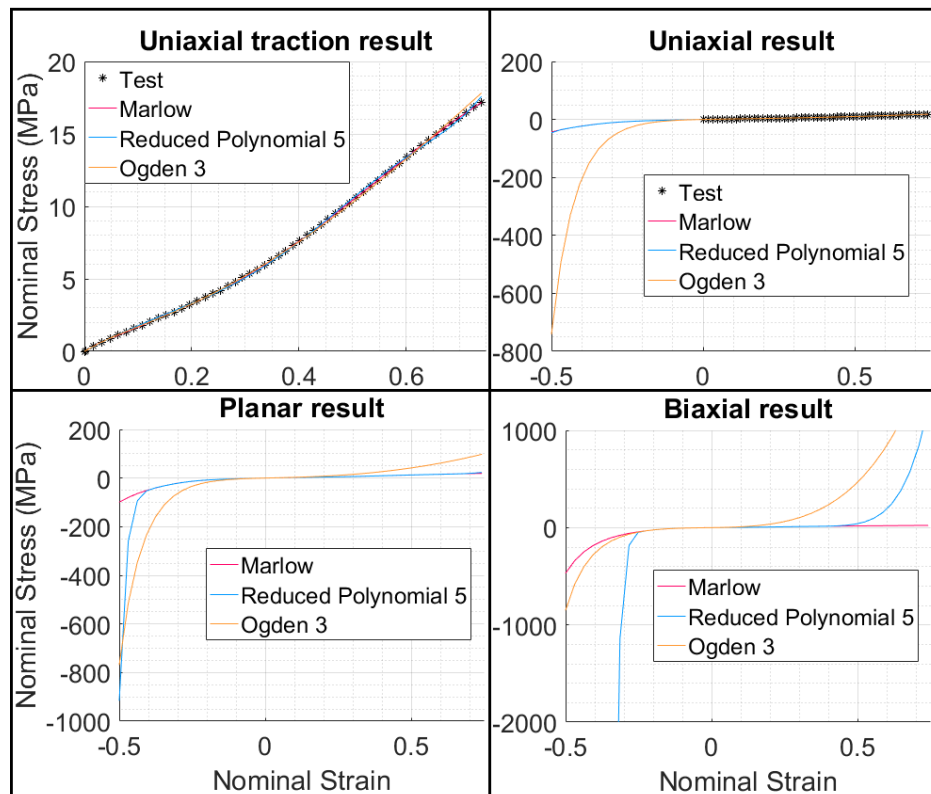
Figure 5-40 Hyperelastic forms - Abaqus® evaluation

Finally, the tension test was fully simulated with the three different forms selected and was compared to the test results. The true stress and strain distribution in the sample is illustrated below. In view of the different symmetry plans, only a quarter of a sample was simulated in order to save computation time. The geometry is considered flat and C3D8 elements were used for the model.
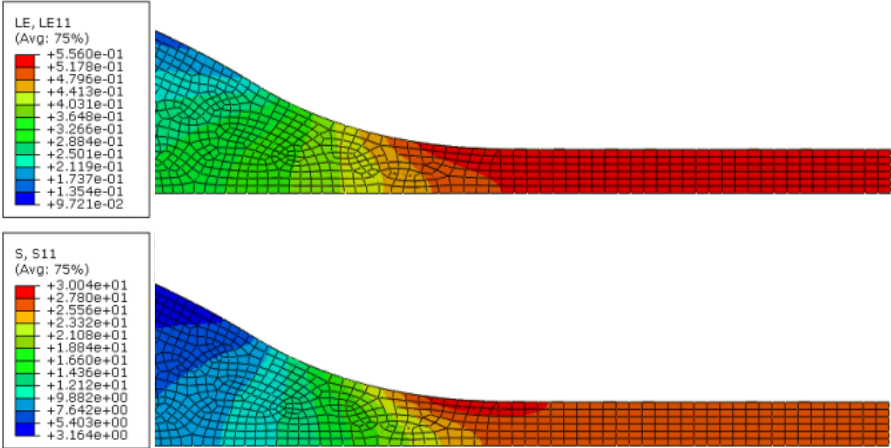
Figure 5-41 Tension test simulation - Marlow true strain-stress at % elongation

In addition, the simulated stress-strain curves are very close to the test curves since the coefficient forms were derived from it. However, for the force-displacement curve which is the real value measured during the test, an underestimation of the force is visible. This difference is explained by the fact that the useful section used to compute it from the stresses is slightly different. Indeed, the curvature of the sample highlighted in 5.4.3 is a demonstration of the presence of a residual stress in the sample due to the manufacturing process that could be not completely relaxed after the peeling of the film from its substrate, and that causes a non-uniform stress distribution in the section. Unfortunately, even if the true strain can be directly measured thanks to the image correlation, the stress can only be assessed from the measured force and cross-section, considering a uniform distribution and without the possibility to measure the real section.
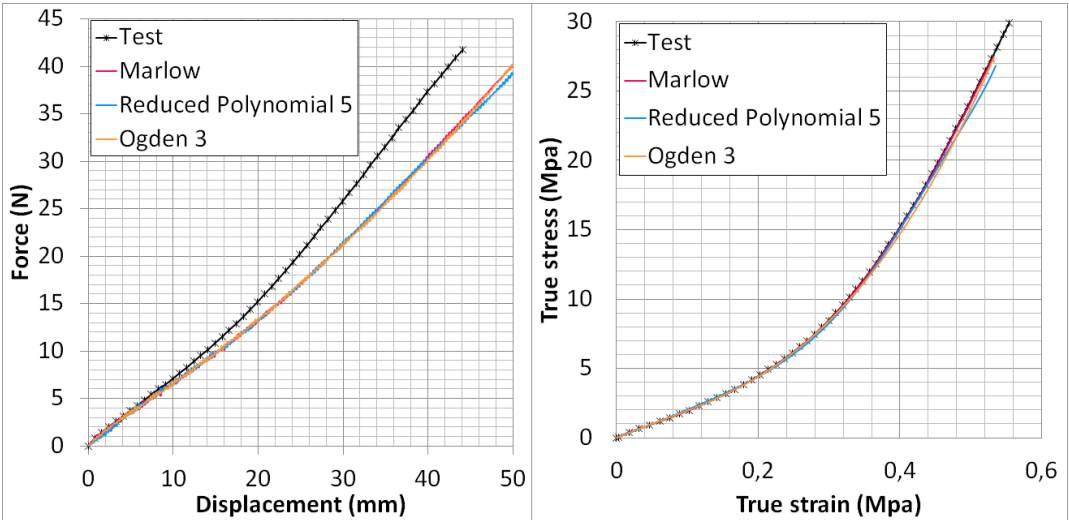
Figure 5-42 Tension test - Experimental vs simulation results

Even with this error of stress estimation, the simulation results are considered acceptable for future models.

In addition to the choice of the hyperelastic form, the Poisson's ratio was considered to be equal to 0.495. This choice is based on the Abaqus® recommendation which does not allow a fully incompressible material in explicit mode. This value is therefore a compromise between solution accuracy and computation efficiency.

Finally, since no strain rate or temperature effect were characterised, no viscous behaviour will be added to this model that will be hyperelastic only.

5.6. Conclusion

The study of the lightning damage mechanism and the parameters influencing its severity has shown the need to characterise the mechanical properties of the paint. It is essential to consider this cosmetic layer as important as the composite structure design and the surface lightning strike protection. In addition to its constriction effect on the arc root, it has a confinement effect on the underlying explosion of the lightning strike protection. This effect will lead to an increase in the overpressure profile on the surface of the composite, increasing the damage. This influence has been observed qualitatively but it is now necessary to assess it quantitatively in order to predict its confinement effect. However, this material is not a structural component of an aircraft. It is aimed to decorate the external surface of the aircraft and protect it against the environment (e.g. UV, fluids). Therefore, a limited amount of data is available regarding the mechanical properties of the paint. Even if some qualification tests exist to validate its adhesion and resistance to impact, they are completely qualitative.

For this purpose, we investigated how to characterise the mechanical properties of the paint in order to use this information in a global model of overpressure prediction. We used the qualification tests made for thin films or fabrics which seemed to be the most suitable for this material. The first main issue was to obtain a paint film, independent of any substrate. This material is made to be applied on a surface and to strongly adhere to it. Again, we investigated a solution for the manufacturing of this layer where the main difficulties to encompass were to ensure the uniformity of the thickness, the wettability of the surface but also the limited surface adhesion after drying. It was necessary to assess the following parameters: the bulk mechanical properties, the break resistance, the break propagation and lastly, the adhesion. For this purpose, we performed DMA, tension, trouser tear and laser shock tests. With the DMA test, it was highlighted that the bulk properties of the paint were highly variable in the expected range of temperature in a laboratory (18 to 30°C) due to the glass transition temperature at 36°C. This variation is not usually monitored during a lightning test and could explain some damage variability for a supposedly identical configuration. In addition, the tension test validated our theory regarding the hyperelastic properties of this layer. This test was therefore used to characterise a model of the paint

with this behaviour which is not trivial compared to a simple elastic behaviour. Then, the trouser test showed the low resistance of the paint to break propagation. Finally, the laser test provided a qualitative result regarding the adhesion of the paint. However, issues concerning the substrate speed measurements and the quantitative characterisation of the shock wave amplitude injected in the composite structure prevented us from characterising the stress required to break the interface between paint and composite.

In order to complete the model developed for the paint, we need to add the break damage in the paint. This work can be developed based on the tension and trouser tear test results in order to validate a model for paint cracking. A way to model this damage could be made through a cohesive interface in the paint mesh. Furthermore, the complete validation of the hyperelastic model needs additional tests with different solicitations such as compression uniaxial, biaxial and planar tests. A further development of the laser test combined with a shock model would finalise the interface characterisation under dynamic solicitation. Finally, the dynamic stress of the paint could generate some heat and consequently change the bulk properties of the paint. This effect was not considered here to limit the complexity of our paint model but would be necessary in the future in order to fully characterise the confinement effect of the paint under strong solicitation.

The work presented in the previous chapters made it possible to characterise the pressure generated by the explosion of the LSP. But the pressure relaxation will be dependent on the confinement of this explosion. The model developed for the paint layer will be added to the global mechanical model presented in the next chapter in order to support the prediction of the paint influence on the overpressure profile after explosion and assess the damage in the laminate.

Chapter 6

Mechanical Model and damage

Objectives

The purpose of this chapter is to propose a numerical model able to reproduce the surface overpressure generated by the explosion of the lightning strike protection and its confinement with the paint. Combined with a damage model, it will be possible to get a predictive tool in order to assess the damage in the composite structure depending on the design configurations (CFRP, LSP and Paint).

Comparisons of numerical damage with lightning experimental ones are presented in order to analyse the predictability of the model.
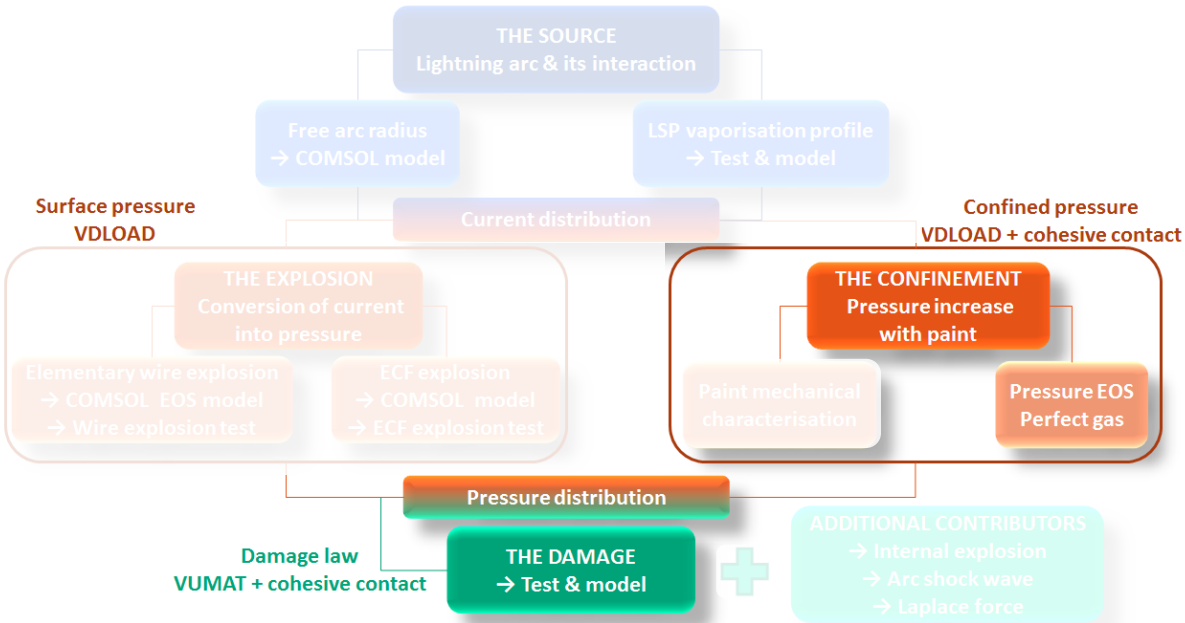
6.1. Introduction

This chapter presents the final step in the damage modelling for lightning strike. In this objective, experimental lightning results will be used for the validation of the model, from the surface overpressure due to the lightning strike explosion and confinement by paint to the damage in the composite. Damage laws developed in previous work [11,130] have been readapted and developed for composite damage modelling due to lightning solicitation. The damage is decomposed into two areas, inter- and intra-laminate, requiring two different laws that are presented in this chapter. The source of the damage is decomposed in a mechanical load applied on the surface of the composite and a thermal load leading to internal damage.
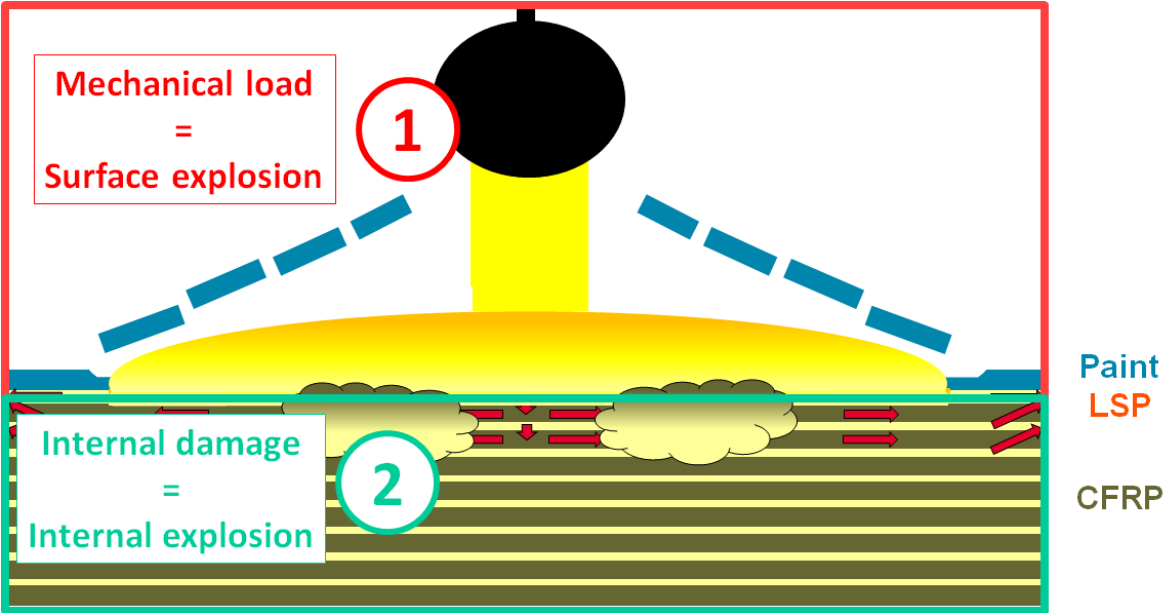
Figure 6-1 Damage source decomposition

The external load arising from surface explosion will be determined in two steps. First, an equivalent surface load that simulates the surface explosion and its confinement is defined from the outcomes of the previous chapters, and is applied on the top face of the composite panel thanks to a VDLOAD. The pressure decay is based on a law fitted to validate the principle of surface explosion. Then, the model of the paint layer is added in order to simulate the confinement of the LSP explosion and predict the overpressure decay.

Internal damage coming from Joule heating in CFRP is added to simulate the internal explosion. At each step, numerical results are compared to the corresponding experimental tests that are defined in section 6.2 below. Comparisons based on rear face displacements and delamination profiles are used for the validation of the numerical model.

6.2. Lightning experimental results

In order to study the different parameters that play a role in the generation of lightning damage, specific lightning tests were performed during the EDIFISS project. All the samples were flat square panels of 450mm lateral dimension, mechanically and electrically perfectly bonded to a circular metallic frame through 12 fasteners distributed along its 370mm diameter. A lightning strike of 100kA following waveform D [3] is performed in the centre of the panel on the front face (side where the LSP is applied). The rear face displacement is measured thanks to the image correlation technique used by DGA-TA [14]. Two high speed cameras Photron SA5 are installed at specific angles behind the panel which has been painted with a black and white pattern calibrated through a focus frame. Pictures are taken at a rate of 262,500 frames per second (fps) with a resolution of 128x128 pixels, covering a central area of the sample of 80x80 mm^2. Figure 6-2 illustrates the test setup:
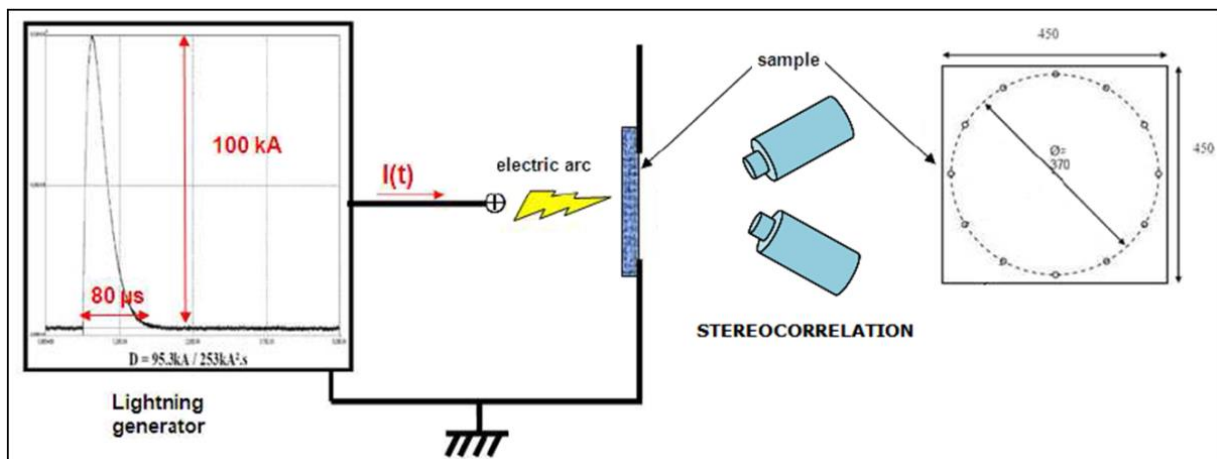
Figure 6-2 Lightning test setup

In a first step, the surface explosion due to Joule heating in LSP layer was studied independently from the CFRP internal damage thanks to specific tests based on the GFRP substrate. Indeed, due to its high resistivity, the lightning current will not be diverted into the glass fibre composite panel and will only flow in the metallic LSP. Therefore, the displacement of the panel is due only to the explosion occurring at the surface. Another interest of this configuration is that no damage is created in the laminate, therefore an elastic model of the panel without a damage law is sufficient to simulate its mechanical behaviour.

In a second step, CFRP substrates were tested. At the surface, the confinement effect was studied through the influence of paint thickness on the damage severity. The paint thicknesses considered were 50μm, 250μm, 400μm, and 1000μm). To distinguish the effect of the thickness over flexibility, one test was done with a rigid plate instead of a paint layer. In the core, the influence of the global panel stiffness on the final extent of damage was studied thanks to a thicker panel. The LSP was in all cases ECF195 from Dexmet®.

A summary of the user cases is listed in Table 6-1 below:

Rationale	Substrate	Paint thickness (µm)	Comparison criteria	EDIFISS sample
Confined surface explosion baseline	GFRP 2,75mm 11 plies	400	Displacement	17
Free surface explosion baseline	GFRP 2,75mm 11 plies	0	Displacement	19
Composite damage baseline	**CFRP 1,651**mm 13 plies	**400**	Displacement & Damage	1
Composite damage with internal explosion & extreme surface confinement	CFRP 1,651mm 13 plies	1000	Displacement & Damage	6
Composite damage with internal explosion and light surface confinement	CFRP 1,651mm 13 plies	250	Displacement & Damage	5
Stiffness impact	CFRP 3,302mm 26 plies	400	Displacement & Damage	100
Stacking and CFRP grade influence	CFRP 1,651mm 9 plies	400	Displacement & Damage	30
Composite damage with internal explosion and surface confinement with different top layer	CFRP 1,651mm 13 plies	400 Tufnol	Displacement & Damage	61

Table 6-1 Summary of experimental results

The profile of the out-of-plane displacement along an 80 mm long line along the (x=0°) direction centred on the rear face central point is reported as a function of time. From the curves, several types of information can be extracted such as the maximum displacement and its rate at the centre versus time, or the slope and base of displacement along (x=0°) versus time. The maximum of displacement is mainly reached before 100µs. The comparison between the model and the test will be performed up to this moment. The principle is illustrated in Figure 6-3.
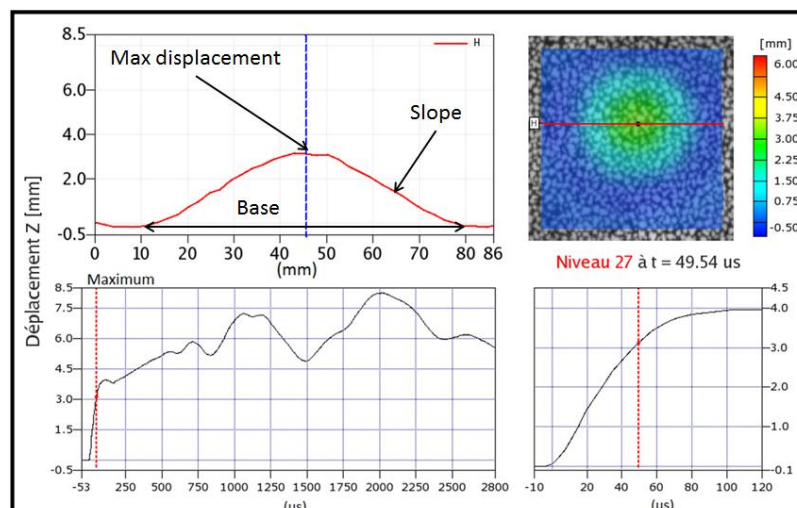
Figure 6-3 Rear face out of plane displacement measurement from image correlation

A Non-Destructive Test (NDT) was performed for each configuration in order to measure the delamination pattern. In addition, micro-cuts were performed in order to determine the complete and accurate distribution of delamination in the depth. The methodology is detailed in Appendix C. Figure 6-4 presents the results of this analysis for our reference configuration: CFRP plate protected with ECF195 and painted with 400µm of paint. The micro-cut NDT reconstruction is "pixelated" due to the separation between each cut but the result is in good agreement with the NDT. The interface 1 is placed between the first ply and the second ply from the back face (opposite to LSP) and the interface 12 is between the 13th ply and the LSP.
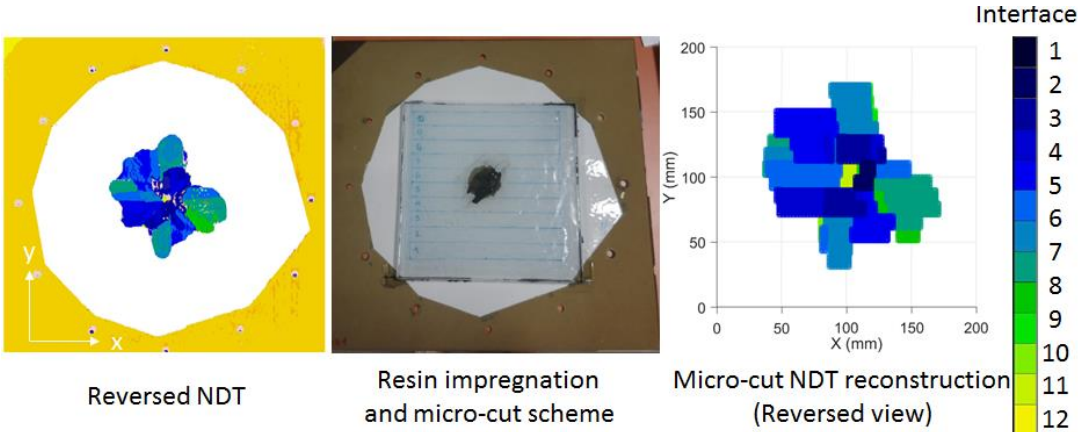
Figure 6-4 Reference case (EDIFISS 1): NDT and micro-cut reconstruction comparison

NDT is based on an ultra-sonic measurement in which the echo of the closest delamination is captured, which hides any delamination that could be present in the top plies. The micro-cut reconstruction is therefore very interesting since the delamination is measured for all the different interfaces: it shows what is hidden. Figure 6-5 illustrates of the hidden delaminated surface. The total delaminated area per interface is therefore bigger than what is measured by NDT. The grey histogram represents the delaminated surface not measured by NDT.
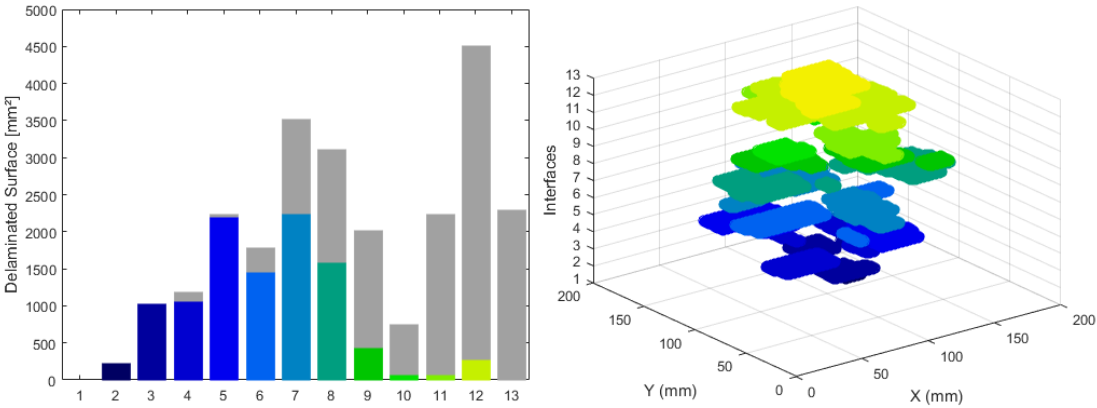
Figure 6-5 Reference case: Delamination distribution (Grey histogram=hidden delamination)

Micro-cuts can also provide the volume of burned zones due to current flow in the CFRP, generating Joule heating. With the micro-cuts, we have a complete view of the damage: In the plies and at the interfaces. These results will be presented when compared to the numerical results.

6.3. Abaqus® CFRP damage model

6.3.1. Global model approach

The damage in the composite structure due to impact has been widely studied and the complete list of references dealing with this issue cannot be given here. On the specific topic of damage comparable to lightning strike, the reader is however invited to consult the following ([131–133]). Because of the fabrication process, comprising the layering of elementary plies, damage of a composite laminate can be decomposed into two parts: inside the plies and between adjacent plies. We adopted the approach taken by Ilyas [130] and Soulas [11] who modelled the ply as a 3D solid and the interply region as an interface, that is as a surface. Surface-based cohesive contacts were considered to model the delamination which is the damage between the plies. This approach will be detailed in 6.3.2. For damage in the ply which is composed of intralaminar cracks, a Diffuse Damage Model (DDM) approach based on continuum mechanics was developed and implemented in a user-defined law of the Abaqus/Explicit® code (VUMAT). The damage inside the ply such as fibre failure and matrix cracks indeed decrease elastic moduli and strengths. This approach will be detailed in 6.3.3.

Due to the circular clamping mechanical boundary condition, only the disk in this area will be modelled and its boundary will be "encastre" in the Abaqus® input file (U1=U2=U3=UR1=UR2=UR3=0). Each ply of the composite is modelled by one layer of reduced integrated 3D solid finite elements (C3D8R). In the central area where the delamination is expected, a structured oriented mesh is built, with one mesh layer per ply. Following the methodology of Soulas and Chen [134], the orientation and the shape of the FE mesh follow the ply fibre's orientation as shown in Figure 6-6. Prismatic finite elements (C3D6) were used to ensure mesh coincidence between plies before delamination initiation. The objective of this structured mesh is to limit the influence of the FE mesh topology on the extent and orientation of delamination (see Chen [134]). Between plies on both sides of interfaces, a frictionless cohesive surface interaction is defined. For a 13-ply panel of a low grade IMA/M21E (127µm), the mesh details are as follows:

No. of elements	Element type	No. of nodes	DOF
1,278,447	C3D8R	4,021,602	12,064,806
1,459,482	C3D6		

Table 6-2 CFRP solid Mesh details
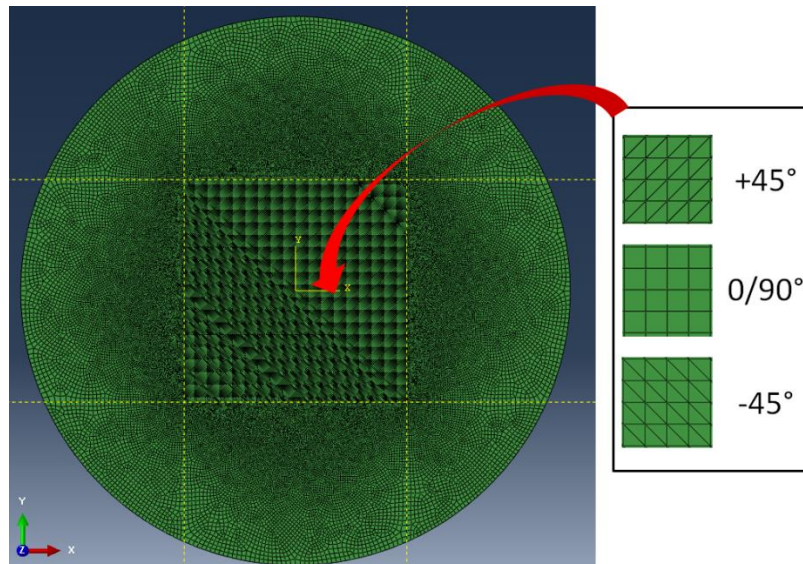
Table 6-3 CFRP mesh approach

6.3.2. Cohesive interaction

6.3.2.1. Theory

The source of delamination is based on three failure modes shown in Figure 6-6:
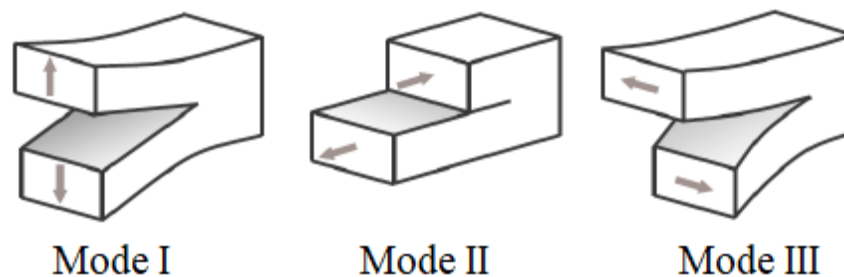
Figure 6-6 Delamination failure modes

- **Mode I (Opening mode):** corresponds to a tensile stress generated by the displacement perpendicular to the crack plane.
- **Mode II (shearing mode):** corresponds to a shear stress in the crack plane generated by the displacement perpendicular to the crack front.
- **Mode III (tearing mode):** corresponds to a shear stress generated by a displacement parallel to the crack front.

In order to model the initiation and the propagation of the crack between two plies, we considered cohesive surfaces. The use of cohesive behaviour is interesting to model the separation between two bonded surfaces and, in our case, delamination in the composite. This law relates the traction at the interface to the separation of its sides. In Abaqus®, it is possible to consider either a cohesive element or a cohesive surface. The advantage of using a cohesive surface over a cohesive element is that it is an interaction property and not a material property. As the thickness of the interface is even smaller than the ply thickness in front of it, the cohesive surface is easy to define.

First, it is necessary to define the traction separation behaviour with the normal and tangential stiffness components K_n, K_s and K_t. K_{1-3} are chosen so as to best fit the F_{max}-delta experimental crack propagation data curve.
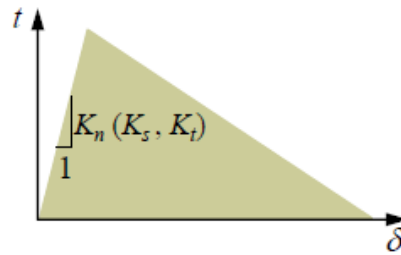
Figure 6-7 Traction separation behaviour

Then, it is necessary to define the damage law considering an initiation criterion and an evolution criterion. For the initiation, it is possible to consider either the peak values at the contact stress ($t_n^{max}, t_s^{max}, t_t^{max}$) or at the contact separation ($\delta_n^{max}, \delta_s^{max}, \delta_t^{max}$). For the evolution, it is possible to consider the total fracture energy G_{TC} or the post-damage initiation separation at failure ($\delta_n^f, \delta_s^f, \delta_t^f$). This law is illustrated in Figure 6-8 below:
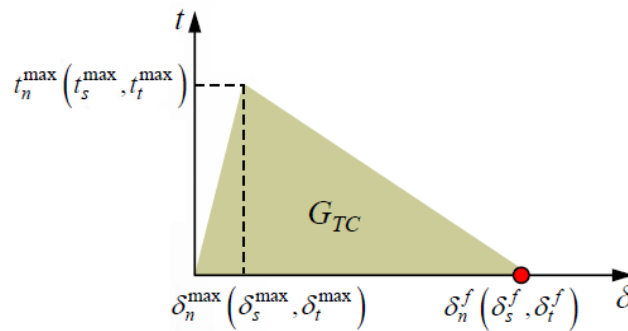
Figure 6-8 Cohesive damage law

In our case, we chose the quadratic stress criterion for initiation:

$$\left(\frac{\langle t_n \rangle}{t_n^{max}}\right)^2 + \left(\frac{t_s}{t_s^{max}}\right)^2 + \left(\frac{t_t}{t_t^{max}}\right)^2 = 1 \qquad \text{6-1}$$

The evolution was based on energy, with a mixed mode defined by Benzeggah-Kenane (BK):

$$G_{IC} + (G_{IIC} - G_{IC})\left(\frac{G_{shear}}{G_T}\right)^\alpha = G_{TC} \qquad \text{6-2}$$

where $G_{shear} = G_{II} + G_{III}$ and $G_T = G_I + G_{II} + G_{III}$.

In order to validate the value of the parameters defined above, i.e. the initiation contact stress ($t_n^{max}, t_s^{max}, t_t^{max}$) and the fracture energies G_{IC} and G_{IIC}, elementary models representing the different failure modes were performed and compared to standard characterization tests:

- Double cantilever beam (DCB) for Mode I testing
- End Notch Flexure (ENF) for Mode II testing
- Mixed-Mode Bending (MMB) for Mode I+II testing

DCB and ENF characterization tests are presented in the following sections with the associated Abaqus® models used to validate the cohesive interface parameters. Since no data are available for the MMB test for our laminates, no simulation was performed.

6.3.2.2. Mode I characterisation: Double Cantilever Beam (DCB)

This test has been standardized in order to characterise the strain release energy for mode I G_{IC} ([135,136]). The method is based on the propagation in mode I of a pre-cracked specimen by the application of opening forces perpendicular to the initial defect. The specimen is thus equivalent to two composite beams in the defect area. The two beams are loaded as cantilever beams, therefore the test is named double cantilever beam test.
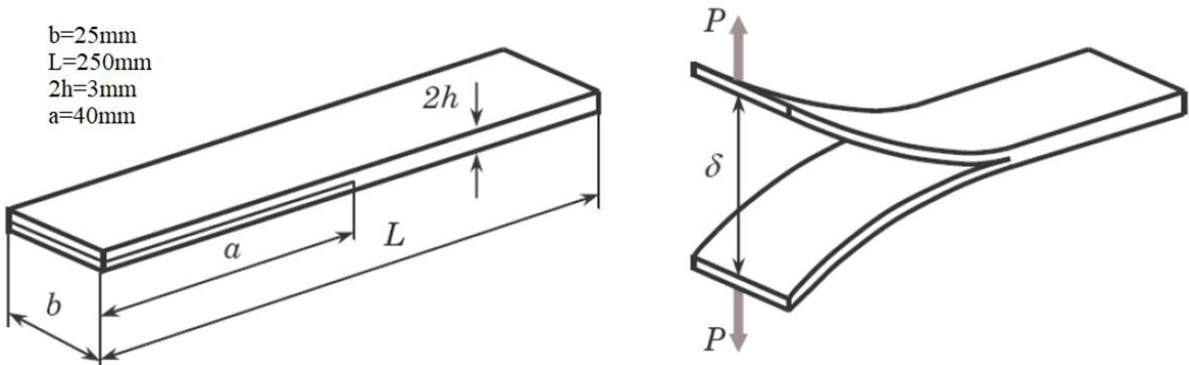
Figure 6-9 Double cantilever beam (DCB) specimen for Mode I testing

The Airbus procedure AITM1-005 [137], based on ISO15024 [136], describes the manufacturing of the specimen and the test method. The Dimensions of the specimen are given in Figure 6-9.The specimen is made of composite tape material at 0° to the specimen length and the number of plies is considered in order to be as close as 2h=3mm. In our case, as we want to characterise a low grade CFRP of 127µm, the total number of plies for a DCB specimen is 24. To introduce the initial crack, a double layer of release film (like PTFE) of about 0.02mm to 0.03mm is placed in the mid thickness of the specimen as shown on the figure. During the test, a perpendicular load is applied at a constant crosshead speed of 5 mm/min and the resulting force P is measured. The calculation of the G_{IC} is based on the curve of the load P as a function of the crosshead displacement δ with the following formula:

$$G_{IC} = \frac{A}{a \times b} \times 10^6 \ (J/m^2)$$

6-3

with:

-   A: the energy required to achieve the total propagated crack length in J (Integration of the area of the load-crosshead displacement diagram according to Figure 6-10)
-   a: the propagated crack length in mm (Final crack minus initial crack)
-   b: the width of the specimen in mm

Figure 6-10 G$_{IC}$ measurement method

The theory considered to predict the load-displacement law for this test based on G$_{IC}$ is the compliance method ([138], [139]) where the compliance C is the inverse of the stiffness K:

$$C = \frac{u}{P} \quad and \quad K = \frac{P}{u} = \frac{2P}{\delta} \qquad\qquad 6\text{-}4$$

where P is the force applied at the beams and u is the displacement of one beam (u=δ/2). Now, considering the beam theory for the DCB test, the compliance C and rigidity K are equal to:

$$C = \frac{u}{P} = \frac{2a^3}{3EI_z} = \frac{8a^3}{Ebh^3} \quad and \quad K = \frac{2P}{\delta} = \frac{Ebh^3}{8a^3} \qquad\qquad 6\text{-}5$$

where a is the crack length, E the Young Modulus and I$_z$ the flexural quadratic momentum of one beam (I$_z$=bh^3/12). We can thus determine the strain release energy in mode I for a prescribed load P by:

$$G_{IC} = \frac{1}{2} P^2 \frac{dC}{d(axb)} = \frac{P^2}{2b} \frac{dC}{da} = \frac{P^2}{2b} \frac{3C}{a} = \frac{3Pu}{2ba} \qquad\qquad 6\text{-}6$$

or for a prescribed aperture δ by:

$$G_{IC} = -\frac{1}{2} \delta^2 \frac{dK}{d(axb)} = \frac{1}{2} \delta^2 \frac{3K}{ba} = \frac{3Pu}{2ba} \qquad\qquad 6\text{-}7$$

We can thus relate the force P and the displacement u by the following equation 6-8:

$$u = \frac{\sqrt{EI_z}}{3P} (bG_{IC})^{3/2} \qquad\qquad 6\text{-}8$$

From the DCB test performed by Airbus on the low grade CFRP, we know that G$_{IC}$=285J/m². This value can be directly used in the Abaqus® model for the damage propagation law in mode I but we need to define the other parameters that are purely numerical and dependent on the mesh (K & σ) that can influence the simulation results. For this purpose, we modelled a DCB test with the same finite element mesh density as will be used for our global lightning model (C3D8R, 0.5mm side cube). As we know that the final crack length is less than 140mm, we model the specimen length with a shorter length 150mm instead of

250mm. The other parameters (a, b and h) were kept identical to the test and the velocity of the load application was $\dot{\delta} = 20\text{mm/min}$ in order to save computation time with an equivalent static behaviour.
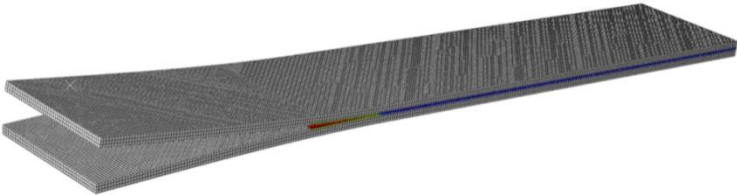
Figure 6-11 DCB model with cohesive damage

For this model, we considered the Young's modulus E=165GPa, defined in Appendix D and for the cohesive interface contact an interface stiffness K_n=100KN/mm^3. The contact was built following Abaqus® training [140]. Several maximum normal stresses in mode I, σ_n, were assessed in order to find the right threshold value, since several values can be found in the literature[141–143], usually for medium (184µm) and high grade (254µm) IMA/M21E but also some on low grade (127µm). In the graph below, the outcome of DCB simulations is compared to the analytical result in black dotted line:
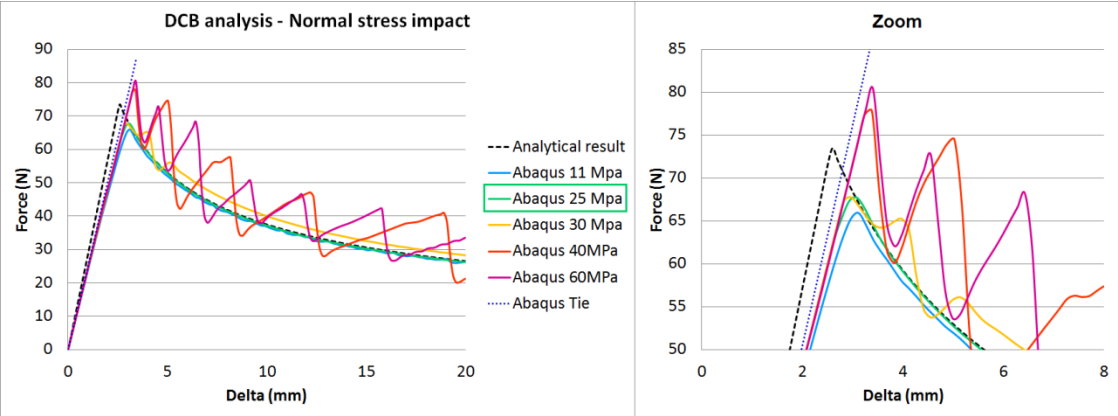
Figure 6-12 DCB simulation and maximum normal stress influence σ_n

In the first phase, before crack propagation, the simulation curve does not fit with the analytical one. Looking at the behaviour of an identical model without cohesive contact but only tie contact to suppress any opening and crack propagation, the apparent slope is also lower than the theory and similar to the configuration with cohesive contact. This means that the apparent stiffness of the simulated beam is slightly lower than what is predicted by theory, no doubt due to the fact that the 3D solid mesh deformation is different from the real one.

In the second phase, where the crack propagates, there is a threshold value for the maximum normal stress for which the cohesive contact is less stable, even at a slower opening speed or smaller element size. The value for the cohesive contact which best fits the analytical law is σ_n=25MPa. This value is valid for a static test and it raises the question of its validity for a dynamic test such as the lightning test, since this value is very low and could lead to unexpected contact breakage.

6.3.2.3. Mode II characterisation: End Notch Flexure (ENF)

This test has been standardized in order to characterise the strain release energy for mode II : G_{IIC} [144]. This method is based on the propagation in mode II of the same pre-cracked specimen as for DCB but, in this case, by the application of a shear loading thanks to a three-point bending test setup. This test can be difficult to interpret since the crack propagation is linked to matrix micro-cracks in the front and there is friction between the sliding surfaces.

b=25mm
L=50mm
2h=3mm
a=35mm
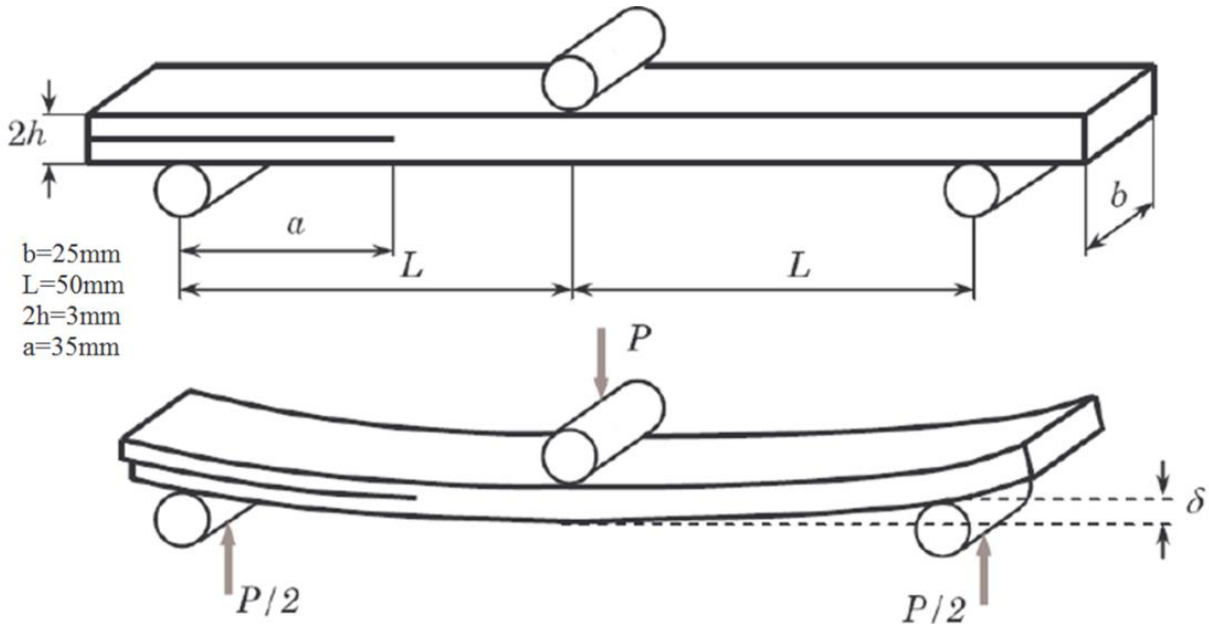
Figure 6-13 End Notch Flexure (ENF) specimen for Mode II testing

The Airbus procedure AITM1-006 [144] describes the manufacturing of the specimen and the test methods. The dimension of the setup and specimen is given in Figure 6-13. As already stated above, the specimen is the same as for the DCB test, i.e. a 24-ply 0° sample but with a shorter initial crack of 110mm. It is placed on two fixed supports positioned 100mm apart in such a way as to ensure an initial crack length of 35mm from the support. During the test, a perpendicular load is applied at a constant crosshead speed of 1 mm/min and the resulting force P is measured. Calculation of the G_{IIC} is based on the curve of the load P as a function of the crosshead displacement δ with the following formula:

$$G_{IIC} = \frac{9 P_c a_0^2 d_c}{2b(1/4\, L^3 + 3a^3)} \times 1000 (J/m^2) \qquad \text{6-9}$$

with:

- P_c: the critical load to start the crack in N
- d_c: the crosshead displacement at crack delamination onset in mm
- a_0: the Initial crack length in mm (=35mm)
- b: the width of the specimen in mm (=25mm)
- L: the span length in mm (=100mm)
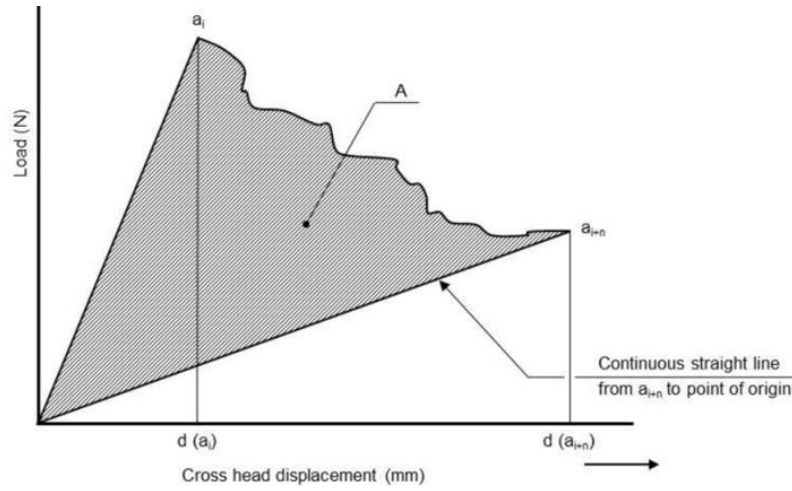
The theory considered to predict the load-displacement law for this test based on G_{IIC} is the compliance method ([138], [139]) and the beam theory as for the DCB test. In this configuration, the compliance differs depending on the crack propagation:

$$\begin{cases} C = \dfrac{u}{P} = \dfrac{L^3 + 12a^3}{384EI_z} & if \ 0 \leq a \leq L/2 \\ C = \dfrac{u}{P} = \dfrac{L^3 - 3(L-a)^3}{96EI_z} & if \ L/2 \leq a \leq L \end{cases}$$

6-10

where a is the crack length, E the Young Modulus and I_z the flexural quadratic momentum of one beam (I_z=bh³/12). We can thus determine the strain release energy in mode II by:

$$\begin{cases} G_{IIC} = \dfrac{P^2}{2b}\dfrac{dC}{da} = \dfrac{18Pua^3}{b(L^3 + 12a^3)} & if \ 0 \leq a \leq L/2 \\ G_{IIC} = \dfrac{P^2}{2b}\dfrac{dC}{da} = \dfrac{9Pu(L-a)^3}{2b(L^3 - 3(L-a)^3)} & if \ L/2 \leq a \leq L \end{cases}$$

6-11

The force P and the displacement u can be related by the following equation 6-12:

$$\begin{cases} u = \dfrac{PL^3}{384EI_z} + \dfrac{16\sqrt{EI_z}}{P^2}\left(\dfrac{bG_{IIC}}{3}\right)^{3/2} & if \ 0 \leq a \leq L/2 \\ u = \dfrac{PL^3}{96EI_z} - \dfrac{16\sqrt{EI_z}}{P^2}\left(\dfrac{bG_{IIC}}{3}\right)^{3/2} & if \ L/2 \leq a \leq L \end{cases}$$

6-12

From the ENF test performed by Airbus on the low grade CFRP, we know that G_{IIC}=845J/m². This value can be directly used in the Abaqus® model for the damage propagation law in mode II but again we need to define the other parameters that are purely numerical and dependent on the mesh (K & σ) which can influence the simulation results in mode II. We consider the same type of model as for the DCB test. The dimensions were kept identical to the test and the final velocity of the load application was $\dot{\delta} = 1$mm/min as higher velocities influenced the result.
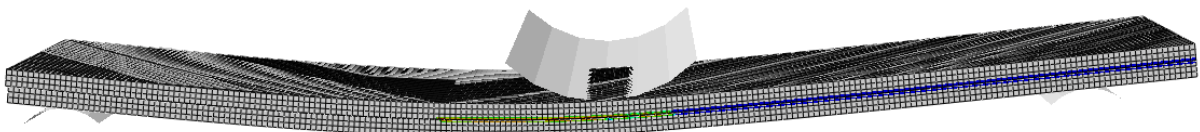
Figure 6-14 ENF model with cohesive damage

For this model, we considered the Young's modulus E=165GPa and for the cohesive interface contact an interface stiffness K_s=100KN/mm³. Several maximum normal stresses in mode II, σ_s, were assessed in order to find the right threshold value. As for σ_n, several values can be found in the literature. In the graph below, the outcome of ENF simulations is compared to the analytical result in black dotted line:
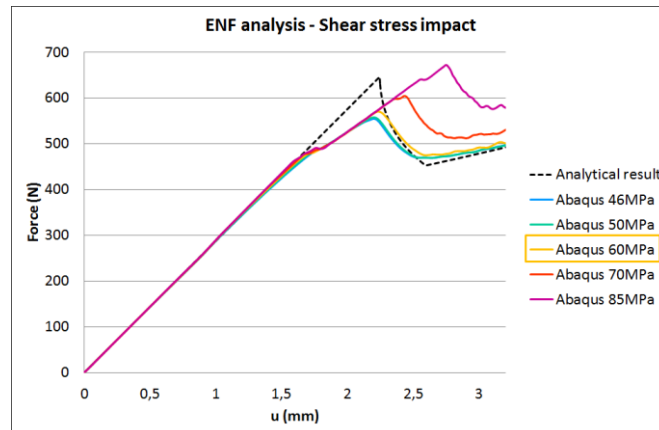
Figure 6-15 ENF simulation and maximum shear stress influence σ_s

In the first phase, before crack propagation, the simulation curve fits the analytical one, following the beam theory. But a slight decay is visible prior to the theoretical crack propagation which cannot be corrected. In the second phase, where the crack propagates, there is a threshold value for the maximum shear stress after which the crack propagation is delayed compared to the test. The value for the cohesive contact which best fits the analytical law is σ_s=60MPa. Again, this raises the question of the validity of this value for a dynamic test.

6.3.2.4. Conclusion

Based on the elementary simulations performed in mode I and II under static load, the law for the cohesive interface is chosen as defined in Table 6-4:

Cohesive behaviour		Damage Initiation		Damage evolution		
K_n (KN/mm^3)	K_s= K_t (KN/mm^3)	σ_n (MPa)	$\sigma_s = \sigma_t$ (MPa)	G_{IC} (J/m^2)	G_{IIC} (J/m^2)	α
100	100	25	60	285	845	1.5

Table 6-4 Cohesive surface parameters for CFRP

### 6.3.3. VUMAT: Abaqus/Explicit® user-defined material model

In order to model the damage inside the ply, we adopted the DDM (Diffuse Damage Model) approach developed by Soulas [11] and Ilyas [130]. While Ilyas proposed a damage model that takes into account strain rate effects for pure mechanical impact loads, Soulas finally kept a quasi-static stress strain law to describe the composite ply behaviour. This approach consists in treating the micromechanical process (fibre and matrix micro-cracks) at a macro scale level. The damage is thus homogenised in the modelled elementary volume. As introduced by Hashin [145], a damage variable d is introduced to model the damage in the material. This variable represents the effective resistance of the material subjected to damage. It can vary from 0 to 1, with d=0 for the pristine material and with d=1 for the complete failure of the material. The evolution of d is defined from irreversible thermodynamic processes linked to a material constitutive law. This is directly linked to the effective section resisting the load. The pristine material had an initial section S_0 which is reduced to S_{ef} due to the damaged area S_d: $S_{ef}=S_0-S_d$.
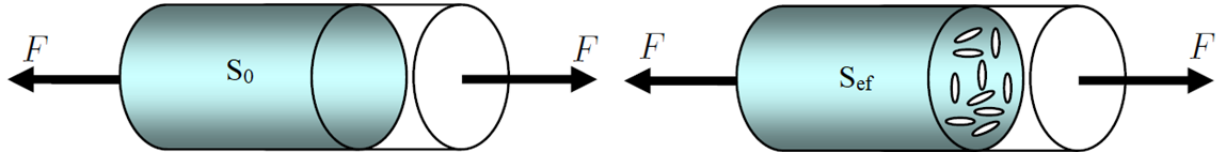
Figure 6-16 Representation of damage and associated section

We can then define d as the ratio of section:

$$d = \frac{S_d}{S_0} = \frac{S_0 - S_{ef}}{S_0} = 1 - \frac{S_{ef}}{S_0}$$

6-13

An associated effective stress $\hat{\sigma}$ can be related to the force F applied to the evolving surface S_{ef}:

$$\hat{\sigma} = \frac{F}{S_{ef}} = \frac{F}{S_0(1 - d)} = \frac{\sigma}{(1 - d)}$$

6-14

If we consider the elastic material deformation due to this effective stress, we have:

$$\varepsilon_e = \frac{\hat{\sigma}}{E}$$

6-15

with ε_e defining the equivalent elastic strain.

Considering E^0 as the pristine material's Young modulus, we can express the module for the damaged material as follows: $\hat{E} = E^0(1 - d)$. We can thus generally degrade the elastic material properties with the damage variable d:

$$E_i = E^0(1 - d_i)$$

6-16

Based on Ilyas' approach to define the behaviour of CFRP under impact, different failure modes are identified and used to assess six damage variables d_i (i=1…6) that will influence the six elastic moduli of the anisotropic material in the flexibility matrix R^{-1}. This matrix relates the strain tensor $\underline{\varepsilon}$ written in the form of a six-component vector, to the stress $\underline{\sigma}$ also written in the form of a six-component vector in the same order, and the damage variables will be used as decreasing factors:

$$R^{-1} = \begin{bmatrix} \frac{1}{(1-d_1)E_{11}^0} & -\frac{\nu_{21}}{E_{22}^0} & -\frac{\nu_{31}}{E_{33}^0} & & & \\ -\frac{\nu_{12}}{E_{11}^0} & \frac{1}{(1-d_2)E_{22}^0} & -\frac{\nu_{32}}{E_{33}^0} & & & \\ -\frac{\nu_{13}}{E_{11}^0} & -\frac{\nu_{23}}{E_{22}^0} & \frac{1}{(1-d_3)E_{33}^0} & & & \\ & & & \frac{1}{(1-d_4)G_{12}^0} & & \\ & & & & \frac{1}{(1-d_5)G_{23}^0} & \\ & & & & & \frac{1}{(1-d_6)G_{13}^0} \end{bmatrix}$$

6-17

It can be noticed that the orthotropic conditions are still respected because the original Young's moduli are unchanged: $\frac{\nu_{21}}{E_{22}^0} = \frac{\nu_{12}}{E_{11}^0}$, $\frac{\nu_{31}}{E_{33}^0} = \frac{\nu_{13}}{E_{11}^0}$ and $\frac{\nu_{23}}{E_{22}^0} = \frac{\nu_{13}}{E_{33}^0}$.

In order to assess the damage variables d_i, we need to consider five failure modes r_j (j=1...5) Within a given region in stress space where the damage will not change, a series of surfaces $f_i(\sigma, d_i, r_i)$ sets the limit of undamaged elasticity. As soon as any one of these boundaries is reached, the corresponding threshold r_j needs to be updated:

$$f(\sigma, d_i, r_i) = f_j(\sigma, d_i) - r_j^2 = \sigma_T F_j \sigma - r_j^2 \qquad \text{6-18}$$

The five failure modes were defined by Ilyas considering five sources of failure:

1. <u>Fibre failure due to tension in the fibre direction:</u>

$$f_1(\sigma, d_1, r_1) = \left(\frac{\langle \sigma_{11} \rangle}{X_T}\right)^2 + \left(\frac{\sigma_{12}^2 + \sigma_{13}^2}{S_{fs}^2}\right) - r_1^2 = 0 \qquad \text{6-19}$$

The effect of shear loadings is taken into consideration, with the material strength S_{fs}, but since the debonding strength of the fibre matrix interface has not been characterized, an appropriate value is chosen based on experience [130]. X_T is the tensile failure stress in the fibre direction.
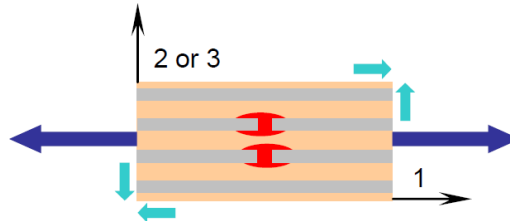
Figure 6-17 Tensile failure in fibre direction

2. <u>Fibre failure due to compression in the fibre direction:</u>

$$f_2(\sigma, d_2, r_2) = \left(\frac{\langle -2\sigma_{11} + \langle -\sigma_{22} - \sigma_{33} \rangle \rangle}{2X_C}\right)^2 - r_2^2 = 0 \qquad \text{6-20}$$

Here, X_c is the compressive failure stress in the fibre direction.
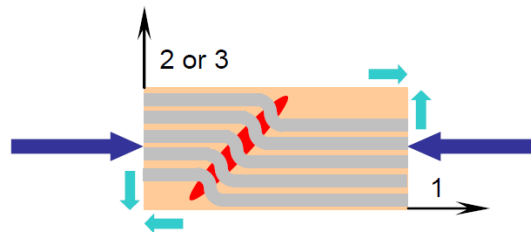
Figure 6-18 Compressive failure in fibre direction

3. <u>Ply failure due to spherical compression:</u>

$$f_3(\sigma, d_3, r_3) = \left(\frac{\langle -\sigma_{11} - \sigma_{22} - \sigma_{33} \rangle}{3Z_C}\right)^2 - r_3^2 = 0 \qquad \text{6-21}$$

This spherical compression type, also called crushing, is active below an impactor in the event of projectile penetration up to perforation. Z_c is the compressive failure stress in the out of plane direction.

4. Ply failure due to shear stresses:

$$f_4(\sigma, d_4, r_4) = \left(\frac{\langle\sigma_{22}\rangle}{Y_T}\right)^2 + \left(\frac{\langle-\sigma_{22}\rangle}{Y_c}\right)^2 + \left(\frac{\sigma_{12}}{S_{12} + \langle-\sigma_{22}\rangle tan\varphi}\right)^2 + \left(\frac{\sigma_{23}}{S_{23} + \langle-\sigma_{22}\rangle tan\varphi}\right)^2 - r_4{}^2 = 0 \qquad \text{6-22}$$

Here, failure due to the tension and compression in the transverse direction (Y_T & Y_C) is considered. Also, the transverse cracking due to σ_{22} is coupled with the in plane shear due to σ_{12} and out of plane shear σ_{23} as shown in Figure 6-19 below:
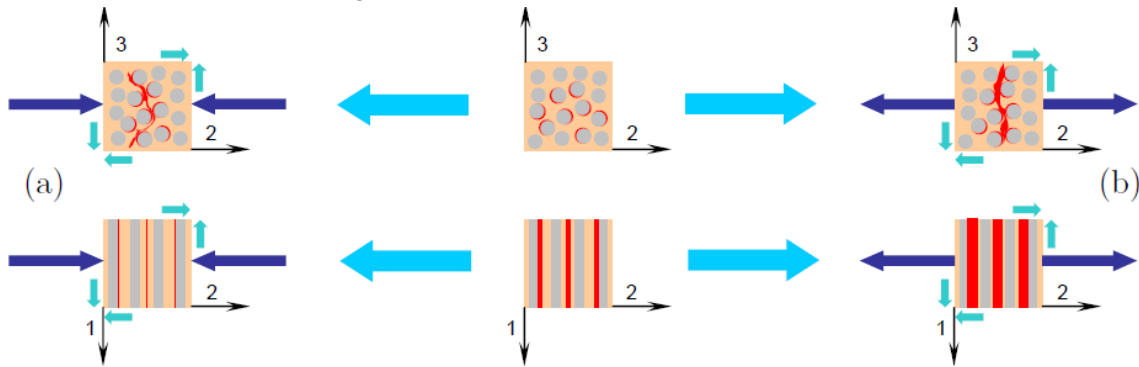
Figure 6-19 (a) Compression and (b) tension in transverse direction

S_{12} and S_{23} are the shear failure stresses in $1-2$ and $2-3$ planes. The failure criteria take into account the difference in mechanical behaviour due to opening or closing of the cracks. The parameter $tan\varphi$ is equivalent to a friction coefficient when the material is loaded in compression. Therefore, the material shear strength is enhanced proportionally to the compressive load.

5. Interface failure (delamination)

$$f_5(\sigma, d_5, r_5) = \left(\frac{\langle\sigma_{33}\rangle}{Z_T}\right)^2 + \left(\frac{\sigma_{13}}{S_{13} + \langle-\sigma_{33}\rangle tan\varphi}\right)^2 + \left(\frac{\sigma_{23}}{S_{23} + \langle-\sigma_{33}\rangle tan\varphi}\right)^2 - r_5{}^2 = 0 \qquad \text{6-23}$$

The objective of this criterion is to handle the out-of-plane tensile failure related to out-of-plane tensile strength (Z_T). This failure mechanism is mainly associated to delamination. Coupling is made with the out of plane stress σ_{33} due to compression with the shear stresses σ_{13} and σ_{23}, respectively parallel and perpendicular to the fibre direction.
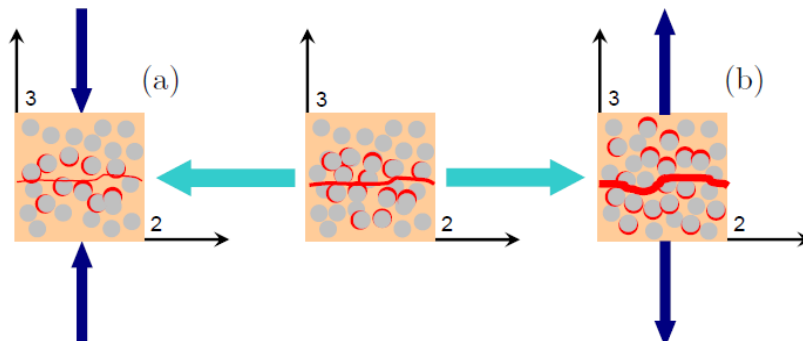
Figure 6-20 (a) Compression and (b) tension in out of plane direction

This last failure criterion, and more generally criteria related to out-of-plane damage, will not be used in our simulations, as the delamination is taken into account by the cohesive surfaces.

The damage variables d_i are calculated [146] as a superposition (q_{ij}) of the different failure modes r_j contribution defined through probability growth functions φ_j:

$$d_i = q_{ij}\varphi_j, j = 1 \dots 5 \; with \; \varphi_j = 1 - e^{\frac{1}{m_j}\left(1-r_j^{m_j}\right)} \; if \; r_j \geq 1 \qquad \text{6-24}$$

m_j has the effect of a softening parameter. Its value is obtained by comparison with tests in order to represent the brittleness or softness of fracture for each failure mode. So it is possible to choose different values for each criterion. In our study, we chose a unique value of m=10 as done by Soulas [11].

The operator q_{ij} is defined in order to choose the failure modes that will contribute to the damage variables d_i [11]. It must also be derived from test campaigns. We used the matrix derived by Soulas.

$$q_{ij} = \begin{bmatrix} 1 & 1 & 0 & 0 & 0 \\ 0 & 0 & 1 & 1 & 0 \\ 0 & 0 & 0 & 0 & 0 \\ 0 & 0 & 0 & 1 & 0 \\ 0 & 0 & 0 & 0 & 0 \\ 0 & 0 & 0 & 0 & 0 \end{bmatrix} \qquad \text{6-25}$$

Again, as the damage in the out of plane direction (direction 3) will be managed by the cohesive surfaces, d_3 related to E_{33}, d_5 related to G_{23} and d_6 related to G_{13} are "switched off". Then, d_1 that will lower E_{11}, is influenced by failure modes purely along the fibre in tension (r_1) and in compression (r_2). For d_2 that will lower E_{22}, we consider the contribution of the spherical compression (r_3) and that of the compression and tension in the transverse direction (r_4). Finally, the plane shear modulus G_{12} is influenced only by r_4. In conclusion, the variables d_i for the damage definition of the CFRP under lightning impact are:

$$\begin{cases} d_1 = \left(1 - e^{\frac{1}{m_1}\left(1-r_1^{m_1}\right)}\right) + \left(1 - e^{\frac{1}{m_2}\left(1-r_2^{m_2}\right)}\right) \\ d_2 = \left(1 - e^{\frac{1}{m_3}\left(1-r_3^{m_3}\right)}\right) + \left(1 - e^{\frac{1}{m_4}\left(1-r_4^{m_4}\right)}\right) \\ d_4 = \left(1 - e^{\frac{1}{m_4}\left(1-r_4^{m_4}\right)}\right) \\ d_3 = d_5 = d_6 = 0 \end{cases} \qquad \text{6-26}$$

All the parameters used in the VUMAT law for CFRP ply damages are defined in Appendix D. In the material definition, three data parameters must be provided: the density, the user material mechanical constants and the number of solution-dependent variables, including the variable number controlling element deletion. The mechanical constants are elastic mechanical properties of the composite but also parameters involved in the damage law such as softening parameters, damage criteria… The solution-dependent variables are used to update the failure criteria, damage parameters and the stresses and strains in each finite element.

6.4. Lightning equivalent load

In this first step, only the composite substrate is modelled and an overpressure profile with prescribed space and time evolution will be applied on its top surface.

6.4.1. Surface VDLOAD

Because the pressure load on the top face of the composite surface is not constant in time and space, we need to use a user subroutine that will allow us to define the magnitude of the load in Abaqus/Explicit® with a space-time function. As explained earlier, one of the main contributors is the overpressure generated by the rapid vaporization of the metallic lightning strike protection that covers the composite aircraft surface and aims at diverting lightning current. Our focus is on ECF195 which is mainly used for lightning protection. Based on the development detailed in 4.1.2, the lightning strike protection is approximated in this part by a web of wires of Ø125µm for this configuration. Each wire is considered as a source of overpressure dependent on current density, which will generate Joule heating, which is assessed as follows:

$$J_n = {I_n}/{S} \qquad\qquad\qquad 6\text{-}27$$

with I_n, the total injected current (100kA for waveform D) divided by the number of wires in intersection with the vaporization profile and S, the section of the wire. In chapter 3.2, the vaporisation profile was obtained thanks to high speed camera measurements through transparent GFRP panels. The boundary of this profile is recorded every micro second and is superimposed on the ECF pattern in order to count the number of intersections as shown in Figure 6-21 below:
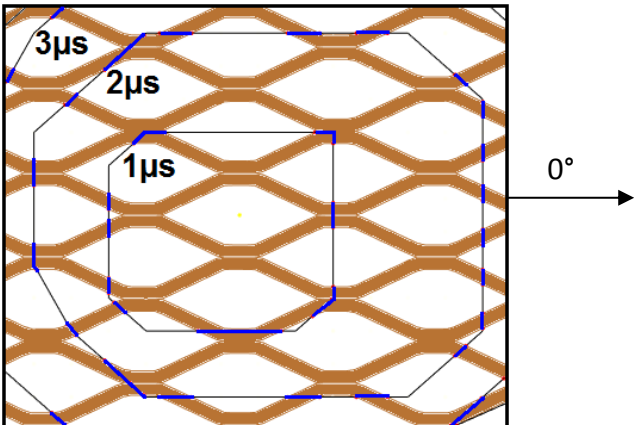
Figure 6-21 Vaporisation profile intersection with ECF

Since the measurement of the vaporisation profile is noisy due to the filter dependency on light intensity which varies during the test, a smooth profile with linear functions was developed. For this purpose, the vaporisation profile was converted into the polar coordinate system and a radius function was defined per angle degree as follows:

$$R(\theta, t) = R_{max}(\theta)\left(1 - e^{-\alpha(\theta)\times t}\right) \qquad \text{6-28}$$

with θ the angle, from 1 to 360°, t the time of the vaporisation profile expansion, R_{max} the maximum radius reached at θ angle direction and α a fitting parameter dependent on the angle. The function is therefore continuous with time and starts at zero:
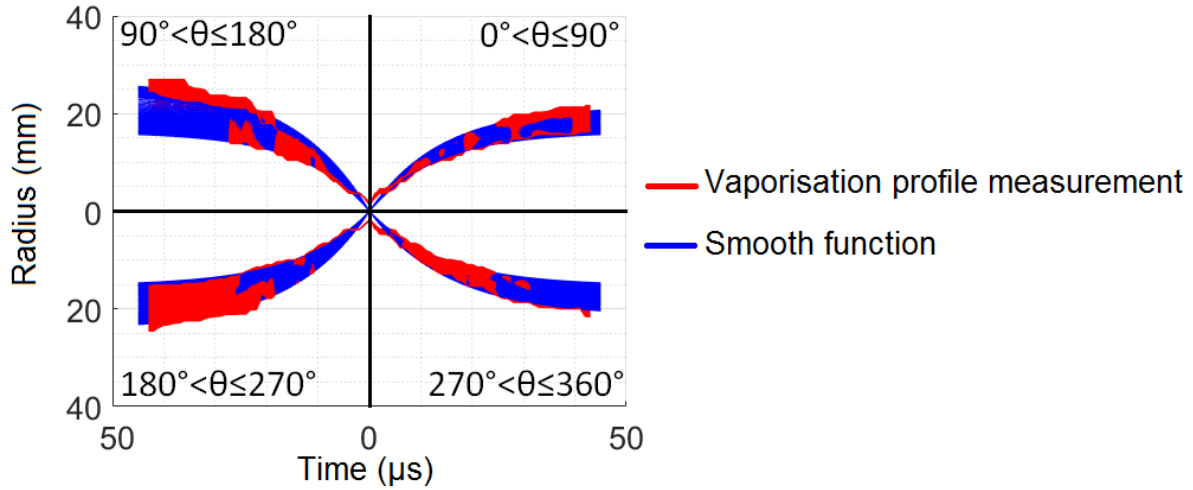
Figure 6-22 Radius fitting function - Angle view

The main advantage of such a definition is that it is independent from the picture sampling per μs and that it removes the variability due to measurement error, giving an increasing profile with time. This linearization of the spatial distribution of the vaporisation profile is illustrated in Figure 6-23 where the profile is projected on the time axis:
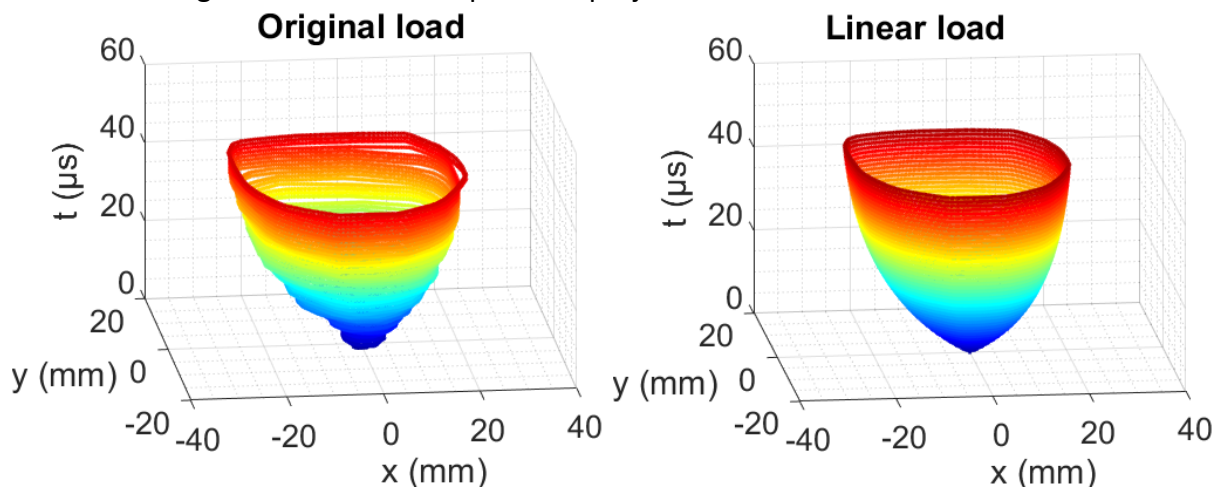
Figure 6-23 Vaporisation profile linearization

Based on this linearization of the spatial vaporisation, we can now assess the number of intersections per wire of ECF at each time step. With this number, a current amplitude per wire can be defined by considering a homogenous distribution of the current along the vaporisation boundary in each wire in intersection at a given time.
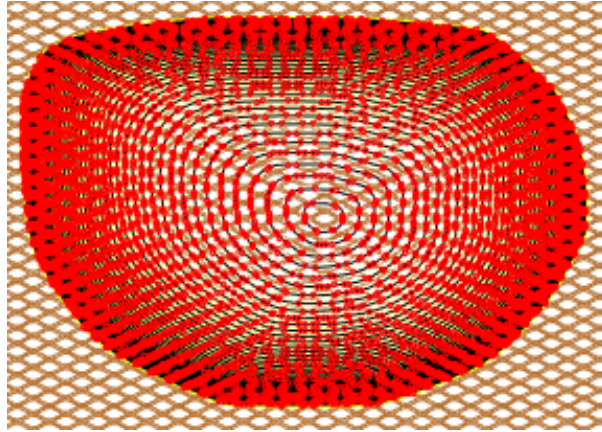
Figure 6-24 Intersection detection with linear vaporisation profile (ECF195+400µm of paint)

Based on the relation defined in 4.2.1.4, we can relate the pressure peak amplitude of the wire explosion to the current amplitude flowing in it based on experimental tests. Then, based on the vaporisation profile defined in the section, we have a relationship between the explosion time and the current amplitude in the wire I_n. Therefore, we can relate the pressure peak directly to the explosion time along the vaporisation profile in order to simplify the VDLOAD as presented in Figure 6-25.
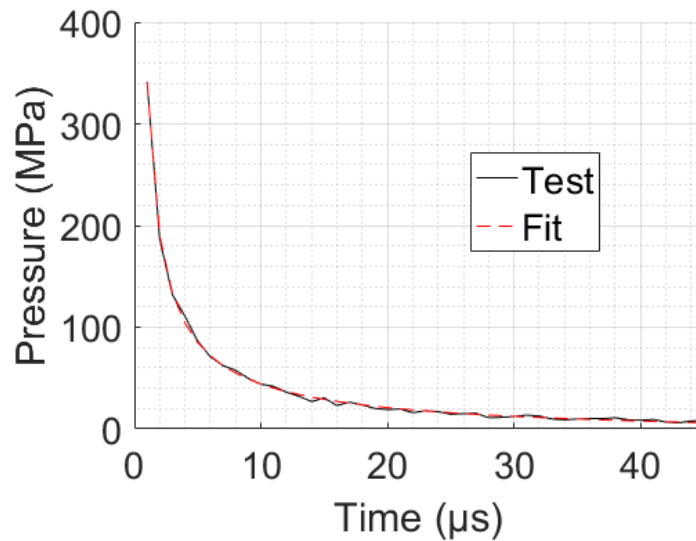
Figure 6-25 Shock wave peak pressure dependency on the explosion time

Knowing the vaporisation profile spatial distribution at each time step, we can associate the peak pressure amplitude with a polynomial function dependent on the explosion time:

$$P_{exp}(t_{exp}) = p_1 t_{exp}^{p_2} + p_3 \qquad \text{6-29}$$

with t_{exp} the explosion time of the wire along the vaporisation profile in µs, P_{exp} the associated peak pressure in MPa. p_1=350.64812 (MPa.µs^{-1}), p_2=-0.81381945 and p_3=-9.6754547 (MPa) for this configuration of the ECF195 vaporisation profile confined by 400µm of paint. This process will be performed for each configuration of LSP and paint thickness since it will change the vaporisation profile, the explosion time and the peak pressure amplitude with the current density.

This function 6-29 will be useful for the VDLOAD, to prescribe the pressure load in each finite element at each instant. Note that, nevertheless, it uses the initial position of the grid to determine the maximum pressure. Consequently, to apply the corresponding pressure, it is necessary to locate the initial position of the application point.

Indeed, in reality, during the load application, a deflection of the sample will occur, thus in the numerical model the finite element mesh cells are expected to move as well from their original position. Therefore, the comparison of the element location with the vaporisation profile distribution will lead to "jumps" in the load condition and an unexpected variation of the pressure with time. Unfortunately, in the source file of an Abaqus® VDLOAD subroutine, it is not possible to identify each mesh element number individually which could have been an easy way to locate its initial position and assign a pressure history. In order to solve the issue, the VDLOAD was not applied on a single top surface but on several surface elements. To achieve this, the mesh coordinates of the composite front surface defined in the Abaqus® '.inp' file were reviewed and superimposed with the space-time vaporisation profile. Each square mesh face of 0.5mmx0.5mm, that is included in the total load profile, was clearly identified and an explosion time was associated. In this case, 4429 elementary surfaces were defined. The '.inp' file was modified to include the elementary surfaces, called "Surf_XXXX" with XXXX the element number defined, and its associated load called "Load_ XXXX". Apart from the '.inp' modification, a text file was created in which an explosion time is associated to the load n°XXXX. During the computation, the VDLOAD applies the load XXX on the associated surface XXX with an amplitude dependent on its associated explosion time. The VDLOAD subroutine calls the text file and identifies the explosion time. Therefore, each load cell is identified and its maximum pressure can be defined thanks to the equation 6-29 established above based on its explosion time.
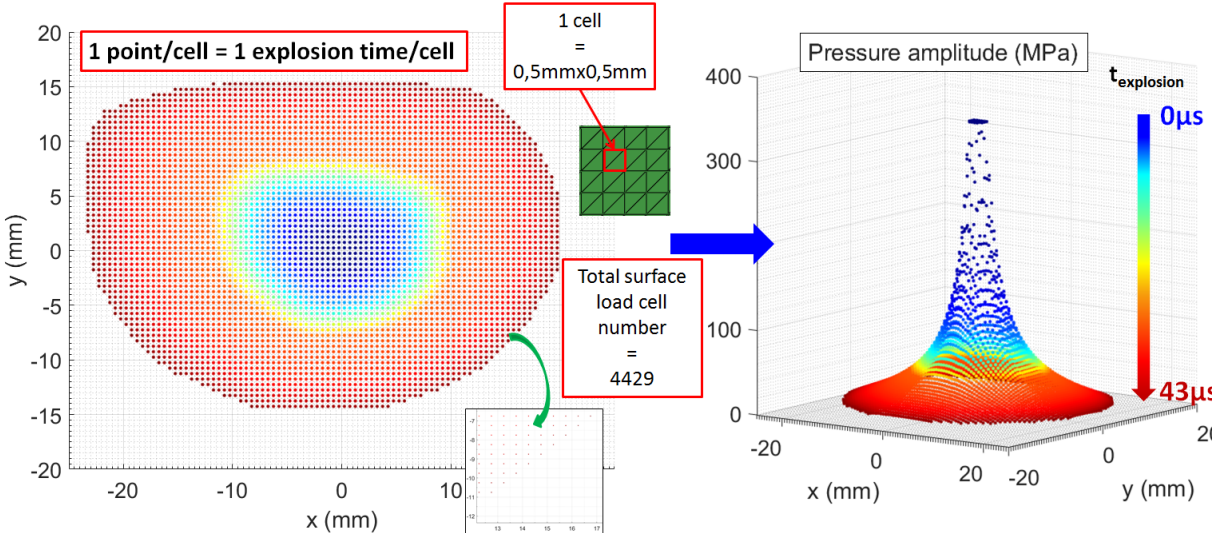
Figure 6-26 Vaporisation profile projection on mesh grid

As shown in Figure 6-26, the vaporisation profile defined as a function of time t and space (x,y) was projected and the explosion time is identified at the centre of each cell. One cell is one square of the mesh on the top face of the composite panel modelled. In our case, the

first composite ply orientation is oriented at 45°, therefore one cell is made of 2 prismatic finite elements' top faces.

The pressure profile per cell will be defined as shown in Figure 6-27. Before the explosion time associated to the cell, no pressure is applied. Then, the pressure linearly increases up to its maximum as defined by equation 6-30 in $\Delta t_{peak}=0.1\mu s$. In theory, the time to peak for a shock wave is considered null but a small Δt is introduced to limit numerical discontinuities. After reaching its maximum, the pressure decreases. The decrease shape and duration (Δt_{decay}) should depend on the confinement. For a free explosion of the LSP, i.e. an unpainted panel, the pressure shape is considered similar to the shock wave law as defined in 4.2.1.3.2 (Friedlander equation):

$$P(t) = P_{exp}e^{-(t-t_{explosion})/\Delta t_{decay\_free}} \times \left(1 - \frac{(t-t_{explosion})}{\Delta t_{decay\_free}}\right) \qquad 6\text{-}30$$

The decay time Δt_{decay_free} is considered dependent on the amplitude of the explosion where the decay is longer with the pressure amplitude decrease. For a confined configuration where a paint layer is present above the LSP and confines the gas of the explosion, this quick decay of the pressure cannot be considered anymore. Several shapes of pressure decay dependent on decay duration were tested and will be presented in the next section. The decay duration is defined dependent on the pressure ratio between the maximum pressure P_{max} that will be applied on the panel, corresponding to the most central area where the current density is the highest, and the cell pressure of explosion P_{exp}. Indeed, our hypothesis is that a high pressure amplitude will quickly eject the paint above and release the pressure. In the meantime, the pressure is almost fully maintained. When the pressure produced by the explosion decreases as the Joule heating in the LSP is lowered, it will delay the ejection of the paint and the pressure will be applied during a longer period.
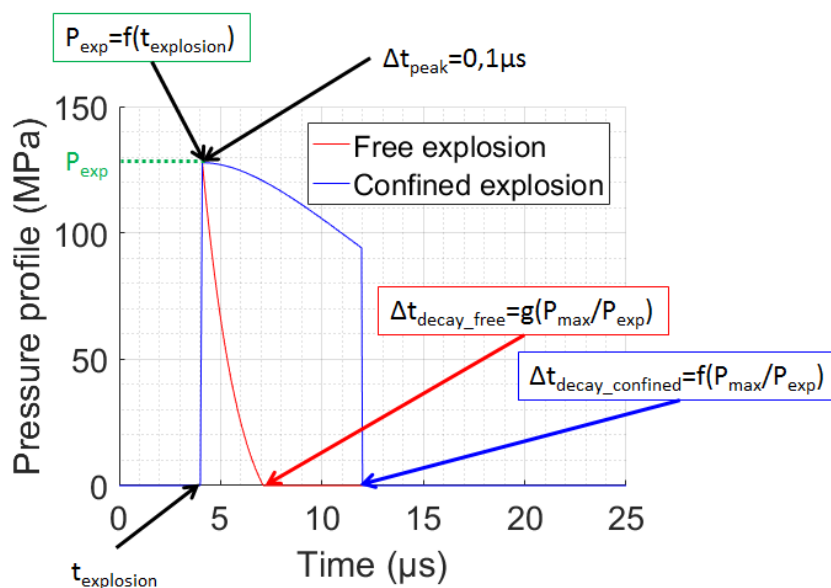
Figure 6-27 Pressure profile for VDLOAD

6.4.2. Results and analyses

6.4.2.1. Surface explosion validation

In order to validate the contribution from the surface explosion only, a simulation for GFRP panels was performed. As already mentioned, specific lightning tests have been performed in laboratories where different LSP have been applied on a GFRP substrate which has the main advantage of being highly resistive. Therefore, all the lightning current will flow in the metallic protection, leading to its explosion. With this configuration, no delamination or Joule heating occur in the laminate, thus the substrate can be simulated with a simple elastic behaviour. In Abaqus/Explicit®, a single layer of shell finite elements (S4R) with GFRP elastic material properties, as defined in Table 6-5, and a user defined load (VDLOAD) on the top surface were implemented, as defined above.

Property	Density	E_{11}	E_{22}	G_{12}	G_{13}	G_{23}	ν_{12}	Ply thickness	Ply number	Stacking
Value	$1{,}88.10^{-3}$	24	24	4.8	4.8	4.5	0.28	0.25	11	0° for all plies
Unit	g/mm^3	GPa	GPa	GPa	GPa	GPa	N/A	mm	N/A	N/A

Table 6-5 GFRP material properties

This model simulates a GFRP panel bonded in the same approach as presented in 6.3.1. A composite layup is defined in the shell property to simulate the 11 plies in the unique shell layer. The mesh details are given below:

No. of elements	Element type	No. of nodes	DOF
64,090	S4R	155,026	930,156
181,468	S3		

Table 6-6 GFRP shell mesh details

The VDLOAD subroutine is used to apply a pressure profile dependent on time and space as described earlier. The only unknown is the decrease in the pressure when the metallic explosion is confined by paint or free. We have thus simulated several load configurations in order to assess the influence of the decay on the panel deflection.

In a first step, we considered the free explosion of the LSP with different decay times Δt_{decay}. It was not possible to use the method defined in 3.2 to derive a space-time vaporisation profile, since the light coming from the arc column was not filtered in the absence of paint and disturbed the light capture. Therefore, we used the vaporisation profile simulated with COMSOL® as defined in 3.3.2.2 since it presented good correlation with the experimental melting profile. The pressure decay follows this law:

$$P(t) = P_{exp}e^{-(t-t_{explosion})/\Delta t_{decay}} \times \left(1 - (t - t_{explosion})/\Delta t_{decay}\right) \qquad \text{6-31}$$

The displacement due to a free explosion of ECF195 is very limited. For the GFRP configuration, the maximum displacement after 100μs is only around 1mm compared to almost 4mm for a confined explosion with 400μm of paint as shown in Figure 5-7. Considering a uniform decay time over the loaded faces no matter what the explosion pressure amplitude, or considering a decay time inversely proportional to the peak pressure resulted in displacement profiles that were never really comparable to the test result: the displacement profile was too sharp at the start of the deflection, then too slow and the displacement away from the vaporisation profile area was not negligible compared to the central area. This led us to the conclusion that a contributor was missing, and we surmised that it could be the acoustic shock wave from the arc column. We therefore added this pressure to the LSP explosion pressure taking into account the definition proposed by Karch [35]. This is an easy-to-use and very pragmatic approach which does not consider any Magneto-Hydro-Dynamic (MHD) effect but provides and gives the correct order of magnitude and can be implemented easily in a VDLOAD. The spatial distribution is a growing disk of a radius R depending on time:

$$R(t) = 1.004 \times \left(\frac{E_0}{\rho_0}\right)^{0.25} \sqrt{t}$$

with ρ_0 the initial air density (kg/m^3) and E_0, the initial arc energy density (J/m). The latter parameter is a function of the maximum amplitude of the lightning current I_{max}:

$$E_0 = 0.45 \times 10^{-2}(I_{max})^{1.25}$$

Then, the amplitude of the shock wave can be defined as follows:

$$P(\eta, t) = 0.18 \times (\rho_0 E_0)^{0.25} \times \frac{f(\eta)}{t}$$

with f(η), defined in [64], a dimensionless shape function dependent on the ratio of the radius within the pressure disk and the shock front radius: η=r/R(t). The shockwave pressure is shown in Figure 6-28, from 1μs to 100μs, illustrating that a pressure is maintained after the shock front passage and slowly decreases:
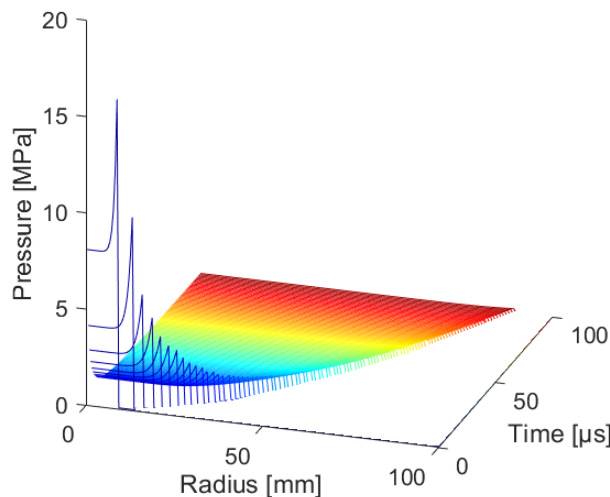
Figure 6-28 Shock wave pressure distribution

Looking at the contribution of the shock wave only on the panel deflection, we can conclude that its contribution is about half the maximum displacement, and so is not negligible compared to a free surface explosion, as illustrated on Figure 6-29:
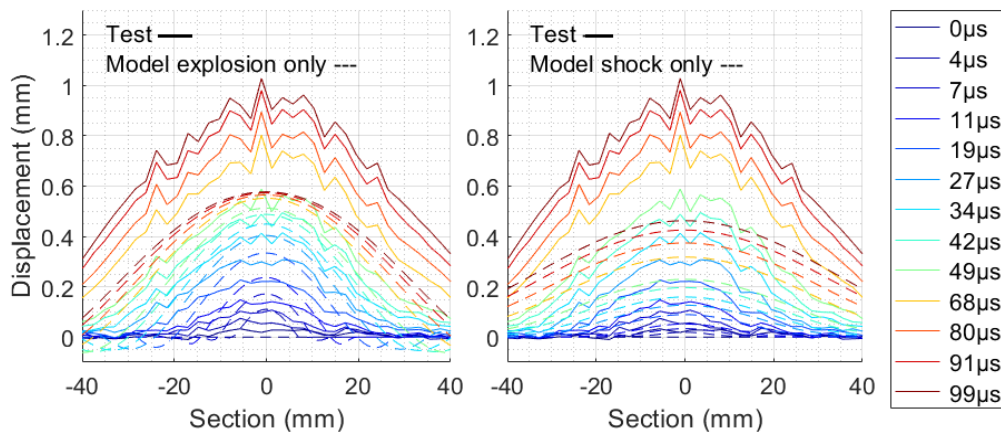
Figure 6-29 GFRP displacement comparison between free explosion lightning test and simulated contribution of explosion only (left) or shock only (right)

Finally, summing both contributions of the arc shock pressure coming from outside the LSP and the explosion of the LSP, the displacement of the GFRP panel, protected with ECF195, unpainted and subjected to lightning waveform D is well simulated (see Figure 6-30). The decay time for the explosion is inversely proportional to the peak pressure and the minimum decay time in the centre is equal to 0.85µs. A comparison of rear face deflections with the LSP surface explosion alone and with the addition of the shock wave is presented in Figure 6-30. Since the explosion is quickly released, the overpressure generated on the panel is limited, hence the need to take into account the shock wave overpressure which lasts longer. Further investigations using the combined overpressure will be presented in § 6.4.2.2.
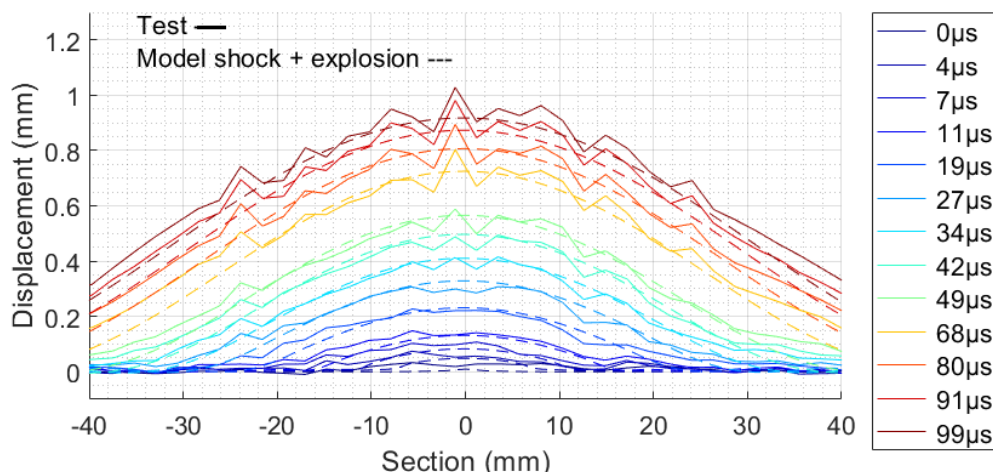
Figure 6-30 GFRP displacement comparison between free explosion lightning test and simulated contribution of explosion and shock wave

In a second step, we will now consider a more complex configuration: the displacement of a GFRP panel, protected with ECF195 and painted. For this case, the deflection of the panel will be enhanced since the surface explosion is confined by the presence of the paint. Adding

only the same pressure as for an unpainted plate subjected to the shock is no longer valid because the paint confines the explosion pressure which is also different due to the arc constriction. The space-time distribution comes from the vaporisation profile measurement as explained in section 3.2. It is therefore necessary to propose another method to estimate the pressure decay after the maximum value given by the explosion.

In order to compare the influence of different explosion profiles with the lightning test result, we chose to consider two criteria of the panel displacement. First, the maximum rear face displacement which occurs at the centre and second, the maximum of the deflection slope ε as defined in Figure 6-31, will be recorded. The maximum slope is computed on the horizontal and central cross section of the centre point displacement profile.
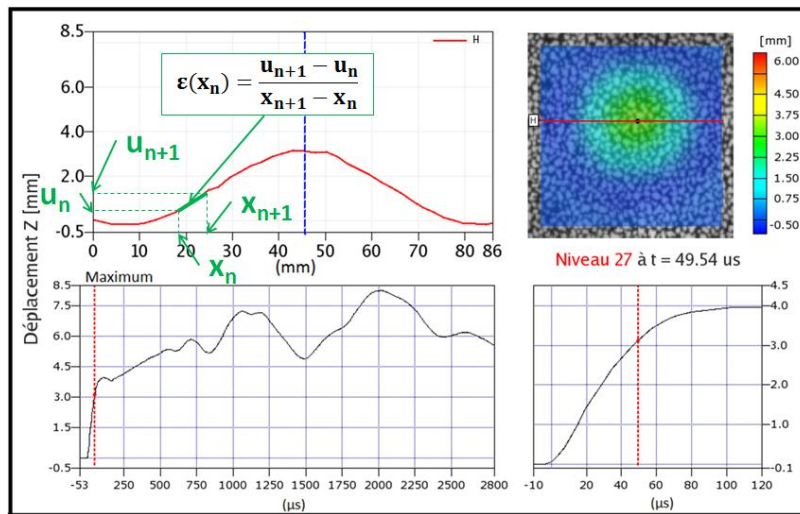
Figure 6-31 Maximum strain definition

Since the effect of the confinement on the explosion is not fully known, different pressure decay waveforms are considered and implemented as a surface load through a VDLOAD. The first configuration sets a constant decay time Δt_{decay} for all elementary loads, whatever the pressure amplitude. The different decay times considered were 25, 20, 15, 10 and 3.2µs. The pressure decay followed the defined law:

$$P(t) = P_{exp}e^{-(t-t_{explosion})/\Delta t_{decay}} \times \left(1 + (t - t_{explosion})/\Delta t_{decay}\right) \qquad 6\text{-}35$$

On Figure 6-32, it is clearly visible that a uniform decay time cannot generate the equivalent overpressure. Compared to the test, the max slope is too steep in the early stage as for the maximum displacement. The configuration that is closest to the maximum of displacement and slope in the latest stage is the configuration with 15µs of decay. This approach cannot represent the overpressure generated on the whole surface. The paint will be ejected depending on the stress generated by the overpressure on the paint. As this overpressure decreases with the current density decrease in the ECF, the paint will take longer and longer to be ejected. The decay time will thus increase with the increase of distance from the centre.
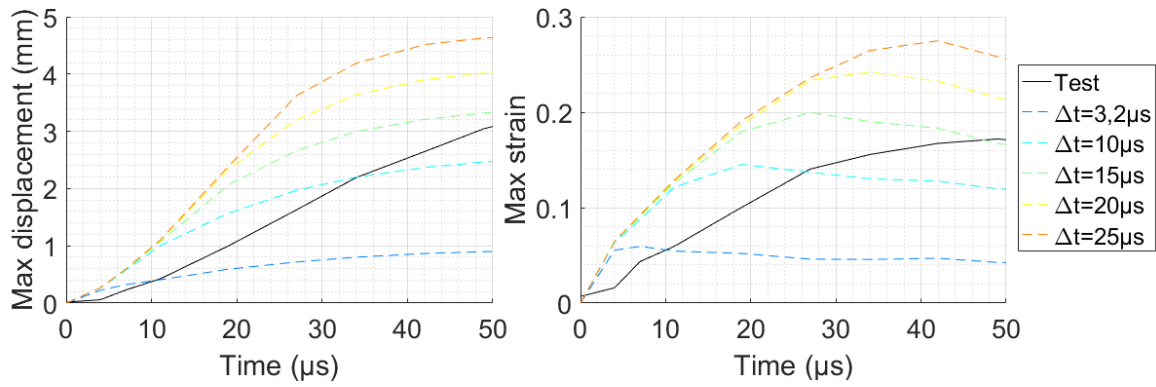
Figure 6-32 Overpressure sensitivity analysis with constant decay time

The second configuration considered has a decay time Δt_{decay} which increases with the inverse of the pressure decrease. Several values chosen a priori were considered: 1, 2, 3, 5 and 10µs. As shown in Figure 6-33, the law which provides the closest deflection behaviour is the one with the minimum decay of 3µs in the centre but again, the max slope and displacement are higher in the early stage.
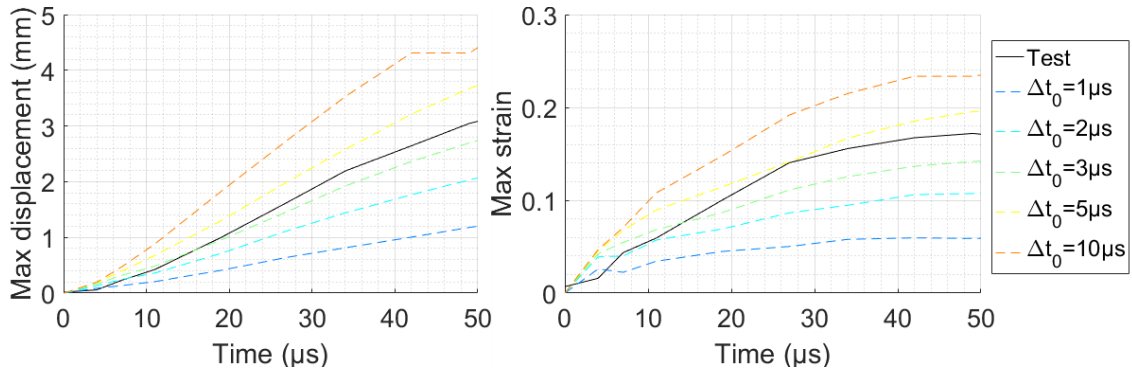
Figure 6-33 Sensitivity analysis of overpressure with inverse decay law – max strain

For this configuration, no shock wave is applied since its contribution cannot be applied directly on the panel, no matter what the configuration of the explosion since the ejection of the paint will disturb the overpressure applied after the shock front. It is too complex to simply add it as another contributor of the total overpressure to the LSP explosion. In our approach, we simulate a confinement of the paint with a chosen decay time and introducing the shock wave would not make a lot of sense. This approximation should not increase the error significantly since the deflection due to the lightning arc shock wave on the GFRP panel is less than a maximum of 0.5mm after 100µs compared to a total deflection of almost 4mm at the same time when there is a confinement with 400µm of paint. The final decay law chosen for this specification configuration is:

$$\begin{cases} \Delta t_{decay} = \Delta t_0 \left(\dfrac{P_{max}}{P_{exp}} \right)^{\alpha} \\ \Delta t_0 = 3 \text{ µs and } \alpha = 0.8 \end{cases} \qquad 6\text{-}36$$

P_{max}=max(P_{exp}) is the maximum pressure explosion reached in the centre where the current density in the copper wire is the highest. Δt_0 is the decay time in the centre and the shortest one to represent the fastest paint release due the highest explosion pressure.

The parameter α drives the decay time increase with the explosion pressure decrease as shown in Figure 6-34:
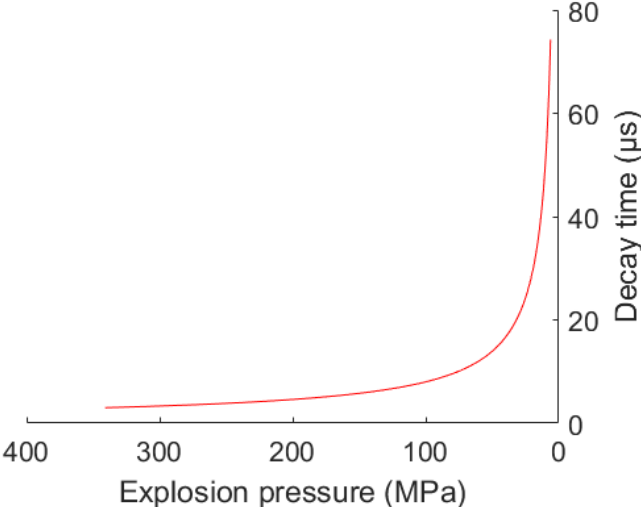
Figure 6-34 Decay time as a function of the explosion pressure

In addition, the pressure profile was linearized as shown previously in Figure 6-23. This pressure profile is the highest in the centre in one point. However, this is not related to any physical phenomenon. Therefore, the pressure load applied in the centre will be on a disk corresponding to the first measured disk in the back light measurement of the vaporisation profile (see 3.2.2). The diameter of this disk is smaller than 4mm.

The deflection measurement of the GFRP panel protected with ECF195 and confined by 400μm of paint during the lightning test performed with WFD is compared with our simulation with the VDLOAD following the decay law defined in Equation 6-36 and is presented in Figure 6-34:
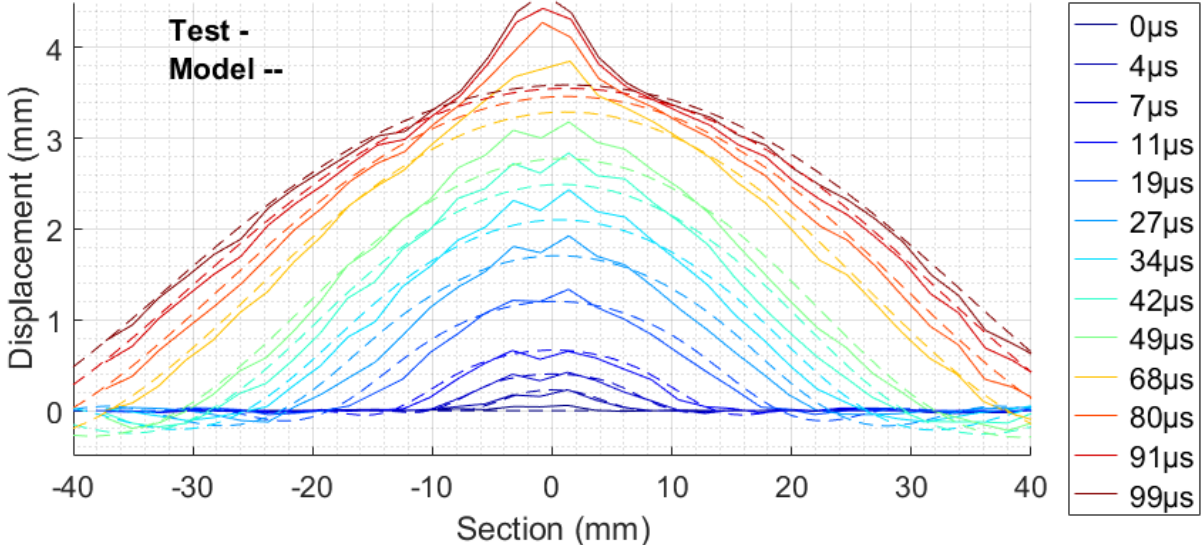
Figure 6-35 GFRP displacement due to ECF195 explosion confined by 400μm of paint with WFD: Test vs shell

The small bump than can be observed in the central area of the test panel deflection is likely related to the ejection of the paint used for the DIC pattern. This disturbs the profile

reconstruction but should not be interpreted as a real local displacement. The deflection profiles between the test and the model are fairly similar. The maximum and the width of displacement are very close. The only main differences concern the maximum strain, as defined in Figure 6-31, and the waves on each side of the main deflection which are more pronounced in the model than in the test. But this is likely to have second order effect on the damage generation.

The maximum amplitudes of the explosion generated by each ECF wire are of key importance in determining the overpressure profile but this is also the case for the decay profile. The sensitivity analyses presented above are extracted from a modelling experimental design considering several decay laws. In order to build the representative law, it will be necessary to simulate the confining effect of the paint and the mechanical constraints necessary to eject the paint. For this purpose, mechanical characterization tests of the paint and of the paint adhesive resistance were performed and were presented in chapter 5. This approach will be detailed in section 6.5.

6.4.2.2. Effect on a CFRP laminate and damage analysis

The interest of the work done previously was to study the deflection of a panel that has no interaction with the lightning arc. A GFRP panel is highly resistive, therefore all the current from the lightning arc will flow in the LSP, leading to its explosion. The comparison between the simulated deflection from our VDLOAD model and the test results presented fairly good agreement. The next step is now to analyse the effect of this overpressure profile on a CFRP structure for which the interaction with the arc is more complex, especially with the presence of paint that will constrain the arc and lead to current injection into the first plies of the CFRP. The current flow in the CFRP which can generate internal damage due to electro-thermal effects was not considered in a first step. In addition, as explained in section 6.2, the overpressure contribution of the CFRP explosion seems very limited compared to the overpressure created by the explosion of the LSP confined by the paint. Therefore, this contribution was not modelled either. Using the same elastic shell model as the one defined for the GFRP analysis, the material properties and the ply configurations were changed to reflect the CFRP configuration, as summarised in Table 6-7:

Property	Density	E_{11}	E_{22}	G_{12}	G_{13}	G_{23}	ν_{12}	Ply thickness	Ply number
Value	$1.58.10^{-3}$	165	8.5	4.2	4.2	3.36	0.35	0.127	13
Unit	g/mm^3	GPa	GPa	GPa	GPa	GPa	N/A	mm	N/A
Stacking	45/-45/90/45/-45/0/90/0/-45/45/90/-45/45								

Table 6-7 CFRP material properties

Considering now the painted configuration, we can observe on Figure 6-36 that the deflection profiles are fairly similar between the test of a painted laminate and the simulation of an elastic laminate in the early stages, but not after 60µs. With this simulation with a simple elastic law, since no damage is allowed, the stiffness of the panel is kept constant. But we know that damage and delamination occur early during the lightning test. This delamination can explain the higher deflection profile for the test that is related to the internal damage that reduces the global flexural rigidity of the panel.
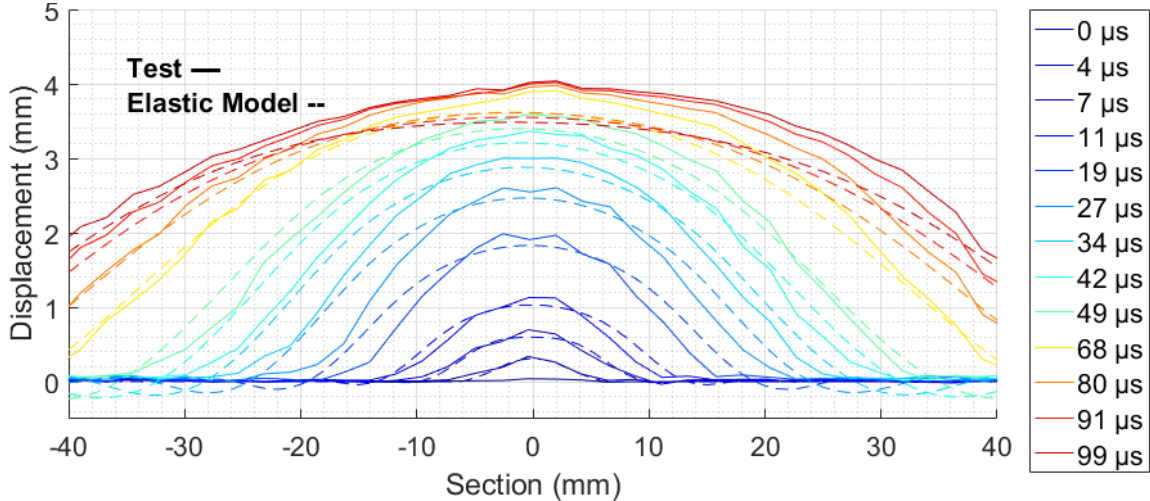
Figure 6-36 CFRP displacement due to ECF195 explosion confined by 400µm of paint with WFD: Test vs shell

In order to assess this point, we will analyse a 3D model as defined in section 6.3 with a user material law in order to simulate the damage in the ply and cohesive interaction to simulate the delamination between each ply. We first validated that there was no difference between the shell model used for our VDLOAD definition and the 3D model with solid elements that will be used for the damage assessment. For this purpose, we applied the same load for the 3D model where no damage was allowed. This means that the solid element behaviour is based on an elastic law and the interactions between the plies are tied, such that no delamination is possible. The review of the deflection profile between the shell and the 3D model is presented in Figure 6-37. The behaviour is almost identical, which validates that the differences between a 3D and a shell model is negligible.
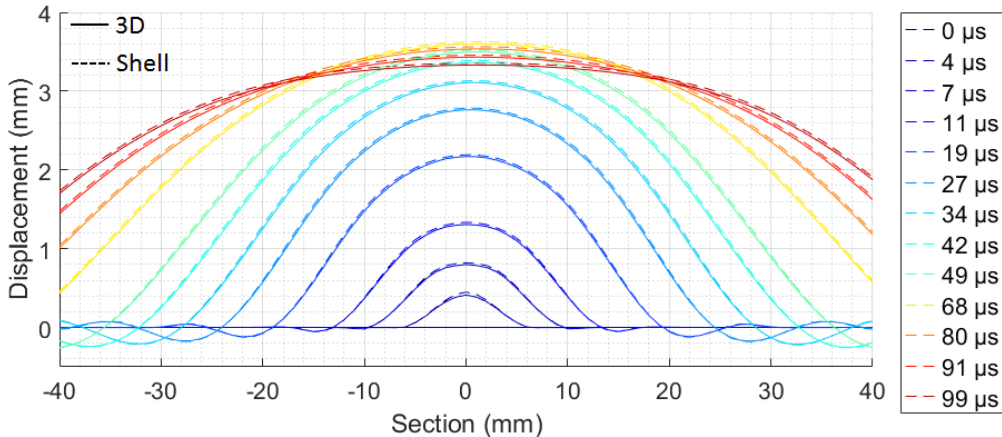
Figure 6-37 CFRP displacement due to ECF195 explosion confined by 400µm of paint with WFD: 3D vs shell

With the introduction of damage in the ply through the VUMAT, the deflection is slightly sharper but the maximum is still reached after 50µs, as shown on the left of Figure 6-38. With this configuration, delamination is not allowed and the damage model is therefore not complete. For this purpose, cohesive interfaces were added but the delamination is too severe, which severely impacts the deflection. As shown on the right side of the figure, this parameter leads to an unrealistic deflection and damage.
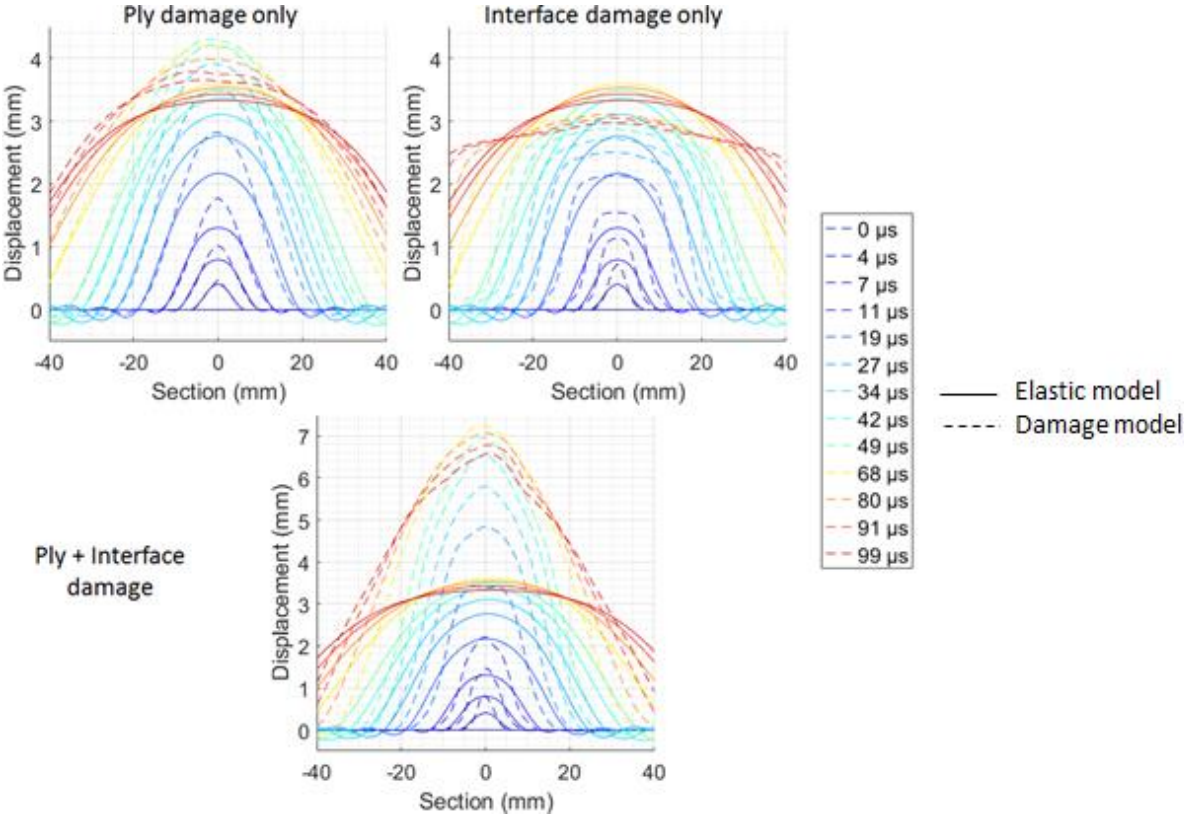
Figure 6-38 CFRP deflection (ECF195+400µm of paint) comparison to elastic model with damage models

The calibration of the cohesive interface is based on a static test to assess the stress for the damage initiation in normal and shear mode but also the strain energy for the crack propagation when open. As the explosion of the LSP by the lightning current flow generates a shock in the CFRP structure which is far from a static stress, the parameters chosen for our cohesive interface might not be valid under such a dynamic solicitation. The work performed by Berthe demonstrated a dependency of the interface but also of the ply's properties themselves on the strain rate [147]. The characterisation of the interface is also difficult and different values can be found in the literature for the same material [130,134,141]. We therefore decided to consider another type of characterisation for the cohesive interfaces. In comparison to our static characterisation, we modified the damage initiation stress criteria for our dynamic model, multiplying the level by around two [130], as shown in Table 6-8:

	σ_n (MPa)	$\sigma_s = \sigma_t$ (MPa)
Static model	25	60
Dynamic model	60	110

Table 6-8 Cohesive interface - Damage initiation definition

With this type of interface, the comparison of the panel deflection is closer to the test results, as shown in Figure 6-39:
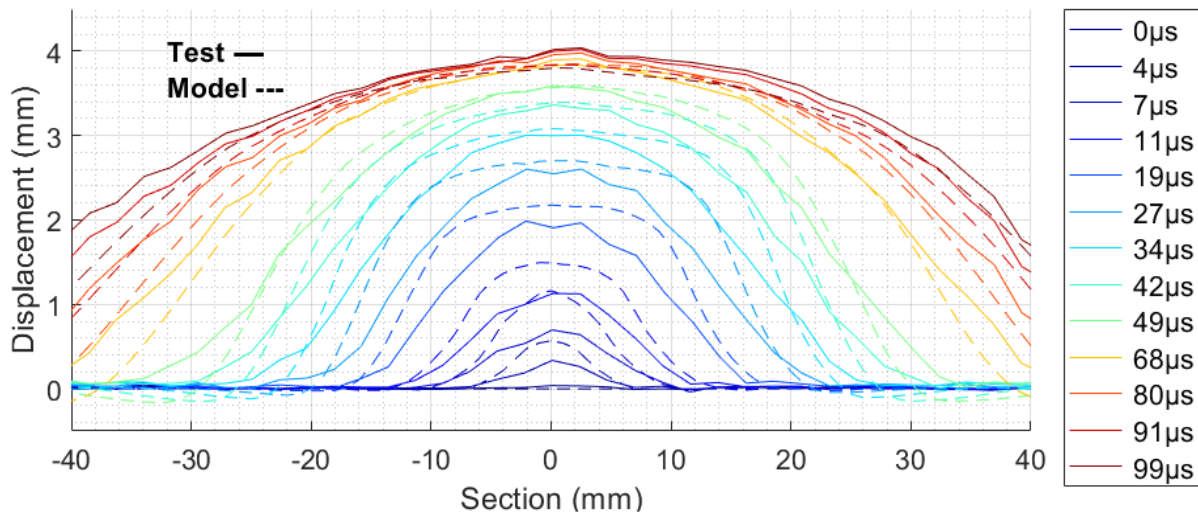
Figure 6-39 CFRP deflection (ECF195+400μm of paint) comparison to model with dynamic cohesive interfaces

However, our main interest is in the damage prediction due to lightning strike. Thanks to the microcuts performed on our tested panel, we can reconstruct the delamination profile interface by interface. Even if this is a destructive measurement, it provides the complete damage profile that NDT cannot give. Also, since the cuts are performed every 18.5 mm, the reconstruction seems pixelated. For this configuration of CFRP panel, there are 13 plies, therefore 12 interfaces studied. The ply 1 is the top ply, just below the ECF, and the ply 13 is the bottom ply, at the back of the panel. The circle illustrates the mechanical boundary conditions of the panel, a clamping on a circular window with a diameter of 370mm using 12 bolts, as shown in Figure 6-2. More details are provided in Appendix C. Based on the comparison of the delamination profiles per interface shown in Figure 6-40, it can be seen that our first model based on a static characterisation of the interfaces (i.e. DCB and ENF tests) presents fairly similar damages on the top interfaces but not on the bottom of the panel. In this area, the shock waves are reflected by the back of the panel, leading to a higher stress. With a static interface model, the delamination is therefore very large but this is not what is observed on the tested panel. With a dynamic model in which the initiation criteria are higher due to the type of solicitation, the delamination trend is more representative on the bottom area but not on the top area.
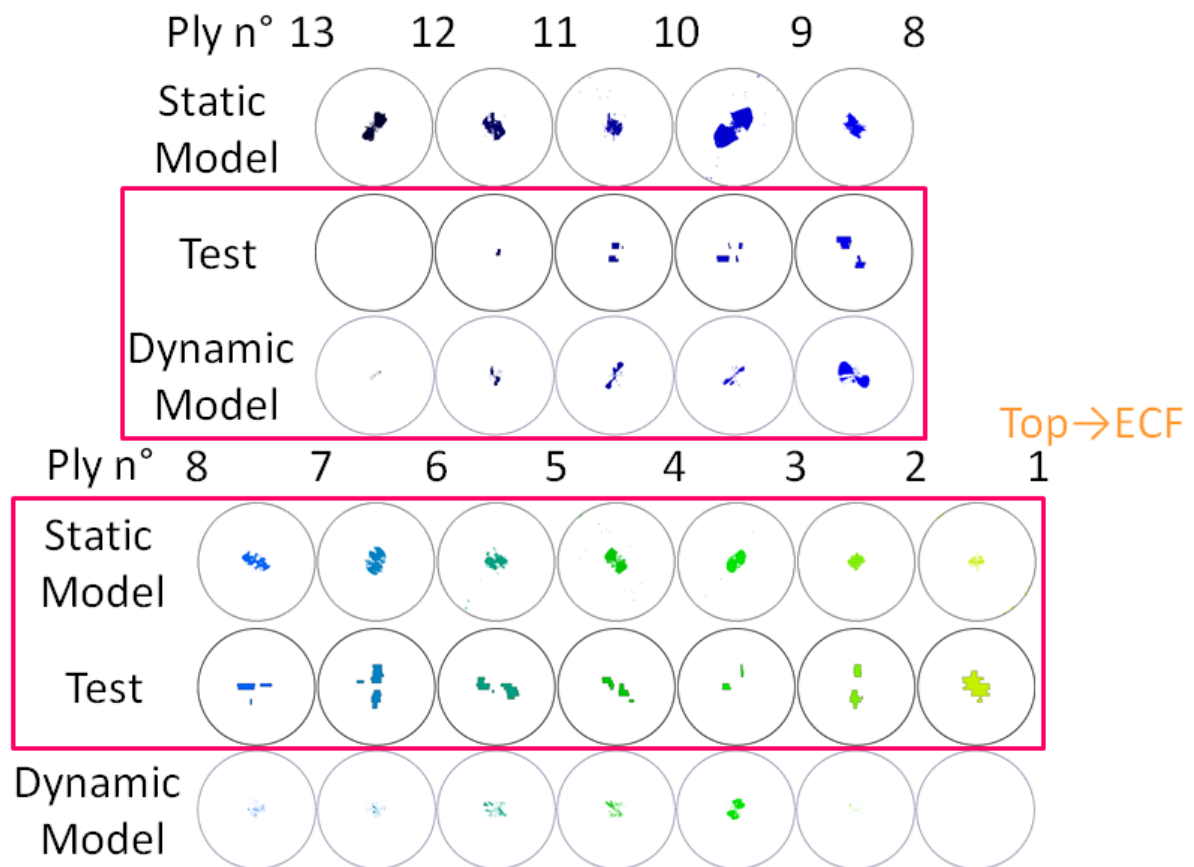
Figure 6-40 Delamination distribution comparison between test and model with different cohesive interface values after 100µs for a CFRP panel made of 13 plies

Finally, neither the static model nor the dynamic model of the interface can predict the total delaminated surface area as presented in Figure 6-41. Indeed, the model of interface does not render the mechanism that lead to the delamination and underestimate the total damage in this configuration.
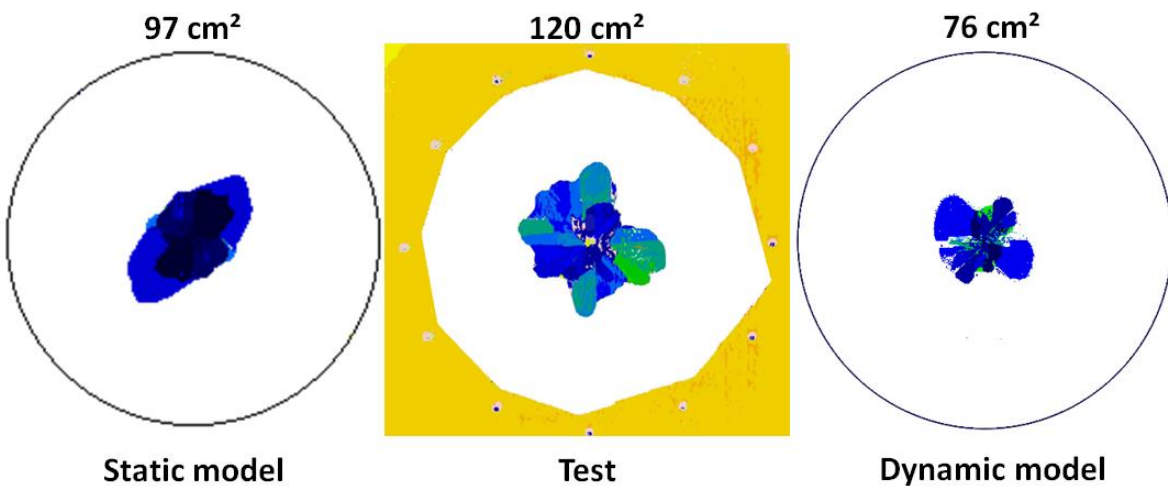
Figure 6-41 NDT comparison between test and equivalent model result (1ms) with static cohesive interface on left hand side and dynamic cohesive interface on right hand side

Therefore, an interface model with constant criteria for delamination is not able to predict the damage distribution. As observed by Berthe [147], a shock generates a different delamination distribution from a static solicitation. The mechanical load generated by a lightning strike and its propagation in the panel is not a purely dynamic solicitation: rather, it is a mixed mode from dynamic to static solicitation. Consequently, the interface model has to consider a dependency of the damage initiation and propagation criteria on the stress rate $\dot{\sigma}$. In order to characterise this tendency, the method proposed by Gay could be used [148]. However, this model is not possible in Abaqus® with the cohesive interface tool. The development of a user-defined law through a subroutine is therefore necessary along with the characterisation of this law with dedicated tests.

6.4.2.3. Effect of explosion confinement

As explained previously, the paint thickness has an influence on the confinement of the LSP explosion. In the previous work, we defined a confinement law for the pressure considering 400μm of paint defined in Equation 6-35 & 6-36. In order to define the parameters of this law, a sensitivity analysis was necessary, requiring the performance of many model computations. However, this confinement law will be different with another paint thickness. In our lightning test campaign, we assessed the damage and deflection of a CFRP panel protected by ECF195 with different paint thicknesses: 250, 400 and 1000μm. In a first simple approach, we consider the effect of the paint on the confinement based on a linear relationship between the initial decay time and the paint thickness:

$$\frac{\Delta t_{0_{\delta \mu m}}}{\Delta t_{0_{\beta \mu m}}} = \frac{\delta \mu m}{\beta \mu m}$$

6-37

The power decay law α was kept identical at 0.8 for all the paint configurations. In addition to adapting the pressure decay law for the pressure amplitude, we used the vaporisation profile measured in Chapter 3 for the spatio-temporal distribution. From chapter 3, the distribution obtained with 200μm of paint, which is close to a diamond shape, was used for the CFRP configuration with 250μm of paint. The distribution with a paint thickness of 550μm is close to an axisymmetric evolution, as shown in Figure 3-21, which means that a higher paint thickness will not change the vaporisation profile significantly. Therefore, this distribution was used for the CFRP configuration with 1000μm of paint. Again, the model used here does not consider damage as it leads to disturbance in the displacement. As with our reference configuration with 400μm of paint, the displacement profile is well predicted by this confinement law dependent on paint thickness.
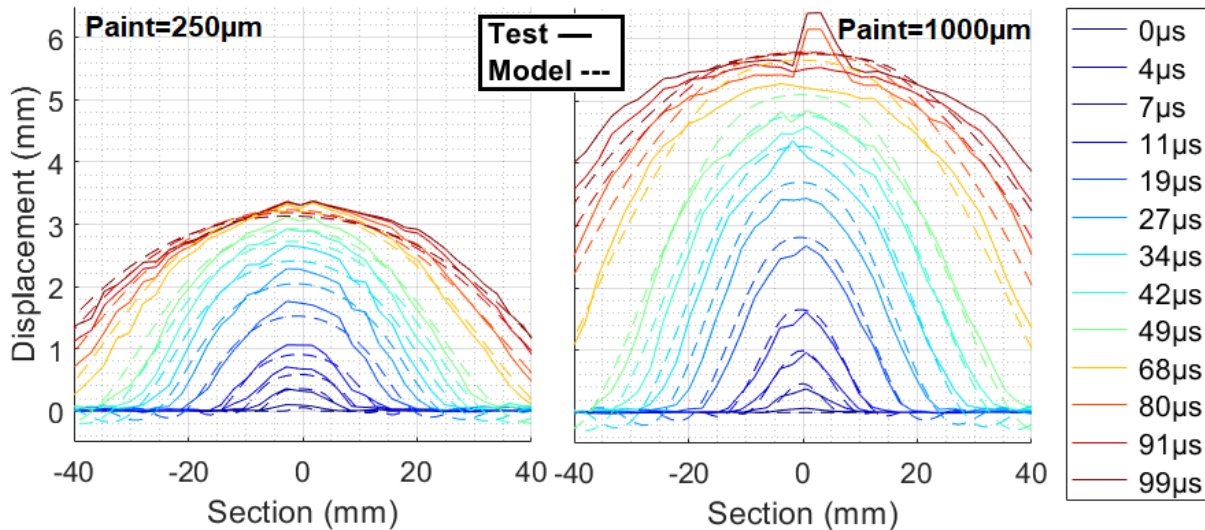
Figure 6-42 Deflection profile comparison between test and model for different paint thicknesses

Now, introducing the damage law, we can analyse the delamination profile obtained with the different simulated mechanical loads. As for the reference configuration, our damage model is not able to predict the damage surface and distribution at the different interfaces. The damage is too deep and too wide for the thin paint configuration (250µm) in our model as shown in Figure 6-43:
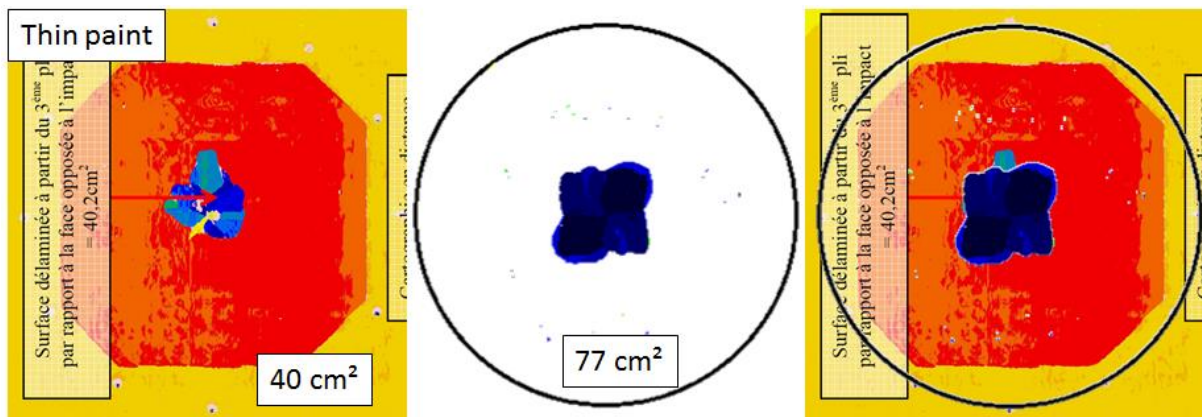
Figure 6-43 NDT comparison between test and equivalent model result (1ms) with static cohesive interface for thin paint configuration (Left: Test/Middle: Model/Right: Overlap)

The reconstruction of the damage is difficult to build due to its small size. But, it illustrates that there is no delamination in the bottom and in the middle of the laminate which is not the case for the model result presenting delamination at every interface (Figure 6-44).
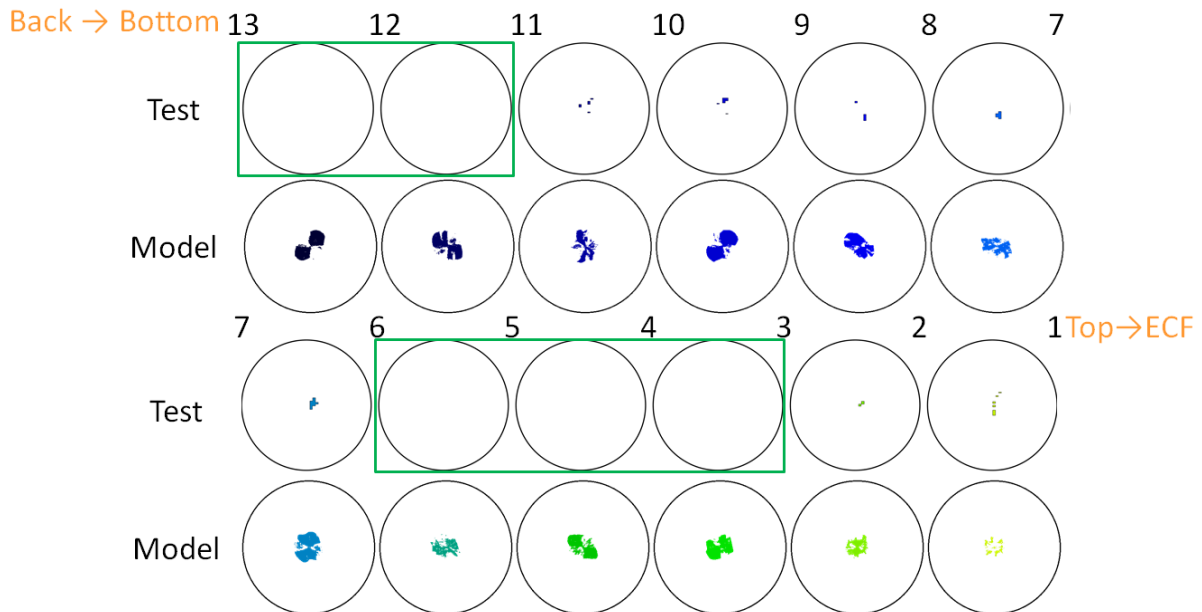
Figure 6-44 NDT comparison between test and equivalent model result with static cohesive interface for thin paint configuration (Microcut reconstruction of delamination for test result)

For the thick paint configuration (1000µm), the delamination is severe but the model underestimates the damage area as for the reference with 400µm of paint (Figure 6-45).
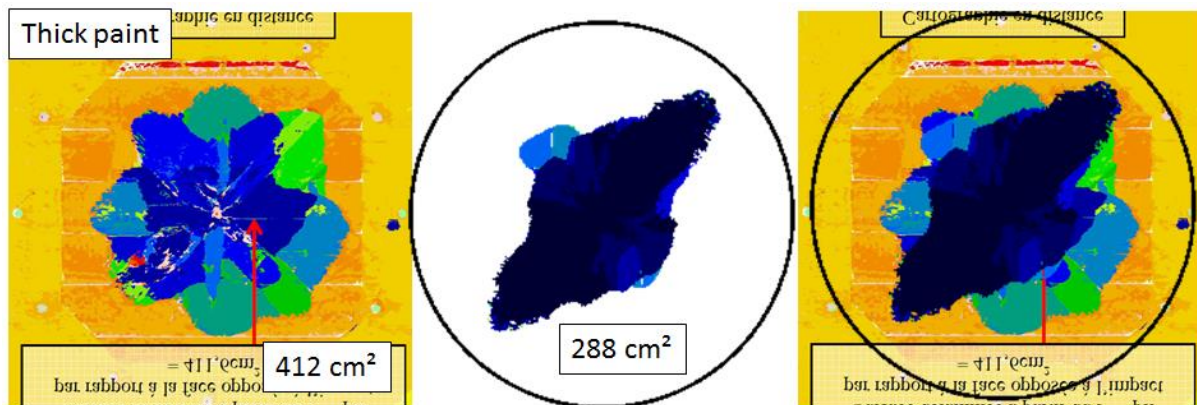
Figure 6-45 NDT comparison between test and equivalent model result with static cohesive interface for thick paint configuration (Left: Test/Middle: Model/Right: Overlap)

The reconstruction of the delamination distribution thanks to microcuts shows that all the plies are delaminated which is also the conclusion of the model. But the simulated delamination profile is not as extended as the one measured for the tested panel. The model tends to concentrate the delamination in the centre of the panel where the solicitation is the highest. The crack propagation is therefore not well approached by the static model. Also, a point to notice is the distribution profile of the delamination for the tested panel that highlights a possible manufacturing mistake. This is shown in Figure 6-46 with the pink circles where the ply orientation seems to be swapped between 0° and 90°.
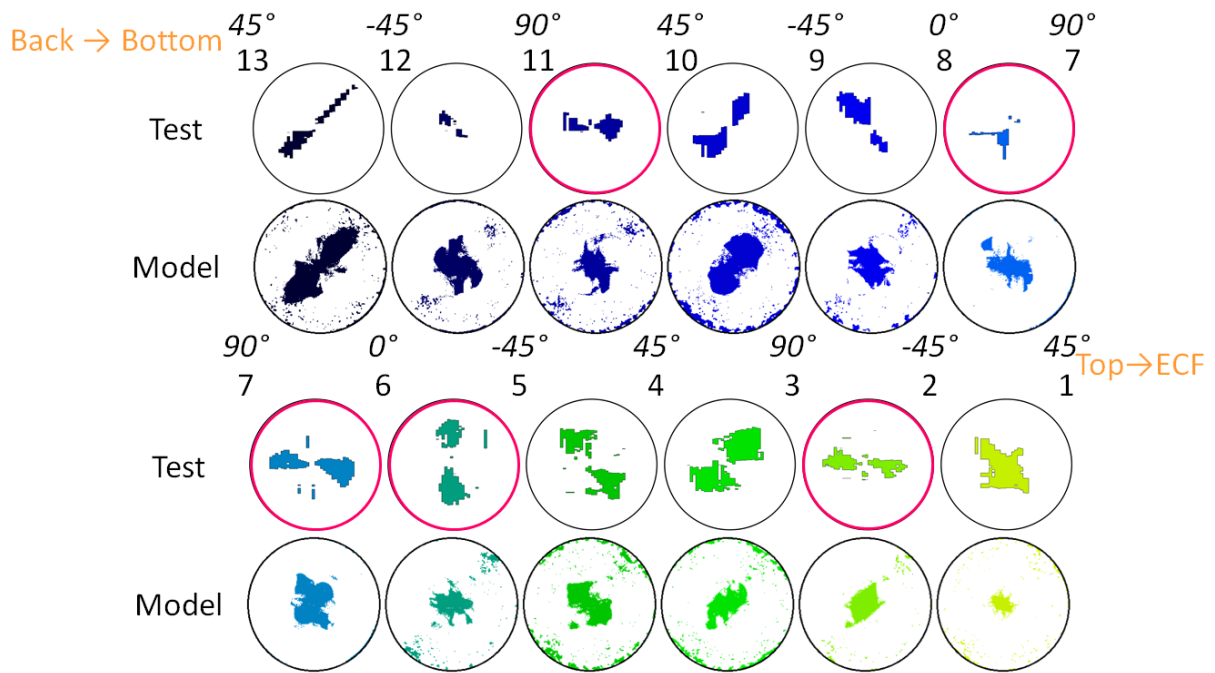
Figure 6-46 NDT comparison between test and equivalent model result (1ms) with static cohesive interface for thick paint configuration (Microcut reconstruction of delamination for test result)

The pressure decay due to confinement can be predicted with different paint thicknesses. However, the confinement of the explosion is due, on the one hand, to the paint layer as we demonstrated, but also to the CFRP substrate on the other hand. Considering now a CFRP substrate twice as thick as our baseline, we can assess the influence of the substrate stiffness in the explosion confinement. If we apply the same mechanical load as our reference configuration (CFRP 13 plies + ECF195 + 400µm of paint) on a configuration that is twice as thick (CFRP 26 plies + ECF195 + 400µm of paint), the deflection profile is higher than expected, as illustrated in Figure 6-47:
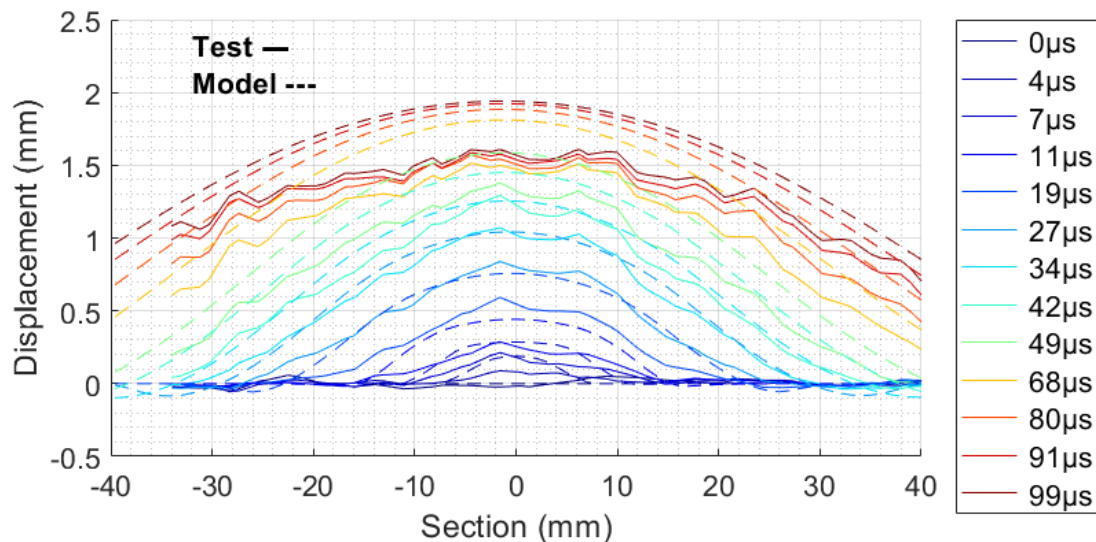
Figure 6-47 CFRP thick configuration (EDIFISS 100) comparison between test and shell model with reference VDLOAD

A substrate with a higher stiffness sustains the pressure from the explosion more, transferring a higher stress to the paint layer on the top. The paint is ejected more quickly, releasing the pressure of the explosion. This theory is illustrated in Figure 6-48 below:
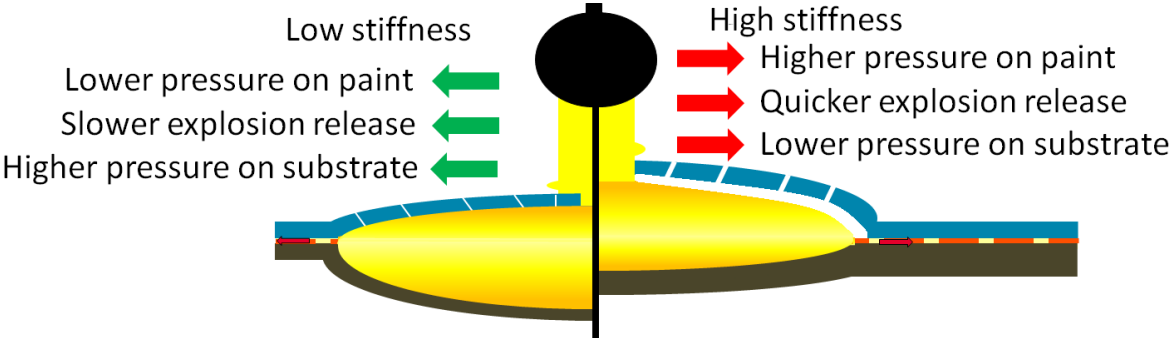
Figure 6-48 Substrate stiffness influence on explosion release

As presented in Chapter 5, we can use the laminate theory [105] to compare the bending modulus of our reference CFRP panel made of 13 plies and its thicker configuration made of 26 plies. In this case, the modulus E_f increases from 27GPa to 43GPa. As for the paint thickness impact, we propose to decrease the decay time Δt_0 with the ratio of E_f for the thick configuration. With the introduction of the influence of the panel bending stiffness in the confinement effect, the mechanical load tends to be more representative. As illustrated in Figure 6-49, the deflection of the panel due to this adapted mechanical load shows better agreement with the test measurement.
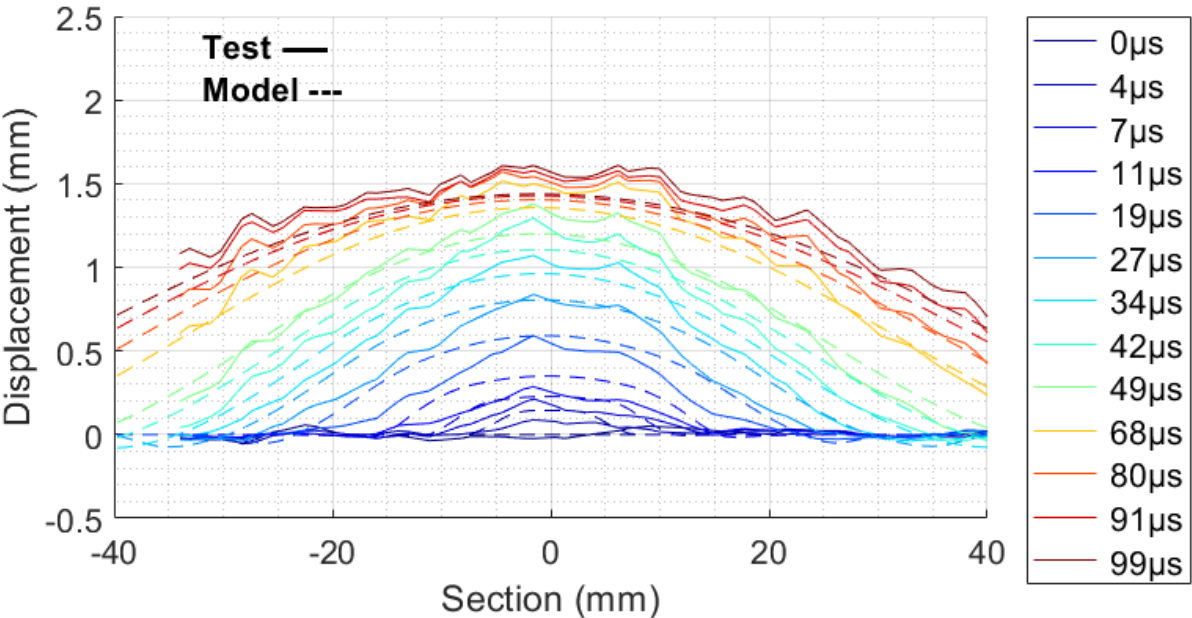
Figure 6-49 CFRP thick configuration (EDIFISS 100) comparison between test and shell model with adapted VDLOAD

On the same principle, we considered a CFRP structure with a different ply grade i.e., the thickness of the ply is 184μm instead of 127μm for the reference. But the construction comprises 9 plies (90/45/-45/0/90/0/-45/45/90) in order to obtain similar mechanical properties. The equivalent bending modulus is only slightly increased from 27GPa to 28GPa,

therefore the same mechanical load as for the reference was applied. As for the reference, the model presents the same deflection in the early stage but the deflection then slows down earlier in comparison to the test results (see Figure 6-50). The construction of the load dependent on the bending modulus of the panel predicts fairly correctly the displacement of the panel due to a lightning strike, validating the strong influence of the surface explosion on the mechanical constraints applied on the structure.
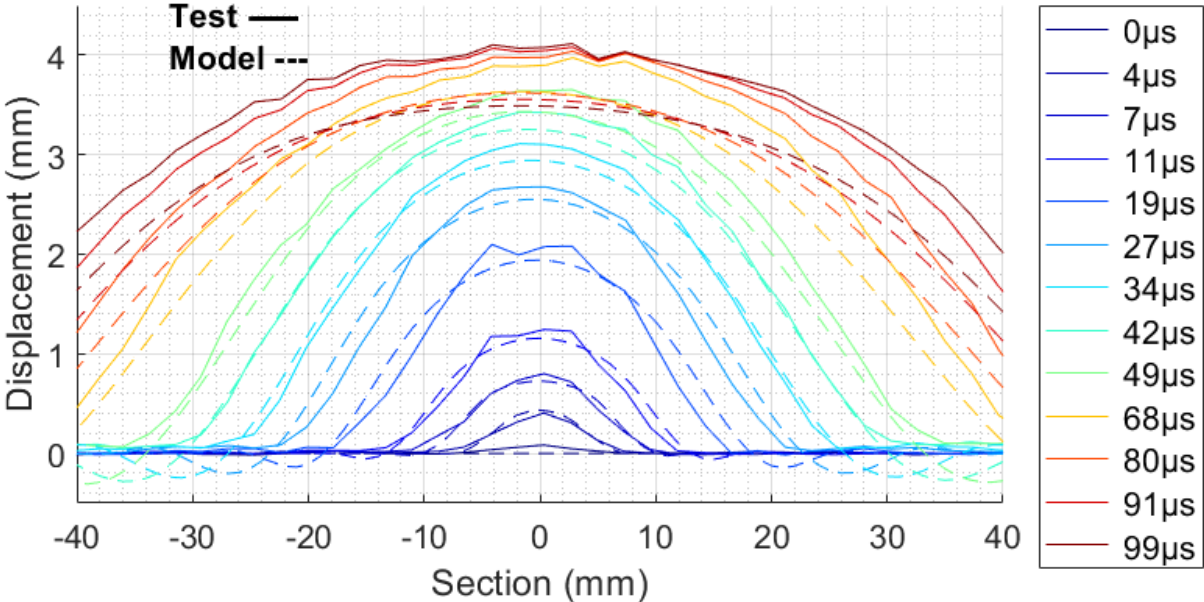
Figure 6-50 CFRP medium grade comparison between test and shell model with reference VDLOAD

The explosion confinement is the mechanism that will change the mechanical load applied on the CFRP structure. The pressure profile and amplitude are modified by the paint ejection which releases the explosion and decreases the pressure on the structure. The paint layer ejection is dependent on its stiffness. Therefore, it is dependent on the paint thickness when it is the same material. Obviously, for a different type of material with different mechanical properties, the ejection of the top layer will be influenced and hence the pressure profile. A lightning test performed with a Tufnol layer, presented in Chapter 5, of similar thickness and density to our reference case demonstrated a very different signature of ejection and damage severity, as presented in Chapter 5 in Figure 5-9. The Tufnol layer was ejected in larger pieces and on a larger area than the paint, suggesting a quicker pressure explosion release. The study of the deflection shown in Figure 6-51 confirms the decrease in the mechanical load applied on the CFRP plate and, as a consequence, a decrease in damage. It should be remembered that the delamination surface after a lightning strike for a protected structure covered by paint (400µm) was 155 cm² and only 64 cm² when covered by Tufnol.
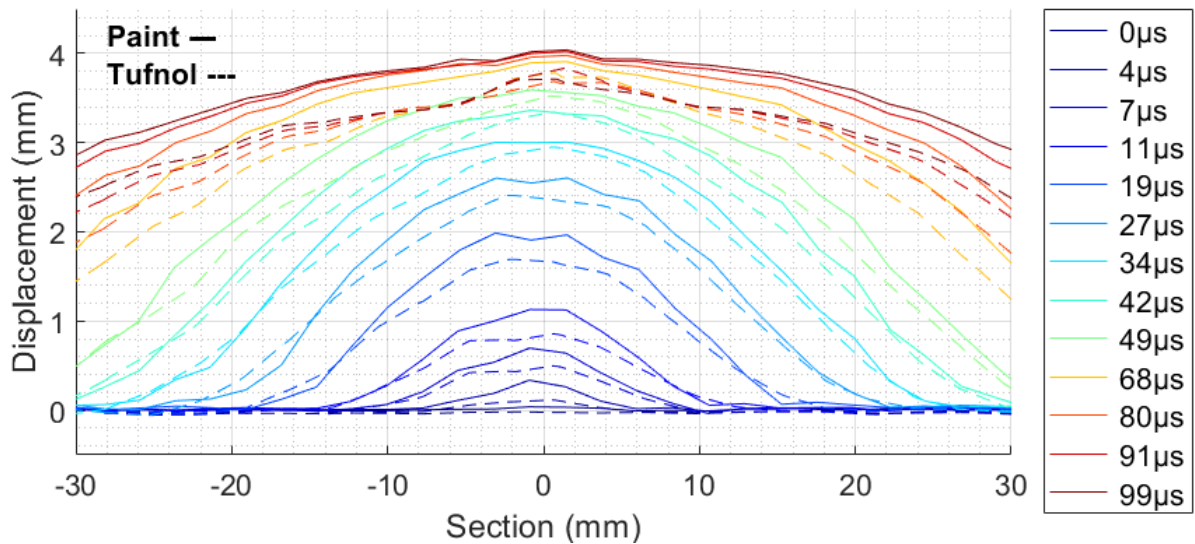
Figure 6-51   Deflection comparison of a CFRP panel protected with ECF195 and covered by paint (400μm) or Tufnol layer

Based on the maximum deflection at 100μs, where the speed decreases to 0, we can classify the confinement effect of the different top layer configurations on the explosion of ECF195. The delamination surface can be related to this parameter in order to propose a phenomenological model for this type of explosion, as shown in Figure 6-52:
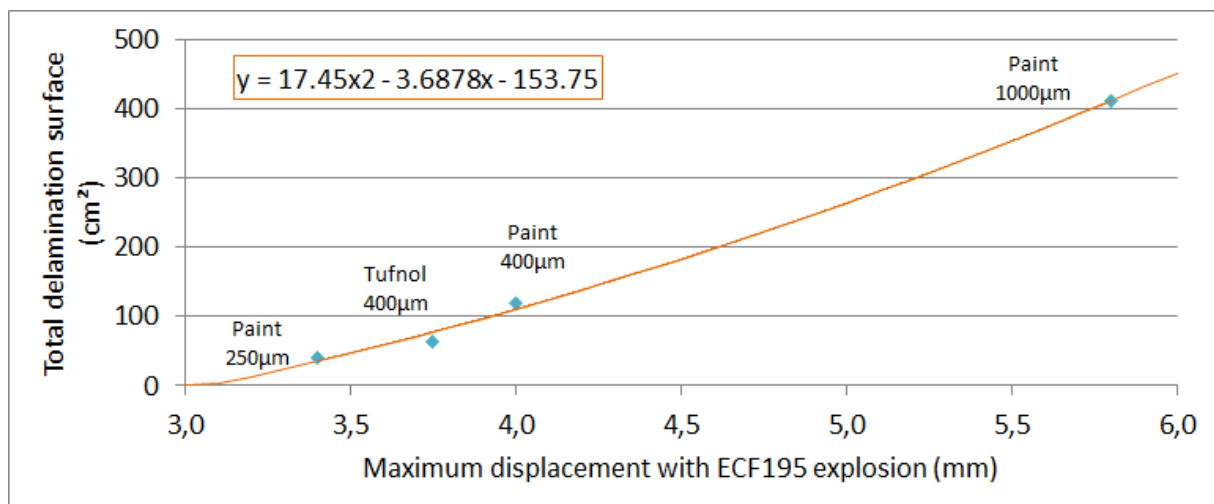
Figure 6-52 Delamination evolution with max displacement at 100μs for different confinements of ECF195 explosion

In this section, we developed a method to calibrate the spatio-temporal pressure distribution due to the explosion of the lightning strike protection and a reference confinement. From this reference, we were able to adapt the pressure law to the paint thickness and the stiffness of the substrate which confine the explosion. This mechanical load is applied as a pressure on the surface of the composite panel. In this model, the confinement and the paint layer are not modelled but only considered in our pressure law thanks to the change in the pressure decay time reference Δt_0. Therefore, in order to support the prediction of the influence of the paint layer and the substrate on the confinement of the explosion, it is necessary to simulate the explosion layer and the paint above it in our current model in replacement of our VDLOAD. This approach is developed and presented in the next section.

6.5. Explosion confinement by paint

For this model, instead of the VDLOAD which applies a pressure on the substrate of the composite structure, we modelled a lightning strike protection and the paint above. For the lightning strike protection where an explosion occurs due to Joule heating, we need to define an Equation Of State (EOS) that simulates the pressure due to the explosion. Therefore, as for the VDLOAD defined in 6.4.1, we identified the elements that will explode, their time of explosion and the maximum amplitude of explosion. These parameters will be used in the EOS. For the part of the LSP which does not explode, we used a simple elastic law based on the mechanical properties of copper. Then, we modelled the layer of paint on top of this explosive layer with the hyperelastic model developed in Chapter 5.

6.5.1. Explosion Equation Of State

An Equation Of State (EOS) relates the pressure and the energy to the temperature and density of the material. There are several possibilities in Abaqus® in order to model an EOS. First, there is an available library of EOS that can be parameters in the interface. The ideal gas EOS is available but it is not possible to include a trigger time where the element will be elastic before the explosion and a gas after. Also, the Jones-Wilkins-Lee (JWL) EOS, which is used for chemical explosions such as TNT, is available. Thanks to the definition of a bulk modulus and a trigger time, it would be possible to model both states of the LSP: Metal and explosion. But the calibration of the six different parameters for the JWL EOS is quite complex and would require specific tests [149]. Another possibility would be to use the VUEOS subroutine which enables the definition of a chosen pressure law for our explosion layer. However, the VUEOS is not made to manage an elastic material when its behaviour is dependent on the stress-strain relationship. Therefore, our final methodology is based on the development of a dedicated VUMAT for our explosive layer which will manage three different states of the LSP:

1. Elastic state prior to the explosion:
   σ=Eε with σ the stress, E the elastic modulus and ε the strain
2. Quick pressure increase due to the explosion:
   P=λ(t-t_0) with t_0 the explosion trigger time, λ=$P_{max}/\Delta t$, Pmax the maximum explosion pressure and Δt the time to reach the maximum chosen equal to 0.1 µs
3. Gas expansion state that was chosen following the ideal gas law:
   $P = (\gamma - 1)\rho E_m$ with $\gamma = 5/3$, ρ the density and E_m the explosion energy

The EOS was adapted in order to be managed by the VUMAT which is made for the definition of a stress-strain law but not for a pressure-density law. In a first step, the VUMAT was tested on a single element to confirm the management of the three states. As shown in Figure 6-53, the three states are clearly visible, which validates the use of the law. For this configuration, the explosion time was set to 1µs and the maximum pressure to 100MPa. During the ideal gas state, the pressure decreases quickly since the expansion is free. With a

confinement due to the presence of the paint on the top and the panel on the bottom, it is expected to produce a different pressure profile with a small pressure decay until the ejection of the paint.
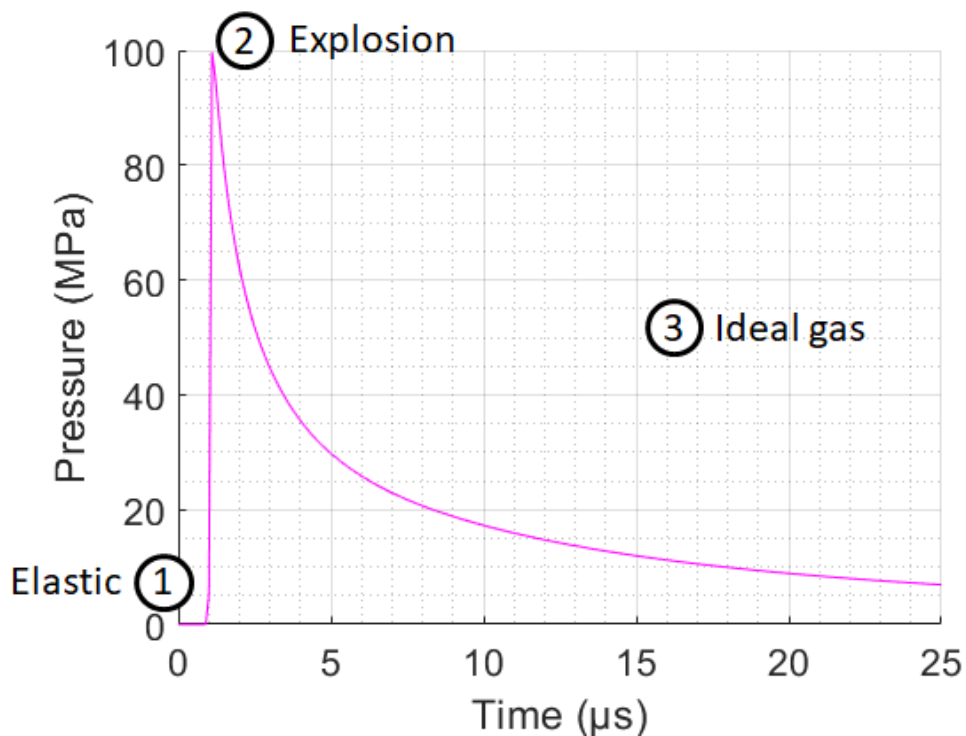
Figure 6-53 Pressure profile in one element from the explosion EOS simulation

This law was then implemented in each element of the explosion, similarly to our approach for the VDLOAD. The '.inp' file was modified to include the element of explosion (3D6R), called "ElemExp_XXXX" with XXXX the element number defined, and its associated material called "MatExp_ XXXX". The element will explode after its allocated trigger time up to the allocated maximum pressure. These values are included in the definition of the material in the '.inp' and managed by our VUMAT in the Fortran file. All the information is included in the '.inp'; no text file is necessary, contrary to the VDLOAD approach. Only a subroutine is necessary to support the VUMAT defining the three states of the element up to its expansion related to the ideal gas law we have defined. In a first approach, the explosion was not confined with a paint layer. In Figure 6-54, a view of the expansion of the explosion on the GFRP shell is presented. Before the explosion, the elements are all thin with a thickness equivalent to the weight of ECF195: 22μm. After 100 μs, the elements are expanded with a higher amplitude in the centre where the explosion pressure is the highest.
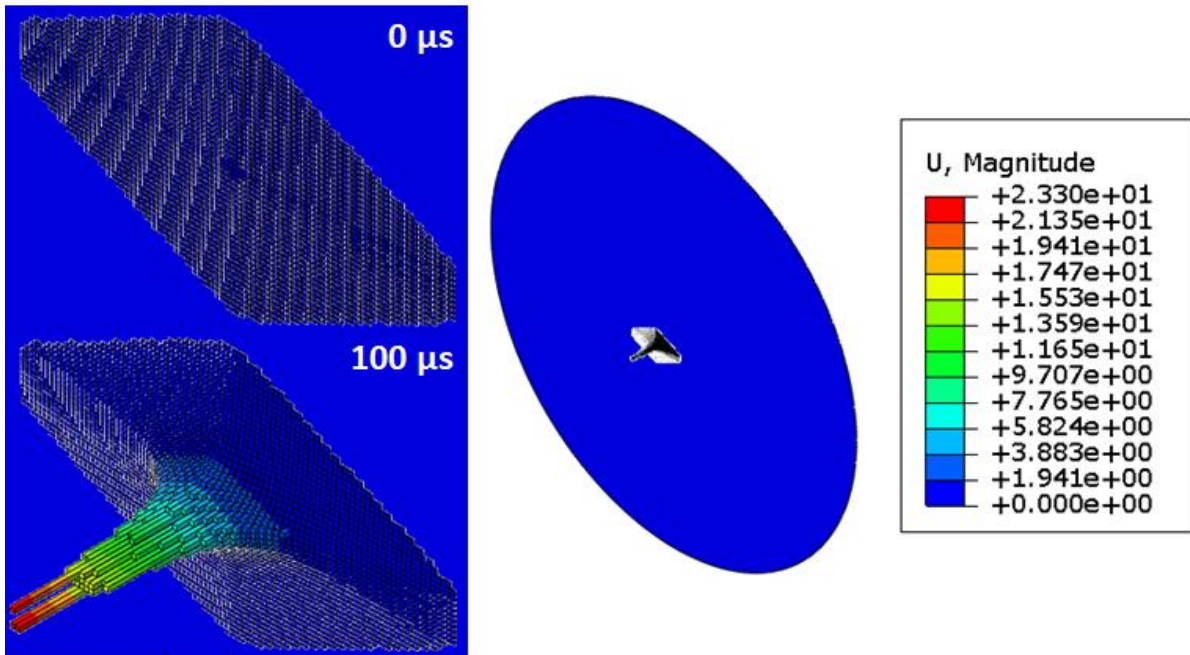
Figure 6-54 Free 3D explosion on a composite shell

Even if the pressure is well reproduced in the elements, the pressure applied on the surface of the shell element is very low. Therefore, the displacement is negligible. This could be due to the free expansion of the explosion as there is no paint layer. In the next section, we will analyse the effect of the paint on the confinement and pressure applied on the composite shell.

6.5.2. Confinement with paint

With the addition of the paint layer that confines the explosion, the expansion of the explosion is constrained by the presence of the top layer as illustrated in Figure 6-55.
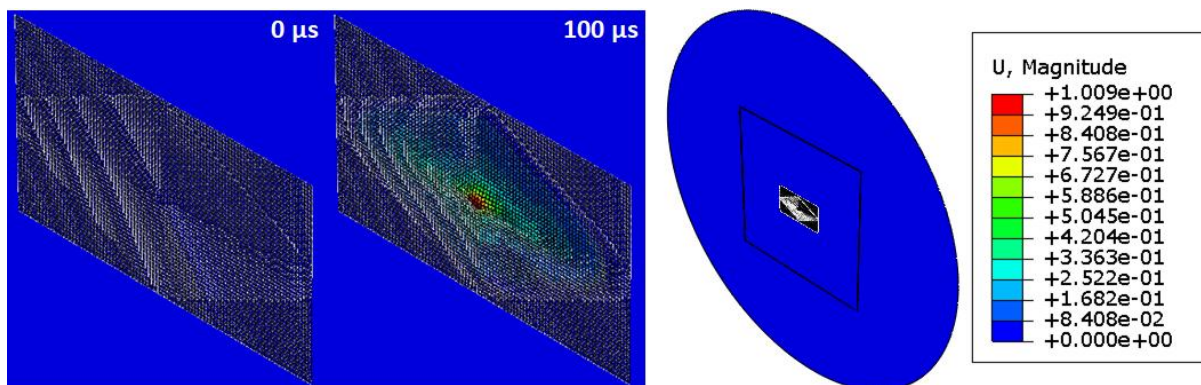
Figure 6-55 Confined 3D explosion on a composite shell

But, the result regarding the mechanical load application is unfortunately very limited. The pressure based on an ideal gas equation of state cannot represent the pressure due to an explosion. Consequently, it is not possible to simulate the mechanical load related to the explosion confinement. It will be necessary to develop an explosive equation of state in order to support the development of this model.

6.6. Internal damage

The damage in the composite protected by LSP due to a lightning strike has two sources, as described in Chapter 2. The first one that we have studied previously in this chapter is a mechanical source due to the surface explosion of the lightning strike protection. This can generate severe and extensive delamination that we measured by NDT, but also microcuts. The second one is a thermal source due to the current flow in the composite. This can break the composite fibres and deteriorate the resin. The mechanism can be assimilated to the explosion of the metallic protection on the surface but with a negligible overpressure compared to the metallic explosion as shown in 5.1.2. However, this damage occurs at the same time as the mechanical load and could impinge the mechanical resistance of the panel to the impact. In this section, the study of the damage due to this thermal source can support the understanding of the current distribution in the composite depending on the LSP and presence of the paint. A thick paint applied on a composite structure constrains the arc expansion as explained in Chapter 3, forcing the lightning current to flow deeper in the composite than with a thinner coating. In Figure 6-56 below, the plies damaged by the current flow are visible thanks to a microcut done in the centre. The first ply in this section is destroyed and the second ply is highly damaged. Even with this very severe configuration where the arc root is highly constrained, the deepest ply burned is the fourth one among the thirteen plies of the panel with a total thickness of 1.65 mm.
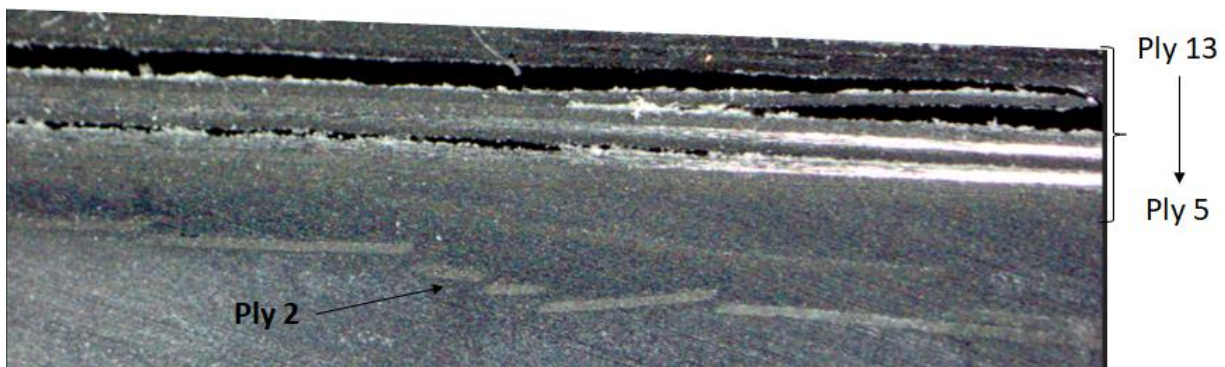
Figure 6-56 Internal damage study for severe configuration: CFRP (13plies) + ECF195 + 1000µm of paint

This configuration is considered severe since 1000µm of paint is not expected on an aircraft, where the usual thickness is between 250µm and 400µm. For this nominal configuration, only the first ply is burned. It is therefore not expected to significantly change the mechanical behaviour of the plate.

Due to the high electrical resistance of the composite, the current penetrates locally in the depth of the laminate but soon after flows back to the surface metallic protection. The thermal damage is therefore highly localised even for a severe configuration as shown in Figure 6-57. Nonetheless, as it will deteriorate the resin and explode the CFRP ply, some delamination in the top plies may be due to the thermal source and not to the mechanical load.

Figure 6-57 Internal damage study for severe configuration: CFRP (13plies) + ECF195 + 1000µm of paint: Top view

In order to study the thermal damage due to the current flow in the composite, a lightning test was performed on an unprotected structure. In this case, there is no diversion of the current by the LSP and all the current will flow in the composite. The amplitude of the current injected was reduced to 25kA instead of 100kA in order to simulate the portion of current that will flow in the CFRP instead of the conductive LSP. In Figure 6-58, the delamination measurement is presented up to the 6th plies since there is no delamination deeper in the laminate for this unprotected configuration. Thanks to microcuts, the distribution of the delamination at each interface was reconstructed. The area is very limited in surface and occurs mainly at the first two interfaces. The first top delamination between plies 1 and 2 is only due to thermal stress from the current flow. Comparing this damage to our reference, i.e. a paint structure protected with ECF195 but tested at 100kA, the damage is more severe (wider and deeper) and envelops the thermal damage.
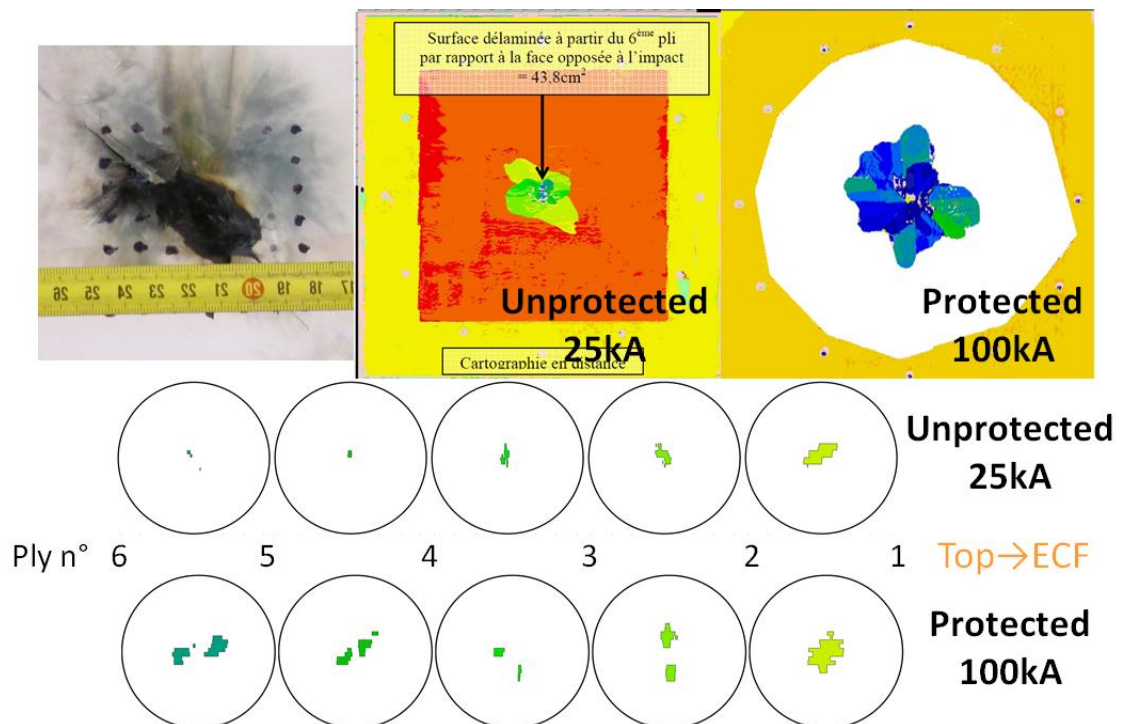
Figure 6-58 NDT result and delamination distribution for a paint CFRP structure with 25kA and comparison with a painted CFRP structure protected with ECF195 tested with 100kA

For a composite structure protected with ECF195 up to a nominal paint thickness (400μm), the thermal stress due to the current flow in the composite is negligible and a mechanical model with a pressure load on its surface as determined in this PhD could be used for the prediction of the damage.

6.7. Conclusion

This chapter is the final stage of our work aiming to reproduce the mechanical constraints due to a lightning strike. We proposed a methodology to simplify this multiphysics phenomenon into a purely mechanical problem. The ability to reproduce the load produced by the lightning strike is key in order to predict the damage generated by such a phenomenon. The final objective is to enable the damage prediction with a mechanical model.

A model was developed in order to simulate the damage in the ply thanks to a VUMAT and between the plies by the introduction of cohesive interfaces. Even with the values provided for the mechanical properties in the material, a numerical calibration of the interface was necessary based on static tests (DCB and ENF).

From the characterisation of the LSP explosion developed in the previous chapters which provided the spatio-temporal distribution of the explosion pressure and its amplitude, we could build a complete equivalent mechanical load. In a first step, the explosion pressure was modelled as a pressure applied on the surface of the composite. We built a methodology to convert this profile into a VDLOAD contained in every face of the substrate that will be stressed by the surface explosion pressure. The source of the model input was modified and associated to the user subroutine we developed.

In order to validate this model, we chose a set of lightning experimental results which provide essential data. The panel deflection due to the lightning strike was measured thanks to a digital image correlation method. The damage was measured by an ultrasonic test which provided the projected surface of delamination. In order to obtain an accurate evaluation of the distribution of the delamination, microcuts were performed and the profiles reconstructed for each interface. The configurations were built in order to change one parameter at a time with respect to our reference.

The surface explosion and its confinement by paint were studied independently. Thanks to the use of a GFRP structure which does not divert the lightning current, we were able to study and calibrate the pressure generated by a confined explosion. The work performed in the previous chapters provided all the data necessary for the explosion pressure model except its relaxation in time. A simple law for the pressure decay time was therefore developed, dependent on the maximum explosion pressure. This law simulated the confinement due to the paint which maintains the pressure before being ejected by this underlying explosion pressure. This pressure profile correctly predicted the deflection of the

CFRP panel with the same LSP (ECF195) and paint thickness (400µm). Our study of different paint thicknesses and panel stiffnesses demonstrated the dependency of the pressure profile on the confinement. The LSP explosion is sandwiched by the paint and the composite structure. Therefore, a change in their mechanical properties will influence its confinement and will maintain, or not, a high pressure on the structure. We were able to linearly relate the pressure decay law to the variation in stiffness of these parts. Again, the panel deflection was well predicted with this simple approach.

With this good prediction of the mechanical load generated by the lightning strike, we confronted the experimental damage measured with that predicted by our model. We demonstrated the limitations of a model based on static characterisations. The dynamic solicitation generated by the lightning strike requires developing a model dependent on the strain rate, especially for the interfaces.

In order to predict the explosion pressure relaxation instead of our calibration, we developed a 3D explosion element with an equation of state. This 3D layer simulates the explosion of the lightning strike protection and it is possible to apply a layer of paint on the top in order to simulate the confinement. The 3D explosion concept was validated but the explosion pressure in the element cannot be represented through an ideal gas equation of state. With the use and characterisation of an explosive equation of state, it will be possible to simulate the explosion confinement and its loading on the structure.

Finally, we should not forget the damage in the composite due to the thermal source of the lightning strike. When the lightning arc is constrained, part of the current flows into the structure, generating Joule heating. The study of this damage on an unprotected panel demonstrated the very local effect of this source. For our reference structure, the thermal damage was limited to the first ply, which validates the use of a mechanical load only for the prediction of the damage in the composite.

General conclusion & perspectives

For an aircraft structure based on composite materials, it is essential to take lightning threats into consideration when designing the structure. Contrary to a metallic structure, the low electrical conductivity of the composite structure makes this material vulnerable to lightning strike. The damage induced can be very severe. Visually, the aircraft skin is burned, with broken fibres and deteriorated resin. The worst damage, however, is hidden: the composite plies are delaminated and cracked over a larger area than the visible damage. After a severe lightning strike, the structure still needs to sustain the flight loads with its mechanical properties decreased by this critical damage, therefore without a complete failure in order to ensure a safe flight and landing. For this reason, a metallic protection is usually integrated on its external surface in order to divert the lightning current and limit the damage. However, the efficiency of the protection is impinged by the presence of a paint coating on the external surface. The lightning damage is therefore difficult to predict as it depends on these three components: the composite structure, the metallic surface protection and the paint. This dependency makes the damage prediction very complex. In order to demonstrate the compliance of the structure, laboratory lightning tests are performed on a simplified composite laminate. However, such test campaigns are expensive and time-consuming. The optimisation of the composite structure and its protection is an industrial constraint which decreases the margin against lightning resistance. Consequently, it is crucial to understand the lightning strike phenomenon and the damage generation in the composite structure.

The lightning damage mechanism has been studied for several decades and many researchers have sought to elucidate it. This phenomenon is highly complex since it involves multiple physics such as electromagnetism, magneto-hydro-dynamics, thermal physics and mechanics. All these physics are coupled, generating powerful forces in a very short space of time. A lightning strike is a current pulse of a hundred thousand amps reached in less than twenty microseconds. This problem has been mainly approached from an electro-thermal perspective. In the literature, the damage is expressed as a consequence of the lightning current flow in the composite, which generates heat and hence thermal deterioration. The arc itself is excluded from this problem and is only a source of current. The damage observed with this model is quite small compared to experiments, however. Therefore, some models were developed to take the mechanical forces generated by the arc into consideration or to consider a lightning strike as an equivalent mechanical impact. In addition, a first theory on the explosion of the protection and the influence of the paint was proposed. These theories, with their associated models and experiments, mainly treated the three components involved in the damage mechanism independently: on the one hand, the composite

structure subjected to a thermal or mechanical source, and on the other hand, the mechanical and thermal forces of the lightning arc. The influence of the surface protection or the paint was considered separately. However, the aircraft design is based on a composite structure, with a lightning strike protection on its surface and a paint coating on the top. The study of the different forces led us to the conclusion that the most detrimental damage, i.e. delamination, was mainly due to one contributor: the explosion of the lightning strike protection confined by the paint. In order to understand the lightning damage mechanism in an aircraft composite structure, it is necessary to study this problem as a whole.

From a scientific perspective, the questions addressed in this study are: for a real aircraft composite design, what are the lightning constraints that will generate damage? How can the interaction between the different contributors be analysed? How can the amplitude and distribution of these constraints be quantified? Can we simplify this complex problem into a mechanical study in order to predict the damage in the composite structure?

In order to answer these questions, the first essential step was to decompose the problem into different bricks. We started from the source: the lightning arc. Then, we studied its interaction with the surface: the lightning strike protection and the paint. The current flowing into the lightning strike protection generates an explosion that we characterised. The mechanical properties of the paint were also studied in order to assess its confinement capability. Finally, these bricks were assembled in order to build an equivalent predictive mechanical load, associated to a damage model in order to assess our ability to predict the damage due to a lightning strike in a complete composite structure, i.e. one that is protected and painted.

The source of the damage is the lightning arc. It was first necessary to study the arc column evolution confronted to that of the arc root in order to understand the influence of the metallic lightning strike protection and the paint dielectric coating on its natural expansion. A first model of the arc column was created in order to support the comparison and analysis of the arc column and root with their interdependencies. As the arc root is hidden by the paint, we developed an innovative method to reveal its spatio-temporal evolution. The method involved recording the light from the vaporisation of the metallic protection with a high-speed camera through a transparent panel. It was observed that the evolution of the arc root contour differs from that of the arc column. The main conclusion from this study was that arc root contour is highly dependent on the surface in interaction. First, the electrical conductivity of the metallic protection relative to the arc column conductivity increases or decreases its expansion. The anisotropic geometry of a protection such as ECF (Expanded Copper Foil) gives an anisotropic electrical conductivity which distorts the arc root expansion accordingly. The high consumption of the protection by Joule heating forces the arc root to expand faster than the column. But this expansion is prevented by the presence of the paint which, on the contrary, constrains the arc root. These two opposing phenomena make it difficult to predict the arc root contour and therefore the current

distribution in the conductors, i.e. the metallic protection and the composite structure. Hence, although we validated our electro-thermal model in order to predict the vaporisation of the protection due to Joule heating, it is essential to determine the distribution of the current entry, which is the interface between the arc root and the structure, in order to predict the vaporisation distribution. However, thanks to our experimental methodology, we were able to characterise and record different vaporisation profiles dependent on the paint and the lightning strike protection. The first brick was therefore built: the spatio-temporal distribution of the surface explosion.

The study of the sudden vaporisation of the metallic protection led us to the conclusion that it is not a smooth change of state to vapour but an explosion. This new approach was supported by the theory of electric explosion. In the literature, the most widely studied configuration is a metallic wire, on which several experiments have been carried out in order to study the shock wave generated by the explosion. The geometry of the expanded copper foil means that the lightning strike protection can be decomposed into a web of elementary wires. The lightning current flowing into the protection was considered to be distributed in each wire according to the vaporisation contour determined by the first brick. As the current density in each wire decreases with the expansion of the vaporisation contour, the associated explosion amplitude also decreases. The experiment we built enabled the current density to be related to an explosion pressure amplitude based on the analyses of the shock wave pressure at different distances from the exploding wire with different current densities. Thus, the distribution of the explosion defined in the first brick was now related to the pressure amplitude. With this second brick, we were therefore able to complete the picture and build all the dimensions of this explosion at the surface of the composite.

In addition, the study of the wire geometry upon explosion and the study of the injected current distortion provided essential information in order to identify the different phases and mechanisms involved in the wire explosion. The most surprising finding was the current shutdown before the explosion. When vaporisation occurs, the resistance of the material increases dramatically, leading to a current decrease. The current restarts when the plasma is generated, creating a conductive path. We built a non-dimensional electro-thermal model in order to predict the phase changes and the explosion moment. This model demonstrated its good prediction capability and showed that Joule heating is the main physical phenomenon at stake. However, the accuracy of the prediction decreases with the decrease in current density. Two modes should be differentiated in the explosion related to the current waveform and amplitude: a fast mode where the distribution is quite homogeneous in the wire, as in our model, and a slow mode where instabilities appear, as was supported by MHD theory. The rate of energy deposited into the metal by the electric current is one of the most important parameters in the explosion severity.

Before integrating this model into a complete and complex lightning model on a composite structure, we undertook an intermediate step: the study of the explosion of the lightning

strike protection on a dumbbell-shaped sample with a conducted lightning current. This approach removes the contribution of the arc forces and its interaction with the structure, thus making it possible to control the lightning current threat. With the complete expanded copper foil geometry, we also demonstrated our ability to predict the explosion moment when the manufacturing features of the mesh are taken into account. This additional study highlighted the influence of the paint in the arc generation as the confinement due to the paint layer tends to increase the current shutdown phase, preventing plasma creation. We also validated the confinement effect of the paint on the explosion based on the observation of the plate deflection. The explosion of an unpainted protection did not generate plate displacement whereas a painted configuration generated a significant displacement.

The third necessary brick was therefore the mechanical characterisation of the paint. The lightning test observations of the damage demonstrated its tremendous influence on the damage severity. The previous work provided a spatio-temporal distribution of the explosion pressure on a protected and painted composite structure struck by lightning. The pressure peak amplitude of the explosion was also determined but the explosion expansion, and thus the pressure release, is dependent on the confinement. As the function of the paint for aeronautical structures is mainly cosmetic, the characterisation was mainly qualitative. We therefore determined a set of tests to characterise its mechanical properties. The bulk modulus, the strain at break but also its adhesion were studied in order to support a confinement model. To carry out these tests, it was first necessary to manufacture a paint film and a specific process was developed to achieve this. From the tests performed, we developed a first hyperelastic model based on the expected behaviour for polyurethane material. This campaign highlighted the significant change in the mechanical properties of the paint at room temperature due to its glass transition temperature (36°) but also due to the manufacturing process (application, curing). This could explain the variability of some lightning test results despite their apparently identical configurations.

Finally, the definition of the lightning constraints as a mechanical load built with these three bricks had to be implemented in a mechanical model of the composite structure in order to assess the model's limitations and validity for load prediction but also for mechanical damage prediction. The first step was to develop a damage model for the ply and the ply interface. The characterisation of the model was based on a static characterisation of the composite material studied, provided by Airbus. The objective of this model was to predict the damage due to this strong dynamic impact. For the validation of the mechanical load and damage, we used a set of lightning tests in which the record of the plate displacement during the test as well as the damage in the laminate were provided thanks to ultrasonic tests and microcuts for a complete damage reconstruction.

The first step was to validate the complete mechanical surface load (P(x,y,t)) due to the lightning strike explosion and the confinement independently of the interaction of the lightning arc with the structure, thanks to a study on a GFRP plate. A sensitivity analysis was

performed in order to calibrate this model with a simple law for the pressure release phase. With this reference load for the explosion of an ECF195, confined by 400µm of paint and subjected to a lightning current of 100kA, we correctly predicted the displacement of a CFRP structure. This final result and the work performed in this PhD validate our theory that the confined surface explosion is the main contributor to the mechanical load compared to the other sources (CFRP explosion, lightning arc shock wave). It is therefore crucial to characterise the variation of this load due to the confinement. We validated a simple model of the pressure law which varies with respect to the reference depending on the mechanical properties of the paint, but also, it is important to point out, of the composite structure. The greater stiffness of a composite structure will accelerate ejection of the paint as it resists the explosion more, ejecting the paint on the opposite side. For the same type of paint, only the thickness parameter needs to be considered and for the structure, the equivalent bending modulus provides a good prediction capability.

In order to enhance our model and provide a prediction capability of the confinement without a calibrated surface law, we developed a model of elements with an equation of state in order to support the simulation of the explosion. The result on a single element was conclusive but the implementation in a complete model with the paint and the structure demonstrated the need to implement an explosive equation of state instead of an ideal gas equation of state in order to finalise the model.

The comparison of the damage between the test and the model highlighted the limitations of a damage law based on static characterisation. The mechanical load generated by a lightning strike is highly dynamic. It is therefore crucial to develop a model that is dependent on the strain rate with the associated material characterisation if an accurate prediction of the damage is required. In addition, the study of the Joule heating in the composite showed that compared to the mechanical force we characterised, Joule heating has only a limited impact on the damage as it does not penetrate the composite and only damages the first top ply.

The approach developed in this PhD in order to understand the lightning damage mechanism as a whole for a real aircraft design was based on a decomposition of this phenomenon in order to limit the complexity and enable the study of each parameter. This understanding was then reconstructed in order to build the complete picture of the generation of lightning constraints on a composite structure. We simplified the lightning strike on a protected and painted composite structure into a surface mechanical load and demonstrated our ability to predict the variation of this load with the paint thickness and structure stiffness with respect to a reference case. In addition, the most detrimental damage, i.e. the parameter in the flight load capability assessment, is delamination. The study of the damage in the laminate showed that the thermal damage in the composite has only a minor influence on the complete damage generation. The main contributor among the different mechanical sources has been demonstrated to be the explosion of the lightning

strike protection confined by the paint. It is therefore possible to simplify the lightning constraint into a mechanical load in order to assess the damage in the structure.

The model developed for the mechanical load is based on experimental characterisations. As perspectives of this research, several developments can be envisioned in order to build a complete prediction model and remove the dependency on the experiments.

First, the explosion profile could be predicted by simulating the lightning current entry into the lightning strike protection. For this purpose, a complete 3D model of the arc in interaction with the metallic protection but also with the presence of paint is necessary. This would require the enhancement of the MHD theory for the lightning field with high current, pressure and temperature of the arc. A further difficulty will be to model the interaction of the arc with a changing interface. The vaporisation of the metallic protection interacts with the arc but also with the paint which forms a barrier for the arc expansion. In addition, the thermal damage distribution in the composite structure could be better analysed thanks to a better assessment of the lightning current entry into the composite and its distribution.

Then, the pressure of the explosion of the metallic lightning strike protection could be predicted by the theory proposed by Chung [101] which couples MHD equations with a copper EOS. Therefore, with the knowledge of the lightning current density and waveform, it will be possible to predict the pressure and energy of the explosion. Another approach that would support an explosion model is the characterisation of the Jones-Wilkins-Lee parameters from dedicated test on exploding copper wire [149].

The external coating, here the paint, has been demonstrated to be a key parameter in the amplitude and distribution of the explosion. The mechanical characterisation of the paint provided useful information for the construction of a hyperelastic model but additional tests will be necessary to complete its validation. The consideration of the viscous and temperature dependent properties of the paint is also a possible development. The paint cracking could be simulated with cohesive interfaces calibrated with the tension and trouser test performed.

The variation in the explosion pressure profile due to its release with paint ejection could be predicted with the explosion equation of state we developed thanks to a VUMAT. This will be possible once the issue related to the interfaces between the explosive element and its surrounding structure, i.e. the paint and the composite panel, is resolved.

Finally, the comparison of our damage model based on a static constant characterisation with the delamination recorded after a lightning test demonstrated the need to develop a damage model that is dependent on the solicitation speed, i.e. the strain rate. The mechanical load generated by a lightning strike is highly dynamic and has to be related to the shock propagation in a composite structure. In parallel, such a model would require dedicated tests for the characterisation of dynamic properties, especially at interfaces.

Bibliography

[1]   Xu, Y., Zhu, J., Wu, Z., Cao, Y., Zhao, Y., and Zhang, W. "A Review on the Design of Laminated Composite Structures: Constant and Variable Stiffness Design and Topology Optimization." *Advanced Composites and Hybrid Materials*, 2018. https://doi.org/10.1007/s42114-018-0032-7.

[2]   Plumer, J. A. *Aicraft Lightning Protection Handbook*. Lightning Technologies, Inc., 1989.

[3]   EUROCAE. *ED-84: Aircraft Lightning Environment And Related Test Waveforms*. 1997.

[4]   Morgan, D., Hardwick, C. J., Haigh, S. J., and Meakins, A. J. "The Interaction of Lightning with Aircraft and the Challenges of Lightning Testing." *AerospaceLab*, No. 5, 2012, pp. 1–10.

[5]   EASA. Certification Specifications and Acceptable Means of Compliance for Large Aeroplanes CS-25 Amendment 24.

[6]   EUROCAE. *ED-91: Aircraft Lightning Zoning*. 2006.

[7]   SAE International. ARP5414B: Aircraft Lightning Zoning.

[8]   SAE International. ARP5412B: Aircraft Lightning Environment and Related Test Waveforms.

[9]   EUROCAE. *ED-105: Aircraft Lightning Test Methods*. 2005.

[10]   SAE International. ARP5416: Aircraft Lightning Test Methods.

[11]   Soulas, F. *Développement d'un Modèle Mécanique Pour La Prédiction Des Dommages de Panneaux Composites Aéronautiques Soumis à Un Choc Foudre*. Toulouse, ISAE, 2016.

[12]   Hardwick, C. J. *Lightning Tests to Aluminium Panels with a Thick Paint Finish*. Publication CLiC/12-16. 2013, p. 13.

[13]   Alhossen, I., Espinosa, C., Chieragatti, R., Hor, A., Pierré, E., Vilcocq, S., Montel, T., and Gnangnon, O. "Experimental Investigation of the Repeatability of Direct Damage Induced by Lightning Strikes on Metallic Panels." *Journal of Physics: Conference Series*, Vol. 1243, 2019. https://doi.org/10.1088/1742-6596/1243/1/012006.

[14]   Lago, F., Fontaine, G., and Larrieu, C. Measurement by a Digital Image Correlation Technique of the Deflection of Panels Submitted to Lightning Impulse. Presented at the ICOLSE, Oxford, UK, 2011.

[15]   Hirano, Y., Katsumata, S., Iwahori, Y., and Todoroki, A. "Artificial Lightning Testing on Graphite/Epoxy Composite Laminate." *Composites Part A: Applied Science and Manufacturing*, Vol. 41, No. 10, 2010, pp. 1461–1470. https://doi.org/10.1016/j.compositesa.2010.06.008.

[16]   Li, Y., Li, R., Lu, L., and Huang, X. "Experimental Study of Damage Characteristics of Carbon Woven Fabric/Epoxy Laminates Subjected to Lightning Strike." *Composites Part A: Applied Science and Manufacturing*, Vol. 79, 2015, pp. 164–175. https://doi.org/10.1016/j.compositesa.2015.09.019.

[17]   Sun, J., Yao, X., Tian, X., Chen, J., and Wu, Y. "Damage Characteristics of CFRP Laminates Subjected to Multiple Lightning Current Strike." *Applied Composite Materials*, Vol. 26, No. 3, 2019, pp. 745–762. https://doi.org/10.1007/s10443-018-9747-4.

[18] Feraboli, P., and Miller, M. "Damage Resistance and Tolerance of Carbon/Epoxy Composite Coupons Subjected to Simulated Lightning Strike." *Composites Part A: Applied Science and Manufacturing*, Vol. 40, No. 6, 2009, pp. 954–967. https://doi.org/10.1016/j.compositesa.2009.04.025.

[19] Abdelal, G., and Murphy, A. "Nonlinear Numerical Modelling of Lightning Strike Effect on Composite Panels with Temperature Dependent Material Properties." *Composite Structures*, Vol. 109, 2014, pp. 268–278. https://doi.org/10.1016/j.compstruct.2013.11.007.

[20] Bigand, A., and Duval, Y. Quantification of the Mechanical Impact of Lightning Strike Protection Explosion Confined by Thick Paint. Presented at the ICOLSE, Nagoya, 2017.

[21] Karch, C., and Metzner, C. Lightning Protection of Carbon Fibre Reinforced Plastics — An Overview. Presented at the 2016 33rd International Conference on Lightning Protection (ICLP), 2016.

[22] Gagné, M., and Therriault, D. "Lightning Strike Protection of Composites." *Progress in Aerospace Sciences*, Vol. 64, 2014, pp. 1–16. https://doi.org/10.1016/j.paerosci.2013.07.002.

[23] Hirano, Y., Yokozeki, T., Ishida, Y., Goto, T., Takahashi, T., Qian, D., Ito, S., Ogasawara, T., and Ishibashi, M. "Lightning Damage Suppression in a Carbon Fiber-Reinforced Polymer with a Polyaniline-Based Conductive Thermoset Matrix." *Composites Science and Technology*, Vol. 127, 2016, pp. 1–7. https://doi.org/10.1016/j.compscitech.2016.02.022.

[24] Russ, M., Rahatekar, S., Koziol, K., Peng, H. X., and Farmer, B. Development of Carbon Nanotube/Epoxy Nanocomposites for Lightning Strike Protection. Presented at the 18th International Conference on Composites Materials, ICCM 2011, 2011.

[25] Kumar, V., Yokozeki, T., Karch, C., Hassen, A. A., Hershey, C. J., Kim, S., Lindahl, J. M., Barnes, A., Bandari, Y. K., and Kunc, V. "Factors Affecting Direct Lightning Strike Damage to Fiber Reinforced Composites: A Review." *Composites Part B: Engineering*, Vol. 183, 2020, p. 107688. https://doi.org/10.1016/j.compositesb.2019.107688.

[26] Sousa Martins, R. *Etude Expérimentale et Théorique d'un Arc de Foudre et Son Interaction Avec Un Matériau Aéronautique*. Université Paris-Saclay, 2016.

[27] Guo, Y., Xu, Y., Wang, Q., Dong, Q., Yi, X., and Jia, Y. "Enhanced Lightning Strike Protection of Carbon Fiber Composites Using Expanded Foils with Anisotropic Electrical Conductivity." *Composites Part A: Applied Science and Manufacturing*, Vol. 117, 2019, pp. 211–218. https://doi.org/10.1016/j.compositesa.2018.11.022.

[28] Espinosa, C., Bhoosnurmath, H., López, A. C., and Lachaud, F. Numerical Modelling of a Lightning Strike on a Protected Composite Panel. Presented at the ICOLSE, Nagoya, 2017.

[29] Lepetit, B., Escure, C., Guinard, S., Revel, I., and Peres, G. Thermo-Mechanical Effects Induced by Lightning on Carbon Fiber Composite Materials. Presented at the ICOLSE, Oxford, UK, 2011.

[30] Karch, C. Contributions of Lightning Current Pulses to Mechanical Damage of CFRP Structures. Presented at the ICOLSE, Toulouse, 2015.

[31] Bigand, A., Espinosa, C., Bauchire, J. M., Flourens, F., and Lachaud, F. Lightning Damage Assessment into Composite Based on Surface Explosion and Fiber Breakage. Presented at the International Conference on Composite Materials (ICCM22), Melbourne (Australia), 2019.

[32]   Rannou, J., Huchette, C., Hurmane, A., and Tholin, F. An Analysis of Lightning Direct Effects on CFRP Panels. Part II, the Electro-Thermo-Mechanical Simulation Strategy. Presented at the ICOLSE, Nagoya, 2017.

[33]   Huchette, C., Rannou, J., Roche, J., Lapeyronnie, P., Beauchêne, P., and Chemartin, L. An Analysis of Lightning Direct Effects on CFRP Panels. Part I, the Experimental and Material Point of View. Presented at the ICOLSE, Nagoya, 2017.

[34]   Chemartin, L., Lalande, P., Peyrou, B., Chazottes, A., Elias, P. Q., Delalondre, C., Cheron, B. G., and Lago, F. "Direct Effects of Lightning on Aircraft Structure: Analysis of the Thermal, Electrical and Mechanical Constraints." *AerospaceLab*, No. 5, 2012, p. p–1.

[35]   Karch, C., Arteiro, A., and Camanho, P. P. "Modelling Mechanical Lightning Loads in Carbon Fibre-Reinforced Polymers." *International Journal of Solids and Structures*, Vol. 162, 2019, pp. 217–243. https://doi.org/10.1016/j.ijsolstr.2018.12.013.

[36]   Lago, F. *Modélisation de l'interaction Entre Un Arc Électrique et Une Surface : Application Au Foudroiement d'un Aéronef*. UNIVERSITE TOULOUSE III, 2004.

[37]   Lepetit, B., Soulas, F., Guinard, S., Revel, I., and Peres, G. "Analysis of Composite Panel Damages Due to a Lightning Strike : Mechanical Effects." *ICOLSE 2013*, , 2013.

[38]   Karch, C., Schreiner, M., Honke, R., and Wolfrum, J. Shock Waves from a Lightning Discharge. Presented at the 2018 34th International Conference on Lightning Protection (ICLP), 2018.

[39]   Foster, P., Abdelal, G., and Murphy, A. "Understanding How Arc Attachment Behaviour Influences the Prediction of Composite Specimen Thermal Loading during an Artificial Lightning Strike Test." *Composite Structures*, Vol. 192, 2018, pp. 671–683. https://doi.org/10.1016/j.compstruct.2018.03.039.

[40]   Neufeld, R. B. Lightning Direct Effects on Anisotropic Materials from Electro-Thermal Simulation. Presented at the ICOLSE, Toulouse, 2015.

[41]   Fu, K., Ye, L., Chang, L., Yang, C., and Zhang, Z. "Modelling of Lightning Strike Damage to CFRP Composites with an Advanced Protection System. Part I: Thermal-Electrical Transition." *Composite Structures*, Vol. 165, 2017, pp. 83–90. https://doi.org/10.1016/j.compstruct.2017.01.008.

[42]   Guo, Y., Dong, Q., Chen, J., Yao, X., Yi, X., and Jia, Y. "Comparison between Temperature and Pyrolysis Dependent Models to Evaluate the Lightning Strike Damage of Carbon Fiber Composite Laminates." *Composites Part A: Applied Science and Manufacturing*, Vol. 97, 2017, pp. 10–18. https://doi.org/10.1016/j.compositesa.2017.02.022.

[43]   Wang, F. S., Ji, Y. Y., Yu, X. S., Chen, H., and Yue, Z. F. "Ablation Damage Assessment of Aircraft Carbon Fiber/Epoxy Composite and Its Protection Structures Suffered from Lightning Strike." *Composite Structures*, Vol. 145, 2016, pp. 226–241. https://doi.org/10.1016/j.compstruct.2016.03.005.

[44]   Ogasawara, T., Hirano, Y., and Yoshimura, A. "Coupled Thermal-Electrical Analysis for Carbon Fiber/Epoxy Composites Exposed to Simulated Lightning Current." *Composites Part A: Applied Science and Manufacturing*, Vol. 41, No. 8, 2010, pp. 973–981. https://doi.org/10.1016/j.compositesa.2010.04.001.

[45]   Dong, Q., Guo, Y., Sun, X., and Jia, Y. "Coupled Electrical-Thermal-Pyrolytic Analysis of Carbon Fiber/Epoxy Composites Subjected to Lightning Strike." *Polymer*, Vol. 56, 2015, pp. 385–394. https://doi.org/10.1016/j.polymer.2014.11.029.

[46]   Dong, Q., Guo, Y., Chen, J., Yao, X., Yi, X., Ping, L., and Jia, Y. "Influencing Factor Analysis Based on Electrical-Thermal-Pyrolytic Simulation of Carbon Fiber Composites Lightning Damage." *Composite Structures*, Vol. 140, 2016, pp. 1–10. https://doi.org/10.1016/j.compstruct.2015.12.033.

[47]   Chippendale, R. *Modelling of the Thermal Chemical Damage Caused to Carbon Fibre Composites*. University of Southampton, 2013.

[48]   Murphy, A. Lightning Strike Direct Effects. In *Polymer Composites in the Aerospace Industry - Second Edition*, Woodhead Publishing, 2020, pp. 561–591.

[49]   Wang, F. S., Ji, Y. Y., Yu, X. S., Chen, H., and Yue, Z. F. "Ablation Damage Assessment of Aircraft Carbon Fiber/Epoxy Composite and Its Protection Structures Suffered from Lightning Strike." *Composite Structures*, Vol. 145, 2016, pp. 226–241. https://doi.org/10.1016/j.compstruct.2016.03.005.

[50]   Liu, Z. Q., Yue, Z. F., Wang, F. S., and Ji, Y. Y. "Combining Analysis of Coupled Electrical-Thermal and BLOW-OFF Impulse Effects on Composite Laminate Induced by Lightning Strike." *Applied Composite Materials*, Vol. 22, No. 2, 2015, pp. 189–207. https://doi.org/10.1007/s10443-014-9401-8.

[51]   Millen, S. L. J., Murphy, A., Abdelal, G., and Catalanotti, G. "Sequential Finite Element Modelling of Lightning Arc Plasma and Composite Specimen Thermal-Electric Damage." *Computers & Structures*, Vol. 222, 2019, pp. 48–62. https://doi.org/10.1016/j.compstruc.2019.06.005.

[52]   Braginskii, S. I. "Theory of the Development of a Spark Channel." *J. Exptl. Theoret. Phys*, Jan 02, 1958, pp. 1548–1557.

[53]   Wang, Y., and Zhupanska, O. I. Evaluation of the Thermal Damage in Glass Fiber Polymer-Matrix Composites in Wind Turbine Blades Subjected to Lightning Strike. Presented at the American Society for Composites, 29th Annual Technical Conference, San Diego, CA, 2014.

[54]   Wang, Y., and Zhupanska, O. I. "Lightning Strike Thermal Damage Model for Glass Fiber Reinforced Polymer Matrix Composites and Its Application to Wind Turbine Blades." *Composite Structures*, Vol. 132, 2015, pp. 1182–1191. https://doi.org/10.1016/j.compstruct.2015.07.027.

[55]   Wan, G., Dong, Q., Zhi, J., Guo, Y., Yi, X., and Jia, Y. "Analysis on Electrical and Thermal Conduction of Carbon Fiber Composites under Lightning Based on Electrical-Thermal-Chemical Coupling and Arc Heating Models." *Composite Structures*, Vol. 229, 2019, p. 111486. https://doi.org/10.1016/j.compstruct.2019.111486.

[56]   Tholin, F., Chemartin, L., and Lalande, P. Numerical Investigation of the Interaction of a Lightning and an Aeronautic Skin during the Pulsed Arc Phase. Presented at the ICOLSE, Toulouse, 2015.

[57]   Soulas, F., Espinosa, C., Lachaud, F., Guinard, S., Lepetit, B., Revel, I., and Duval, Y. "A Method to Replace Lightning Strike Tests by Ball Impacts in the Design Process of Lightweight Composite Aircraft Panels." *International Journal of Impact Engineering*, Vol. 111, 2018, pp. 165–176.

[58]   Gineste, P.-N., Clerc, R., Castanie, C., Andreu, H., and Buzaud, E. Assessment of Lightning Direct Effects Damages by Modelling Techniques. Presented at the ICOLSE, Pittsfield, USA, 2009.

[59]   Kawakami, H. *Lightning Strike Induced Damage Mechanisms of Carbon Fiber Composites*. Ph.D. University of Washington, United States -- Washington, 2011.

[60] Muñoz, R., Delgado, S., González, C., López-Romano, B., Wang, D.-Y., and LLorca, J. "Modeling Lightning Impact Thermo-Mechanical Damage on Composite Materials." *Applied Composite Materials*, Vol. 21, No. 1, 2014, pp. 149–164. https://doi.org/10.1007/s10443-013-9377-9.

[61] Lee, J., Lacy, T. E., Pittman, C. U., and Reddy, J. N. "Numerical Estimations of Lightning-Induced Mechanical Damage in Carbon/Epoxy Composites Using Shock Wave Overpressure and Equivalent Air Blast Overpressure." *Composite Structures*, Vol. 224, 2019, p. 111039. https://doi.org/10.1016/j.compstruct.2019.111039.

[62] Lin, S. "Cylindrical Shock Waves Produced by Instantaneous Energy Release." *Journal of Applied Physics*, Vol. 25, No. 1, 1954, pp. 54–57. https://doi.org/10.1063/1.1721520.

[63] Plooster, M. N. "Shock Waves from Line Sources. Numerical Solutions and Experimental Measurements." *Physics of Fluids*, Vol. 13, No. 11, 1970, p. 2665. https://doi.org/10.1063/1.1692848.

[64] Karch, C., and Wulbrand, W. *Lightning Direct Effects - Lightning Shock Waves*. Publication CTO/IW-SE-2010-82. EADS, 2010.

[65] Naghipour, P., and Pineda, E. J. Simulating Damage Due to a Lightning Strike Event: Effects of Temperature Dependent Properties on Interlaminar Damage. Presented at the SIMULIA Community Conference, 2014.

[66] Naghipour, P., Pineda, E. J., and Arnold, S. M. "Simulation of Lightning-Induced Delamination in Un-Protected CFRP Laminates." *Applied Composite Materials*, Vol. 23, No. 4, 2016, pp. 523–535. https://doi.org/10.1007/s10443-016-9472-9.

[67] Kamiyama, S., Hirano, Y., and Ogasawara, T. "Delamination Analysis of CFRP Laminates Exposed to Lightning Strike Considering Cooling Process." *Composite Structures*, Vol. 196, 2018, pp. 55–62. https://doi.org/10.1016/j.compstruct.2018.05.003.

[68] Espinosa, C., Montel, T., Pons, J. M., Lachaud, F., and Soulas, F. A Numerical Study of the Pressure Applied on CFRP Panels during a Lightning Strike Using a Coupled Electro-Thermal-Mechanical Model. Presented at the ICOLSE, Nagoya, 2017.

[69] Wang, J., Yuan, P., Guo, F., Qie, X., Ouyang, Y., and Zhang, Y. "The Spectra and Temperature of Cloud Lightning Discharge Channel." *Science in China Series D: Earth Sciences*, Vol. 52, No. 7, 2009, pp. 907–912. https://doi.org/10.1007/s11430-009-0108-x.

[70] Uman, M. A. "The Peak Temperature of Lightning." *Journal of Atmospheric and Terrestrial Physics*, Vol. 26, No. 1, 1964, pp. 123–128.

[71] Gleizes, A., Gonzalez, J. J., and Freton, P. "Thermal Plasma Modelling." *Journal of Physics D: Applied Physics*, Vol. 38, No. 9, 2005, pp. R153–R183. https://doi.org/10.1088/0022-3727/38/9/R01.

[72] Murphy, A. B. "A Perspective on Arc Welding Research: The Importance of the Arc, Unresolved Questions and Future Directions." *Plasma Chemistry and Plasma Processing*, Vol. 35, No. 3, 2015, pp. 471–489. https://doi.org/10.1007/s11090-015-9620-2.

[73] D'Angola, A., Colonna, G., Gorse, C., and Capitelli, M. "Thermodynamic and Transport Properties in Equilibrium Air Plasmas in a Wide Pressure and Temperature Range." *The European Physical Journal D*, Vol. 46, No. 1, 2008, pp. 129–150. https://doi.org/10.1140/epjd/e2007-00305-4.

[74] Perera, C., Rahman, M., Fernando, M., Liyanage, P., and Cooray, V. "The Relationship between Current and Channel Diameter of 30 Cm Long Laboratory Sparks." *Journal of Electrostatics*, Vol. 70, No. 6, 2012, pp. 512–516. https://doi.org/10.1016/j.elstat.2012.08.003.

[75] Aleksandrov, N. L., Bazelyan, É. M., and Shneider, M. N. "Effect of Continuous Current during Pauses between Successive Strokes on the Decay of the Lightning Channel." *Plasma Physics Reports*, Vol. 26, No. 10, 2000, pp. 893–901. https://doi.org/10.1134/1.1316830.

[76] Peyrou, B. *Modélisation MHD d'un Arc de Foudroiement d'aéronef*. thesis. Rouen, 2012.

[77] Pechereau, F., Tholin, F., Zaepffel, C., Sousa Martins, R., and Lalande, P. MHD Simulation of a Lightning Column during the Pulsed Arc Phase. Presented at the ICOLSE, Wichita (USA), 2019.

[78] Lisnyak, M., Cunha, M. D., Bauchire, J.-M., and Benilov, M. S. "Numerical Modelling of High-Pressure Arc Discharges: Matching the LTE Arc Core with the Electrodes." *Journal of Physics D: Applied Physics*, Vol. 50, No. 31, 2017, p. 315203. https://doi.org/10.1088/1361-6463/aa76d3.

[79] Chemartin, L. *Modélisation Des Arcs Electriques Dans Le Contexte Du Foudroiement Des Aéronefs*. Faculté des Sciences de l'université de Rouen, 2008.

[80] Gigliotti, M., Lafarie-Frenot, M. C., Lin, Y., and Pugliese, A. "Electro-Mechanical Fatigue of CFRP Laminates for Aircraft Applications." *Composite Structures*, Vol. 127, 2015, pp. 436–449. https://doi.org/10.1016/j.compstruct.2015.01.023.

[81] Feraboli, P., and Kawakami, H. "Damage of Carbon/Epoxy Composite Plates Subjected to Mechanical Impact and Simulated Lightning." *Journal of Aircraft*, Vol. 47, No. 3, 2010, pp. 999–1012. https://doi.org/10.2514/1.46486.

[82] Zaepffel, C., Chemartin, L., Martins, R. S., and Lalande, P. Laboratory Simulation of Lightning Direct Effect Using GRIFON Test Bench at ONERA. Presented at the ICOLSE, Toulouse, 2015.

[83] Bigand, A., Espinosa, C., Bauchire, J.-M., Flourens, F., and Lachaud, F. Estimation of the Load Produced by the Electro-Thermal Behaviour of Lightning Strike Protection Layers on a Composite Panel. Presented at the European Conference on Composite Materials-ECCM18, Athens (Greece), 2018.

[84] Vacquie, S. *Arc Electrique*. Eyrolles, 2000.

[85] Vorob'ev, V. S., Malyshenko, S. P., Tkachenko, S. I., and Fortov, V. E. "What Initiates the Explosion of a Current-Carrying Conductor?" *JETP Letters*, Vol. 75, No. 8, 2002, pp. 373–377.

[86] Borisevich, A. E., and Cherkas, S. L. "Effect of the Conductor Radius on the Electric Explosion Dynamics: Magnetohydrodynamic Simulation." *Technical Physics*, Vol. 57, No. 10, 2012, pp. 1380–1386. https://doi.org/10.1134/S1063784212100027.

[87] Liu, H., Zhao, J., Wu, Z., Zhang, L., and Zhang, Q. "Experimental Investigations on Energy Deposition and Morphology of Exploding Aluminum Wires in Argon Gas." *Journal of Applied Physics*, Vol. 125, No. 10, 2019, p. 103301. https://doi.org/10.1063/1.5078811.

[88] Grinenko, A. U. Experimental and Theoretical Study of Strongly Coupled Copper Plasma Generated by Underwater Electrical Wire Explosion. In *6th International Conference on Dense Z-Pinches*, No. 808, 2006, pp. 91–94.

[89]   Romanova, V. M., Ivanenkov, G. V., Mingaleev, A. R., Ter-Oganesyan, A. E.,
        Shelkovenko, T. A., and Pikuz, S. A. "Electric Explosion of Fine Wires: Three Groups of
        Materials." *Plasma Physics Reports*, Vol. 41, No. 8, 2015, pp. 617–636.
        https://doi.org/10.1134/S1063780X15080085.

[90]   Han, R., Zhou, H., Wu, J., Qiu, A., Ding, W., and Zhang, Y. "Relationship between
        Energy Deposition and Shock Wave Phenomenon in an Underwater Electrical Wire
        Explosion." *Physics of Plasmas*, Vol. 24, No. 9, 2017, p. 093506.
        https://doi.org/10.1063/1.4989790.

[91]   Sinars, D. B., Hu, M., Chandler, K. M., Shelkovenko, T. A., Pikuz, S. A., Greenly, J. B.,
        Hammer, D. A., and Kusse, B. R. "Experiments Measuring the Initial Energy
        Deposition, Expansion Rates and Morphology of Exploding Wires with about 1
        KA/Wire." *Physics of Plasmas*, Vol. 8, No. 1, 2001, pp. 216–230.
        https://doi.org/10.1063/1.1323759.

[92]   Sasaki, T., Nakajima, M., Kawamura, T., and Horioka, K. "Electrical Conductivities of
        Aluminum, Copper, and Tungsten Observed by an Underwater Explosion." *Physics of
        Plasmas*, Vol. 17, No. 8, 2010, p. 084501. https://doi.org/10.1063/1.3475430.

[93]   Grinenko, A., Sayapin, A., Gurovich, V. Tz., Efimov, S., Felsteiner, J., and Krasik, Ya. E.
        "Underwater Electrical Explosion of a Cu Wire." *Journal of Applied Physics*, Vol. 97,
        No. 2, 2005, p. 023303. https://doi.org/10.1063/1.1835562.

[94]   Pikuz, S. A., Tkachenko, S. I., Barishpol'tsev, D. V., Ivanenkov, G. V., Mingaleev, A. R.,
        Romanova, V. M., Ter-Oganes'yan, A. E., and Shelkovenko, T. A. "Interpreting
        Experimental Data on the Electric Explosion of Thin Wires in Air." *Technical Physics
        Letters*, Vol. 33, No. 8, 2007, pp. 651–654.
        https://doi.org/10.1134/S1063785007080081.

[95]   Ivanenkov, G. V., Gus'kov, S. Y., and Barishpol'tsev, D. V. "Current Shunting and
        Formation of Stationary Shock Waves during Electric Explosions of Metal Wires in
        Air." *Plasma Physics Reports*, Vol. 36, No. 1, 2010, pp. 67–76.
        https://doi.org/10.1134/S1063780X10010058.

[96]   Vorob'ev, V. S., Eronin, A. A., and Malyshenko, S. P. "Phase Explosion of Conductor
        with Current." *High Temperature*, Vol. 39, No. 1, 2001, pp. 97–103.

[97]   Tkachenko, S. I., Vorob'ev, V. S., and Malyshenko, S. P. "Parameters of Wires during
        Electric Explosion." *Applied Physics Letters*, Vol. 82, No. 23, 2003, pp. 4047–4049.
        https://doi.org/10.1063/1.1580996.

[98]   Caupin, F. *Les Transitions de Phases Par l'exemple*. M2 Sciences de la Matière – ENS
        Lyon, 2016.

[99]   Luo, B.-Q., Sun, C.-W., Zhao, J.-H., and He, J. "Unified Numerical Simulation of
        Metallic Foil Electrical Explosion and Its Applications." *IEEE Transactions on Plasma
        Science*, Vol. 41, No. 1, 2013, pp. 49–57. https://doi.org/10.1109/TPS.2012.2227827.

[100]   Le Blanc, G., Petit, J., Chanal, P.-Y., L'Eplattenier, P., and Avrillaud, G. Modelling the
        Dynamic Magnto-Thermomechanical Behaviour of Materials Using a Multi-Phase
        EOS. Presented at the 7th European LS-DYNA conference, Salzburg, 2009.

[101]   Chung, K.-J., Lee, K., Hwang, Y. S., and Kim, D.-K. "Numerical Model for Electrical
        Explosion of Copper Wires in Water." *Journal of Applied Physics*, Vol. 120, No. 20,
        2016, p. 203301. https://doi.org/10.1063/1.4968396.

[102]   Ray, A., Srivastava, M. K., Kondayya, G., and Menon, S. V. G. "Improved Equation of
        State of Metals in the Liquid-Vapor Region." *Laser and Particle Beams*, Vol. 24, No.
        03, 2006. https://doi.org/10.1017/S0263034606060381.

[103] Cunrath, R. J. M., and Wickert, M. Numerical Analysis of the Response of Thick Wires to Extreme Dynamic Electro-Mechanical Loads. Presented at the 2014 17th International Symposium on Electromagnetic Launch Technology, 2014.

[104] Murillo, R., Flourens, F., Garcia, V., Duval, Y., and Cavaliere, F. Lightning Strike Protection of Carbon Composite Skin. Kinetic and Signature of the Damage. Presented at the ICOLSE, Nagoya, 2017.

[105] Gay, D. *Matériaux Composites*. 1997.

[106] Hercule, K. M., Yan, Z., and Christophe, M. M. "Preparation and Characterization of Waterborne Polyurethane Crosslinked by Urea Bridges." *International Journal of Chemistry*, Vol. 3, No. 2, 2011, p. p88. https://doi.org/10.5539/ijc.v3n2p88.

[107] Tufnol. Tufnol - Data Sheet. https://docs.rs-online.com/d0bd/0900766b807259ec.pdf.

[108] Cambridge University Engineering Department. *Material Data Book*. 2003.

[109] Airbus Industrie. AIMS 04-04-014 - Airbus Industrie Material Specification - External Paint System: Primer+intermediate Coat+top Coat Material Specification.

[110] International Standard. ISO 2409 - Paints and Varnishes — Cross-Cut Test.

[111] International Standard. ISO 6272 - Paints and Varnishes – Rapid-Deformation (Impact Resistance) Tests – Part 1: Falling-Weight Test, Large-Area Indenter.

[112] International Standard. ISO1518 - Paints and Varnishes – Determination of Scratch Resistance – Part 1: Constant- Loading Method.

[113] International Standard. ISO1519 - Paints and Varnishes — Bend Test (Cylindrical Mandrel).

[114] International Standard. *ISO 527-1: Plastics — Determination of Tensile Properties — Part 1: General Principles*. 2012.

[115] Verron, E. "Modèles hyperélastiques pour le comportement mécanique des élastomères." *Techniques de l'ingénieur - "Plastiques et composites,"* Mar 10, 2018.

[116] Pawlikowski, M. "Non-Linear Approach in Visco-Hyperelastic Constitutive Modelling of Polyurethane Nanocomposite." *Mechanics of Time-Dependent Materials*, Vol. 18, No. 1, 2014, pp. 1–20. https://doi.org/10.1007/s11043-013-9208-2.

[117] International Standard. ISO6383 - Plastiques — Film et Feuille — Détermination de La Résistance Au Déchirement — Partie 1 : Méthode de Déchirement Pantalon.

[118] International Standard. ISO4578 - Adhesives - Determination of Peel Resistance of High-Strength Adhesive Bonds - Floating-Roller Method.

[119] ASTM International. ASTM D4708 - Preparation of Uniform Free Films of Organic Coatings.

[120] ASTM International. ASTM D823 - Producing Films of Uniform Thickness of Paint, Coatings and Related Products on Test Panels.

[121] Knudsen, O., Bjørgum, A., Polanco-Loria, M., Øyen, A., and Johnsen, R. "Internal Stress And Mechanical Properties Of Paint Films." *NACE - International Corrosion Conference Series*, 2007, pp. 070031–070039.

[122] International Standard. *ISO 527-3: Plastics — Determination of Tensile Properties — Part 3: Test Conditions for Films and Sheets*. Bsi., 1996.

[123] Arrigoni, M., Schalk, M., Carrère, N., Alexandru, A., Cojan, B., Boustie, M., and Berthe, L. "Étude Expérimentale et Numérique de l'adhérence d'interfaces Collées Soumises à Des Ondes Mécaniques Brèves et Intenses." *Revue des composites et des matériaux avancés*, No. 2, 2015, pp. 201–223.

[124]   Loison, D. *Etude Expérimentale et Numérique Du Micro Écaillage de Cibles Métalliques Soumises à Des Chocs Laser*. ENSMA, Poitiers, 2012.

[125]   Zagouri, D., and Boustie, M. *Ondes de Choc Dans Les Solides*. SimChoc S.A.S., 2019.

[126]   Arrigoni, M. *Ondes de choc dans la matière condensée - Cours ENSIETA 3ème année - Option Ingénierie des Matériaux Energétiques*. 2008, p. 108.

[127]   Peyre, P., Berthe, L., Vigual, V., Popa, I., and Baudin, T. "Analysis of Laser Shock Waves and Resulting Surface Deformations in an Al–Cu–Li Aluminum Alloy." *J. Phys. D: Appl. Phys.*, No. 45, 2012. https://doi.org/10.1088/0022-3727/45/33/335304.

[128]   Courapied, D. *Etude de l'interaction laser matière en régime de confinement par eau avec deux impulsions laser. Application au test d'adhérence par choc laser.* phdthesis. Ecole nationale supérieure d'arts et métiers - ENSAM, 2016.

[129]   Abaqus. Hyperelastic Behavior of Rubberlike Materials. https://abaqus-docs.mit.edu/2017/English/SIMACAEMATRefMap/simamat-c-hyperelastic.htm.

[130]   Ilyas, M. *Damage Modeling of Carbon Epoxy Laminated Composites Submitted to Impact Loading*. 2010.

[131]   Abrate, S. "Modeling of Impacts on Composite Structures." *Composite Structures*, Vol. 51, No. 2, 2001, pp. 129–138. https://doi.org/10.1016/S0263-8223(00)00138-0.

[132]   P.E. Irving, and C. Soutis. *Polymer Composites in the Aerospace Industry - Second Edition*. Elsevier, 2020.

[133]   Camanho, P. P., Dávila, C. G., Pinho, S. T., and Remmers, J. J. C. *Mechanical Response of Composites*. 2008.

[134]   Chen, C. *Contribution à La Prise En Compte Des Effets de l'environnement Sur La Tolérance Aux Dommages d'impact de Stratifiés Composites*. thesis. Toulouse, ISAE, 2015.

[135]   ASTM International. *ASTM D5528-01: Test Method for Mode I Interlaminar Fracture Toughness of Unidirectional Fiber-Reinforced Polymer Matrix Composites*. ASTM International, 2001.

[136]   International Standard. ISO 15024 - Fibre-Reinforced Plastic Composites — Determination of Mode I Interlaminar Fracture Toughness, GIC, for Unidirectionally Reinforced Materials.

[137]   Airbus Industrie. *AITM 1-0005: Determination of Interlaminar Fracture Toughness Energy – Mode I (G1C Test)*. 2015.

[138]   Bouvet, C. "Mécanique de La Rupture Des Composites : Délaminage et Fissuration." *Techniques de l'ingénieur*, No. ref. article : trp4043, 2019.

[139]   de Barros, S. *Modèle d'interface Pour La Simulation Du Comportement Des Assemblages Collés*. Université de Versailles Saint-Quentin, 2005.

[140]   3DS Simulia. *Analysis of Composite Materials with Abaqus*. 2009.

[141]   Lachaud, F., Paroissien, E., and Michel, L. "Validation of a Simplified Analysis for the Simulation of Delamination of CFRP Composite Laminated Materials under Pure Mode I." *Composite Structures*, 2020, p. 111897. https://doi.org/10.1016/j.compstruct.2020.111897.

[142]   Reinoso, J., Blázquez, A., Estefani, A., París, F., Cañas, J., Arévalo, E., and Cruz, F. "Experimental and Three-Dimensional Global-Local Finite Element Analysis of a Composite Component Including Degradation Process at the Interfaces." *Composites Part B: Engineering*, Vol. 43, No. 4, 2012, pp. 1929–1942. https://doi.org/10.1016/j.compositesb.2012.02.010.

[143] Schueler, D., Toso-Pentecôte, N., and Voggenreiter, H. "Effects of Static Preloads on the High Velocity Impact Response of Composite Plates." *Composite Structures*, Vol. 153, 2016, pp. 549–556. https://doi.org/10.1016/j.compstruct.2016.06.062.

[144] Airbus Industrie. *AITM 1-0006: Determination of Interlaminar Fracture Toughness Energy – Mode II (G2C Test)*. 1994.

[145] Hashin, Z. "Failure Criteria for Unidirectional Fiber Composites." *Journal of Applied Mechanics*, Vol. 47, No. 2, 1980, pp. 329–334. https://doi.org/10.1115/1.3153664.

[146] Matzenmiller, A., Lubliner, J., and Taylor, R. L. "A Constitutive Model for Anisotropic Damage in Fiber-Composites." *Mechanics of Materials*, Vol. 20, No. 2, 1995, pp. 125–152. https://doi.org/10.1016/0167-6636(94)00053-0.

[147] Berthe, J., Joudon, V., and Portemont, G. "Strain Rate Dependencies of Intra and Inter Laminar Properties of Organic Matrix Composite Materials." *Revue des composites et des matériaux avancés*, No. 2, 2015, pp. 117–130.

[148] Gay, E., Berthe, L., Boustie, M., Arrigoni, M., and Buzaud, E. "Effects of the Shock Duration on the Response of CFRP Composite Laminates." *Journal of Physics D: Applied Physics*, , 2014.

[149] Castedo, R., Natale, M., López, L. M., Sanchidrián, J. A., Santos, A. P., Navarro, J., and Segarra, P. "Estimation of Jones-Wilkins-Lee Parameters of Emulsion Explosives Using Cylinder Tests and Their Numerical Validation." *International Journal of Rock Mechanics and Mining Sciences*, Vol. 112, 2018, pp. 290–301. https://doi.org/10.1016/j.ijrmms.2018.10.027.

[150] Arblaster, J. W. "Thermodynamic Properties of Copper." *Journal of Phase Equilibria and Diffusion*, Vol. 36, No. 5, 2015, pp. 422–444. https://doi.org/10.1007/s11669-015-0399-x.

[151] Electrical Conductivity of Metals at High Temperature – Field Precision Software Tips. http://fieldp.com/myblog/2012/electrical-conductivity-of-metals-at-high-temperature/.

[152] Tucker, T. J., and Toth, R. P. *EBW1: A Computer Code for the Prediction of the Behavior of Electrical Circuits Containing Exploding Wire Elements*. Publication SAND--75-0041, 4229184. 1975.

[153] Mills, K. C. *Recommended Values of Thermophysical Properties for Selected Commercial Alloys*. Woodhead Publishing, 2002.

[154] Desai, P. D., James, H. M., and Ho, C. Y. "Electrical Resistivity of Aluminum and Manganese." *Journal of Physical and Chemical Reference Data*, Vol. 13, No. 4, 1984, pp. 1131–1172. https://doi.org/10.1063/1.555725.

[155] Tolias, P., and Team, the Euro. M. "Analytical Expressions for Thermophysical Properties of Solid and Liquid Tungsten Relevant for Fusion Applications." *Nuclear Materials and Energy*, Vol. 13, 2017, pp. 42–57. https://doi.org/10.1016/j.nme.2017.08.002.

[156] Rizk, J. *Study of Burned Zones in a Composite Structure Subjected to Lightning*. ISAE, Toulouse, 2020, p. 38.

[157] Ciborski, A., Espinosa, C., and Bigand, A. *Experimental Studies of the Behaviour of Lightning Struck Composite Plates*. ISAE, Toulouse, 2020, p. 107.

[158] Montes, A. *Analyse Des Dommages Causés à Des Panneaux Composites CFRP Par Un Choc Foudre et de Leur Sensibilité Aux Paramètres d'essais*. ISAE, 2019, p. 47.

Appendices

Appendix A – Pressure measurement

_____

This appendix presents the pressure measurements at several distances from the exploding wire.
The pressure is expressed in kPA.

	WF	Current (kA)	Distance (mm)

	WF	Current (kA)	5	10	11	15	15,5	16	16,5	17	17,5	18	26	27	27,5	28	29	38	39	40	41	42	43	79	80	81	82	83	84	85	86	87	88
Cu 125	1	10												167					168						43								
		5	393	384				220		200				110					92		92										26		24	24
		3.57																		72	73											23	22	
		2.27																		41													14	
		1.47						70		65			32	37						27													10	11
		1																		10													5	5
		0.81	18	19						12			8																					
		0.8																		2	2													
	5A	10						414	242							193			138	113				38										
		5				200				220			100	80							74									28	29			
		3.57																				65	65								19			
		1.47				87		102					45	45						30	35										10	11		
		0.81						40						22						15	16										8			
Cu75	1	10																	45	35	26						19		18			5	
		5																	28	19	13		21				6	8		6			
		3.57																		20	23											7	
		2.27																			22								10				
		1.47				275			86	106			64			64	82			12									6				
	5A	5						48		34	20		25	14																			

Group	Sub	Val	1	2	3	4	5	6	7	8	9	10	11	12	13	14	15	16	17	18	19	20	21	22
		1.47																53	46					16	
		0.81	17	160																					
AI125	1	10						243							149			195				34	
		5	220			211		240		184			150											
		1.47	155			66				46			41		38									
		0.81	61		27			17	17					14	14									
	5A	10								260			156				94	82					26	26
		5				174		169					100		94									
		1.47				62				68			43		32									
		0.81				29	23								18									
W100	1	10						190					119		111				77				22	
		5						103		111			69		72									
		1.47	40							38			21		40									
		0.81	2	15				7					6											
	5A	10											105		81		57	52				19	20	
		5						42		48														
		1.47								19		18	9											
		0.81				50	38								51	46								

Appendix B – Metal thermodynamic properties

_____

This Appendix details the electrical and thermal properties considered for the vaporisation model of copper, aluminium and tungsten.

The most widely studied material is copper whose the properties can be easily found in the literature.

	Density ρ (g/cm^3)	Molar mass M (g/mol)	Specific Heat Cp (J/mol.K) [150]	Phase change temperature T (K)	Phase change enthalpy ΔH (kJ/kg)	Electrical resistivity ρ (Ω.m) [151],[152]
Solid	8.96	63.546	$22.650 + 6.666.10^{-3}T$	/	/	$1.59987.10^{-14}T^2 + 5.27959.10^{-11}T + 1.2317.10^{-10}$
Solid → Liquid			/	1357.57	205.8	$1.376.10^{-7}$
Liquid			33.52	/	/	$1.43621.10^{-14}T^2 + 4.00975.10^{-11}T + 1.33614.10^{-7}$
Liquid → Vapour			/	2835.15	4735	$9.02812.10^{-6}x^2 - 8.39541.10^{-7}x + 3.62740.10^{-7}$
Burst	/	/	/	/	/	$6.2.10^{-6}$

Table 1 Physical properties of copper

	Density ρ (g/cm^3)	Molar mass M (g/mol)	Specific Heat Cp (J/mol.K) [153]	Phase change temperature T (K)	Phase change enthalpy ΔH (kJ/kg)	Electrical resistivity ρ (Ω.m) [154],[152]
Solid	2.699	26.982	$21.235 + 1.129.10^{-2}T$	/	/	$2.93783.10^{-14}T^2 + 8.59274.10^{-11}T - 8.45569.10^{-10}$
Solid → Liquid			/	933.45	399.9	$1.767.10^{-7}$
Liquid			31.9	/	/	$-2.12274.10^{-14}T^2 + 1.9798710^{-10}T + 8.2018510^{-8}$
Liquid → Vapour			/	2740.15	10896.3	$5.92917.10^{-6}x^3 - 3.00375.10^{-6}x^2 + 5.89583.10^{-7}x + 4.15000.10^{-7}$
Burst	/	/	/	/	/	$3.93.10^{-6}$

Table 2 Physical properties of aluminium

|	Density ρ (g/cm^3)	Molar mass M (g/mol)	Specific Heat Cp (J/mol.K) [35]	Phase change temperature T (K)	Phase change enthalpy ΔH (kJ/kg)	Electrical resistivity ρ (Ω.m) [155],[152]
Solid	19.3	183.84	$21.868372 + 8.068661.10^{-3}T -3.756196.10^{-6}T^2 +1.075862.10^{-9}T^3 +1.406637.10^{4}/T^2$	/	/	$(2.0.79.10^{-13}T^4 - 1.8517.10^{-9}T^3 + 7.826.10^{-6}T^2 + 1.9274.10^{-2}T - 0.968)*10^{-8}$
Solid → Liquid			/	3695	284.5	$1.287.10^{-6}$
Liquid			51.3	/	/	$(135 - 1.855.10^{-3}(T-T_m) + 4.42.10^{-6}(T-T_m)^2)*10^{-8}$
Liquid → Vapour			/	5912.15	4498.5	$9.34630.10^{-7}x3 - 1.49648.10^{-7}x2 - 1.11298.10^{-8}x + 1.52615.10^{-6}$
Burst	/	/	/	/	/	$2.3.10^{-6}$

Table 3 Physical properties of tungsten
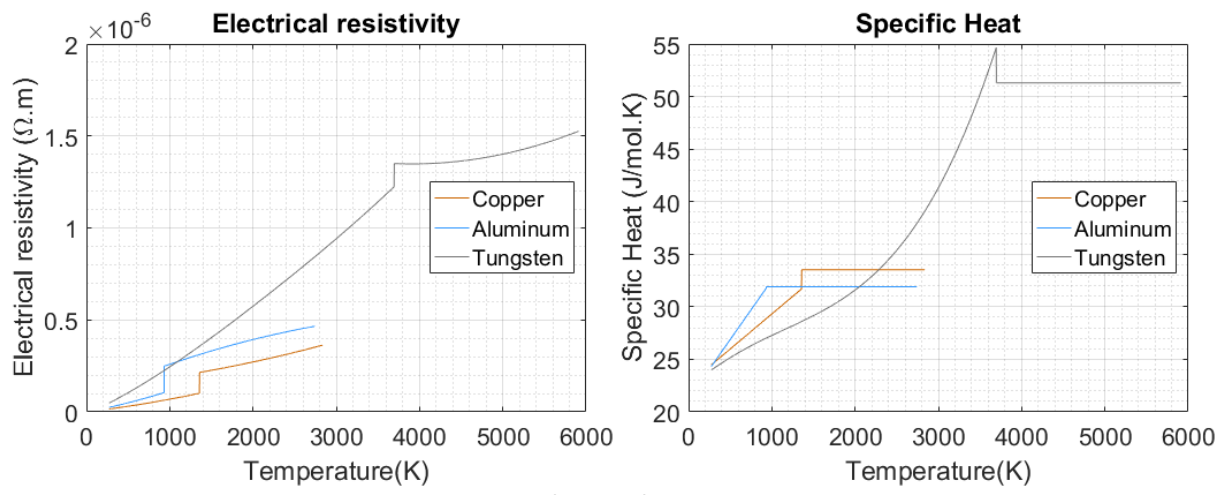
Figure 1 Metal material property curves

Appendix C – Micro-cut analysis

_____

The work done by ISAE student in the support of this PhD has been done with help of students in a collaborative way, through their academic projects of the ISAE-SUPAERO cursus, the Ecole de l'Air [156,157] or technician internship [158]. In order to reconstruct the complete delamination profile that an ultrasonic scan cannot provide, a destructive measurement was developed. The NDT method measures the echo of the delamination from the back of the panel, therefore the top delamination are hidden by the deepest one.

The composite plate subjected to lightning strike was covered by a square of resin plot on its top surface in order to fix the damage and prevent damage creation during the cutting process. Depending on the tufted fibres due to the thermal damage, the plot can quite thick from 15 to 30mm. Figure 2 presents one panel example with the resin plot contour highlighted in yellow and the paint contour in black.
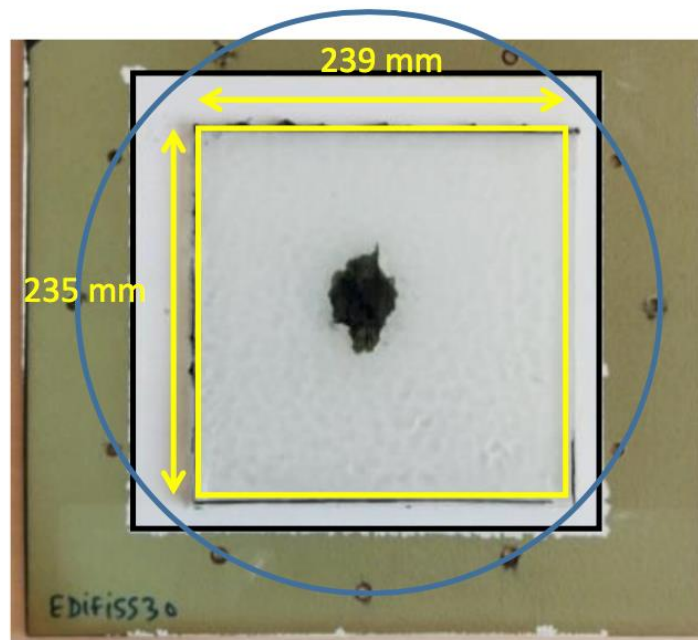
Figure 2 Example of resin plot application (EDIFISS 30)

A choice was made for the strips width that is extracted from the plate. The blade width of 2.2 mm and the risk of strip break during cutting require a minimum pitch between each cut of 14mm. The cutting scheme is illustrated in Figure 3.
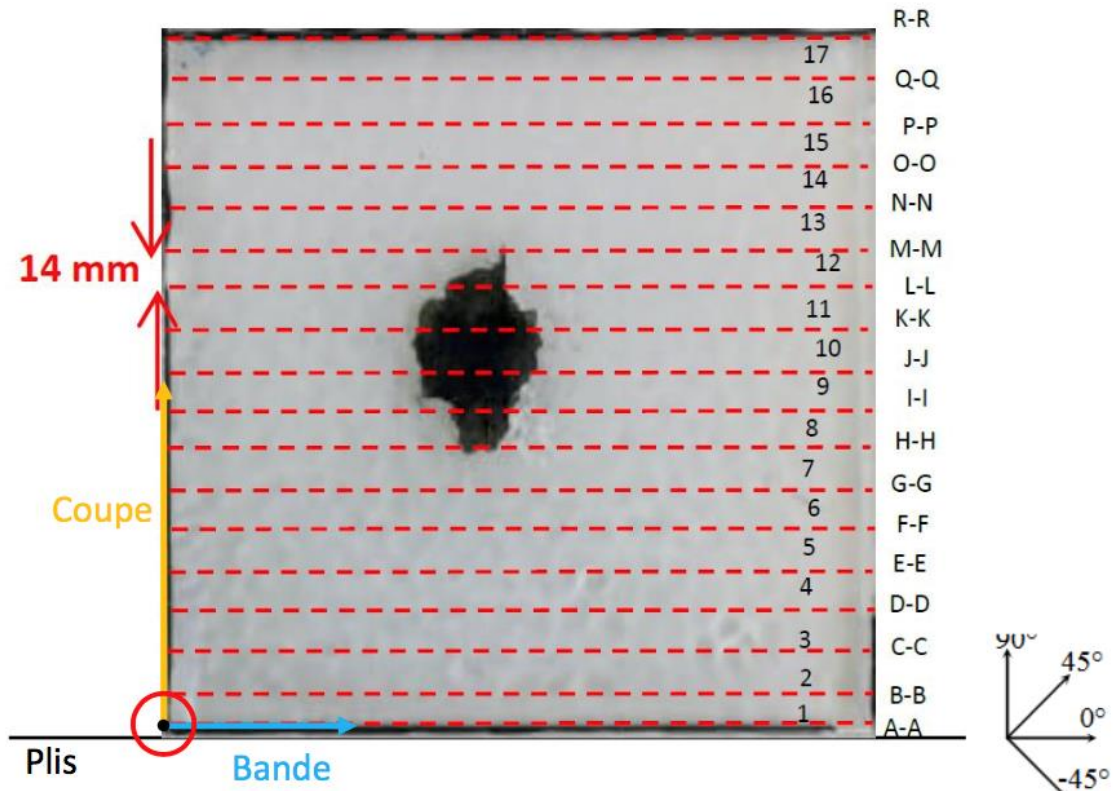
Figure 3 Strips cutting scheme (EDIFISS 30)

From this cutting scheme, the panel with the resin is cut as shown in Figure 4:
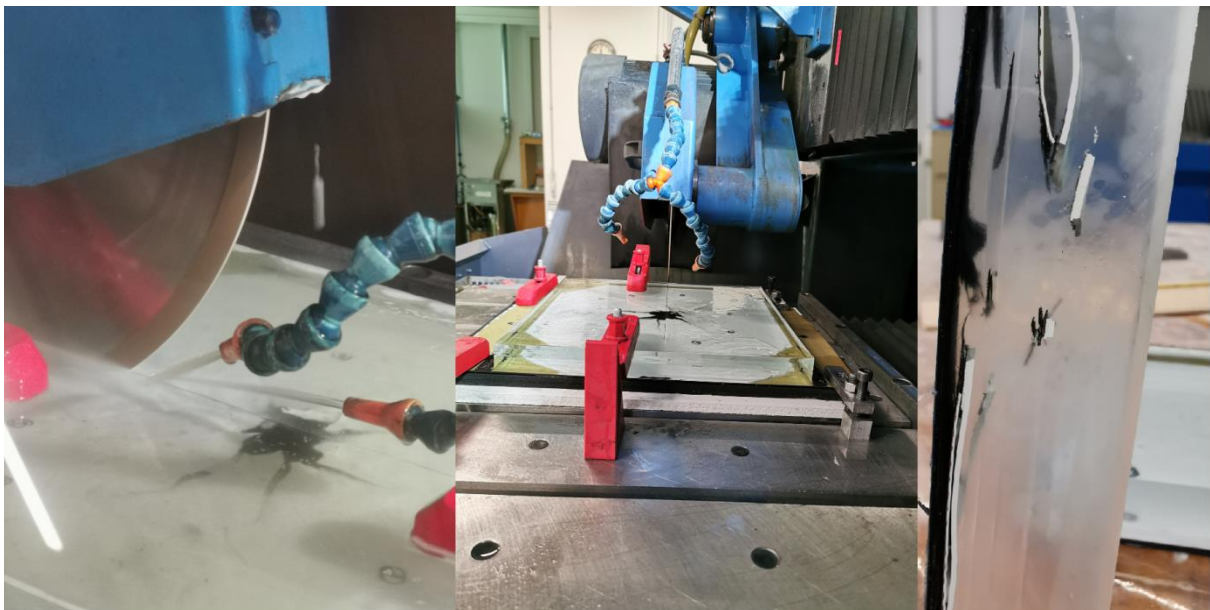
Figure 4 Cutting process (EDIFISS 6)

The strips are then polished with sandpaper. This process removes scratches from the blade and helps to obtain a clear picture. Then, for each side of the strips micrographic examination is performed and the delamination is reported in an Excel file as illustrated in Figure 5:

8D Debut D

Délaminage aux interfaces 1, 2, 5, 8 et 9, avec rupture des plis 8 et 9.
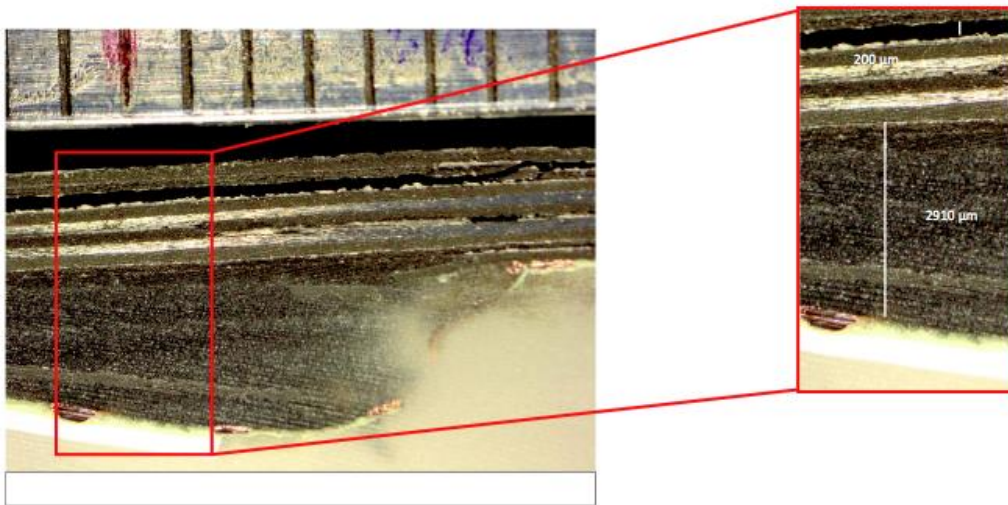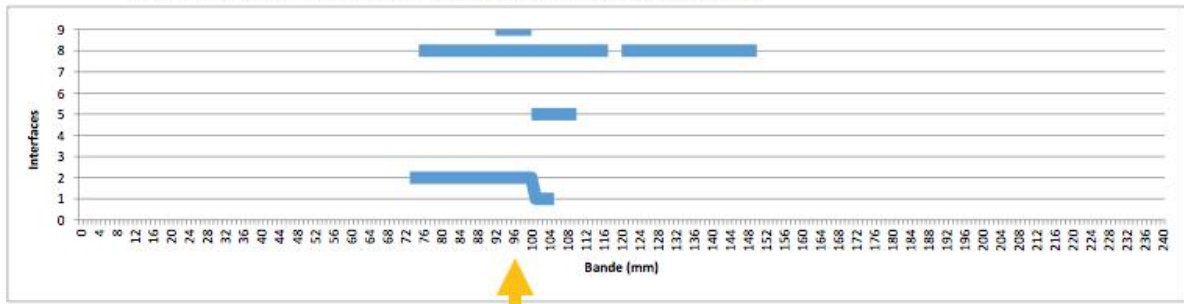
Figure 5 Micrographic inspection and delamination record example

A Matlab® code was developed in order to reconstruct the delamination profile per interface. It is now possible to study the 3D distribution of the damage in the laminated after a lightning strike. The profile is pixelated because of the strip width but provides accurate data on the interface delaminated compared to ultrasonic scan. This NDT method is based on the measurement of the echo propagation and the bending of the plate can create some issues in the discrimination of the delaminated interface.
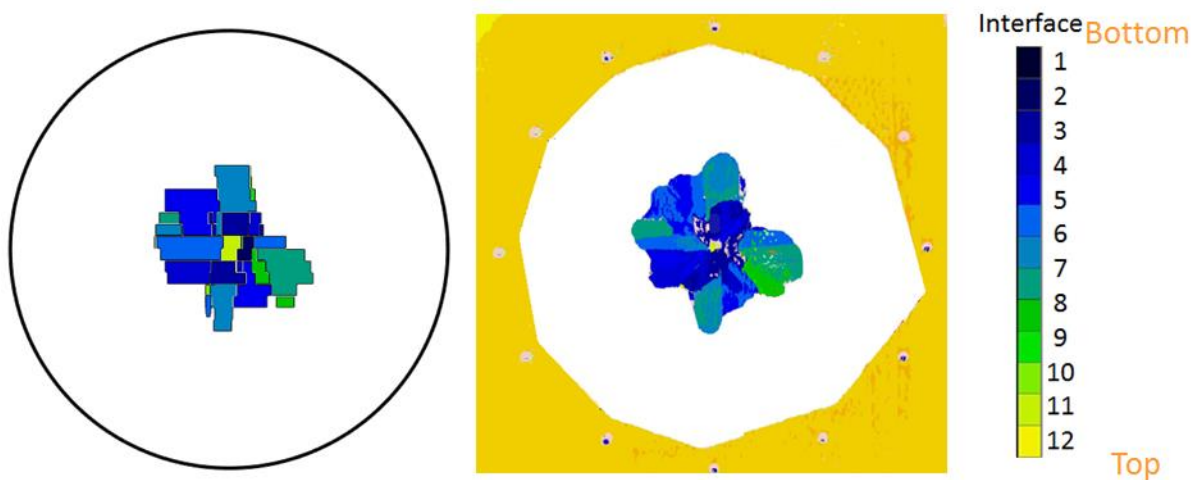
Figure 6 Profile reconstruction comparison with NDT result

With this method, the hidden delamination can be measured as illustrated in Figure 7. The left histogram is an obvious illustration of the missed information by the histogram produced by NDT compared to the reconstruction. The delaminated surfaces from NDT are in colour and the remaining delaminated surface obtained thanks to the reconstruction is added in grey.

Figure 7 Reference case: Delamination distribution (Grey histogram=hidden delamination)

Appendix D – Material mechanical properties and damage parameters

_____

The CFRP low grade used for A350 has been characterised by Airbus and the mechanical properties are summarised below:

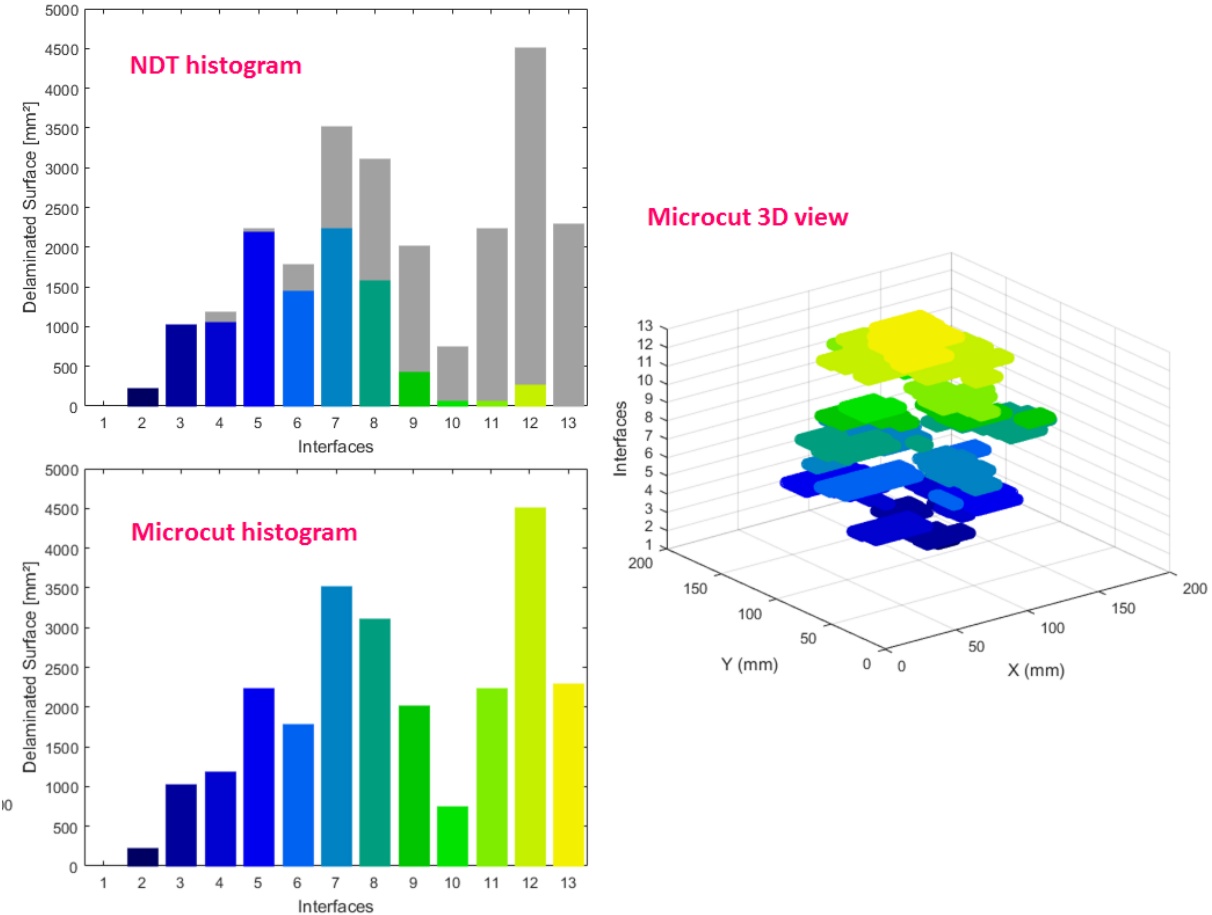| CFRP low grade properties	Definition	Value	Unit
E_{11t}	Tensile modulus in fibre direction	163	GPa
E_{11c}	Compressive modulus in fibre direction	145	GPa
E_f	Flexural modulus	154	GPa
E_{22}	Tensile modulus along the transverse direction	8.5	GPa
E_{33}	Tensile modulus in out of plane direction	8.5	GPa
v_{12}	Poisson ratio in 1 – 2	0.35	N/A
v_{23}	Poisson ratio in 2 – 3	0.26	N/A
v_{13}	Poisson ratio in 1 – 3	0.35	N/A
G_{12}	Shear modulus in 1 – 2	4.2	GPa
G_{23}	Shear modulus in 2 – 3	3.36	GPa
G_{13}	Shear modulus in 1 – 3	4.2	GPa
X_T	Tensile failure stress in fibre direction	2.61	GPa
X_C	Compressive failure stress in fibre direction	1.45	GPa
Y_T	Failure stress in tensile loading in the transverse direction	0.055	GPa
Y_C	Failure stress in compressive loading in the transverse direction	0.285	GPa
Z_T	Tensile failure stress in out of plane direction	0.065	GPa
Z_C	Compressive failure stress in out of plane direction	0.25	GPa
S_{12}	Shear failure stress in 1 – 2	0.105	GPa
S_{23}	Shear failure stress in 2 – 3	0.068	GPa
S_{13}	Shear failure stress in 1 – 3	0.068	GPa
G_{Ic}	Mode I strain release energy	285	J/m²
G_{IIc}	Mode II strain release energy	745	J/m²

Table 4 CFRP low grade properties

In addition, damage variables are defined for the ply damage in the VUMAT:

| Damage variables	Definition	Value	Unit
S_{fs}	Shear failure stress for debonding of fibre matrix interface	1.5	GPa
m_i	Softening parameter	10	N/A
φ	$\tan\varphi$: coefficient of friction for material in compression	10	N/A
d_{c1}	Max damage for d_1	0.95	N/A
d_{cm}	Max damage for d_i with i≠1	0.98	N/A

Table 5 CFRP damage variables

Résumé en français

_____

Evaluation de l'endommagement dans les structures composites en aéronautique généré par la contrainte foudre

1. Introduction

Au cours des 40 dernières années, l'utilisation des composites a considérablement augmenté dans l'industrie aéronautique, car les composites renforcés de fibres de carbone (CFRP) présentent une résistance et un rapport rigidité/masse plus élevés que les structures métalliques. Ces avantages ont conduit les constructeurs aéronautiques à utiliser de plus en plus la technologie des composites. Au sein de la flotte Airbus, les composites représentaient environ 10 % pour les premiers modèles et sont passés à 50 % avec le tout nouveau A350 XWB. La grande étape a été l'utilisation de composites pour les structures primaires du fuselage et des ailes par rapport aux programmes précédents.

Figure 1 Evolution de l'utilisation du composite au sein de la flotte Airbus [1]
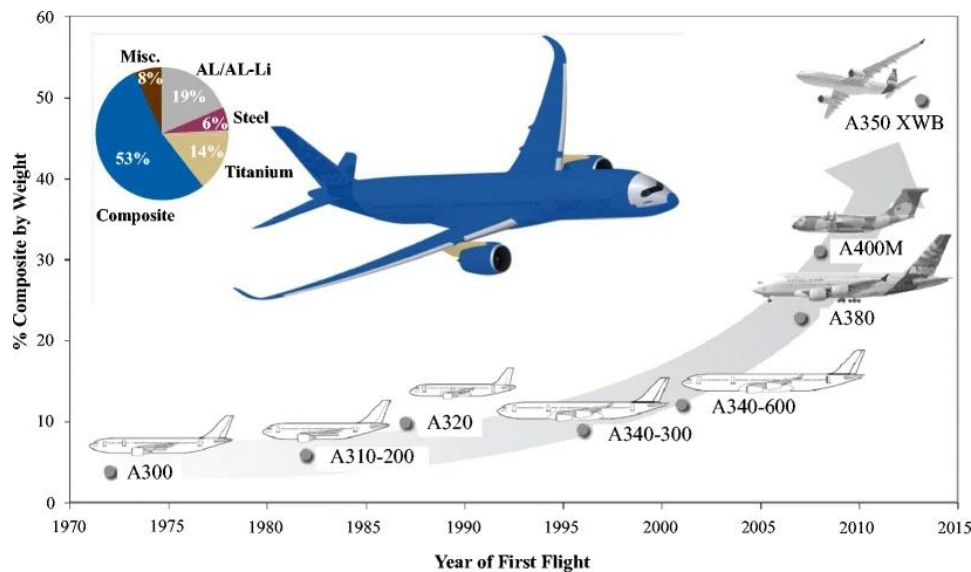
L'introduction des composites a eu un impact important sur la stratégie de certification de la foudre pour cet avion. Les structures métalliques peuvent facilement supporter un coup de foudre grâce à leur conductivité électrique élevée qui dissipe le courant sans dommage majeur, lequel est limité à un petit point de fusion dans le pire des cas. Malgré leurs excellentes propriétés mécaniques, les composites sont de mauvais conducteurs, ce qui les rend plus susceptibles de subir de graves dommages dus à la foudre, tels qu'un délaminage important, une brûlure et éventuellement une perforation [2]. Afin de protéger les structures composites, une couche de protection contre la foudre est appliquée sur la

surface extérieure. Cette protection est généralement un fin maillage de métal (cuivre, bronze...) qui a la fonction d'un pli sacrificiel qui va dissiper le courant et se vaporiser. Malheureusement, la présence de peinture diminue l'effet protecteur de la couche métallique. Comme les endommagements ne sont pas complètement évités et peuvent même être sévères dans les structures minces, des tests de foudre sont effectués en laboratoire afin d'évaluer ces dommages et de démontrer qu'un vol et un atterrissage continus et sûrs après un coup de foudre sévère sont possibles. Cependant, une campagne de tests de foudre est très coûteuse et prend beaucoup de temps. Dans le cadre du développement d'un programme avion, la validation de la foudre peut faire partie du chemin critique pour la validation de la conception car une modification de la structure ou de la protection contre la foudre peut être nécessaire. Il est donc important de disposer des moyens adéquats pour soutenir la validation de la conception en fonction des étapes du programme. Au cours du développement de l'A350, de nombreux tests de foudre ont été effectués avant la certification afin de valider la conception de tous les composants composites de l'avion, tests qui ont coûté des centaines de milliers d'euros et ont pris plusieurs mois. Pour les futurs programmes, il est nécessaire de mieux comprendre le mécanisme de détérioration par la foudre des structures peintes et de mettre en place une capacité de modélisation pour permettre un développement plus efficace.

Dans ce contexte, un projet de recherche financé par la DGAC avec des partenaires industriels de l'industrie aéronautique et des universitaires a été lancé en 2015. Le projet nommé EDIFISS (Effets DIrects de la Foudre Induits sur les Structures et Systèmes) visait à étudier les différentes conséquences d'un coup de foudre. Bien qu'il ne soit pas inclus dans le projet EDIFISS, ce doctorat y contribue et a pour objectif de comprendre les paramètres clés qui influencent les dommages dus à la foudre dans les structures composites peintes. La foudre est, en effet, un phénomène extrêmement rapide et multi-physique qui interagit avec la structure, ce qui rend l'étude et la compréhension très complexes. La plupart des approches scientifiques existantes considèrent deux événements distincts. L'arc de foudre, d'une part, est considéré comme une source de courant fixe et indépendante. Le composite nu, d'autre part, est considéré comme un « collecteur » qui sera endommagé en raison des effets électrothermiques induits, parfois combinés à des effets mécaniques. Ce travail de thèse est une première contribution à l'analyse des phénomènes d'interaction complexes qui se produisent dans les couches de protection et de l'effet nuisible de la peinture. Ainsi, une approche globale est proposée qui considère un panneau complet représentatif de la configuration réelle d'un composant d'avion : le composite, la couche de protection contre la foudre et la peinture. Cette approche décompose le phénomène en quatre événements à partir de la source : l'arc de foudre, son interaction avec la couche de protection contre la foudre à la surface du panneau, l'effet de la peinture et la première couche composite, et enfin la structure composite et les dommages consécutifs.

2. Etat de l'art

2.1 La foudre et sa définition en aéronautique

La foudre est un phénomène naturel qui génère une décharge de courant et de tension élevée [3]. Ce mécanisme est dû à l'accumulation de charges électriques dans les nuages, produite par les mouvements des gouttes d'eau et des particules de glace, qui entraînent des collisions et des fragmentations. Cela produit un champ électrique qui peut augmenter au point d'ioniser l'air et de générer une décharge de foudre. Un avion est généralement frappé une à deux fois par an en fonction de sa situation géographique et de son exploitation. Un impact de foudre sur un avion est un risque qui doit être pris en compte car il peut mettre en danger la sécurité du vol s'il n'est pas correctement géré. Au cours du processus de certification, la conception de l'aéronef doit être conforme au règlement CS-25 [4] afin de garantir qu'aucun événement catastrophique ne puisse se produire après un coup de foudre. À cette fin, des normes relatives à la menace foudre ont été établies afin de définir les différentes zones de l'aéronef qui seront touchées et le niveau de menace, c'est-à-dire le courant, qui y est associé.

Lors d'un éclair, l'avion sera frappé à plusieurs reprises pendant qu'il se déplace au cours du phénomène. Les zones pointues de l'avion déclenchent le coup de foudre. Ces zones sont appelées zone 1 en raison de leur forte probabilité de déclenchement par la foudre. Ensuite, l'arc va balayer la surface de l'avion en vol avec une décharge consécutive. Ces dernières zones sont appelées zone 2. En dehors de ces zones, cela ne signifie pas qu'un coup de foudre ne peut pas se produire, mais la probabilité est très faible. Néanmoins, le courant de la foudre peut circuler par conduction dans les zones qui se trouvent entre l'entrée et la sortie. Ces zones sont appelées zone 3. En plus de cette définition de zonage de haut niveau, il est nécessaire d'envisager pour les zones 1 et 2 la possibilité que l'arc se déplace (catégorie A) sur la structure ou soit maintenu parce qu'il a atteint la limite de la structure (catégorie B). Les documents ED-91[5] / ARP5114[6] donnent les recommandations pour la définition du zonage dont voici un exemple :
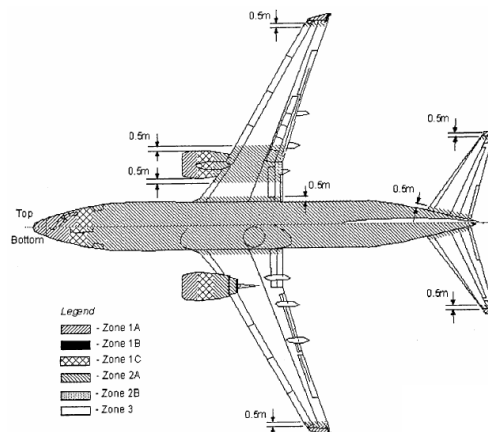

Figure 2 Exemple de zonage [5]

Sur la base de ce zonage, il est alors possible d'associer un courant de foudre normalisé composé de plusieurs formes d'onde afin de représenter le scénario de foudre tel que défini par ED-84[3]/ARP5412[7]. Par exemple, pour une zone 2A, on associe les formes D+B+C*.
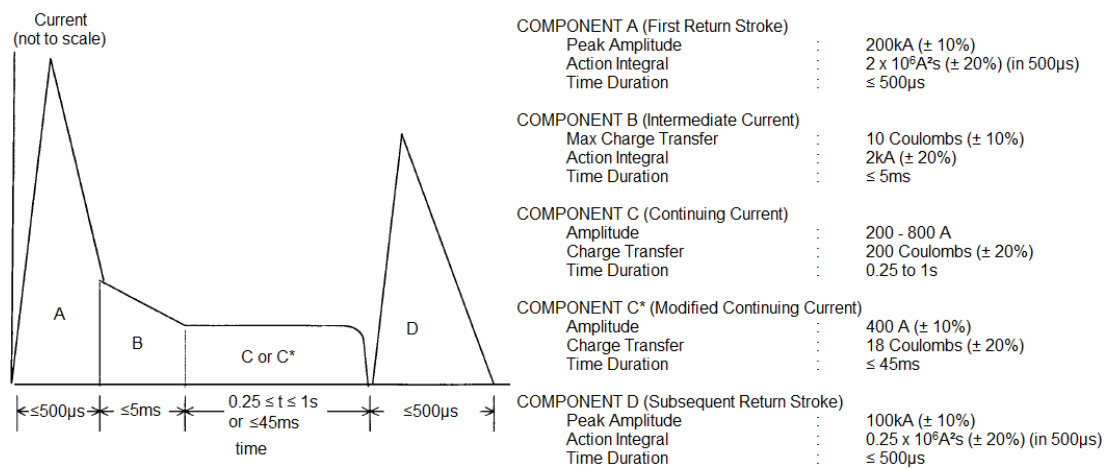

Figure 3 Définition des formes d'onde foudre

A partir de ces définitions, un essai foudre en laboratoire suivant les recommandations de ED-105[8]/ARP5416[9] est effectué sur un échantillon afin d'évaluer l'endommagement sur la structure. Afin de limiter les coûts, l'échantillon est une plaque plate de 500 mm de côté environ dont l'épaisseur est conditionnée par l'épaisseur minimum de la structure à valider. Après l'essai foudre, un contrôle non-destructif (CND) par ultrason permet de mesurer la zone délaminée pour un composite.

2.2 La foudre et l'endommagement dans les structures

La conductivité des fibres de carbone est environ 1000 fois inférieure à celle du métal et la conductivité transverse (à la fois dans le plan et dans l'épaisseur du stratifié) est encore plus mauvaise à cause de la matrice de résine qui est un diélectrique. Afin de mieux comprendre le mécanisme d'endommagement du composite, de nombreuses études ont été réalisées ([10–14]). Ces endommagements peuvent être sévères avec des ruptures des fibres et dommages aux fibres (ressemblant à des touffes), de la détérioration de la résine et du délaminage du composite. Afin de limiter les dégâts, les constructeurs d'avions utilisent une protection contre la foudre (LSP = Lightning Strike Protection) appliquée sur la surface externe du composite. Il s'agit d'une couche sacrificielle conductrice qui est utilisée pour évacuer le courant de la foudre du CFRP. La couche est faite d'un matériau conducteur afin d'agir comme chemin principal du courant en raison de sa faible résistivité par rapport au CFRP. De nombreuses protections contre la foudre (LSP) [15] ont été développées pour la protection des structures composites contre les dommages causés par la foudre. Les technologies les plus courantes qui répondent aux contraintes industrielles sont les feuilles métalliques expansées telles que les feuilles de cuivre expansé (ECF) et les mailles métalliques telles que les mailles de bronze (BM), comme l'illustre la Figure 4.
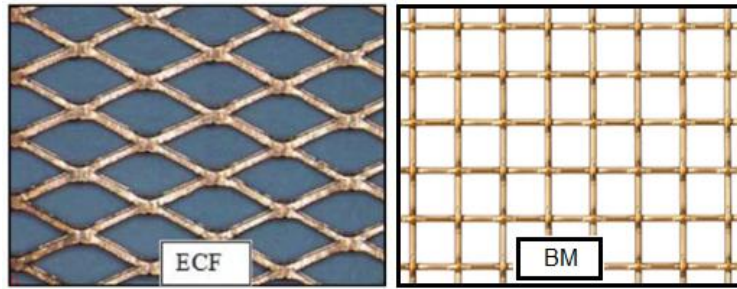
Figure 4 Common Lightning Strike Protection [16]

Dans les différents développements des technologies de protection contre la foudre, un paramètre important est rarement pris en compte : la peinture, qui est considérée comme un simple élément cosmétique sans propriétés structurelles. Cependant, les dommages causés par la foudre dépendent fortement de l'interaction entre l'arc et la structure. Un pied d'arc libre s'étend rapidement dans l'air en fonction de la conductivité électrique de la surface : plus la conductivité de la surface est faible par rapport à l'arc, plus l'expansion du pied d'arc est rapide par rapport à la colonne d'arc [17]. Comme la protection contre la foudre en surface est plus conductrice que la structure composite sous-jacente, le courant circulera principalement dans la couche externe et la plupart de l'énergie sera dissipée dans cette couche. À cet égard, toute protection contre la foudre sera plus efficace qu'un composite nu [18]. Bien évidemment, les avions sont peints afin de protéger la structure de l'environnement (UV, fluides, etc.) et aussi pour répondre au souhait de décoration de la compagnie aérienne. Mais en réalité, l'efficacité d'une protection contre la foudre en surface, mais sous la peinture, diminue considérablement avec l'épaisseur de la peinture. Voici une illustration de ce mécanisme pour l'ECF195 protégeant une plaque de CFRP de 1,6 mm d'épaisseur mesurant 450 mm par 450 mm avec un attachement mécanique circulaire de 370 mm de diamètre (trou de boulon visible sur la photo) :

Figure 5 Evolution de l'endommagement du composite avec l'épaisseur de peinture (projet EDIFISS)

Peu d'études existent sur cet effet. Des études menées par Lepetit [19] et Karch [20] ont considéré l'effet de confinement de la peinture comme une simple masse qui a un effet inertiel sur la surpression qui se produit à la surface. Des travaux internes à Airbus ont montré, lors de tests en laboratoire sur la foudre, que la peinture était éjectée par une explosion sous-jacente. On suppose que ce phénomène est dû à l'échauffement par effet Joule de la protection métallique, qui a entraîné son explosion. Le confinement de la surpression par la peinture augmente les contraintes et accroît les dommages [21].

Si l'on considère l'ensemble du système (CFRP, LSP et peinture), les dommages peuvent être décomposés en différents éléments :

- Les **endommagements de surface** qui peuvent être mesurés par une simple inspection visuelle :
  - Cosmétique : Vaporisation du LSP et éjection de la peinture (rouge)
  - Structurel : Fibres sèches (touffes) dues à la détérioration de la résine et fibres cassées (vert)
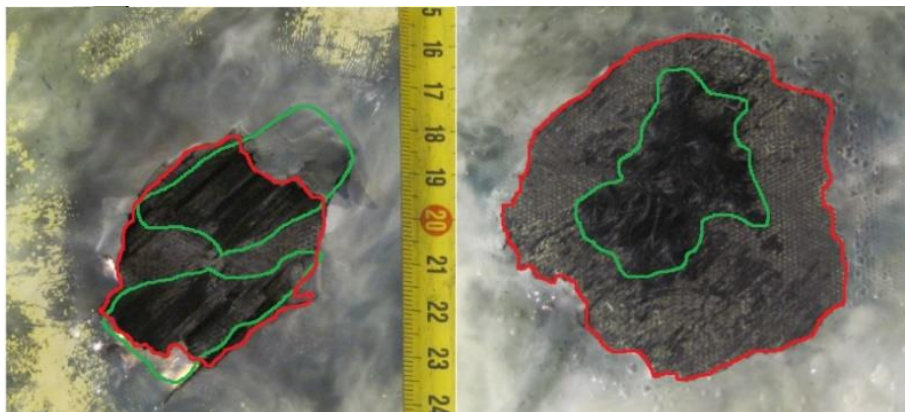
Figure 6 Exemple d'endommagement visible

Ce dommage ([22], [19])est principalement dû à l'effet électrothermique du courant de foudre dans le LSP et dans le composite.

- **L'endommagement structurel** qui nécessite une inspection spécifique telle qu'un balayage ultrasonique afin de mesurer le délaminage. Ce type de dommage est également appelé "dommage à cœur" ([22], [19])

Il peut également y avoir des dommages thermiques concentrés au centre de l'impact en raison de l'augmentation de l'injection de courant dans la profondeur du stratifié avec l'arc contraint, mais le principal problème est le délaminage qui a une origine mécanique [22].

Figure 7 Décomposition de l'endommagement foudre [30]

La foudre est un phénomène bien plus complexe que les dommages thermiques dus à la circulation du courant dans la structure [24,25]. Les différentes forces qui créent les dommages doivent être correctement appréhendées afin de proposer un modèle pertinent pour l'endommagement du composite dû à la foudre.

2.3 La modélisation de la foudre

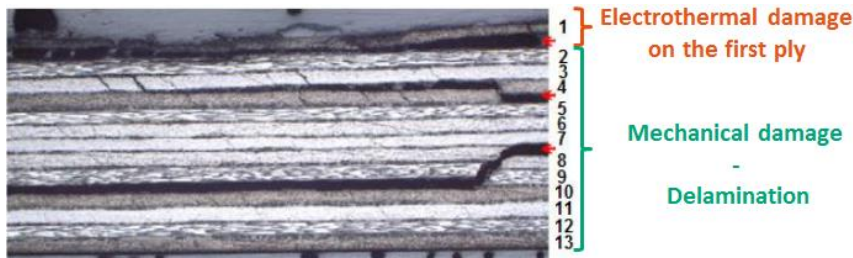Il est difficile de quantifier l'importance de chacun des différents phénomènes physiques qui font partie d'un coup de foudre, et encore moins de quantifier leur interaction et leur couplage les uns avec les autres. Une représentation des forces physiques possibles impliquées (forces thermiques, électro, magnétiques et mécaniques) est proposée sur la Figure 8 avec un lien vers les dommages observés sur le matériau composite frappé par la foudre.

Actuellement, il reste difficile de prédire les dommages qui pourraient être générés par la foudre sur une structure composite en raison de sa phénoménologie complexe et des différentes forces impliquées [26,27]. Il s'agit en effet d'un phénomène hautement dynamique et multi-physique. Il n'existe pas de théorie entièrement validée sur tous les phénomènes physiques impliqués par l'arc et son interaction avec la structure ou la chronologie associée. Néanmoins, une proposition des différentes forces impliquées a été élaborée :
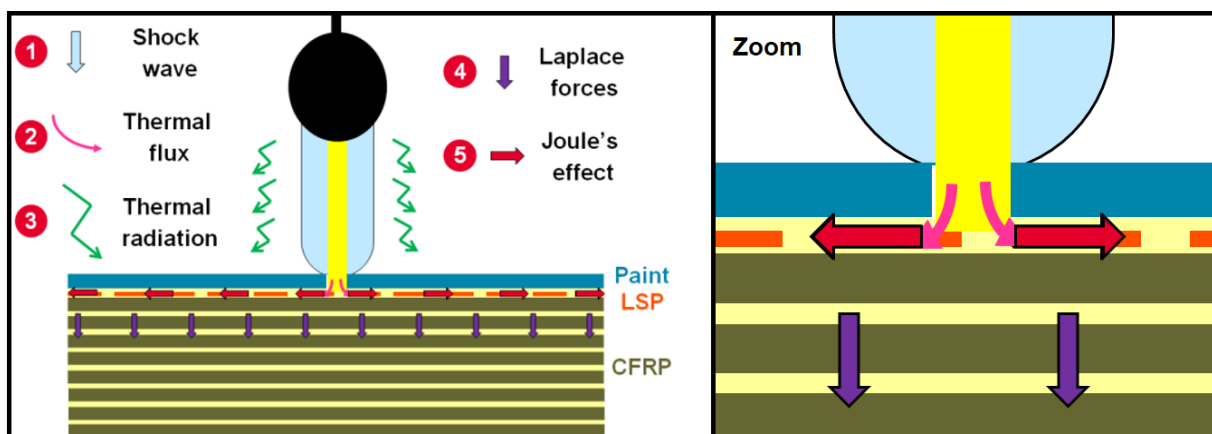

Figure 8 Les forces générées par la foudre en interaction avec les structures composites

On distingue les phénomènes physiques suivants lors d'un coup de foudre sur une structure composite protégée et peinte. Les *forces thermiques* comprennent : le **flux thermique** venant de l'interaction du plasma avec la structure générant une source de chaleur vers la structure qui dépend du courant, du rayon de l'arc et de l'état de la structure [26], ensuite le **rayonnement thermique** de l'arc que l'on considère négligeable [28] et enfin l'**effet Joule** dû au courant de foudre dans la protection métallique et la structure composite qui augmente leur température rapidement jusqu'à la vaporisation qui est en fait une explosion des matériaux. L'explosion de la protection crée une onde de choc qui est transmise à la structure. De plus, les fibres supérieures se brisent et la résine disparaît par pyrolyse [20], [29]. Les *forces mécaniques* comprennent : les **forces de Laplace** dues à la circulation du courant circulant dans la protection foudre qui induit une pression magnétique [20] et l'**onde de choc** provenant de la création de l'arc. En effet, la température (jusqu'à 30 000 K en quelques µs) et la pression augmentent rapidement entrainant la dilation du canal ionisé créant l'onde de choc. Sa pression diminuera rapidement avec la propagation et seul le tonnerre se fera entendre. Cependant, à l'endroit où se forme l'arc, la surpression sera importante [30].

Les différentes forces et dommages auront une certaine influence les uns sur les autres, ce qui rend le modèle des dommages encore plus compliqué. En outre, la validation du modèle est difficile car l'étendue des mesures possibles lors d'un test de foudre est limitée en raison de la rapidité du phénomène dans lequel les dommages sont générés dans les premières microsecondes (< 20 µs), et de l'intensité de l'arc de foudre qui crée un fort champ électromagnétique (100 kA atteint en environ 15 µs) et une source de très haute température (jusqu'à 30000K [31]). Dans un environnement aussi violent, il est impossible d'installer des capteurs au contact ou à proximité de l'arc.

Les travaux réalisés dans le passé ont d'abord été basés sur une approche électrothermique simple [14,32–34] dans laquelle le flux de courant dans le composite génère de la chaleur qui va créer des dommages. Ces modèles ont ensuite été affinés en tenant compte de la dégradation de la résine par pyrolyse [14,34–38]. Dans de nombreux cas, l'arc a été modélisé comme une source de courant équivalente avec une zone d'injection fixe. Pourtant, il a été démontré que la racine de l'arc interagit avec la structure et que son injection est variable dans le temps et l'espace, comme montré par Tholin [39] et Lago [28]. Enfin, cette approche a montré ses limites puisqu'elle s'est révélée incapable de prévoir le délaminage sous-jacent provenant d'une contrainte mécanique. Les dommages prédits par les modèles ont toujours été inférieurs aux dommages observés lors des tests de foudre en laboratoire [10], même avec une injection de courant plus complexe [40] basée sur l'expansion du rayon de la colonne d'arc par Braginskii [41].
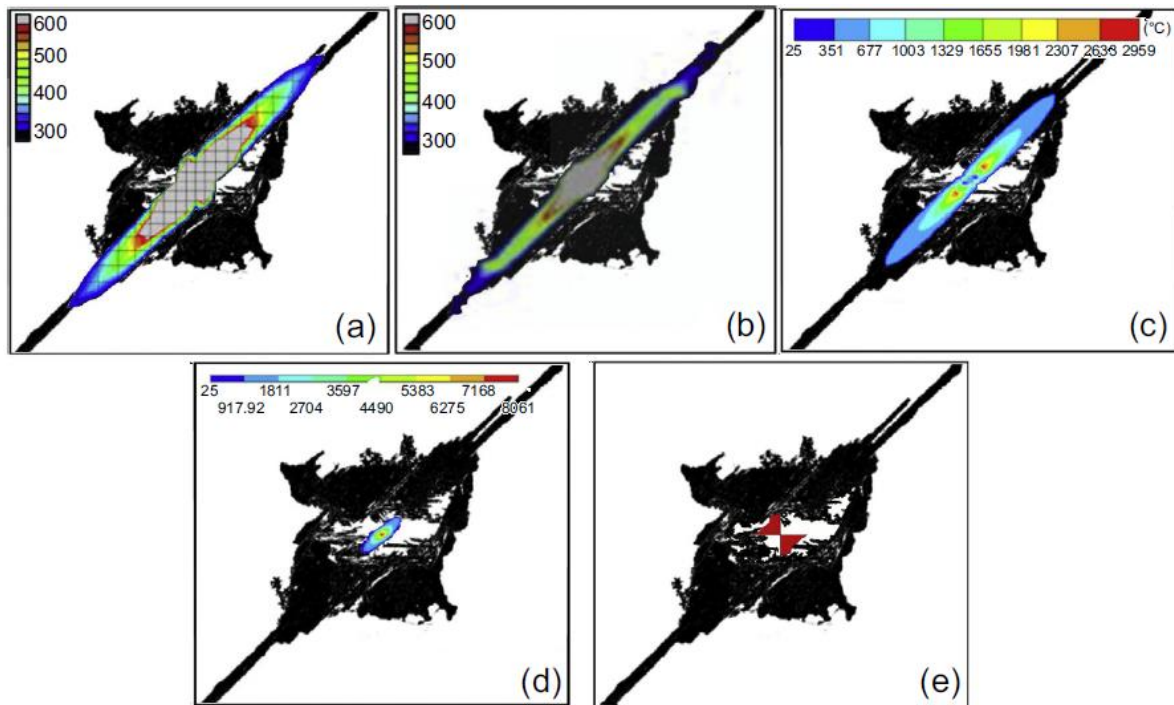
Figure 9 Comparaison entre la décomposition thermique de la résine [10] et la distribution modélisée de la température [40] (a: [35], b: [37], c: [42], d: [43], e: [14])

Afin d'évaluer le délaminage, qui est l'effet le plus préjudiciable pour la durabilité de la structure, des modèles des sources de pressions générées par l'arc, c'est-à-dire l'onde de choc de l'arc et la pression magnétique, ont été introduits. L'évaluation de la pression de l'arc et du flux de courant à la surface a fait l'objet d'une étude approfondie [20,26,44–47]. Pour la pression magnétique, on distingue deux zones : la zone sous le pied d'arc (r ≤ R_{arc}), à l'injection, et la zone à l'extérieur où le courant circule dans la protection de surface (r > R_{arc}).

La dépendance de ces forces à l'évolution du rayon du pied de l'arc rend très difficile la pondération correcte de ces deux contributeurs (Onde de choc provenant de la création de l'arc et pression magnétique). Même si un modèle plus précis pourrait être développé, cela ne suffirait pas à prédire les dommages car les valeurs de ces forces ne sont pas assez élevées pour générer une contrainte significative dans le composite.

Cela a conduit certains chercheurs à étudier l'effet d'explosion du composite mais aussi le rôle de la protection métallique à la surface de la structure, car le courant foudre très élevé circulant dans le conducteur entraîne une augmentation rapide de la température jusqu'à l'explosion. La pression générée par ce phénomène n'est évidemment pas négligeable et doit être étudiée plus en détail.

Des approches intéressantes d'équivalent mécanique ont été développés comme par exemple Liu [43] qui propose un explosif basé sur les équations d'état de Jones-Wilkins-Lee

(JWL) pour simuler l'explosion dans le carbone, ou encore Soulas [22] qui propose l'équivalent avec un l'impact d'une bille métallique.

Mais, il ne suffit pas de considérer les différentes forces qui peuvent être générées par un coup de foudre. Il faut également prendre en compte le système global qui interagira avec ces forces. Bien sûr, la structure composite où la prévision des dommages est essentielle en fait partie. Mais en outre, la protection contre la foudre et la peinture doivent être introduits dans le modèle. Certaines études ont tenté de modéliser le comportement des protections métalliques, mais l'ont rarement comparé aux résultats des tests, et un seul groupe, Karch [20] et Lepetit [19], a examiné la contribution de la peinture dans son modèle par le biais de la masse ajoutée qui a un effet de confinement.
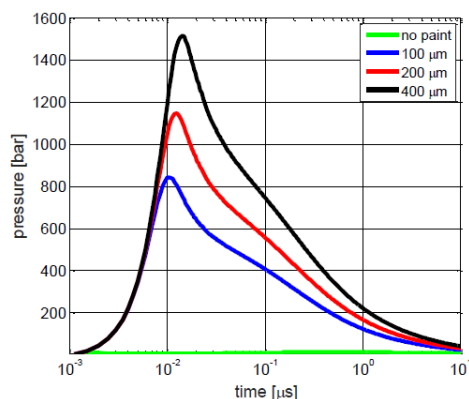

Figure 10: Effet de l'épaisseur de peinture sur la pression équivalente lié à la vaporisation de la protection foudre [20]

Ce travail est d'une importance capitale et doit être développé car il n'a pas pris en compte l'effet de constriction de la peinture sur l'arc et le confinement de l'explosion qui dépend de ses propriétés mécaniques et de son adhérence.

2.4 Conclusion

Les recherches développées dans le cadre de cette thèse visent à décomposer les différents phénomènes impliqués dans la génération des forces de la foudre et donc les dommages consécutifs. La foudre est un phénomène tellement complexe qu'il est important de comprendre ses contributeurs avant de construire une approche complète pour définir le couplage entre chacun d'eux, leur poids et distribution associés. Pour cela, le travail commence par l'étude de la source qui est l'arc de foudre lui-même et son interaction avec la structure complète (LSP et peinture) car il a été démontré qu'une injection fixe n'est pas réaliste. Sur la base de ce développement, il sera possible de prédire l'explosion de la protection contre la foudre en surface, qui est un facteur important de la surpression appliquée sur la structure. De plus, la peinture est caractérisée afin de comprendre son effet de confinement sur l'explosion du LSP.

Comme cette thèse vise également à prédire les dommages les plus préjudiciables à la structure, c'est-à-dire le délaminage, la source de surpression modélisée qui dépend du LSP et de la peinture sera injectée dans un modèle mécanique. Le modèle d'endommagement développé par Soulas [22] est réutilisé et développé pour évaluer les dommages. La méthode développée dans cette thèse est résumée ci-dessous mettant clairement en évidence les différentes briques qui sont étudiées individuellement afin de construire un modèle de foudre plus complet pour la prédiction du délaminage:
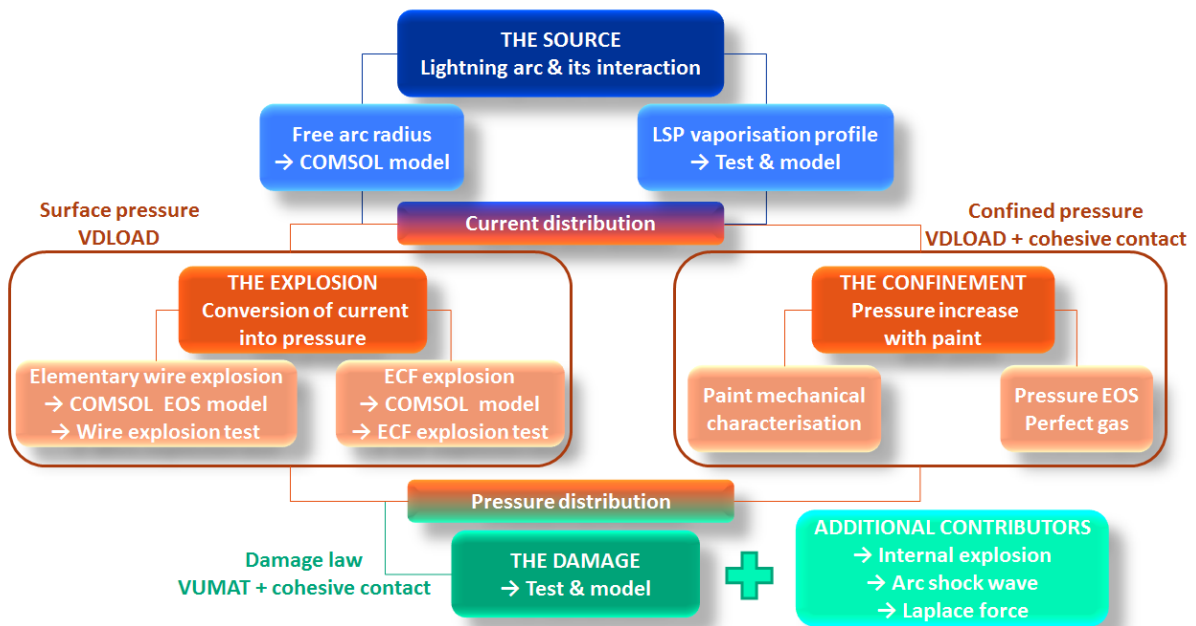

Figure 11 Modèle des endommagements causés par la foudre et décomposition

3. L'arc foudre et ses interactions

L'objectif de ce chapitre est de proposer un modèle pour le profil de vaporisation de la protection foudre métallique (LSP) puisque la surpression générée à la surface de la structure composite est la conséquence de son explosion qui va endommager le stratifié. L'origine de cette explosion est la vaporisation soudaine de la protection métallique due à l'échauffement par effet Joule. Il est donc nécessaire de comprendre comment le courant de l'arc de foudre est injecté dans la protection. Pour cette raison, une étude de la colonne de l'arc a été faite puis confrontée à l'évolution du pied d'arc qui interagit avec la protection contre la foudre (LSP) et est contraint par la présence de peinture.

3.1 Etat de l'art

Le canal de l'arc foudre peut être considéré comme une colonne de plasma très chaud atteignant une température de 40000K [17,48]. Cette colonne de gaz ionisé est définie comme un plasma thermique qui est un fluide conducteur qui sera influencé par un champ électromagnétique. Par conséquent, les lois qui piloteront le comportement d'un arc sont

basées sur un système d'équations de conservation. Les équations de Navier-Stokes pour la partie fluide, les équations de Maxwell pour la partie électromagnétique et l'équation de conservation de l'énergie sont couplées notamment par des contributions thermiques telles que le chauffage par effet Joule et les pertes radiatives. Le modèle de la physique de l'arc est basé sur la théorie de la magnétohydrodynamique (MHD). La plupart des modèles sont basés sur des courants plus faibles et plus lents que la foudre mais une étude très poussée a été développée par l'ONERA à travers des essais [17,49] et des modèles MHD [49–51] :
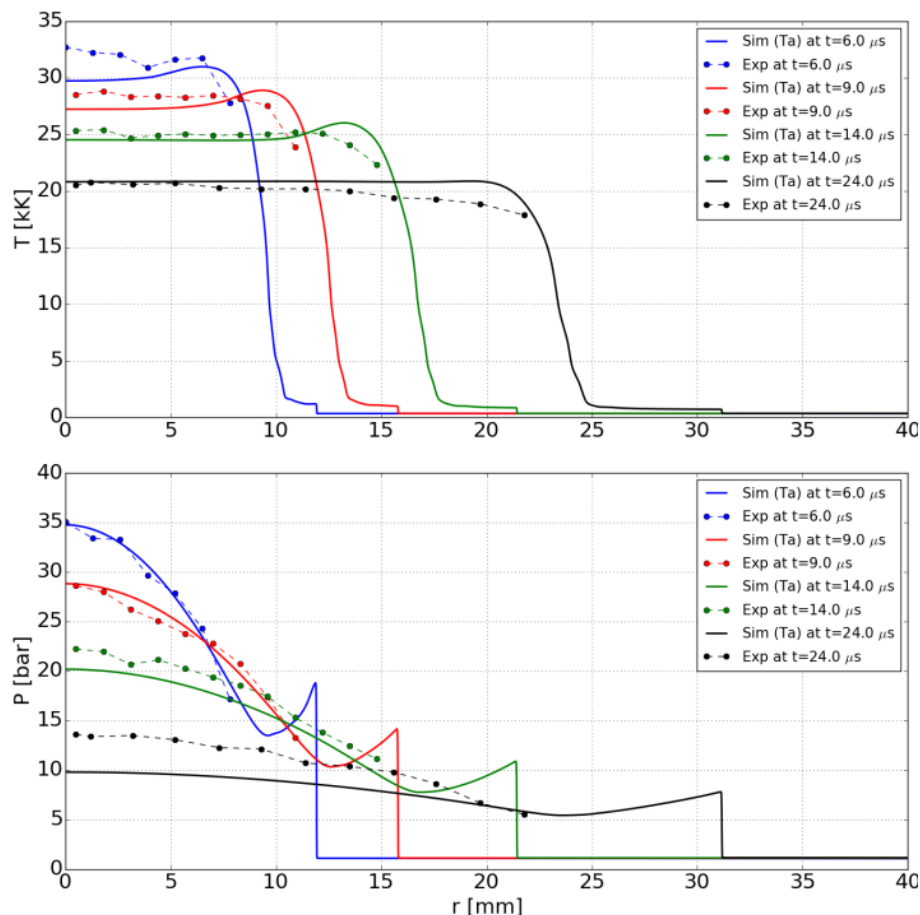
Figure 12 Profils de pression et température pour un arc foudre (100 kA) : Comparaison entre la simulation MHD et les mesures expérimentales [49]

La modélisation de l'interaction du pied d'arc est encore plus complexe. Les modèles ne considèrent pas de dégradation du conducteur en interface comme sa vaporisation qui pourrait perturber l'arc lui-même. C'est le cas pour la protection foudre métallique très fine qui se vaporise très vite avec le passage du courant de foudre. Mais il a été démontré que la conductivité électrique de la plaque en interface avait une influence sur la forme et la vitesse d'expansion du pied d'arc [39].

Figure 13 Comparaison du pied d'arc pour différentes conductivités électriques d'électrode à 26µs [39]

Enfin, la présence de la peinture va également perturber le pied de l'arc en créant une barrière physique à son expansion. Cette couche diélectrique empêche l'arc de s'accrocher sur le conducteur intact et va en resserrer le pied [17]:

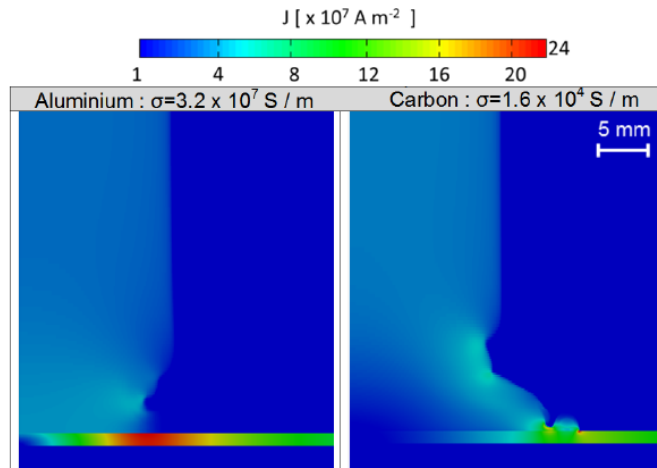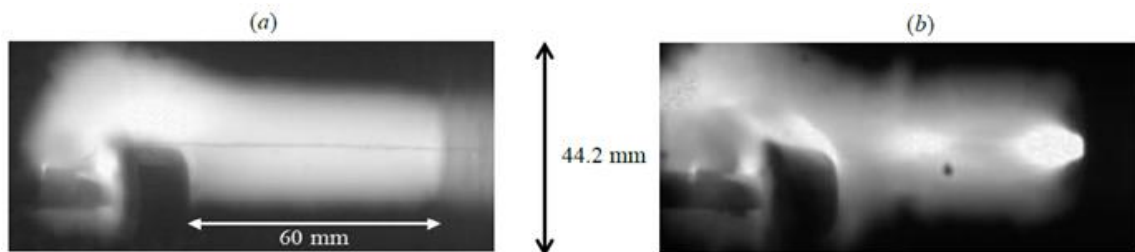**Figure 14 Expansion du pied d'arc à 15µs pour un arc de foudre à 100kA : a) Panneau d'aluminium nu contre b) panneau d'aluminium peint (électrode à jet à gauche et panneau à droite)**

L'évolution du pied d'arc et donc de l'injection du courant dans la protection foudre va modifier le profil de vaporisation de la protection, c'est-à-dire son explosion. Cette évolution est dépendante des propriétés de la protection conductrice mais aussi de la peinture diélectrique. Nous allons étudier ces influences dans la section suivante.

3.2 Essai foudre : Profil de vaporisation

Le principal problème dans l'étude du coup de foudre sur un composite est la difficulté liée à la mesure. L'élaboration d'une théorie ou d'un modèle doit être confrontée à des données d'essai réelles pour étayer sa validation. Mais l'intensité de phénomènes tels que la lumière, la température ou le champ magnétique rend presque impossible toute mesure en raison des perturbations qu'elle pourrait générer sur un capteur. Dans notre cas, il a fallu mesurer le profil de vaporisation de la protection, mais celui-ci est entièrement caché entre la plaque composite (CFRP), la peinture et la colonne d'arc foudre. Nous avons donc développé un dispositif de test spécifique afin d'observer ce phénomène à l'aide d'une caméra rapide à un millions d'images par seconde.
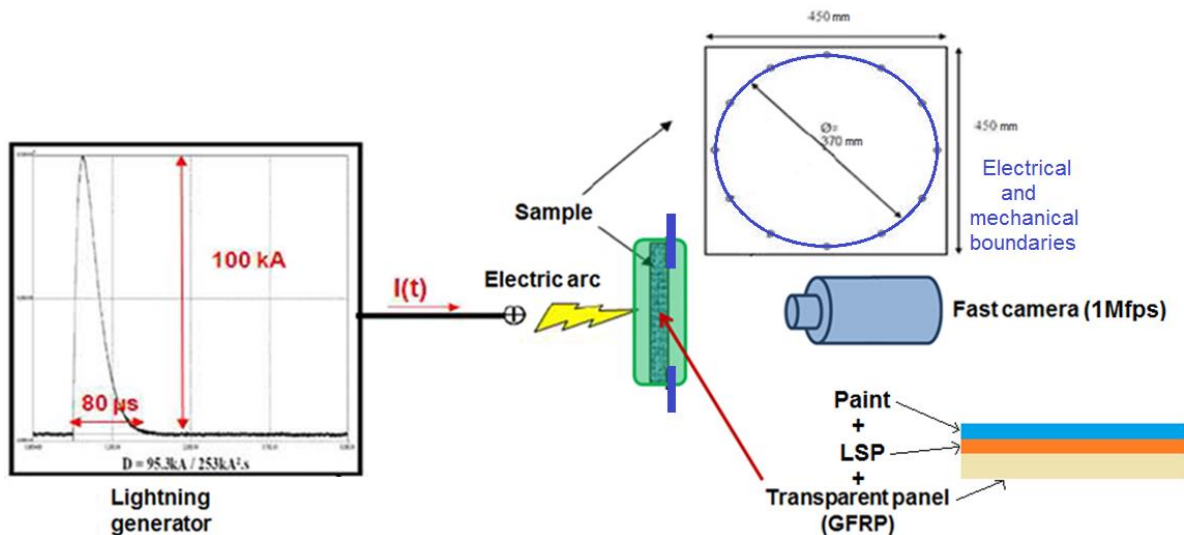
Figure 15 Set-up d'essai pour la mesure du profil de vaporisation

L'utilisation d'un panneau GFRP transparent pour enregistrer la lumière à travers celui-ci a été très utile pour observer la vaporisation pendant le test. L'épaisseur de la peinture a un effet de constriction, comme le montre la Figure 17. Pour une configuration de peinture mince, la consommation du métal est proche de la forme d'un diamant, à l'instar de son motif géométrique. La taille du motif est de 1,23 mm (SWD) par 2,54 mm (LWD).
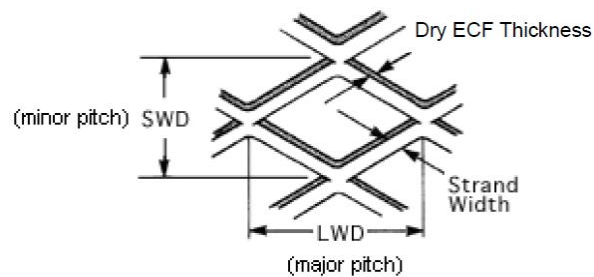
Figure 16 Motif de la protection foudre étudiée: Expanded Copper Foil (ECF)

Mais, avec l'augmentation de l'épaisseur de la peinture, la constriction de la racine de l'arc est de plus en plus visible, ce qui conduit à des profils axisymétriques de vaporisation de l'ECF. Les diamètres horizontal et vertical de l'ellipse ont tendance à être identiques avec l'augmentation de l'épaisseur de la peinture. En outre, sur la base de la mesure du diamètre de la colonne de l'arc de Sousas [17], nous pouvons observer que le profil de vaporisation est plus petit que la colonne de l'arc.
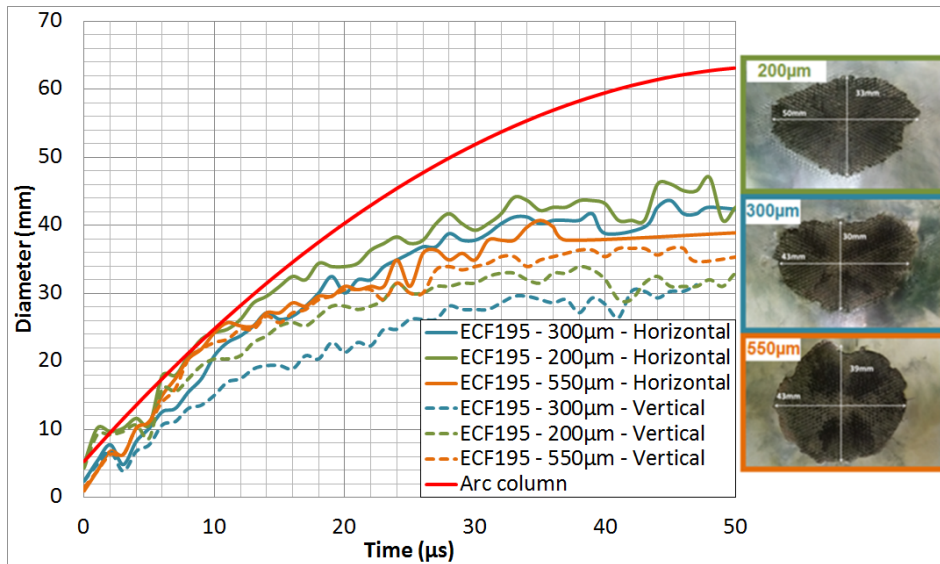
Figure 17 Influence de la peinture sur le profil de vaporisation d'une protection anisotrope (ECF195)

Nous fondant sur ces résultats d'essais, nous avons proposé la théorie suivante illustrée sur la figure suivante. L'explication détaillée de cette théorie est donnée en 3.2.2.

* CFRP = Carbon Fibre Reinforced Plastic, LSP = Lightning Strike Protection (usually ECF = Expanded Copper Foil)
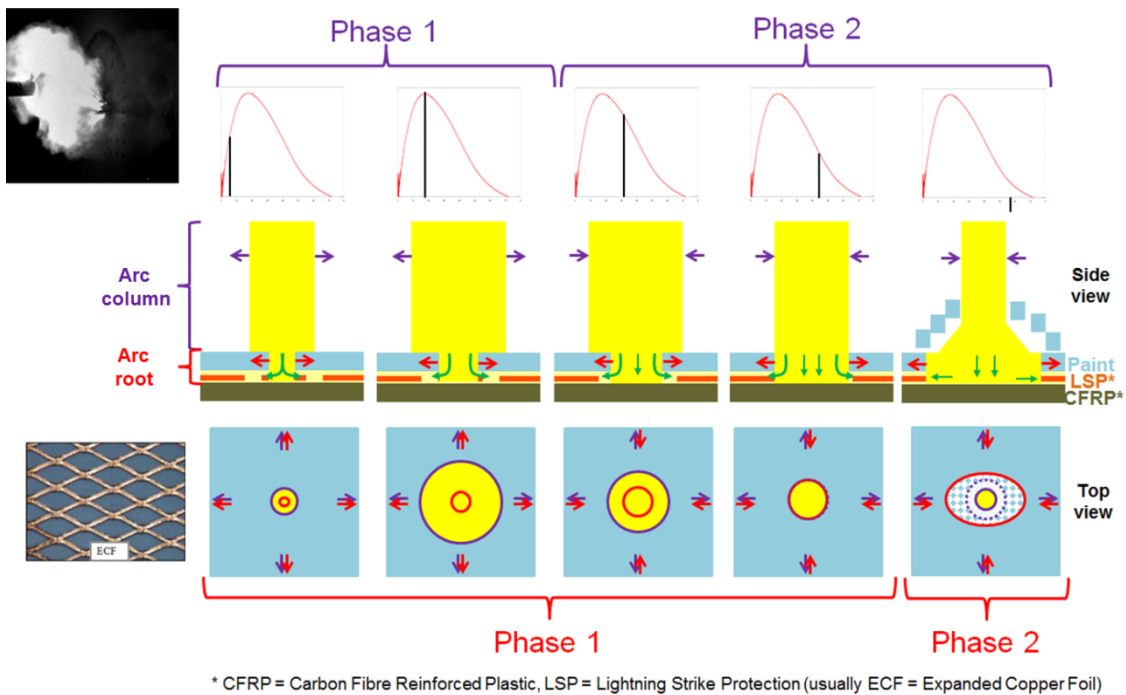
Figure 18 Théorie de l'expansion de l'arc

Nous avons ainsi pu expliquer l'influence de la peinture sur le profil de vaporisation et donc sur le pied de l'arc. Le profil de vaporisation est la conséquence de la colonne de l'arc et de l'expansion du pied de l'arc en raison des propriétés électrothermiques de la protection foudre mais aussi de la présence de peinture. La résistance mécanique de cette couche de peinture modifie l'expansion du pied d'arc et, par conséquent, l'injection de courant et le profil de vaporisation.

3.3 Modélisation

Une tentative de modélisation de la colonne d'arc a été faite dans COMSOL® afin de confirmer notre théorie concernant les différentes phases d'expansion radiale de la colonne et de son pied qui sont en compétition. Une approche a été proposée afin de modéliser l'arc de foudre dans le domaine temporel par la résolution de l'équation d'Elenbaas-Heller modifiée [52]. Cependant, la grande amplitude et le caractère transitoire du courant ont conduit à des problèmes numériques tendant à surestimer la température. De plus, il est nécessaire d'intégrer la dépendance à la pression de l'arc afin de compléter le modèle. Ceci est difficile car la pression dans l'arc à son initiation notamment n'est pas connue.
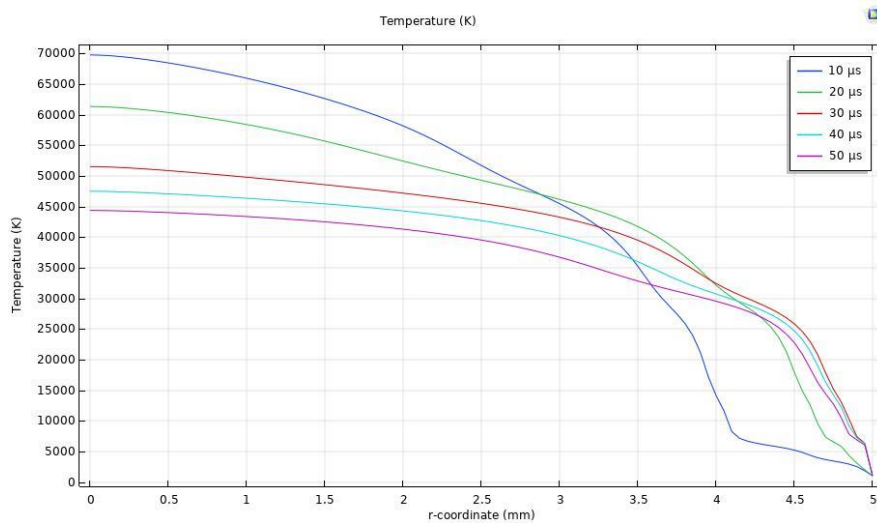
Figure 19 Foudre WF1 à 10kA: Profil de température de l'arc à différents instants

Enfin, pour la prédiction du profil de vaporisation, nous avons développé un modèle électro-thermique dans COMSOL®. Dans le logiciel, le chauffage par effet Joule a été calculé par l'ajout des modules "courant électrique" et "transfert de chaleur" qui sont couplés au module "Multiphysique". Afin de le valider, nous avons effectué une analyse de sensibilité sur une configuration simple, une protection homogène telle qu'une feuille métallique (SCF).
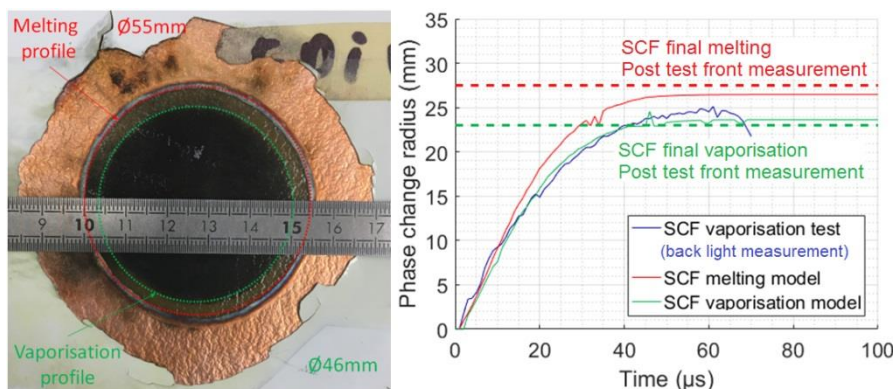
Figure 20 Comparaison du profil de fusion et vaporisation pour le SCF

Nous avons pu démontrer une bonne prédiction de notre modèle et surtout la possibilité de négliger la contribution de la diffusion thermique (liée à la conductivité thermique) et l'énergie consommée par les changements de phase.

Nous avons ensuite progressivement augmenté la complexité afin de prendre en compte tous les paramètres liés à une feuille de cuivre expansé avec sa géométrie.
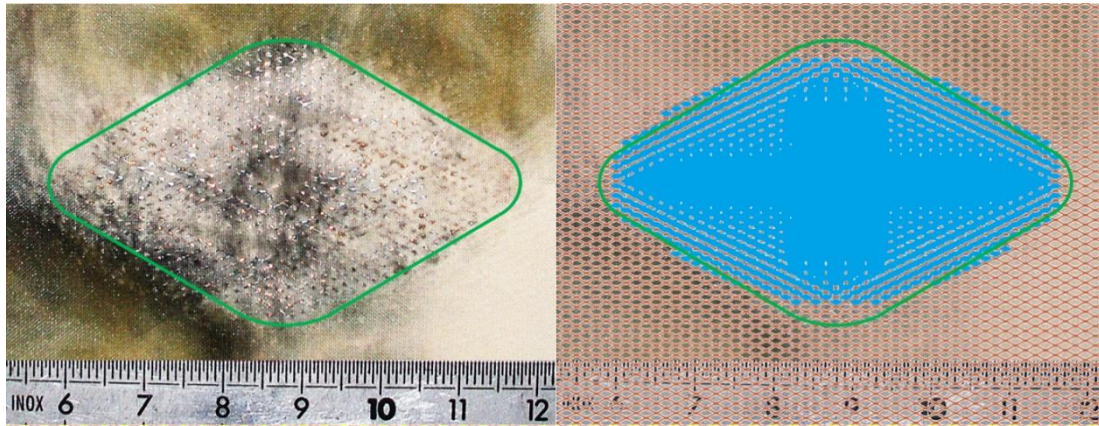
Figure 21 Surface totale fusionnée pour un ECF195 soumis à la WFD (100kA) : Comparaison entre le modèle 3D et le test sur une surface libre

Ce type de modèle est très gourmand en temps de calcul du fait de la géométrie de la protection requérant un grand nombre d'éléments. Nous avons donc proposé une configuration afin de gagner du temps de calcul en se basant sur une feuille équivalente mais dont l'anisotropie de la géométrie est couverte par le paramètre physique le plus important : la conductivité électrique. En prenant en compte les valeurs du fournisseur, nous pouvons obtenir une matrice de conductivité pour la feuille équivalente donnant ensuite une bonne prédiction du profil de métal fondu.

3.4 Conclusion

La définition de la distribution de la vaporisation dans le temps et dans l'espace est une donnée importante qui sera utilisée pour la définition d'un chargement mécanique équivalent aux contraintes de la foudre, afin d'évaluer les dommages dans une structure composite. Grâce aux travaux réalisés dans ce chapitre, plusieurs profils ont été établis pour différentes épaisseurs de peinture et de protection foudre, ce qui permettra de développer des profils de chargement mécanique équivalents spécifiques. À cette fin, il est nécessaire de combiner ce profil spatio-temporel avec un profil de pression due à l'explosion de la protection foudre. Cette prochaine étape, c'est-à-dire la pression d'explosion, est étudiée dans le chapitre suivant.

Une étape importante a été franchie dans la compréhension de l'influence de la peinture et de la protection foudre sur le pied de l'arc. L'arc électrique ne peut pas être considéré comme une simple injection de courant en un point. Au contraire, il est nécessaire de

considérer une injection qui va croître dans le temps et l'espace. Son contour dépend des paramètres peinture et de ceux de la protection foudre. Afin de prédire le profil de vaporisation et les forces liées au coup de foudre, la modélisation de la colonne d'arc ainsi que de son pied doit être développée et finalisée. Avec la combinaison de de modèle, qui permettra de connaitre le profil d'injection du courant, à celui de la vaporisation du métal développé dans ce chapitre, il sera possible de prédire le profil spatio-temporel complet de la vaporisation de la protection foudre.

4. L'explosion de la protection foudre

L'objectif de ce chapitre est de prévoir la surpression générée par la vaporisation soudaine de la protection de surface due au courant de foudre.

4.1 La théorie de l'explosion de surface

Sur la base de notre observation face avant d'un panneau soumis à un coup de foudre avec une caméra rapide, nous avons mis en évidence que la couche de peinture recouvrant le panneau composite est éjectée par une surpression sous-jacente.
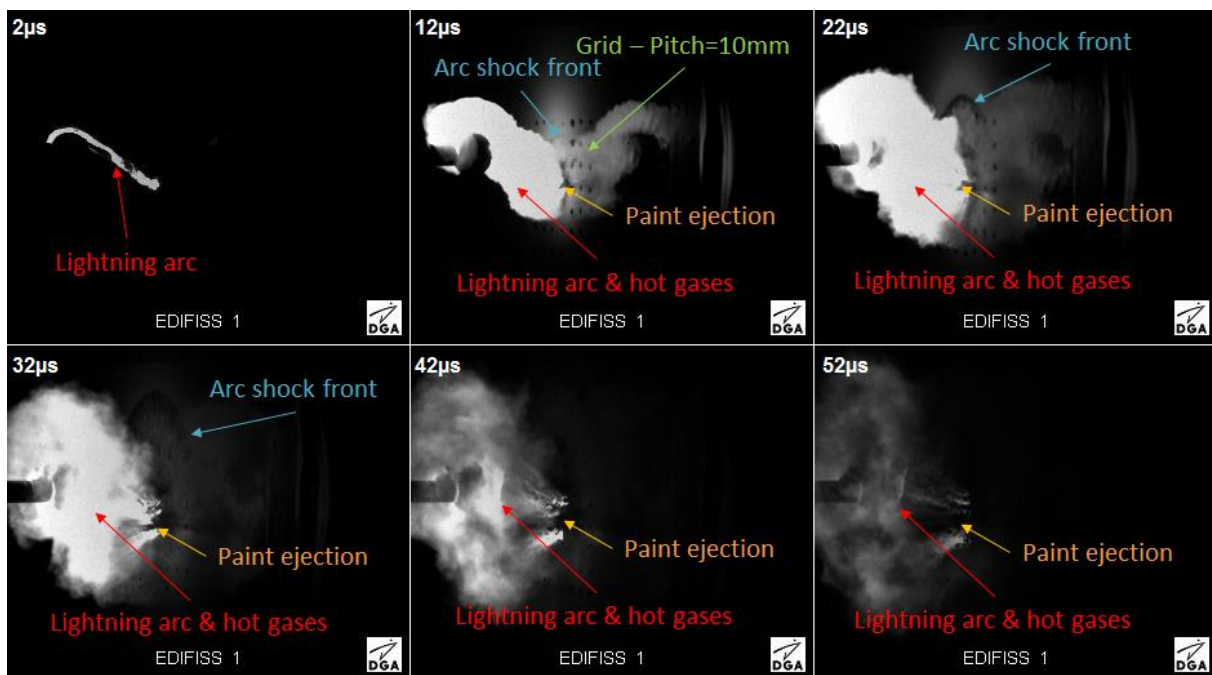
Figure 22 Essai foudre (WFD=100 kA) sur un panneau CFRP protégé et peint – Vue de face avec une caméra rapide

Le courant de foudre est principalement dévié par la protection métallique contre la foudre qui se vaporise en raison de l'échauffement par effet Joule. Il ne s'agit pas d'un simple changement d'état vers une phase gazeuse mais d'une explosion [19,27]. En fait, une grande quantité d'énergie est injectée dans la protection conductrice en très peu de temps, ce qui conduit à ce que nous avons défini comme une explosion électrique [53]. Il n'y a pas aujourd'hui de consensus sur la théorie liée à ce phénomène, mais l'étude de ce phénomène

dans la littérature, principalement effectuée sur des fils métalliques, nous a permis de comprendre les paramètres qui influencent l'intensité de l'explosion (diamètre du fil [54], longueur du fil [55,56], propriétés physiques du fil en fonction de la température [57], caractéristiques électriques de l'injection de courant [58] et du milieu environnant [59]) et comment identifier ses différentes phases à partir de l'analyse du courant [58]. Ces phases sont illustrées dans la figure suivante ci-dessous et détaillées en 4.1.3.
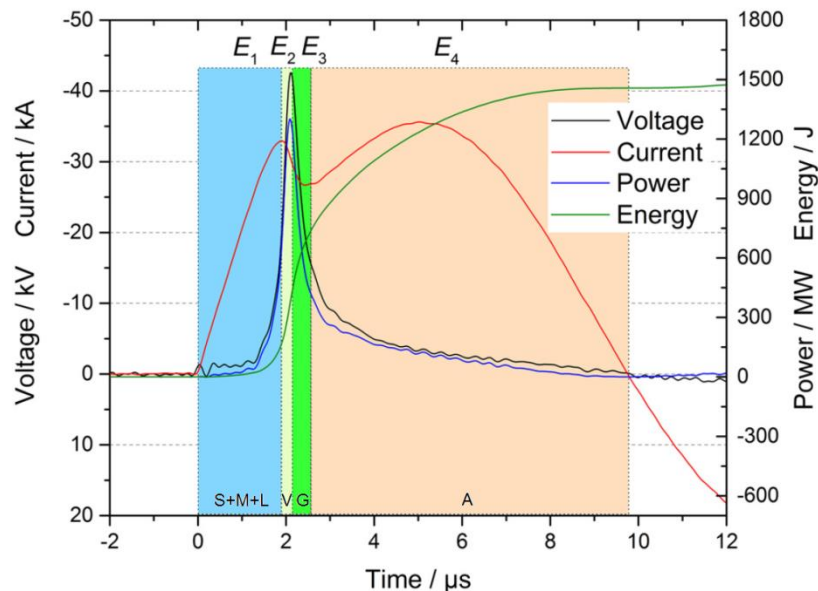
Figure 23 Les différentes phases de l'explosion électrique [58] avec identification basée sur l'étude du courant (S=Solide/M=Fusion/L=Liquide/V=Vaporisation/G=Gaz/A=Arc)

L'hypothèse d'une explosion du LSP due au passage du courant de foudre concordait avec nos observations de test et devait être caractérisée. En outre, l'observation de la surface d'un panneau testé après un coup de foudre a montré que l'empreinte de l'ECF, la protection visée dans le présent travail, était visible dans la résine. Cela démontre que l'explosion du métal est le principal facteur de surpression puisque la résine reste presque intacte, sauf là où elle a été éjectée par l'explosion du LSP.
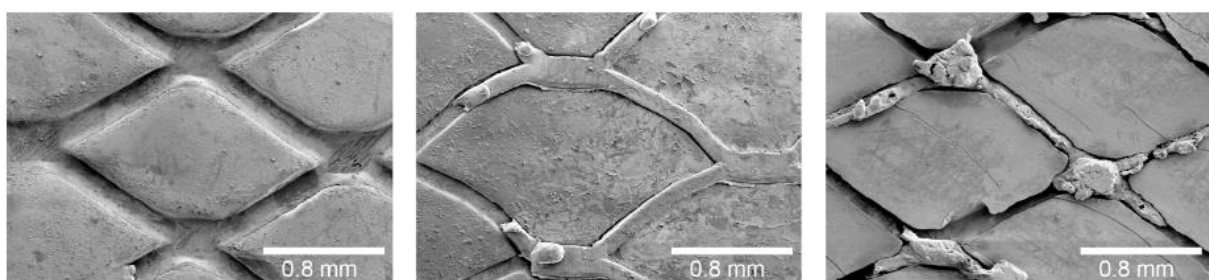
Figure 24 Vue au microscope de l'ECF vaporisé après un test foudre [18]

Afin de simplifier l'étude de l'explosion des LSP, nous avons proposé de décomposer la protection en un fil élémentaire qui peut être étudié indépendamment. Cette approche est possible pour la protection ECF en raison de sa forme spécifique. De plus, à partir du chapitre 3, la vaporisation du LSP peut être localisée à chaque instant lors de l'injection du

courant de foudre. En comparant le profil de vaporisation obtenu dans le chapitre précédent, nous pouvons évaluer la densité de courant dans chaque fil.
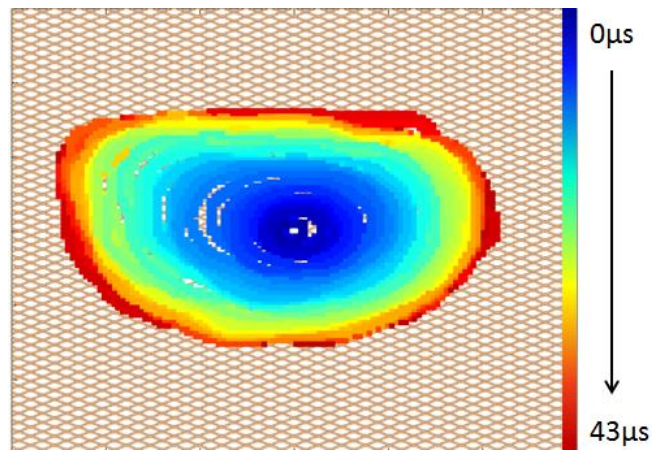
Figure 25 Distribution temporelle du profil de vaporisation dans le modèle ECF

4.2 Essai et modélisation d'explosion électrique du fil

Dans le but de définir l'explosion produite par un fil élémentaire d'ECF avec différentes amplitudes de courant de foudre, des tests spécifiques de laboratoire ont été définis. Le principe de ces tests était d'injecter un courant impulsionnel à travers un fil métallique et d'étudier son changement de phase et la création d'une onde de choc.
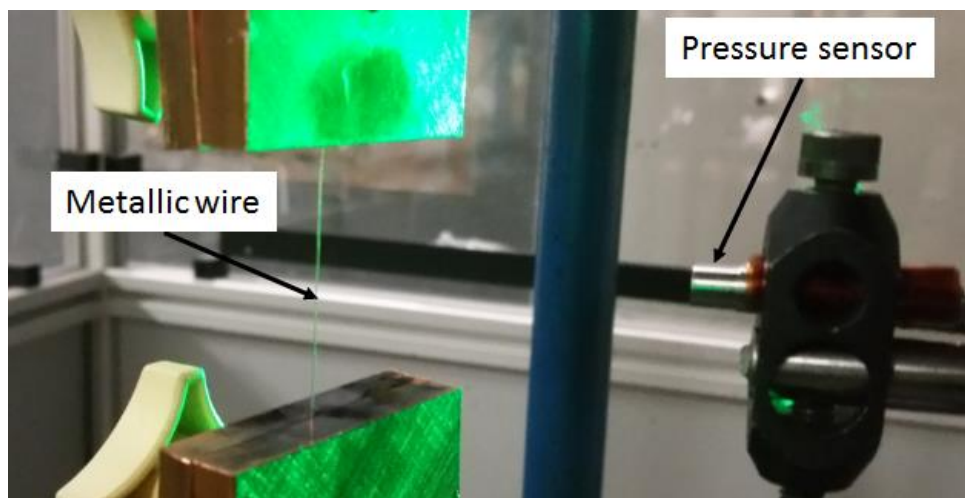
Figure 26 Montage d'essai avec le capteur de pression

Dans un premier temps, nous avons démontré notre capacité à prédire les différents changements de phase du fil jusqu'à son explosion pour différents types de métal (cuivre, aluminium et tungstène). Une identification claire des différents états du fil pendant le test était essentielle afin de créer une matrice de résultats de test cohérente. Cela a été rendu possible grâce à notre compréhension de la déformation du courant de foudre associée à l'état du métal. Dans la figure ci-dessous, on peut voir un exemple de la méthode d'identification des différentes phases par l'étude du courant :
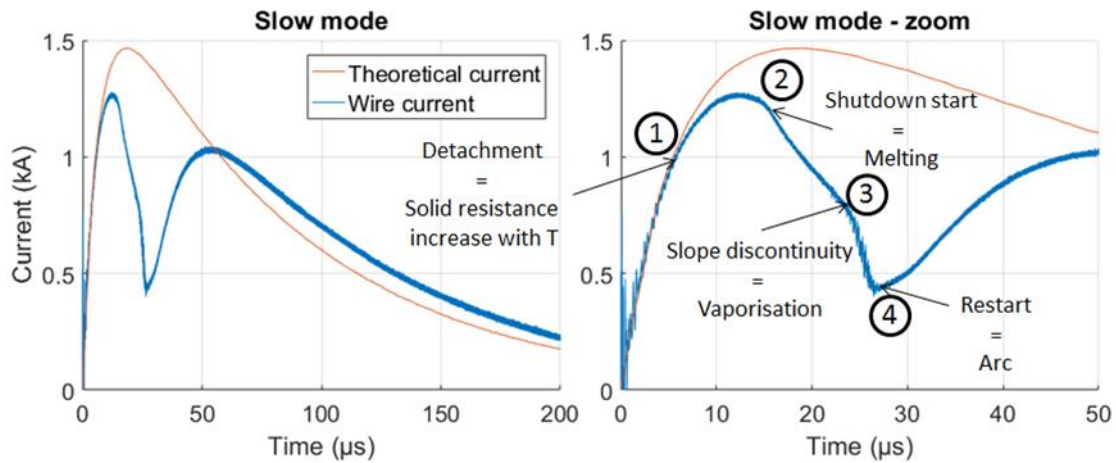
Figure 27 Identification des changements d'état typiques des fils grâce à la mesure du courant - Mode lent

En parallèle, nous avons développé un modèle dans Matlab® qui a permis de résoudre le système d'équations thermiques différentielles (4-10) avec la puissance électrique comme source. Comme le mécanisme d'explosion peut être influencé par le type de fil et la forme d'onde du courant, nous avons choisi des configurations supplémentaires afin de confirmer notre capacité à prédire la fusion et la vaporisation d'un fil métallique, quelles que soient la forme d'onde du courant ou les propriétés du fil. Le modèle développé a montré une bonne concordance avec les essais avec une différence inférieure à 20% pour toutes les configurations. Certains écarts peuvent être liés à des instabilités apparaissant dans le fil à cause des forces magnétiques [60]. Ces phénomènes n'étant pas pris en compte dans notre modèle électrothermique. Ces instabilités sont illustrées ci-dessous :
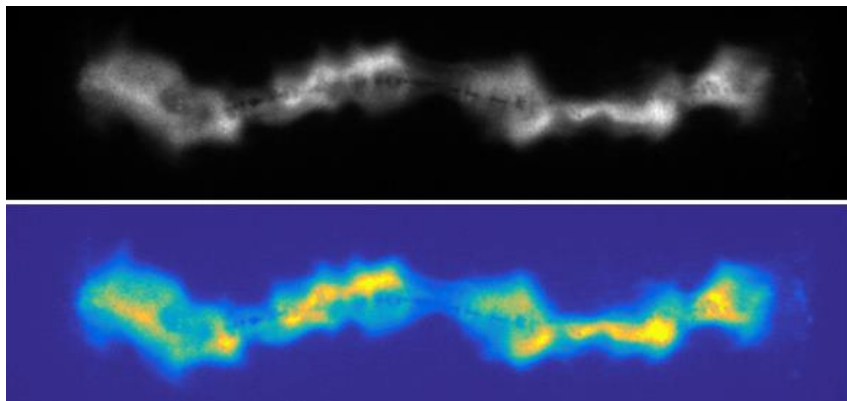
Figure 28 Photo au moment de la vaporisation avec ECF195 à 3 kA (caméra ICCD, TTL = 1 µs, vue de dessus = image originale et vue de dessous = image colorisée)

Ensuite, comme la pression du fil lui-même ne peut pas être mesurée, la pression de l'onde de choc a été mesurée à plusieurs distances du fil, afin de remonter à la pression au moment de l'explosion. Sur la base de cette campagne, nous avons construit un modèle phénoménologique qui relie la surpression maximale à l'amplitude maximale du courant. Pour notre cas d'étude qui est l'ECF195 avec un courant de foudre de type WF1, la loi obtenue est la suivante :

$$\Delta P^+ = a \times I_p{}^b + c \qquad\qquad 1.$$

Dans cette configuration, a = 80,3 (MPa.A^{-b}), b = 0,64 et c = -62,88 (MPa).

Cette méthode est très intéressante car elle pourrait être appliquée à d'autres types de LSP basés sur le même principe de construction que l'ECF afin de construire une loi de pression.

4.3 Essai et modélisation de l'explosion électrique d'une éprouvette altère

Avant de considérer le LSP complet soumis à un arc de foudre qui est assez complexe, nous avons effectué une étape intermédiaire en étudiant l'explosion électrique du LSP due à un courant de foudre conduit. À cette fin, nous avons conçu un échantillon en forme d'altère pour la protection foudre, dont la densité de courant est bien connue.
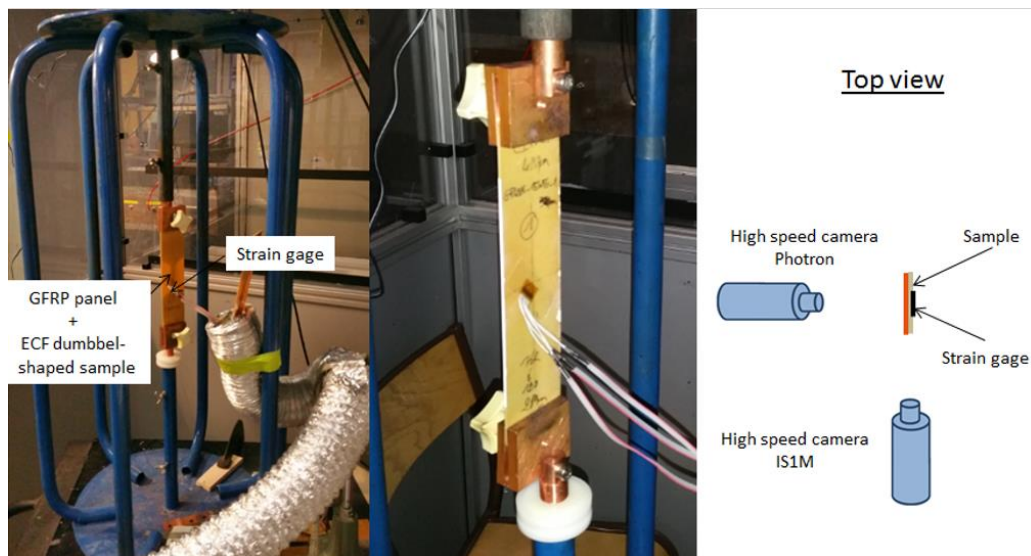
Figure 29 Installation avec l'éprouvette altère

Sur le même principe que pour l'étude du fil, nous avons validé notre capacité à prédire la vaporisation d'une telle protection. Nous avons donc construit un nouveau modèle avec COMSOL® pour résoudre l'échauffement par effet Joule dans une configuration 2D. Les résultats ont montré que le processus de fabrication a une influence sur les propriétés du LSP qui influencera le mécanisme de vaporisation. En effet, pour l'ECF, l'étirement puis l'écrouissage de la feuille entraine une fissuration aux nœuds de la protection, réduisant sa section. Ce lieu devient donc l'endroit où la vaporisation aura lieu en premier.
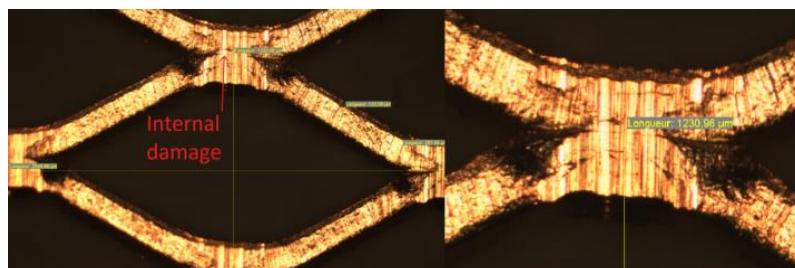
Figure 30 Observation microscope de l'ECF (zoom sur l'image de droite)

Basé sur l'étude de la géométrie réelle de la protection, le modèle a démontré une bonne capacité de prédiction pour la vaporisation de l'ECF (Figure 4-50). L'étude de la surpression créée par son explosion n'a pas pu être réalisée comme pour le fil, car sa géométrie complexe génère une onde de choc qui n'est pas cylindrique et donc plus difficile à mesurer. Nous avons cependant observé le déplacement de la plaque sur laquelle la protection (LSP) était placée.
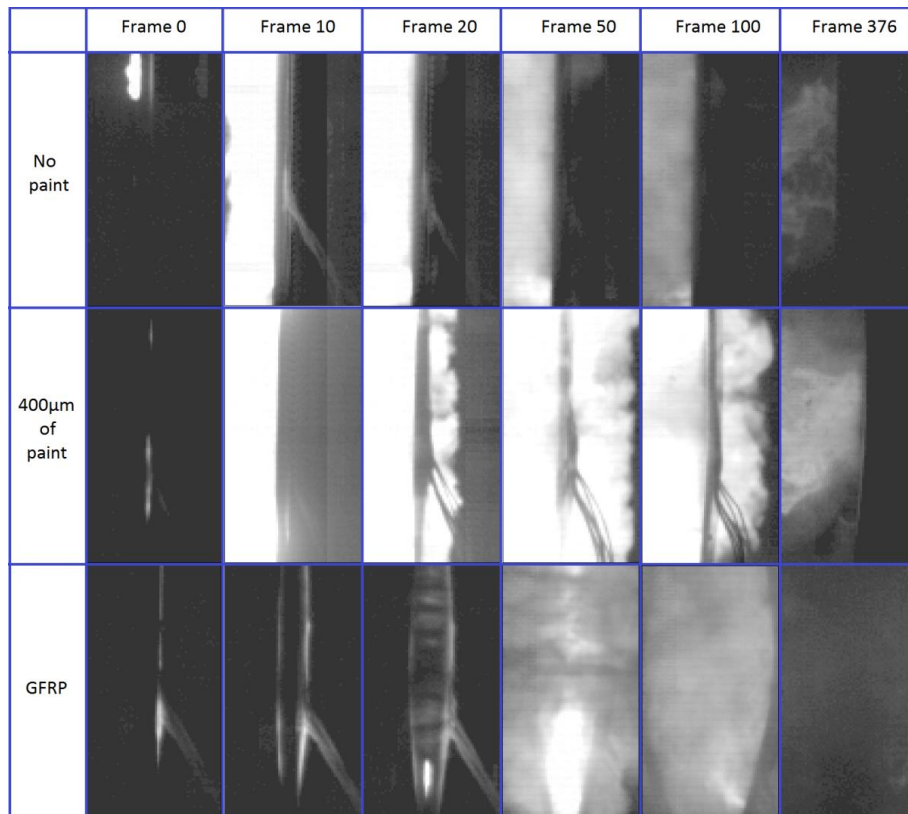
Figure 31 Caméra rapide (300kfps) - Vue latérale de l'explosion ECF195 sur GFRP avec différentes configurations de confinement

Même si ce n'est pas un résultat quantitatif, cela a mis en évidence l'influence significative du confinement dans l'amplitude de la surpression. Lorsqu'il n'y a pas de peinture et que l'explosion peut s'étendre librement, il y a un déplacement négligeable. Par contre, avec un confinement seulement créé par une couche de peinture, le déplacement est important ce qui montre qu'une pression importante a été appliquée. De plus, l'étude du courant a montré que le confinement n'influence pas le mécanisme de vaporisation mais retarde le passage à l'arc. Le métal vaporisé avant la création de l'arc est hautement résistif, ce qui entraine une diminution significative du courant, presque jusqu'à son extinction. C'est le passage à l'état plasma et donc au déclenchement d'un arc que le milieu redevient conducteur et le courant augmente à nouveau. Le confinement retarde la création de ce courant de dérivation et l'effondrement du courant est donc plus prononcé car la pression est de plus en plus importante avec un confinement accru. Cette pression plus élevée nécessite une température plus élevée pour ioniser le canal et créer le plasma [61].
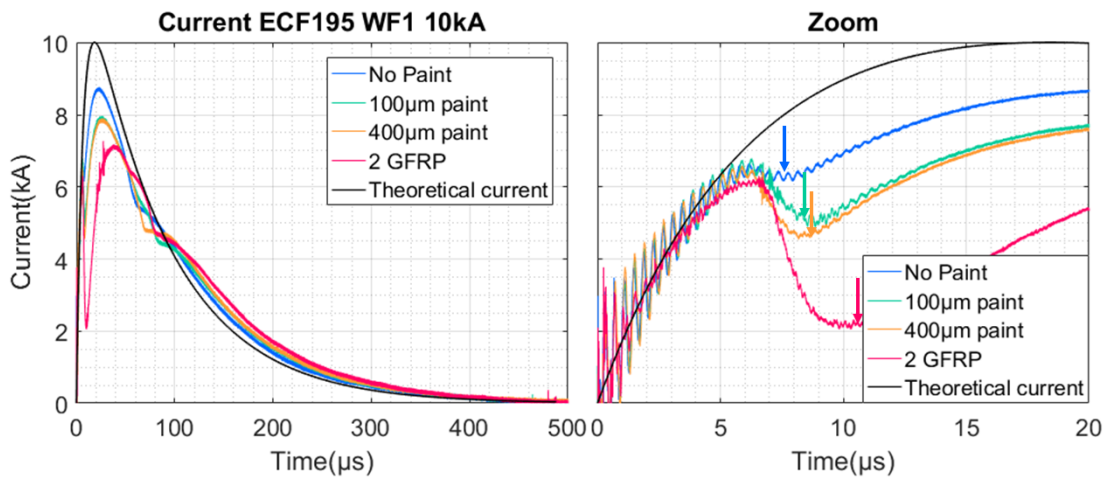
Figure 32 Impact du confinement sur le courant pour l'ECF195 (zoom sur la figure de droite)

4.4 Conclusion

Les travaux réalisés dans ce chapitre qui fournissent une dépendance de la loi de pression avec l'amplitude du courant de foudre pour l'ECF195 peuvent être combinés avec le profil de vaporisation spatio-temporel construit dans le chapitre précédent. À partir de cette combinaison, nous sommes maintenant en mesure de construire un profil de pression spatio-temporel pour le chargement mécanique d'un panneau composite. C'est un résultat important qui sera utilisé dans notre dernier chapitre 6 afin de remplacer la sollicitation de la foudre par un chargement mécanique et de prédire les dommages consécutifs dans le stratifié composite.

En plus de l'objectif spécifique de cette thèse, ce travail fournit un cadre préliminaire pour l'étude de l'explosion électrique dans une géométrie complexe telle que l'ECF. Les instabilités observées dans le métal avant son explosion doivent être étudiées plus en profondeur afin de pouvoir mieux modéliser la distribution de la température mais aussi l'énergie déposée dans le métal. La prédiction de la distribution de l'énergie avant et après l'explosion doit être améliorée car elle a une influence sur l'amplitude de pression de l'onde de choc. Pour cela, la théorie proposée par Chung [62] qui couple les équations MHD avec l'EOS du cuivre pourrait être développée. Elle remplacerait le modèle phénoménologique défini dans ce chapitre pour relier la pression de l'explosion au courant et pourrait être étendue à des configurations plus complexes.

5. La peinture

L'étude du mécanisme des dommages causés par la foudre et des paramètres influençant leur sévérité a montré la nécessité de caractériser les propriétés mécaniques de la peinture comme illustré en Figure 5. Cette figure montre l'augmentation du dommage avec l'épaisseur de peinture, pour une configuration identique (composite + ECF195) testée avec une WFD à 100kA.

5.1 L'influence de la peinture sur l'endommagement foudre

Il est essentiel de considérer cette couche cosmétique comme aussi importante que la conception de la structure composite et la protection de surface contre la foudre. En plus de son effet de constriction sur le pied de l'arc, elle a un effet de confinement sur l'explosion sous-jacente de la protection foudre. Cet effet entraînera une augmentation du profil de surpression à la surface du composite comme montré ci-dessous. Cette augmentation du chargement mécanique augmente les dommages. En effet, aucun délaminage n'est créé pour le composite protégé par l'ECF195, alors qu'avec une peinture de 400µm au-dessus, une surface délaminée importante peut être mesurée.
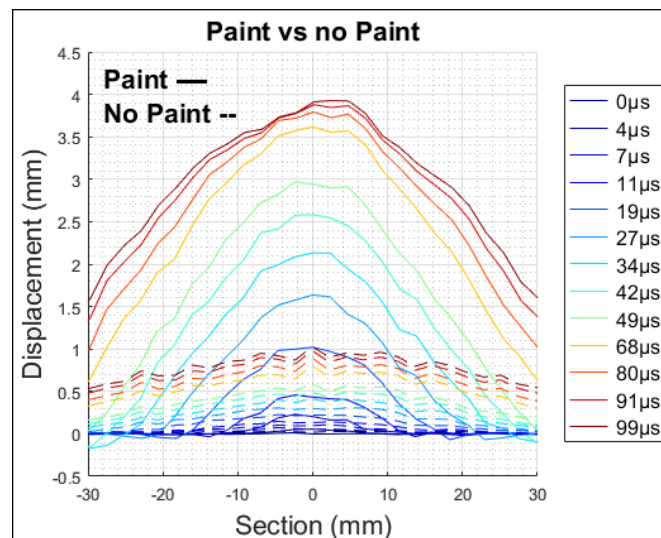
Figure 33 Comparaison des profils de déplacement: Peinture (400µm) ou sans peinture

Cette influence a été observée qualitativement, mais il est maintenant nécessaire de l'évaluer quantitativement afin de prévoir son effet de confinement. Cependant, ce matériau n'est pas un composant structurel d'un avion. Il est destiné à décorer la surface extérieure de l'avion et à le protéger contre l'environnement (par exemple, les UV, les fluides). Par conséquent, on dispose d'un nombre limité de données concernant les propriétés mécaniques de la peinture. Même si certains tests de qualification ([63], [64], [65], [66]) existent pour valider son adhérence et sa résistance aux chocs, ils sont tout à fait qualitatifs.

5.2 Caractérisation mécanique de la peinture

À cette fin, nous avons étudié comment caractériser les propriétés mécaniques de la peinture afin d'utiliser ces informations dans un modèle global de prédiction de la surpression. Nous avons utilisé les tests de qualification réalisés pour les films minces ou les tissus qui nous semblaient les plus adaptés à ce matériau. La première question principale était d'obtenir un film de peinture, indépendant de tout substrat. Ce matériau est fait pour être appliqué sur une surface et pour y adhérer fortement. Là encore, nous avons étudié une solution [67] pour la fabrication de cette couche où les principales difficultés à prendre en

compte étaient d'assurer l'uniformité de l'épaisseur, la mouillabilité de la surface mais aussi l'adhérence limitée de la surface après le séchage. Il a fallu évaluer les paramètres suivants : les propriétés mécaniques du volume, la résistance à la rupture, la propagation de la rupture et enfin, l'adhérence. Pour ce faire, nous avons effectué des tests de DMA qui ont permis de mettre en évidence que le module d'Young de la peinture était très variable dans la plage de température prévue en laboratoire (18 à 30°C) en raison de la température de transition vitreuse à 36°C. La température n'est pas toujours enregistrée lors d'un test de foudre et pourrait expliquer une certaine variabilité des dommages pour une configuration supposée identique.
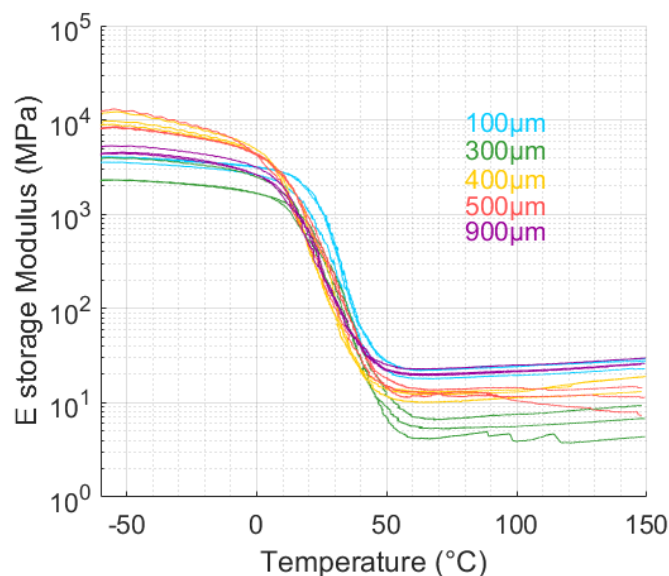
Figure 34 Evolution du module d'Young en fonction de la température

Ensuite, le test de traction, basé sur l'ISO 527 ([68,69]), sur une éprouvette altère de peinture nous permet de construire les courbes contrainte-déformation de la peinture pour différentes épaisseurs. L'éprouvette est étirée à vitesse constante et la force résultante est mesurée. Ainsi, la contrainte σ peut être estimée à partir de la section de l'éprouvette et la mesure de la déformation ε est réalisée à l'aide de la stéréocorrélation qui permet de reconstruire le profil de l'éprouvette dans les 3 dimensions.
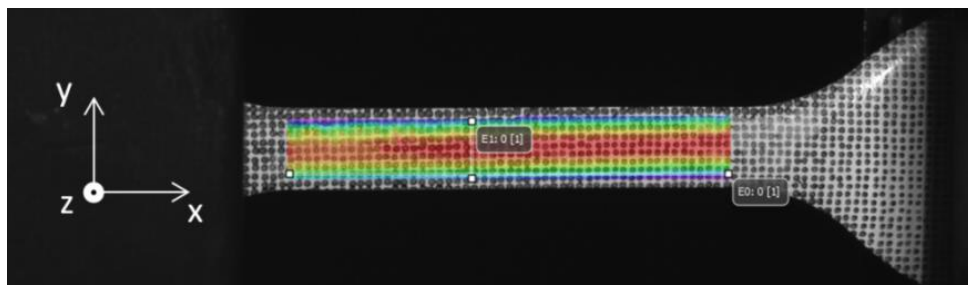
Figure 35 Modèle de corrélation d'images et mesure de la déformation Z à l'aide du VIC 3D (0 à 160µm)

Ces mesures ont validé notre intuition concernant les propriétés hyperélastiques de cette couche.

Par la suite, nous avons procédé à des tests de déchirement appelés tests pantalon. Ce test a montré la faible résistance de la peinture à la propagation de la rupture (3,8 N/mm). Cela montre que lorsque la fissure a été amorcée, elle va s'étendre très facilement. L'essai de traction a montré que la contrainte à rupture était comprise entre 35 et 60 MPa.

Figure 36 Montage de l'essai pantalon (Gauche: Avant essai/Droite: Pendant l'essai)

Comme on pouvait s'y attendre, le comportement diffère selon les différentes épaisseurs de film, mais les différences ne peuvent pas être attribuées uniquement à ce paramètre. Les propriétés finales de la peinture peuvent être influencées par l'environnement (température, pression, humidité de l'air...) pendant le processus de fabrication et de séchage, car il peut influencer la composition chimique du film sec après l'évaporation des solvants ou la porosité.

Enfin, des tests de choc laser ont été réalisés afin de mesurer la tenue mécanique de l'interface. Ces tests ont fourni des résultats qualitatifs sur l'adhérence de la peinture. Un minimum de flux laser (GW/m²) a pu être mesurée mais pour connaitre l'équivalence en terme de pression déposée à la surface du composite, il faut pouvoir calibrer ce flux à l'aide d'essais spécifiques [70]. La méthode utilisée a été développée par Arrigoni [71]:
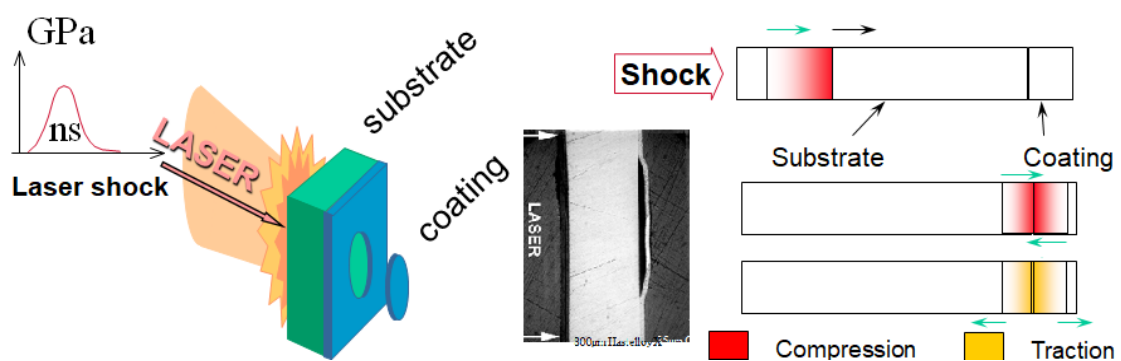
Figure 37 LASAT: principe [72]

Cependant, des problèmes concernant les mesures de la vitesse du substrat et la caractérisation quantitative de l'amplitude de l'onde de choc injectée dans la structure composite nous ont empêchés de caractériser la contrainte nécessaire pour rompre l'interface entre la peinture et le composite.

5.3 Modélisation

Le test de traction a été utilisé pour construire un modèle mécanique de la peinture avec un comportement qui est plus complexe qu'un simple comportement élastique. En examinant la réponse uniaxiale des polymères, au lieu d'une courbe linéaire dans le cas d'un comportement élastique parfait, on peut observer une courbe en S à 3 parties, comme l'illustre la Figure 38 :

- Une première pente avec une faible déformation (l/l_0) due à la réorganisation du polymère où l'orientation des chaînes est alignée sur la direction de traction.
- Une deuxième pente, plus douce, où les chaînes sont dépliées, donc une petite contrainte est nécessaire pour étirer le matériau.
- Une troisième et dernière pente raide où la rigidité est augmentée puisque les chaînes ont presque atteint leur taille maximale.
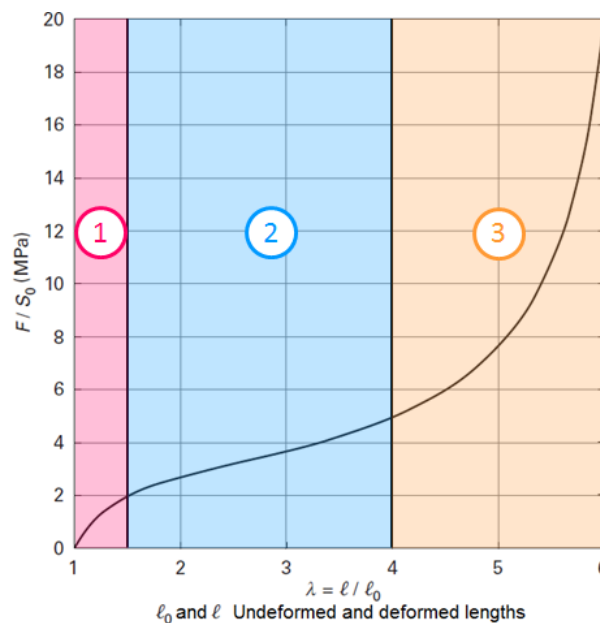
Figure 38 Courbe contrainte-déformation pour un essai de traction uniaxiale [73]

Parmi les différents modèles hyperélastiques disponibles dans Abaqus® (Ogden, Marlow, Polynôme réduits…), nous avons choisi le modèle Marlow qui présente une bonne prédiction en traction uniaxiale par rapport à l'essai et une faible divergence en compression comme présenté en Figure 39. Outre le choix de la loi hyperélastique, le coefficient de Poisson a été considéré comme égal à 0,495. Ce choix est basé sur la recommandation d'Abaqus® qui ne permet pas un matériau totalement incompressible en mode explicite. Cette valeur est donc un compromis entre la précision de la solution et l'efficacité du calcul.

Enfin, comme aucune vitesse de déformation ni aucun effet de température n'ont été caractérisés, aucun comportement visqueux ne sera ajouté à ce modèle qui sera seulement hyperélastique.
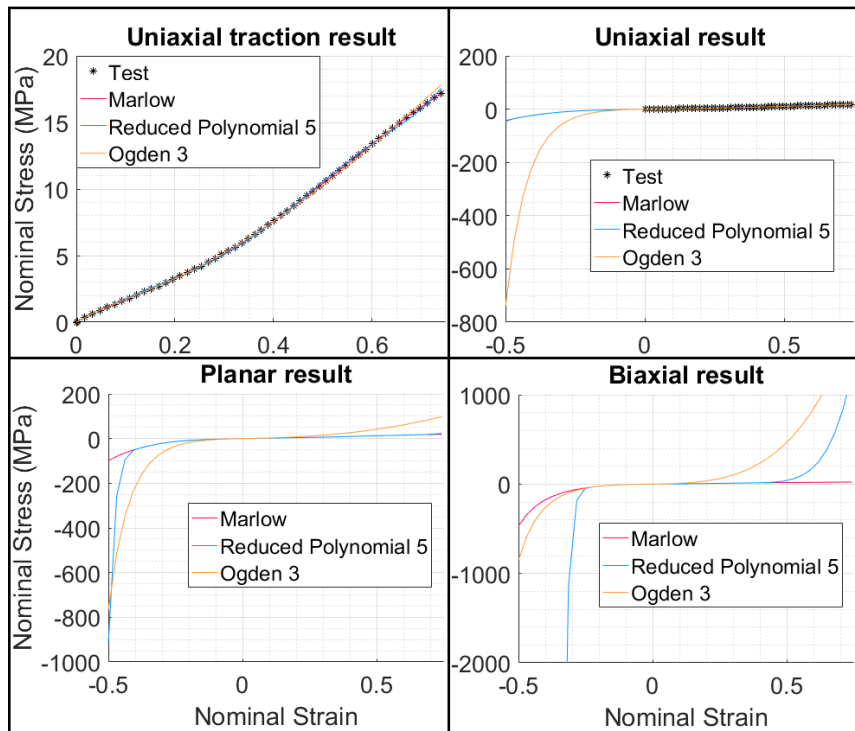
Figure 39 Loi Hyperelastique – Evaluation Abaqus®

5.4 Conclusion

Afin de compléter le modèle développé pour la peinture, nous devons ajouter les dommages de rupture dans la peinture. Ce travail peut être développé sur la base des résultats des tests de tension et de déchirure du pantalon afin de valider un modèle de fissuration de la peinture. Une façon de modéliser ces dommages pourrait être faite à travers une interface cohésive dans le maillage de la peinture. De plus, la validation complète du modèle hyperélastique nécessite des tests supplémentaires avec différentes sollicitations telles que des tests de compression uniaxiale, biaxiale et plane. Un développement plus poussé du test laser combiné à un modèle de choc permettrait de finaliser la caractérisation de l'interface sous sollicitation dynamique. Enfin, la sollicitation dynamique de la peinture pourrait générer de la chaleur et par conséquent modifier les propriétés de la peinture. Cet effet n'a pas été considéré ici pour limiter la complexité de notre modèle de peinture. Mais il sera nécessaire à l'avenir pour caractériser complètement l'effet de confinement de la peinture sous forte sollicitation, d'améliorer la fabrication des éprouvettes, et de caractériser proprement le comportement et la déchirure.

Les travaux présentés dans les chapitres précédents ont permis de caractériser la pression générée par l'explosion de la protection foudre. Mais la décroissance de la pression dépendra du confinement de cette explosion. Le modèle développé pour la couche de peinture sera ajouté au modèle mécanique global présenté dans le chapitre suivant afin de soutenir la prédiction de l'influence de la peinture sur le profil de surpression après l'explosion et d'évaluer les dommages dans le stratifié.

6. Modèle mécanique et endommagement

Ce chapitre est la dernière étape de notre travail visant à reproduire les contraintes mécaniques dues à un coup de foudre. Nous avons proposé une méthodologie pour simplifier ce phénomène multiphysique en un problème purement mécanique. La capacité à reproduire le chargement produit par la foudre est essentielle pour prédire les dommages générés par un tel phénomène. L'objectif final est de permettre la prédiction des dommages à l'aide d'un modèle mécanique.

6.1 Essai foudre

Afin de valider ce modèle, nous avons choisi un ensemble de résultats expérimentaux sur la foudre qui fournissent des données capitales comme résumé ci-dessous. Les configurations ont été construites de manière à modifier un paramètre à la fois par rapport à notre référence.

Justification	Substrat	Epaisseur peinture (µm)	Critère de comparaison	Eprouvette EDIFISS
Référence : Explosion confinée	GFRP 2,75mm 11 plis	400	Déplacement	17
Référence : Explosion libre	GFRP 2,75mm 11 plis	0	Déplacement	19
Référence : Endommagement composite	**CFRP 1,651**mm 13 plis	**400**	Déplacement & Dommages	1
Endommagement composite avec explosion interne & confinement extrême	CFRP 1,651mm 13 plis	1000	Déplacement & Dommages	6
Endommagement composite avec explosion interne & confinement léger	CFRP 1,651mm 13 plis	250	Déplacement & Dommages	5
Influence de la raideur du substrat composite	CFRP 3,302mm 26 plis	400	Déplacement & Dommages	100
Influence de l'épaisseur du pli et de l'empilement	CFRP 1,651mm 9 plis	400	Déplacement & Dommages	30
Endommagement composite avec explosion interne & confinement avec propriétés mécaniques différentes	CFRP 1,651mm 13 plis	400 Tufnol	Déplacement & Dommages	61

Table 1 Résultat expérimentaux utilisés

La déflexion du panneau due à la foudre a été mesurée grâce à une méthode de stéréocorrélation.
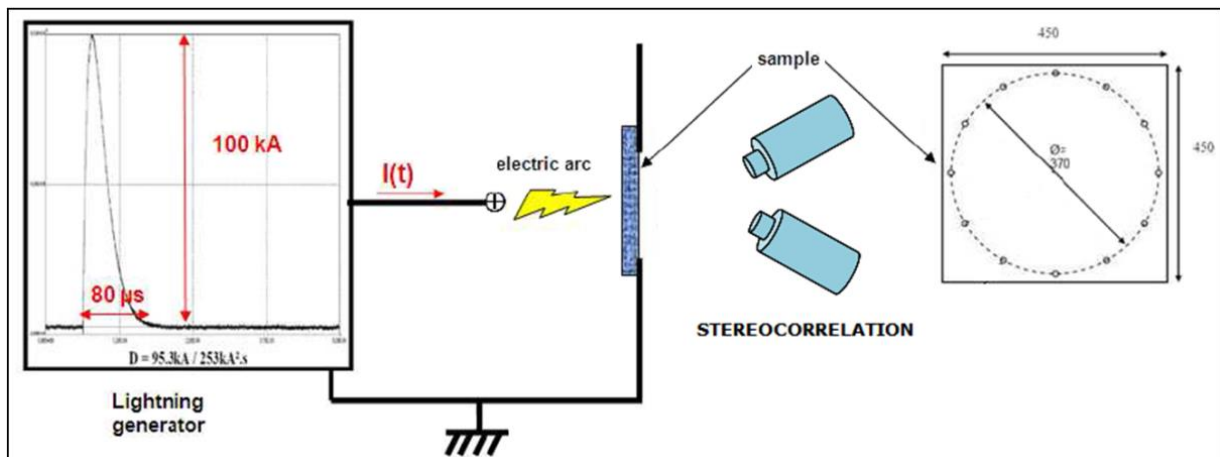
Figure 40 Montage de l'essai foudre

Les dommages ont été mesurés post-mortem par une analyse ultrasonore qui a fourni la surface projetée des délaminages. Afin d'obtenir une évaluation précise de la répartition des délaminages dans l'épaisseur, des coupes à la scie et des analyses au microscope ont été effectuées, puis les profils ont été reconstruits. Il faut noter que les coupes ont permis de suivre les délaminages dans chaque interface même si la plaque conserve une déflection résiduelle, alors que le C-Scan reconstitue des profils d'obstacles à une profondeur donnée. Les coupes sont effectuées par bandes larges de 14 à 20 mm.
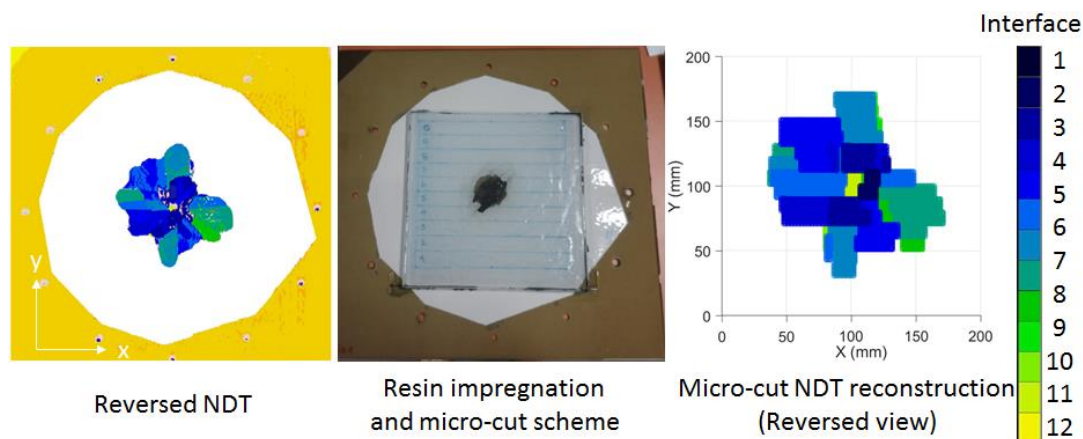
Figure 41 Cas de référence (EDIFISS 1): C-Scan et reconstruction au microscope après découpe

6.2 Construction d'un modèle d'endommagement du composite

Un modèle de simulation numérique sous Abaqus® a été développé afin de simuler les dommages dans le pli grâce à une routine utilisateur VUMAT et entre les plis par l'introduction d'interfaces cohésives. Pour l'endommagement dans le pli volumique, on a utilisé l'approche d'Ilyas [74] et Soulas [22]. Le comportement du CFRP sous impact est défini à partir de différents modes de ruine identifiés qui sont utilisés pour évaluer six variables de dommage di (i=1...6) qui influenceront les six modules élastiques du matériau anisotrope dans la matrice de souplesse R^{-1}. Cette matrice met en relation le tenseur de déformation ε écrit sous la forme d'un vecteur à six composantes, avec la contrainte σ également écrite

sous la forme d'un vecteur à six composantes dans le même ordre, et les variables de dommages seront utilisées comme facteurs d'abattement:

$$
R^{-1} = \begin{bmatrix}
\dfrac{1}{(1-d_1)E_{11}^0} & -\dfrac{\nu_{21}}{E_{22}^0} & -\dfrac{\nu_{31}}{E_{33}^0} & & & \\
-\dfrac{\nu_{12}}{E_{11}^0} & \dfrac{1}{(1-d_2)E_{22}^0} & -\dfrac{\nu_{32}}{E_{33}^0} & & & \\
-\dfrac{\nu_{13}}{E_{11}^0} & -\dfrac{\nu_{23}}{E_{22}^0} & \dfrac{1}{(1-d_3)E_{33}^0} & & & \\
& & & \dfrac{1}{(1-d_4)G_{12}^0} & & \\
& & & & \dfrac{1}{(1-d_5)G_{23}^0} & \\
& & & & & \dfrac{1}{(1-d_6)G_{13}^0}
\end{bmatrix}
\qquad 2
$$

Il y a cinq modes de ruine considérés : Rupture en traction sens fibre, Rupture en compression sens fibre, Rupture par compression sphérique, Rupture par cisaillement plan et enfin Rupture hors plan. Ces deux derniers modes de ruine ne sont pas introduits dans la loi d'endommagement car ils seront gérés par l'interface cohésive. On obtient donc :

$$
\begin{cases}
d_1 = \left(1 - e^{\frac{1}{m_1}(1-r_1^{m_1})}\right) + \left(1 - e^{\frac{1}{m_2}(1-r_2^{m_2})}\right) \\
d_2 = \left(1 - e^{\frac{1}{m_3}(1-r_3^{m_3})}\right) + \left(1 - e^{\frac{1}{m_4}(1-r_4^{m_4})}\right) \\
d_4 = \left(1 - e^{\frac{1}{m_4}(1-r_4^{m_4})}\right) \\
d_3 = d_5 = d_6 = 0
\end{cases}
\qquad 3
$$

Pour l'interface cohésive dans Abaqus®, même avec les valeurs fournies par des essais Airbus pour les propriétés mécaniques du matériau, un calibrage numérique de l'interface a été nécessaire sur la base de tests statiques. A partir de l'énergie de propagation ([75,76]) G_C obtenue en essai et de la raideur du matériau K, on peut calibrer la contrainte d'amorçage du modèle pour libérer progressivement la liaison cohésive.
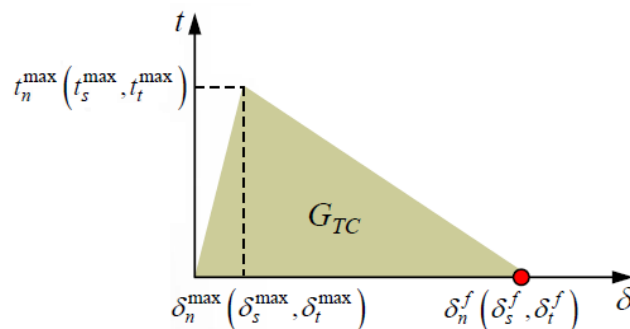
Figure 42 Loi cohésive d'endommagement

Le premier essai DCB basé sur l'AITM1-005 [77] et l'ISO15024 [76], permet de calibrer l'interface en mode I, c'est-à-dire en ouverture. Le deuxième essai ENF basé sur l' AITM1-006 [78] permet de calibrer l'interface en mode II, c'est-à-dire en cisaillement.

Sur la base des simulations élémentaires effectuées en mode I et II sous chargement statique, la loi de l'interface cohésive est choisie telle que définie dans Table 2:

Comportement cohésif		Initiation du dommage		Evolution du dommage		
K_n (KN/mm^3)	$K_s = K_t$ (KN/mm^3)	σ_n (MPa)	$\sigma_s = \sigma_t$ (MPa)	G_{IC} (J/m²)	G_{IIC} (J/m²)	α
100	100	25	60	285	845	1.5

Table 2 Cohesive surface parameters for CFRP

6.3 Création du chargement mécanique équivalent

À partir de la caractérisation de l'explosion de la protection foudre développée dans les chapitres précédents qui a fourni la distribution spatio-temporelle de la pression d'explosion et de son amplitude, nous avons pu construire un chargement mécanique complet équivalent. Dans un premier temps, la pression d'explosion a été modélisée comme une pression appliquée à la surface du composite. Nous avons construit une méthodologie pour convertir ce profil en une VDLOAD contenue dans chaque face du substrat qui sera contrainte par la pression d'explosion en surface. Pour une configuration calibrée, c'est-à-dire un profil de vaporisation mesuré pour un couple protection foudre et revêtement de surface (peinture avec son épaisseur), on connait la distribution de courant dans chaque brin d'ECF, à quel moment il explose et donc à quelle amplitude de pression. On peut donc créer une loi qui relie le maximum de la pression d'explosion à l'instant d'explosion :

$$P_{exp}(t_{exp}) = p_1 t_{exp}{}^{p_2} + p_3 .$$

Et pour chaque face d'élément qui sera chargée en pression, on lui associe un temps d'explosion.
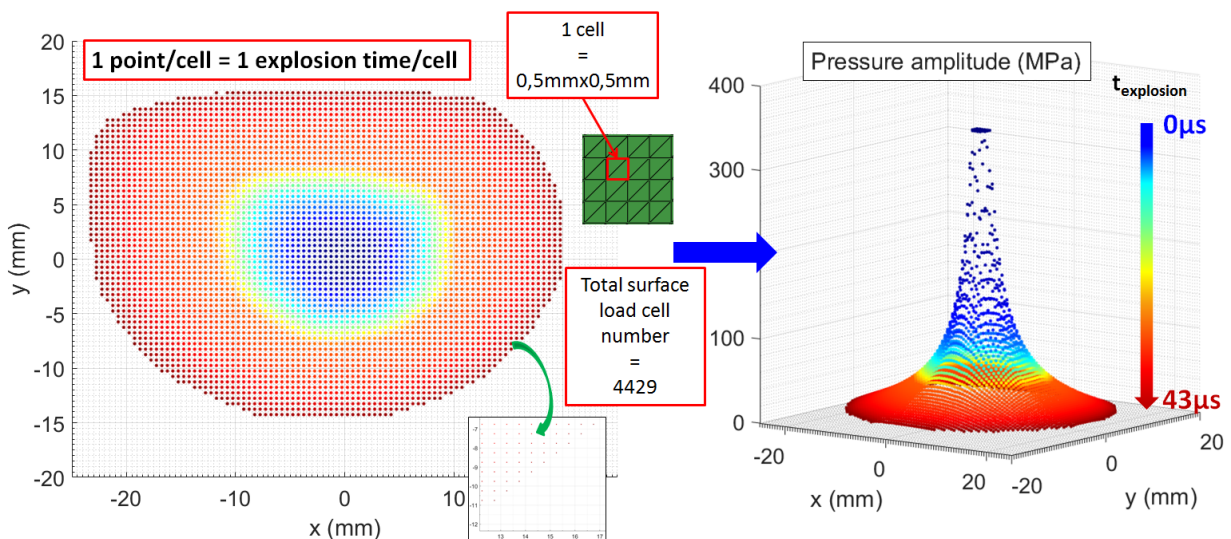
Figure 43 Projection du profil d'explosion sur le maillage du modèle

La source d'entrée du modèle a été modifiée et associée au sous-programme utilisateur que nous avons développé.

L'explosion de surface et son confinement par la peinture ont été étudiés indépendamment. Grâce à l'utilisation d'une structure en GFRP qui ne dévie pas le courant de foudre, nous avons pu étudier et calibrer la pression générée par une explosion confinée. Les travaux réalisés dans les chapitres précédents ont fourni toutes les données nécessaires au modèle de pression d'explosion, à l'exception de la durée de sa relaxation. Une loi simple pour la décroissance de la pression a donc été élaborée, en fonction de la pression maximale de l'explosion.

$$P(t) = P_{exp}\,e^{-(t-t_{explosion})/\Delta t_{decay}} \times \left(1 + (t - t_{explosion})/\Delta t_{decay}\right) \qquad 4$$

Cette loi simule le confinement dû à la peinture qui maintient la pression avant d'être éjectée par cette pression d'explosion sous-jacente. A partir d'une analyse de sensibilité, les paramètres de la loi pour l'explosion de l'ECF195 confiné par 400µm de peinture ont été définis :

$$\begin{cases} \Delta t_{decay} = \Delta t_0 \left(\dfrac{P_{max}}{P_{exp}}\right)^{\alpha} \; et \; P_{max} = \max(P_{exp}) \\ \Delta t_0 = 3\,\mu s \; and \; \alpha = 0.8 \end{cases} \qquad 5$$

P_{max} est la pression maximale atteinte au centre par l'explosion où la densité de courant dans le fil de cuivre est la plus élevée. Δt_0 est le temps de décroissance au centre qui est le plus court pour représenter la libération de peinture la plus rapide due à la pression d'explosion la plus élevée. Le paramètre α entraîne l'augmentation du temps de décroissance avec la diminution de la pression d'explosion.

Ce profil de pression a correctement prédit la déflexion du panneau en CFRP avec la même LSP (ECF195) et la même épaisseur de peinture (400µm).

Figure 44 Déplacement de la plaque GFRP dû à l'explosion ECF195 confinée par 400µm de peinture avec WFD: Essai contre model

Notre étude des différentes épaisseurs de peinture et des rigidités des panneaux a démontré la dépendance du profil de pression sur le confinement. L'explosion du LSP est prise en sandwich par la peinture et la structure composite. Par conséquent, une modification de leurs propriétés mécaniques influencera son confinement et maintiendra ou non une pression élevée sur la structure. Nous avons pu établir une r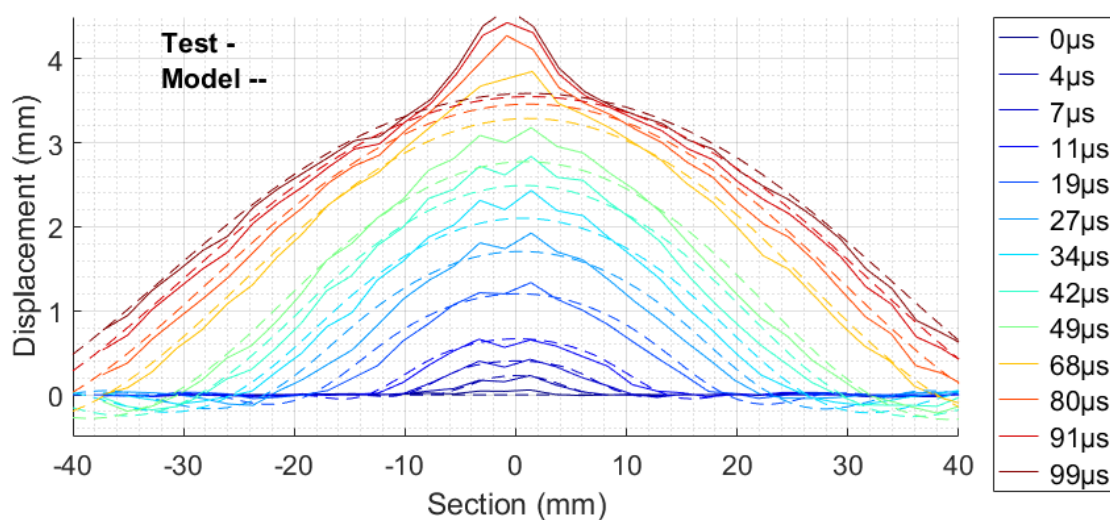elation linéaire entre la loi de décroissance de la pression et la variation de la rigidité de ces éléments. Pour un même type de peinture, on l'a donc linéairement reliée à l'épaisseur de peinture et pour le stratifié, à son module de flexion calculé à partir de la théorie classique des stratifiés [79]. Là encore, la déflexion du panneau a été bien prédite avec cette approche simple.

Avec cette bonne prédiction du chargement mécanique généré par la foudre, nous avons confronté les dommages expérimentaux mesurés avec ceux prédits par notre modèle de simulation numérique représentant les plis par des couches d'éléments volumiques et les interfaces par des liaisons cohésives. Nous avons démontré les limites d'un modèle basé sur des caractérisations statiques des résistances mécaniques et un délaminage important est présent dans toute l'épaisseur de stratifié ce qui n'est pas le cas de l'essai. En effet, la tenue du cohésif est trop faible par rapport à un chargement dynamique. Le travail effectué par Berthe a démontré une dépendance de l'interface mais aussi des propriétés du pli lui-même sur la vitesse de déformation [80]. Afin de vérifier ce point, nous avons donc choisi une valeur d'amorçage de l'ouverture du cohésif deux fois plus élevée pour simuler des propriétés dites dynamiques. Dans les deux cas, la propagation du délaminage est sous-estimée.

97 cm²   **120 cm²**   **76 cm²**

Static model   **Test**   **Dynamic model**
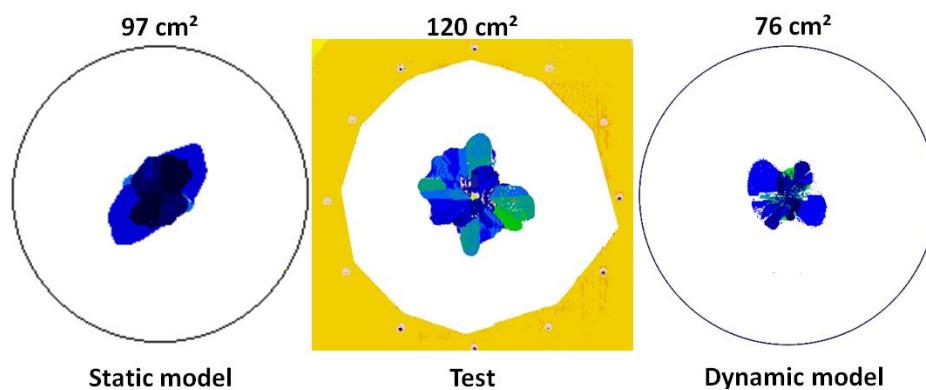
Figure 45 Comparaison de la surface projetée du délaminage entre le test (centre) et le résultat équivalent du modèle (1ms) avec une interface cohésive statique du côté gauche et une interface cohésive dynamique du côté droit

Le chargement mécanique généré par un coup de foudre et sa propagation dans le panneau n'est pas une sollicitation purement dynamique : il s'agit plutôt d'un mode mixte allant de la sollicitation dynamique à la sollicitation statique. Par conséquent, le modèle d'interface doit tenir compte de la dépendance des critères d'amorçage et de propagation des dommages par rapport au taux de contrainte $\dot{\sigma}$. Afin de caractériser cette tendance, la méthode proposée par Gay pourrait être utilisée [81]. Cependant, ce modèle n'est pas possible dans Abaqus® avec l'outil d'interface cohésif. Le développement d'une loi définie par l'utilisateur via une routine est nécessaire ainsi que la caractérisation de cette loi avec des tests dédiés.

6.4 Confinement de l'explosion par la peinture

Afin de prédire la relaxation de la pression d'explosion au lieu de notre étalonnage, nous avons développé un élément d'explosion en 3D avec une équation d'état. Cette couche 3D simule l'explosion de la protection. Par conséquent, notre méthodologie finale est basée sur le développement d'une VUMAT dédiée à notre couche explosive qui gérera trois états différents :

1. L'état élastique avant l'explosion :
   $\sigma = E\varepsilon$ avec σ la contrainte, E le module d'élasticité et ε la déformation
2. Augmentation rapide de la pression due à l'explosion :
   $P = \lambda(t - t_0)$ avec t_0 le temps de déclenchement de l'explosion, $\lambda = P_{max}/\Delta t$, P_{max} la pression maximale de l'explosion et Δt le temps pour atteindre le maximum choisi égal à 0,1 μs
3. État d'expansion du gaz qui a été choisi selon la loi des gaz parfaits :
   $P = (\gamma-1)\rho E_m$ avec $\gamma = 5/3$, ρ la masse volumique et E_m l'énergie massique d'explosion

L'explosion libre sur le panneau est illustrée ci-dessous :
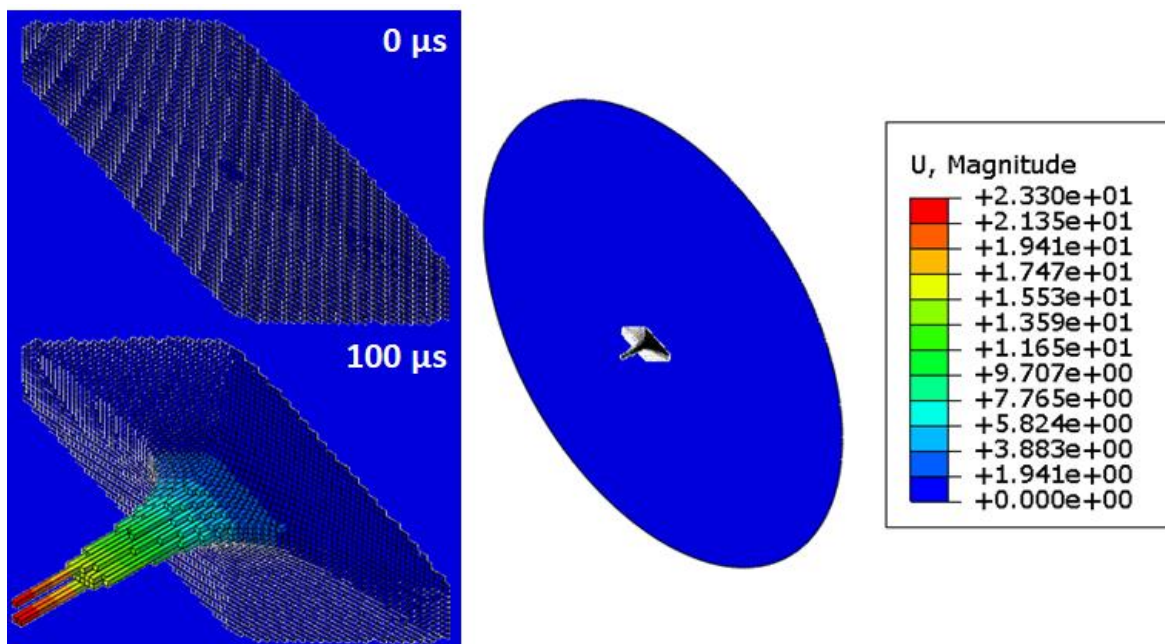
Figure 46 Explosion libre sur plaque composite

Il est ensuite possible d'appliquer une couche de peinture sur le dessus afin de simuler le confinement. L'explosion 3D a été validée, mais la pression d'explosion dans l'élément n'a pas été correctement transférée à la peinture et à la structure. Avec la résolution de ce problème purement liée à l'outil de simulation numérique, il sera possible de simuler le confinement de l'explosion et sa charge sur la structure.

6.5 Endommagement interne

Enfin, il ne faut pas oublier les dégâts dans le composite dus à la source thermique du coup de foudre. Lorsque l'arc de foudre est contraint, une partie du courant circule dans la structure, générant un échauffement par effet Joule. L'étude de ces dommages sur un panneau non protégé a démontré l'effet très local de cette source. Pour un cas sévère avec un confinement dû à une peinture d'1mm d'épaisseur, l'endommagement thermique était limité au centre jusqu'au 4ème pli du stratifié composé de 13 plis.

Figure 47 Endommagement interne pour une configuration sévère: CFRP (13plis) + ECF195 + 1000µm de peinture

Pour notre structure de référence qui comporte 400µm de peinture, l'endommagement thermique a été limité à la première couche, ce qui valide l'utilisation d'un chargement mécanique uniquement pour la prédiction de l'endommagement dans le composite.

7. Conclusion et perspectives

Pour un avion fabriqué en composite, il est essentiel de prendre en considération les menaces de la foudre lors de la conception de la structure. Contrairement à une structure métallique, la faible conductivité électrique de la structure composite rend ce matériau vulnérable aux coups de foudre. Les dommages induits peuvent être très importants. Visuellement, la peau de l'avion est brûlée, avec des fibres cassées et de la résine détériorée. Les dommages les plus graves, cependant, sont cachés : les couches de composite sont délaminées et fissurées sur une surface plus grande que les dommages visibles. Après un violent coup de foudre, la structure doit encore supporter les charges de vol avec ses propriétés mécaniques amoindries par ce dommage critique, donc sans défaillance complète afin d'assurer un vol et un atterrissage en toute sécurité. Pour cette raison, une protection métallique est généralement intégrée sur sa surface extérieure afin de dévier le courant de la foudre et de limiter les dégâts. Cependant, l'efficacité de la protection est compromise par la présence d'un revêtement de peinture sur la surface extérieure. Les dégâts causés par la foudre sont donc difficiles à prévoir car ils dépendent de ces trois éléments : la structure composite, la protection de la surface métallique et la peinture. Cette dépendance rend la prédiction des dommages très complexe. Afin de démontrer la conformité de la structure, des tests de foudre en laboratoire sont effectués sur un stratifié composite simplifié. Toutefois, ces campagnes d'essais sont coûteuses et longues. L'optimisation de la structure

composite et de sa protection est une contrainte industrielle qui diminue la marge de résistance à la foudre. Par conséquent, il est crucial de comprendre le phénomène de foudroiement et la génération de dommages dans la structure composite.

L'étude des différentes forces et de la littérature nous a amenés à la conclusion que les dommages les plus préjudiciables, c'est-à-dire le délaminage, étaient principalement dus à un facteur : l'explosion de la protection foudre confinée par la peinture. Afin de comprendre le mécanisme des dommages causés par la foudre dans une structure composite d'avion, il est nécessaire d'étudier ce problème dans son ensemble.

D'un point de vue scientifique, les questions abordées dans cette étude sont les suivantes : pour la conception d'un véritable composite d'avion, quelles sont les contraintes de la foudre qui vont générer des dommages ? Comment analyser l'interaction entre les différents contributeurs ? Comment quantifier l'amplitude et la distribution de ces contraintes ? Peut-on simplifier ce problème complexe en une étude mécanique afin de prévoir les dommages dans la structure composite ?

L'approche développée dans le cadre de cette thèse pour comprendre l'ensemble du mécanisme des dommages causés par la foudre pour la conception avion est basée sur une décomposition de ce phénomène afin de limiter la complexité et de permettre l'étude de chaque paramètre. Cette compréhension a ensuite été reconstruite afin de dresser un tableau complet de la génération des contraintes dues à la foudre sur une structure composite. Nous avons simplifié le coup de foudre sur une structure composite protégée et peinte en un chargement mécanique de surface et démontré notre capacité à prédire la variation de ce chargement avec l'épaisseur de la peinture et la rigidité de la structure par rapport à un cas de référence. En outre, le dommage le plus préjudiciable, c'est-à-dire le paramètre de l'évaluation de la capacité de charge en vol, est le délaminage. L'étude des dommages dans le stratifié a montré que les dommages thermiques dans le composite n'ont qu'une influence mineure sur la génération complète des dommages. Parmi les différentes sources mécaniques, il a été démontré que le principal facteur contributif est l'explosion de la protection foudre confinée par la peinture. Il est donc possible de simplifier la contrainte de la foudre en un chargement mécanique afin d'évaluer les dommages dans la structure.

Le modèle développé pour le chargement mécanique est basé sur des caractérisations expérimentales. Dans la perspective de cette recherche, plusieurs développements peuvent être envisagés afin de construire un modèle de prédiction complet et de supprimer la dépendance aux expériences.

Tout d'abord, le profil d'explosion pourrait être prédit en simulant l'entrée du courant de foudre dans la protection foudre. Pour ce faire, un modèle 3D complet de l'arc en interaction avec la protection métallique mais aussi avec la présence de peinture est nécessaire. Cela nécessiterait l'amélioration de la théorie MHD pour l'application du cas de la foudre avec un

courant, une pression et une température de l'arc élevés. Une autre difficulté consistera à modéliser l'interaction de l'arc avec une interface changeante. La vaporisation de la protection métallique interagit avec l'arc mais aussi avec la peinture qui forme une barrière pour l'expansion de l'arc. En outre, la distribution des dommages thermiques dans la structure composite pourrait être mieux analysée grâce à une meilleure évaluation de l'entrée du courant de foudre dans le composite et de sa distribution.

Ensuite, la pression de l'explosion de la protection métallique pourrait être prédite par la théorie proposée par Chung [62] qui couple les équations MHD avec une équation d'état étendue du cuivre. Par conséquent, avec la connaissance de la densité du courant de foudre et de la forme d'onde, il sera possible de prédire la pression et l'énergie de l'explosion. Une autre approche qui soutiendrait un modèle d'explosion est la caractérisation des paramètres de Jones-Wilkins-Lee à partir d'un test dédié sur l'explosion d'un fil de cuivre [82].

Il a été démontré que le revêtement extérieur, ici la peinture, est un paramètre clé de l'amplitude et de la distribution de l'explosion. La caractérisation mécanique de la peinture a fourni des informations utiles pour la construction d'un modèle hyperélastique, mais des tests supplémentaires seront nécessaires pour compléter sa validation. La prise en compte des propriétés visqueuses et dépendantes de la température de la peinture est également un développement possible. La rupture de la peinture peut être simulée avec des interfaces cohésives calibrées avec les tests de traction et de déchirure effectués dans cette thèse.

La variation du profil de pression de l'explosion due à sa libération avec l'éjection de peinture pourrait être prédite avec l'équation d'état d'explosion que nous avons développée grâce à une VUMAT une fois que le problème numérique lié aux interfaces entre l'élément explosif et sa structure environnante, c'est-à-dire la peinture et le panneau composite, aura été résolu.

Enfin, la confrontation de notre modèle d'endommagement basé sur une caractérisation statique avec le délaminage enregistrée après un test de foudre a démontré la nécessité de développer un modèle d'endommagement dépendant de la vitesse de sollicitation, c'est-à-dire de la vitesse de contrainte et déformation. Le chargement mécanique généré par un coup de foudre est très dynamique et doit être lié à la propagation du choc dans une structure composite. En parallèle, un tel modèle nécessiterait des tests spécifiques pour la caractérisation des propriétés dynamiques.

Bibliographie

[1]   Xu, Y., Zhu, J., Wu, Z., Cao, Y., Zhao, Y., and Zhang, W. "A Review on the Design of Laminated Composite Structures: Constant and Variable Stiffness Design and Topology Optimization." *Advanced Composites and Hybrid Materials*, 2018. https://doi.org/10.1007/s42114-018-0032-7.

[2]   Plumer, J. A. *Aicraft Lightning Protection Handbook*. Lightning Technologies, Inc., 1989.

[3]   EUROCAE. *ED-84: Aircraft Lightning Environment And Related Test Waveforms*. 1997.

[4]   EASA. Certification Specifications and Acceptable Means of Compliance for Large Aeroplanes CS-25 Amendment 24.

[5]   EUROCAE. *ED-91: Aircraft Lightning Zoning*. 2006.

[6]   SAE International. ARP5414B: Aircraft Lightning Zoning.

[7]   SAE International. ARP5412B: Aircraft Lightning Environment and Related Test Waveforms.

[8]   EUROCAE. *ED-105: Aircraft Lightning Test Methods*. 2005.

[9]   SAE International. ARP5416: Aircraft Lightning Test Methods.

[10]   Hirano, Y., Katsumata, S., Iwahori, Y., and Todoroki, A. "Artificial Lightning Testing on Graphite/Epoxy Composite Laminate." *Composites Part A: Applied Science and Manufacturing*, Vol. 41, No. 10, 2010, pp. 1461–1470. https://doi.org/10.1016/j.compositesa.2010.06.008.

[11]   Li, Y., Li, R., Lu, L., and Huang, X. "Experimental Study of Damage Characteristics of Carbon Woven Fabric/Epoxy Laminates Subjected to Lightning Strike." *Composites Part A: Applied Science and Manufacturing*, Vol. 79, 2015, pp. 164–175. https://doi.org/10.1016/j.compositesa.2015.09.019.

[12]   Sun, J., Yao, X., Tian, X., Chen, J., and Wu, Y. "Damage Characteristics of CFRP Laminates Subjected to Multiple Lightning Current Strike." *Applied Composite Materials*, Vol. 26, No. 3, 2019, pp. 745–762. https://doi.org/10.1007/s10443-018-9747-4.

[13]   Feraboli, P., and Miller, M. "Damage Resistance and Tolerance of Carbon/Epoxy Composite Coupons Subjected to Simulated Lightning Strike." *Composites Part A: Applied Science and Manufacturing*, Vol. 40, No. 6, 2009, pp. 954–967. https://doi.org/10.1016/j.compositesa.2009.04.025.

[14]   Abdelal, G., and Murphy, A. "Nonlinear Numerical Modelling of Lightning Strike Effect on Composite Panels with Temperature Dependent Material Properties." *Composite Structures*, Vol. 109, 2014, pp. 268–278. https://doi.org/10.1016/j.compstruct.2013.11.007.

[15]   Gagné, M., and Therriault, D. "Lightning Strike Protection of Composites." *Progress in Aerospace Sciences*, Vol. 64, 2014, pp. 1–16. https://doi.org/10.1016/j.paerosci.2013.07.002.

[16]   Bigand, A., and Duval, Y. Quantification of the Mechanical Impact of Lightning Strike Protection Explosion Confined by Thick Paint. Presented at the ICOLSE, Nagoya, 2017.

[17]   Sousa Martins, R. *Etude Expérimentale et Théorique d'un Arc de Foudre et Son Interaction Avec Un Matériau Aéronautique*. Université Paris-Saclay, 2016.

[18]   Guo, Y., Xu, Y., Wang, Q., Dong, Q., Yi, X., and Jia, Y. "Enhanced Lightning Strike Protection of Carbon Fiber Composites Using Expanded Foils with Anisotropic Electrical Conductivity." *Composites Part A: Applied Science and Manufacturing*, Vol. 117, 2019, pp. 211–218. https://doi.org/10.1016/j.compositesa.2018.11.022.

[19]   Lepetit, B., Escure, C., Guinard, S., Revel, I., and Peres, G. Thermo-Mechanical Effects Induced by Lightning on Carbon Fiber Composite Materials. Presented at the ICOLSE, Oxford, UK, 2011.

[20]   Karch, C. Contributions of Lightning Current Pulses to Mechanical Damage of CFRP Structures. Presented at the ICOLSE, Toulouse, 2015.

[21]   Espinosa, C., Bhoosnurmath, H., López, A. C., and Lachaud, F. Numerical Modelling of a Lightning Strike on a Protected Composite Panel. Presented at the ICOLSE, Nagoya, 2017.

[22]   Soulas, F. *Développement d'un Modèle Mécanique Pour La Prédiction Des Dommages de Panneaux Composites Aéronautiques Soumis à Un Choc Foudre*. Toulouse, ISAE, 2016.

[23]   Bigand, A., Espinosa, C., Bauchire, J. M., Flourens, F., and Lachaud, F. Lightning Damage Assessment into Composite Based on Surface Explosion and Fiber Breakage. Presented at the International Conference on Composite Materials (ICCM22), Melbourne (Australia), 2019.

[24]   Rannou, J., Huchette, C., Hurmane, A., and Tholin, F. An Analysis of Lightning Direct Effects on CFRP Panels. Part II, the Electro-Thermo-Mechanical Simulation Strategy. Presented at the ICOLSE, Nagoya, 2017.

[25]   Huchette, C., Rannou, J., Roche, J., Lapeyronnie, P., Beauchêne, P., and Chemartin, L. An Analysis of Lightning Direct Effects on CFRP Panels. Part I, the Experimental and Material Point of View. Presented at the ICOLSE, Nagoya, 2017.

[26]   Chemartin, L., Lalande, P., Peyrou, B., Chazottes, A., Elias, P. Q., Delalondre, C., Cheron, B. G., and Lago, F. "Direct Effects of Lightning on Aircraft Structure: Analysis of the Thermal, Electrical and Mechanical Constraints." *AerospaceLab*, No. 5, 2012, p. p–1.

[27]   Karch, C., Arteiro, A., and Camanho, P. P. "Modelling Mechanical Lightning Loads in Carbon Fibre-Reinforced Polymers." *International Journal of Solids and Structures*, Vol. 162, 2019, pp. 217–243. https://doi.org/10.1016/j.ijsolstr.2018.12.013.

[28]   Lago, F. *Modélisation de l'interaction Entre Un Arc Électrique et Une Surface : Application Au Foudroiement d'un Aéronef*. UNIVERSITE TOULOUSE III, 2004.

[29]   Lepetit, B., Soulas, F., Guinard, S., Revel, I., and Peres, G. "Analysis of Composite Panel Damages Due to a Lightning Strike : Mechanical Effects." *ICOLSE 2013*, , 2013.

[30]   Karch, C., Schreiner, M., Honke, R., and Wolfrum, J. Shock Waves from a Lightning Discharge. Presented at the 2018 34th International Conference on Lightning Protection (ICLP), 2018.

[31]   Wang, J., Yuan, P., Guo, F., Qie, X., Ouyang, Y., and Zhang, Y. "The Spectra and Temperature of Cloud Lightning Discharge Channel." *Science in China Series D: Earth Sciences*, Vol. 52, No. 7, 2009, pp. 907–912. https://doi.org/10.1007/s11430-009-0108-x.

[32] Foster, P., Abdelal, G., and Murphy, A. "Understanding How Arc Attachment Behaviour Influences the Prediction of Composite Specimen Thermal Loading during an Artificial Lightning Strike Test." *Composite Structures*, Vol. 192, 2018, pp. 671–683. https://doi.org/10.1016/j.compstruct.2018.03.039.

[33] Guo, Y., Dong, Q., Chen, J., Yao, X., Yi, X., and Jia, Y. "Comparison between Temperature and Pyrolysis Dependent Models to Evaluate the Lightning Strike Damage of Carbon Fiber Composite Laminates." *Composites Part A: Applied Science and Manufacturing*, Vol. 97, 2017, pp. 10–18. https://doi.org/10.1016/j.compositesa.2017.02.022.

[34] Wang, F. S., Ji, Y. Y., Yu, X. S., Chen, H., and Yue, Z. F. "Ablation Damage Assessment of Aircraft Carbon Fiber/Epoxy Composite and Its Protection Structures Suffered from Lightning Strike." *Composite Structures*, Vol. 145, 2016, pp. 226–241. https://doi.org/10.1016/j.compstruct.2016.03.005.

[35] Ogasawara, T., Hirano, Y., and Yoshimura, A. "Coupled Thermal-Electrical Analysis for Carbon Fiber/Epoxy Composites Exposed to Simulated Lightning Current." *Composites Part A: Applied Science and Manufacturing*, Vol. 41, No. 8, 2010, pp. 973–981. https://doi.org/10.1016/j.compositesa.2010.04.001.

[36] Dong, Q., Guo, Y., Sun, X., and Jia, Y. "Coupled Electrical-Thermal-Pyrolytic Analysis of Carbon Fiber/Epoxy Composites Subjected to Lightning Strike." *Polymer*, Vol. 56, 2015, pp. 385–394. https://doi.org/10.1016/j.polymer.2014.11.029.

[37] Dong, Q., Guo, Y., Chen, J., Yao, X., Yi, X., Ping, L., and Jia, Y. "Influencing Factor Analysis Based on Electrical-Thermal-Pyrolytic Simulation of Carbon Fiber Composites Lightning Damage." *Composite Structures*, Vol. 140, 2016, pp. 1–10. https://doi.org/10.1016/j.compstruct.2015.12.033.

[38] Chippendale, R. *Modelling of the Thermal Chemical Damage Caused to Carbon Fibre Composites*. University of Southampton, 2013.

[39] Tholin, F., Chemartin, L., and Lalande, P. Numerical Investigation of the Interaction of a Lightning and an Aeronautic Skin during the Pulsed Arc Phase. Presented at the ICOLSE, Toulouse, 2015.

[40] Murphy, A. Lightning Strike Direct Effects. In *Polymer Composites in the Aerospace Industry - Second Edition*, Woodhead Publishing, 2020, pp. 561–591.

[41] Braginskii, S. I. "Theory of the Development of a Spark Channel." *J. Exptl. Theoret. Phys*, Jan 02, 1958, pp. 1548–1557.

[42] Wang, F. S., Ji, Y. Y., Yu, X. S., Chen, H., and Yue, Z. F. "Ablation Damage Assessment of Aircraft Carbon Fiber/Epoxy Composite and Its Protection Structures Suffered from Lightning Strike." *Composite Structures*, Vol. 145, 2016, pp. 226–241. https://doi.org/10.1016/j.compstruct.2016.03.005.

[43] Liu, Z. Q., Yue, Z. F., Wang, F. S., and Ji, Y. Y. "Combining Analysis of Coupled Electrical-Thermal and BLOW-OFF Impulse Effects on Composite Laminate Induced by Lightning Strike." *Applied Composite Materials*, Vol. 22, No. 2, 2015, pp. 189–207. https://doi.org/10.1007/s10443-014-9401-8.

[44] Gineste, P.-N., Clerc, R., Castanie, C., Andreu, H., and Buzaud, E. Assessment of Lightning Direct Effects Damages by Modelling Techniques. Presented at the ICOLSE, Pittsfield, USA, 2009.

[45] Kawakami, H. *Lightning Strike Induced Damage Mechanisms of Carbon Fiber Composites*. Ph.D. University of Washington, United States -- Washington, 2011.

[46] Muñoz, R., Delgado, S., González, C., López-Romano, B., Wang, D.-Y., and LLorca, J. "Modeling Lightning Impact Thermo-Mechanical Damage on Composite Materials." *Applied Composite Materials*, Vol. 21, No. 1, 2014, pp. 149–164. https://doi.org/10.1007/s10443-013-9377-9.

[47] Soulas, F., Espinosa, C., Lachaud, F., Guinard, S., Lepetit, B., Revel, I., and Duval, Y. "A Method to Replace Lightning Strike Tests by Ball Impacts in the Design Process of Lightweight Composite Aircraft Panels." *International Journal of Impact Engineering*, Vol. 111, 2018, pp. 165–176.

[48] Uman, M. A. "The Peak Temperature of Lightning." *Journal of Atmospheric and Terrestrial Physics*, Vol. 26, No. 1, 1964, pp. 123–128.

[49] Pechereau, F., Tholin, F., Zaepffel, C., Sousa Martins, R., and Lalande, P. MHD Simulation of a Lightning Column during the Pulsed Arc Phase. Presented at the ICOLSE, Wichita (USA), 2019.

[50] Aleksandrov, N. L., Bazelyan, É. M., and Shneider, M. N. "Effect of Continuous Current during Pauses between Successive Strokes on the Decay of the Lightning Channel." *Plasma Physics Reports*, Vol. 26, No. 10, 2000, pp. 893–901. https://doi.org/10.1134/1.1316830.

[51] Peyrou, B. *Modélisation MHD d'un Arc de Foudroiement d'aéronef*. thesis. Rouen, 2012.

[52] Vacquie, S. *Arc Electrique*. Eyrolles, 2000.

[53] Vorob'ev, V. S., Malyshenko, S. P., Tkachenko, S. I., and Fortov, V. E. "What Initiates the Explosion of a Current-Carrying Conductor?" *JETP Letters*, Vol. 75, No. 8, 2002, pp. 373–377.

[54] Borisevich, A. E., and Cherkas, S. L. "Effect of the Conductor Radius on the Electric Explosion Dynamics: Magnetohydrodynamic Simulation." *Technical Physics*, Vol. 57, No. 10, 2012, pp. 1380–1386. https://doi.org/10.1134/S1063784212100027.

[55] Liu, H., Zhao, J., Wu, Z., Zhang, L., and Zhang, Q. "Experimental Investigations on Energy Deposition and Morphology of Exploding Aluminum Wires in Argon Gas." *Journal of Applied Physics*, Vol. 125, No. 10, 2019, p. 103301. https://doi.org/10.1063/1.5078811.

[56] Grinenko, A. U. Experimental and Theoretical Study of Strongly Coupled Copper Plasma Generated by Underwater Electrical Wire Explosion. In *6th International Conference on Dense Z-Pinches*, No. 808, 2006, pp. 91–94.

[57] Romanova, V. M., Ivanenkov, G. V., Mingaleev, A. R., Ter-Oganesyan, A. E., Shelkovenko, T. A., and Pikuz, S. A. "Electric Explosion of Fine Wires: Three Groups of Materials." *Plasma Physics Reports*, Vol. 41, No. 8, 2015, pp. 617–636. https://doi.org/10.1134/S1063780X15080085.

[58] Han, R., Zhou, H., Wu, J., Qiu, A., Ding, W., and Zhang, Y. "Relationship between Energy Deposition and Shock Wave Phenomenon in an Underwater Electrical Wire Explosion." *Physics of Plasmas*, Vol. 24, No. 9, 2017, p. 093506. https://doi.org/10.1063/1.4989790.

[59] Sinars, D. B., Hu, M., Chandler, K. M., Shelkovenko, T. A., Pikuz, S. A., Greenly, J. B., Hammer, D. A., and Kusse, B. R. "Experiments Measuring the Initial Energy

Deposition, Expansion Rates and Morphology of Exploding Wires with about 1 KA/Wire." *Physics of Plasmas*, Vol. 8, No. 1, 2001, pp. 216–230. https://doi.org/10.1063/1.1323759.

[60]   Cunrath, R. J. M., and Wickert, M. Numerical Analysis of the Response of Thick Wires to Extreme Dynamic Electro-Mechanical Loads. Presented at the 2014 17th International Symposium on Electromagnetic Launch Technology, 2014.

[61]   D'Angola, A., Colonna, G., Gorse, C., and Capitelli, M. "Thermodynamic and Transport Properties in Equilibrium Air Plasmas in a Wide Pressure and Temperature Range." *The European Physical Journal D*, Vol. 46, No. 1, 2008, pp. 129–150. https://doi.org/10.1140/epjd/e2007-00305-4.

[62]   Chung, K.-J., Lee, K., Hwang, Y. S., and Kim, D.-K. "Numerical Model for Electrical Explosion of Copper Wires in Water." *Journal of Applied Physics*, Vol. 120, No. 20, 2016, p. 203301. https://doi.org/10.1063/1.4968396.

[63]   Airbus Industrie. AIMS 04-04-014 - Airbus Industrie Material Specification - External Paint System: Primer+intermediate Coat+top Coat Material Specification.

[64]   International Standard. ISO 6272 - Paints and Varnishes – Rapid-Deformation (Impact Resistance) Tests – Part 1: Falling-Weight Test, Large-Area Indenter.

[65]   International Standard. ISO1518 - Paints and Varnishes – Determination of Scratch Resistance – Part 1: Constant- Loading Method.

[66]   International Standard. ISO1519 - Paints and Varnishes — Bend Test (Cylindrical Mandrel).

[67]   ASTM International. ASTM D4708 - Preparation of Uniform Free Films of Organic Coatings.

[68]   International Standard. *ISO 527-1: Plastics — Determination of Tensile Properties — Part 1: General Principles*. 2012.

[69]   International Standard. *ISO 527-3: Plastics — Determination of Tensile Properties — Part 3: Test Conditions for Films and Sheets*. Bsi., 1996.

[70]   Peyre, P., Berthe, L., Vigual, V., Popa, I., and Baudin, T. "Analysis of Laser Shock Waves and Resulting Surface Deformations in an Al–Cu–Li Aluminum Alloy." *J. Phys. D: Appl. Phys.*, No. 45, 2012. https://doi.org/10.1088/0022-3727/45/33/335304.

[71]   Arrigoni, M., Schalk, M., Carrère, N., Alexandru, A., Cojan, B., Boustie, M., and Berthe, L. "Étude Expérimentale et Numérique de l'adhérence d'interfaces Collées Soumises à Des Ondes Mécaniques Brèves et Intenses." *Revue des composites et des matériaux avancés*, No. 2, 2015, pp. 201–223.

[72]   Zagouri, D., and Boustie, M. *Ondes de Choc Dans Les Solides*. SimChoc S.A.S., 2019.

[73]   Verron, E. "Modèles hyperélastiques pour le comportement mécanique des élastomères." *Techniques de l'ingénieur - "Plastiques et composites,"* Mar 10, 2018.

[74]   Ilyas, M. *Damage Modeling of Carbon Epoxy Laminated Composites Submitted to Impact Loading*. 2010.

[75]   ASTM International. *ASTM D5528-01: Test Method for Mode I Interlaminar Fracture Toughness of Unidirectional Fiber-Reinforced Polymer Matrix Composites*. ASTM International, 2001.

[76]   International Standard. ISO 15024 - Fibre-Reinforced Plastic Composites — Determination of Mode I Interlaminar Fracture Toughness, GIC, for Unidirectionally Reinforced Materials.

[77] Airbus Industrie. *AITM 1-0005: Determination of Interlaminar Fracture Toughness Energy – Mode I (G1C Test)*. 2015.

[78] Airbus Industrie. *AITM 1-0006: Determination of Interlaminar Fracture Toughness Energy – Mode II (G2C Test)*. 1994.

[79] Gay, D. *Matériaux Composites*. 1997.

[80] Berthe, J., Joudon, V., and Portemont, G. "Strain Rate Dependencies of Intra and Inter Laminar Properties of Organic Matrix Composite Materials." *Revue des composites et des matériaux avancés*, No. 2, 2015, pp. 117–130.

[81] Gay, E., Berthe, L., Boustie, M., Arrigoni, M., and Buzaud, E. "Effects of the Shock Duration on the Response of CFRP Composite Laminates." *Journal of Physics D: Applied Physics*, , 2014.

[82] Castedo, R., Natale, M., López, L. M., Sanchidrián, J. A., Santos, A. P., Navarro, J., and Segarra, P. "Estimation of Jones-Wilkins-Lee Parameters of Emulsion Explosives Using Cylinder Tests and Their Numerical Validation." *International Journal of Rock Mechanics and Mining Sciences*, Vol. 112, 2018, pp. 290–301. https://doi.org/10.1016/j.ijrmms.2018.10.027.

Titre: Evaluation de l'endommagement dans les structures composites en aéronautique généré par la contrainte foudre

Résumé:
L'utilisation des matériaux composites dans l'industrie aéronautique s'étant largement étendue, le dimensionnement de ces structures et de leur protection vis-à-vis de la foudre est devenu un enjeu majeur. Il est important de pouvoir développer des outils prédictifs permettant d'obtenir une conception de structure répondant aux critères de certification avec des temps et coûts de conception maitrisés. L'interaction de la foudre avec une structure composite est un phénomène multiphysique complexe, avec une difficulté ajoutée par la présence d'une protection métallique en surface et d'une couche de peinture. Dans ce contexte, cette étude a visé à développer la compréhension par rapport aux forces générées par la foudre et d'en évaluer ses conséquences quant à l'endommagement du composite. Dans cet objectif, le phénomène a d'abord été décomposé pour en étudier ses différentes parties et définir l'impact des interactions. Dans un premier temps, l'arc libre a été comparé au pied d'arc en interaction avec différents substrats permettant de définir un modèle de vaporisation de la protection foudre. Dans un second temps, la surpression générée par l'explosion de la protection en surface lors de la vaporisation a été évaluée pour définir des profils de pression spatio-temporels. Dans un troisième temps, une caractérisation mécanique de la peinture a été développée afin de quantifier son effet de confinement sur l'explosion de surface. A chaque étape, une théorie a été développée et analysée via des modèles numériques et des essais. Enfin, ces trois différentes briques ont été rassemblées dans un modèle mécanique simulant l'impact foudre sur une structure composite afin d'en prédire l'endommagement. De plus, une loi utilisateur a été développée pour appliquer ce chargement complexe ainsi qu'une loi d'endommagement. Ces modèles sont comparés aux résultats d'essai foudre en laboratoire afin d'en déterminer les limites de validité et leur capacité à prédire l'endommagement.

Mots clés: Foudre, Composite, Aéronautique, Délaminage, Dynamique rapide non linéaire, Peinture

Title: Damage assessment on aircraft composite structure due to lightning constraints

Abstract:
As composite materials are now widely used in the aeronautical industry, the sizing of these structures and their protection against lightning has become a major issue. It is important to develop predictive tools to obtain a structure concept that meets certification requirements with a controlled time and cost during the design phase. The interaction of lightning with a composite structure is a complex multi-physics phenomenon, with a further difficulty due to the presence of a metallic protection on the surface and a layer of paint. In this context, this study aimed to develop an understanding of the forces generated by lightning and to assess its consequences in terms of damage to the composite. To this end, the phenomenon was first broken down to study its different components and define the impact of their interactions. In a first step, the free arc was compared to the arc root in interaction with different substrates to define a vaporisation model of the lightning protection. In a second step, the overpressure generated by the explosion of the surface protection during vaporisation was evaluated to define spatio-temporal pressure profiles. In a third step, a mechanical characterization of the paint was developed in order to quantify its confinement effect on the surface explosion. At each stage, a theory was developed and analysed via numerical models and tests. Finally, these three different bricks are brought together in a mechanical model simulating the lightning impact on a composite structure in order to predict the damage. In addition, a user subroutine has been developed to apply this complex loading as well as a damage law. These models are compared with lightning laboratory test results to determine their validity limits and their ability to predict the damage.

Keywords: Lightning, Composite, Aeronautics, Delamination, Transient non-linear Dynamics, Paint